



BINDING SERVICES
Tel +44 (0)29 2087 4949
Fax +44 (0)29 20371921
e-mail bindery@cardiff.ac.uk

Numerical Simulations of Binary Star Formation

David Anthony Hubber

A thesis submitted to
Cardiff University,
for the degree of

Doctor of Philosophy

October 2006

UMI Number: U584846

All rights reserved

INFORMATION TO ALL USERS

The quality of this reproduction is dependent upon the quality of the copy submitted.

In the unlikely event that the author did not send a complete manuscript and there are missing pages, these will be noted. Also, if material had to be removed, a note will indicate the deletion.



UMI U584846

Published by ProQuest LLC 2013. Copyright in the Dissertation held by the Author.
Microform Edition © ProQuest LLC.

All rights reserved. This work is protected against
unauthorized copying under Title 17, United States Code.



ProQuest LLC
789 East Eisenhower Parkway
P.O. Box 1346
Ann Arbor, MI 48106-1346

Acknowledgements

I would first like to thank the members of the Cardiff star formation group who have helped me through my PhD. First and foremost, my thanks go to my supervisor, Anthony Whitworth, who has guided me through my PhD and various undergraduate projects for the best part of six years. His very mathematical approach to analysing problems has certainly rubbed off on me. I also appreciate his patience with my grammar in the early drafts of this thesis. Simon Goodwin, who wrote the SPH code DRAGON, was always willing to help when I got stuck with his program, and also provided me with plenty of conversations about star formation which has helped me in this work. I would also like to thank other members of the star formation group, particularly Rhianne Attwood, Annabel Cartwright, David Nutter, Dimitrios Stamatellos, Jason Kirk and Derek Ward-Thompson for helpful discussions during the course of my PhD.

I thank Sverre Aarseth for taking the time to guide me through his NBODY codes and for helpful correspondence. I would like to thank Rhianne Attwood, Edward Gomez, Haley Gomez, and Simon Goodwin for useful comments on parts of my thesis chapters. I owe a big debt to Haley Gomez, who has helped me more than anyone else with the non-star formation parts of my PhD and pretty much everything else I've done in the last four years. I certainly owe her plenty of favours.

I thank my good friend and flatmate Ian Bacchus, and also my other good friends Tim Waskett and Sarah Roberts for many entertaining conversations and discussions. I would also like to thank some of the former members of the department like Dean Trolley, Kris Wojciechowski and Hannah Loebel who helped me through the tough first year.

I would like to thank my family, my mother Jackie and my brother Chris for their patience and support during my time in University. I should also apologise to Francis for allowing my PhD to take up so much of my time.

Abstract

Binary star formation is the dominant mode of star formation, in contrast to the traditional picture of single star formation. The work in this thesis investigates the properties of binary stars with the aid of numerical simulations, using N-body and Smoothed Particle Hydrodynamics codes.

First, we develop a simple model of isolated binary star formation assuming prestellar cores fragment due to rotational instabilities into a ring of \mathcal{N} (≤ 6) stars. We follow the decay of this small-N cluster into singles and multiple systems using the N-body code NBODY3. We can reproduce most of the observed stellar and binary properties of young stars, including the high multiplicity and wide separation distribution, in low-mass star forming regions like Taurus. We extend this further into a model of clustered binary star formation assuming 100 small-N clusters form in fractal clusters of radius ~ 1 pc, similar to many young embedded clusters. We follow the dynamical interactions of these clusters using the N-body code NBODY6. We find that disruptive binary-binary encounters in dense clusters can explain the differences between binary properties in low-density and high-density star forming regions.

We develop a new test of Smoothed Particle Hydrodynamics (SPH) called the Jeans Test. We demonstrate that SPH correctly models fragmentation and that under-resolved SPH simulations suppress real fragmentation rather than promote artificial fragmentation. Thus binary and multiple systems produced in SPH simulations are real and not the result of numerical effects. Finally, we perform simulations of turbulent prestellar cores in the context of binary star formation. We extend the work of Goodwin, Whitworth & Ward-Thompson (2004) by investigating $2.17 M_{\odot}$ and $4.34 M_{\odot}$ cores.

Contents

1	Introduction	1
1.1	Theoretical star formation	1
1.1.1	Binary and multiple systems	1
1.1.2	The life cycle of stars	2
1.1.3	The goals of this thesis	2
1.2	The main stages of star formation	2
1.2.1	Molecular clouds and star forming regions	3
1.2.2	Prestellar cores and Young stellar objects	4
1.2.3	Embedded clusters	6
1.2.4	Open clusters and OB associations	6
1.2.5	The Main Sequence	7
1.3	Numerical star formation	7
1.3.1	N-body simulations	8
1.3.2	Hydrodynamical codes	8
1.4	Overview of thesis	9
2	Binary Stars : Observations and Theory	11
2.1	Binary stars	11
2.1.1	Orbits of binary stars	12
2.1.2	Higher-order multiple systems	13
2.2	Orbital parameters and statistics of binary stars	14
2.3	Observational techniques	16
2.4	Surveys of Binary Stars	17
2.4.1	The galactic field	21
2.4.2	Star-forming regions	23
2.4.3	Young open clusters	28
2.4.4	Mass-ratios	30
2.4.5	Eccentricity	31

2.5	Theories of Binary Star Formation	32
2.5.1	Fission	32
2.5.2	Capture	32
2.5.3	Disc capture	33
2.5.4	Core fragmentation	33
2.5.5	Problems involving binary star formation	35
3	N-body codes	37
3.1	Newton's law of gravity	37
3.2	The NBODY codes	37
3.3	Integration scheme	38
3.3.1	Force Polynomials	38
3.3.2	Hermite scheme	39
3.4	Timesteps	41
3.4.1	Multiple particle timesteps	41
3.5	N-body units	42
3.6	Regularisation	42
3.6.1	The 2-body singularity and gravity softening	42
3.6.2	KS regularisation	43
3.6.3	Higher-order regularisation schemes	44
3.7	Ahmad-Cohen Neighbour scheme	44
3.8	Co-moving co-ordinates	45
3.9	Stellar evolution	45
3.10	Binary identification	45
4	Ring Fragmentation	47
4.1	Introduction	47
4.1.1	Previous N-body work	48
4.1.2	Ring fragmentation	49
4.2	Observations of cores	50
4.2.1	Core masses	50
4.2.2	Core radii	50
4.2.3	Core rotation	50
4.3	Outline of model	52
4.3.1	Assumptions and aims	52
4.3.2	The model	53
4.4	Dimensionless simulations	54

4.4.1	Initial Conditions	54
4.4.2	Numerical method	55
4.4.3	Parameters	55
4.4.4	Dissolution timescale	56
4.4.5	Multiplicity	56
4.4.6	The dimensionless separation distribution	57
4.4.7	Eccentricities	60
4.4.8	Mass-ratios	60
4.5	Convolving with the core-mass spectrum	62
4.5.1	The resultant IMF	62
4.5.2	Multiplicity	64
4.5.3	Eccentricity	65
4.5.4	Mass-ratio	66
4.6	Convolving with the distribution of core rotation rates	67
4.6.1	The binary separation distribution	67
4.6.2	Dissolution timescales	69
4.7	Summary	70
5	The evolution of binary properties in young clusters	73
5.1	Introduction	73
5.2	Observations of young clusters	74
5.2.1	Embedded clusters	74
5.2.2	The fractal properties of young clusters	74
5.3	Previous work on cluster dissolution	75
5.4	Model	76
5.4.1	Assumptions and Aims	76
5.4.2	Initial conditions	76
5.4.3	Numerical method	77
5.4.4	Parameters	78
5.5	Results	79
5.5.1	Standard runs : $N_{\text{CORES}} = 100$, $D_f = 2.5$, $R_c = 0.5 \text{ pc}$, 1.0 pc , 2.0 pc . .	81
5.5.2	Changing the fractal dimension : $N_{\text{CORES}} = 100$, $D_f = 1.5$, $R_c = 1.0 \text{ pc}$, 2.0 pc	85
5.6	Summary and Discussion	88

6	Smoothed Particle Hydrodynamics	91
6.1	Numerical Hydrodynamics	91
6.2	Basic principles of Smoothed Particle Hydrodynamics	92
6.3	Calculating vector properties in SPH	94
6.4	The kernel function	95
6.5	The smoothing length	97
6.6	The hydrodynamical equations in SPH	98
6.7	Artificial Viscosity	98
6.7.1	The Balsara switch	99
6.7.2	Time-dependent viscosity	100
6.8	Gravity in SPH	100
6.8.1	Tree-gravity	101
6.8.2	Kernel-softened gravity	103
6.8.3	Periodic gravity	104
6.9	Integration scheme	105
6.10	Simulating star formation using SPH	106
6.10.1	The Equation of State	106
6.10.2	Resolution criterion of SPH	107
6.10.3	Particle splitting	108
6.10.4	Sink particles	108
6.10.5	Correcting for the self-gravity of an individual SPH particle	109
7	Tests of SPH	111
7.1	Introduction	111
7.2	The isothermal Sod test	112
7.2.1	Standard artificial viscosity	112
7.2.2	Artificial viscosity with the Balsara switch	113
7.2.3	Time-dependent artificial viscosity	113
7.3	Colliding isothermal flows	116
7.3.1	Standard artificial viscosity	117
7.3.2	Artificial viscosity with the Balsara switch	118
7.3.3	Time-dependent artificial viscosity	119
7.4	Shear-flow test	121
7.4.1	Standard artificial viscosity	121
7.4.2	Artificial viscosity with the Balsara switch	121
7.4.3	Time-dependent artificial viscosity	123
7.5	Jeans instability test	123

7.5.1	Initial conditions	126
7.5.2	Results	127
7.5.3	Density and forces	127
7.5.4	Timescales	133
7.5.5	Including the correction term	133
7.6	Discussion	134
7.6.1	Artificial viscosity	134
7.6.2	Fragmentation	134
8	Binary formation from turbulent prestellar cores	137
8.1	Introduction	138
8.1.1	Previous work on turbulent star formation	138
8.2	Model	139
8.2.1	Assumptions and Aims	139
8.2.2	Initial conditions	140
8.2.3	Modelling turbulence in molecular clouds	140
8.2.4	Numerics	141
8.2.5	Setting up the initial conditions	142
8.2.6	Resolution	142
8.2.7	DRAGON features	143
8.2.8	Input parameters	143
8.3	Results	144
8.3.1	Number of objects formed	144
8.3.2	Mass distribution	144
8.3.3	Binary separation distribution	147
8.3.4	Eccentricity distribution	149
8.3.5	Mass-ratio distribution	149
8.4	Discussion	150
8.4.1	Multiplicity	150
8.4.2	Binary separation distribution	150
8.4.3	Eccentricity and mass-ratio distributions	150
8.4.4	Viscosity	151
8.4.5	Future work	151
8.5	Summary	151

9	Summary	153
9.1	Observations of Binary stars	153
9.2	Binary star formation from Ring Fragmentation	154
9.3	Binary star formation in a cluster environment	154
9.4	Tests of Smoothed Particle Hydrodynamics	155
9.5	Simulations of turbulent prestellar cores	156
9.6	Future work	156
9.6.1	N-body codes	156
9.6.2	N-body simulations	156
9.6.3	SPH codes	157
9.6.4	SPH simulations	157

List of Figures

1.1	The Ophiuchus molecular cloud observed in the Infra-red using IRAS (Wheelock et al. 1991, IRAS Sky Survey Atlas Explanatory Supplement). The grey-scale shows the intensity of thermal emission from dust (dark - low emission, light - high emission). This image shows the filamentary structure of a molecular cloud.	3
2.1	The possible orbits resulting from two-body interactions under gravity. (a) A circular orbit with eccentricity $e = 0$ for two bound objects. (b) An elliptical orbit with eccentricity $0 < e < 1$ for two bound objects. The main orbital parameters are shown: a - semi-major axis, b - semi-minor axis, c - distance between focus and centre of ellipse. (c) A parabolic (hyperbolic) orbit for 2 unbound objects with eccentricity $e = 1$ ($e \geq 1$).	12
2.2	Examples of common multiple systems. Circular orbits are used here for simplicity, with each diagram in the centre of mass frame. (a) An hierarchical triple system; stars 1 and 2 are part of a bound binary, which is represented by its centre of mass, A. Binary A and star 3 orbit their centre of mass as would 2 single stars in a binary system. (b) An hierarchical quadruple system; stars 1 and 2 form a bound binary system, A, and stars 3 and 4 form a bound binary system, B; Binaries A and B orbit their centre of mass as would 2 single stars in a binary. (c) A planetary multiple system; The mass of the central star, A, is much greater than that of the other stars; Stars 1, 2 and 3 orbit around the star A. . . .	13
2.3	(a) The observed separation distribution of field G-dwarf binaries (Duquennoy & Mayor 1991), which is fitted with a lognormal function given by Equation 2.8. This lognormal is used in all other figures of binary separation as a reference curve. (b) The observed separation distribution of field K-dwarf binaries (Mayor et al. 1992). (c) The observed separation distribution of field M-dwarf binaries (Fischer & Marcy 1992)	22

2.4	(a) Separation distribution of binaries in Taurus (Leinert et al. 1993) (b) Separation distribution of binaries in Taurus, including PMS binaries identified using the X-ray ROSAT survey (Köhler & Leinert 1998) (c) Separation distribution of binaries in ρ Ophiuchi (Barsony et al. 2003). (d) Separation distribution of binaries in ρ Ophiuchus (Ratzka et al. 2005). The DM91 lognormal fit to the separation distribution of G-dwarf field binaries is shown as a thin line for comparison.	24
2.5	Observations of the multiplicity of low-mass PMS stars in the Trapezium cluster (Prosser et al. 1994; Padgett et al. 1997; Scally et al. 1999; Köhler 2004). . . .	25
2.6	(a) Separation distribution of PMS binaries from the Ophiuchus, Lupus, Chamaeleon and Corona Australis star formation regions (Reipurth & Zinnecker 1993) (b) Observations of spectroscopic binaries in the Ophiuchus-Scorpius, Chamaeleon, Lupus and Corona Australis star formation regions (Melo 2003) combined with observations by Ghez et al. (1993) and Ghez et al. (1997) (c) Compilation of observations of the binary separation distribution for binaries in Taurus, Ophiuchus, Lupus, Chamaeleon and Corona Australis (Patience et al. 2002)	26
2.7	(a) Separation distribution of binaries in the Hyades cluster (Patience et al. 2002). (b) Separation distribution of spectroscopic and visual binaries in the Pleiades cluster (Bouvier et al. 1997). (c) Separation distribution of visual binaries in the Praesepe cluster (Bouvier et al. 2001).	28
2.8	Observed mass-ratio distribution for (a) field G-dwarf binaries with periods $P_d > 10^3$ (Duquennoy & Mayor 1991), and (b) field G-dwarf binaries with periods $P_d < 10^3$ (Mazeh et al. 1992).	30
2.9	Observed eccentricity distribution for (a) field G-dwarf binaries with periods $P_d > 10^3$ (Duquennoy & Mayor 1991), and (b) field G-dwarf binaries with periods $P_d < 10^3$ (Duquennoy & Mayor 1991). (c) Period vs. eccentricity for G-dwarf binaries (Duquennoy & Mayor 1991); this graph shows the observed circularisation cut-off at around 10 days.	31
2.10	Example of ring fragmentation in numerical simulations of star formation (from Cha & Whitworth 2003b).	34
4.1	The histogram and the dotted curve represent the distribution of observed β -values from Goodman et al. (1993), scaled to 56% (since they only measured rotation for 24 out of 43 cores). The dashed line represents the log-normal distributions of Case A ($\overline{\log \beta} = -2.0$, $\sigma_{\log \beta} = 1.2$) and the dash-dot line represents the log-normal distribution of Case B ($\overline{\log \beta} = -2.2$, $\sigma_{\log \beta} = 1.7$).	51
4.2	Dimensionless lifetimes of small- \mathcal{N} rings for $\mathcal{N} = 5$ and $\sigma_{\log M} = 0.6$	56

- 4.3 The dimensionless separation distribution, $dN/d \log_{10} a$, resulting from simulations with parameters $\sigma_{\log M} = 0.2$ (solid line), $\sigma_{\log M} = 0.4$ (dashed line) and $\sigma_{\log M} = 0.6$ (dotted line), and (a) $\mathcal{N} = 3$, (b) $\mathcal{N} = 4$, (c) $\mathcal{N} = 5$ and (d) $\mathcal{N} = 6$ 58
- 4.4 The total eccentricity distribution, dN/de , resulting from simulations with parameters $\sigma_{\log M} = 0.2$ (solid line), $\sigma_{\log M} = 0.4$ (dashed line) and $\sigma_{\log M} = 0.6$ (dotted line), and (a) $\mathcal{N} = 3$, (b) $\mathcal{N} = 4$, (c) $\mathcal{N} = 5$ and (d) $\mathcal{N} = 6$ 59
- 4.5 The total mass-ratio distribution, dN/dq , resulting from simulations with parameters $\sigma_{\log M} = 0.2$ (solid line), $\sigma_{\log M} = 0.4$ (dashed line) and $\sigma_{\log M} = 0.6$ (dotted line), and (a) $\mathcal{N} = 3$, (b) $\mathcal{N} = 4$, (c) $\mathcal{N} = 5$ and (d) $\mathcal{N} = 6$ 61
- 4.6 (a) The model IMF for $\mathcal{N} = 3$ with $\sigma_{\log M} = 0.2$ (thin solid line), $\sigma_{\log M} = 0.4$ (dashed line) and $\sigma_{\log M} = 0.6$ (dotted line). (b) as (a) but for $\mathcal{N} = 4$. (c) as (a) but for $\mathcal{N} = 5$. (d) as (a) but for $\mathcal{N} = 6$. The observed IMF (Kroupa, 2001) is shown as a heavy solid line on each panel. 62
- 4.7 The multiplicity frequency as a function of primary mass for (a) $\mathcal{N} = 3$, (b) $\mathcal{N} = 4$, (c) $\mathcal{N} = 5$, and (d) $\mathcal{N} = 6$, all with $\sigma_{\log M} = 0.2, 0.4$ and 0.6 . The four plotted points with error bars are observational values taken from Martín et al. (2000), FM92, DM91 and Shatsky & Tokovinin (2002). The hashed box represents the extrapolated multiplicity of PMS stars (Patience et al. 2002) 63
- 4.8 The G-dwarf eccentricity distribution resulting from convolving the dimensionless results with the observed core-mass spectrum (Equation 4.1) for parameters $\sigma_{\log M} = 0.2$ (solid line), $\sigma_{\log M} = 0.4$ (dashed line) and $\sigma_{\log M} = 0.6$ (dotted line), and (a) $\mathcal{N} = 3$, (b) $\mathcal{N} = 4$, (c) $\mathcal{N} = 5$ and (d) $\mathcal{N} = 6$. Also plotted in all panels is the observed G-dwarf binary eccentricity distribution for high-period binaries ($P_d > 10^3$ days; DM91). 65
- 4.9 The G-dwarf mass-ratio distribution resulting from convolving the dimensionless results with the observed core-mass spectrum (Equation 4.1) for parameters $\sigma_{\log M} = 0.2$ (solid line), $\sigma_{\log M} = 0.4$ (dashed line) and $\sigma_{\log M} = 0.6$ (dotted line), and (a) $\mathcal{N} = 3$, (b) $\mathcal{N} = 4$, (c) $\mathcal{N} = 5$ and (d) $\mathcal{N} = 6$. Also plotted in all panels is the observed G-dwarf binary mass-ratio distribution for high-period binaries ($P_d > 10^3$ days; DM91). 66

- 4.10 (a) The histogram shows the observed distribution of semi-major axes for pre-Main Sequence binaries in Taurus, as collated by Patience et al. (2002), and the dashed line is their best fit to this distribution. The dotted line shows the predictions of our model for Case A ($\overline{\log \beta} = -2.0$ and $\sigma_{\log \beta} = 1.2$) with parameters $\mathcal{N} = 5$ and $\sigma_{\log M} = 0.6$. The peak and width of the model predictions are fairly close to the observations, with a similarly high overall multiplicity. (b) The histogram shows the observed distribution of semi-major axes for binaries with G-dwarf primaries in the field from DM91, and the dashed line is their log-normal fit to this distribution. The dotted line shows the predictions of our model for Case B ($\overline{\log \beta} = -2.2$ and $\sigma_{\log \beta} = 1.7$) with parameters $\mathcal{N} = 5$ and $\sigma_{\log M} = 0.6$. The peak and width of the model predictions are similar to the observations, but the overall multiplicity is higher. 68
- 4.11 Lifetimes of all clusters with $\mathcal{N} = 5$ and $\sigma_{\log M} = 0.6$ when convolved over the core mass spectrum and the β distribution in Myrs. 69
- 5.1 Fractal clusters. (a) A fractal cluster with fractal dimension $D_f = 2.5$ containing 100 cores (400 stars), (b) a fractal cluster with fractal dimension $D_f = 1.5$ containing 100 cores. 78
- 5.2 The multiplicity frequency as a function of primary mass resulting from the dissolution of clusters $D_f = 2.5$ containing 100 cores with radius (a) $R_c = 2.0$ pc, (b) $R_c = 1.0$ pc, (c) $R_c = 0.5$ pc; all clusters have fractal dimension $D_f = 2.5$ and contain 100 cores. The dotted line represents the multiplicity frequency resulting from the dissolution of isolated ring clusters with $\mathcal{N} = 4$ and $\sigma_{\log M} = 0.6$ as shown in Figure 4.7b. The four plotted points with error bars are observational values taken from Martín et al. (2000), FM92, DM91 and Shatsky & Tokovinin (2002). The hashed box represents the extrapolated multiplicity of PMS stars (Patience et al. 2002). 80
- 5.3 The G-dwarf separation distribution resulting from the dissolution of clusters (histogram) with radius (a) $R_c = 2.0$ pc, (b) $R_c = 1.0$ pc, (c) $R_c = 0.5$ pc; all clusters have fractal dimension $D_f = 2.5$ and contain 100 cores. The dotted line represents the lognormal fit to the separation distribution for pre-Main sequence binaries with primary mass in the range $0.5 M_\odot \leq M \leq 5.0 M_\odot$, as collated by Patience et al. (2002); this is also the separation distribution resulting from the dissolution of isolated cores in our model (See Chapter 4). The dashed line represents the separation distribution of field G-dwarf binaries as observed by DM91. 82

- 5.4 The G-dwarf eccentricity distribution resulting from the dissolution of clusters with radius (a) $R_c = 2.0$ pc, (b) $R_c = 1.0$ pc, (c) $R_c = 0.5$ pc; all clusters have fractal dimension $D_f = 2.5$ and contain 100 cores. The dot-dash histogram represents the observed G-dwarf binary eccentricity distribution for high-period binaries ($P > 10^3$ days; DM91). 83
- 5.5 The G-dwarf mass-ratio distribution resulting from the dissolution of clusters with radius (a) $R_c = 2.0$ pc, (b) $R_c = 1.0$ pc, (c) $R_c = 0.5$ pc; all clusters have fractal dimension $D_f = 2.5$ and contain 100 cores. The dot-dash histogram represents the observed G-dwarf binary mass-ratio distribution for high-period binaries ($P > 10^3$ days; DM91). 84
- 5.6 The multiplicity frequency as a function of primary mass resulting from the dissolution of clusters with radius (a) $R_c = 2.0$ pc, (b) $R_c = 1.0$ pc. all clusters have fractal dimension $D_f = 1.5$ and contain 100 cores. The dotted line represents the multiplicity frequency resulting from the dissolution of isolated ring clusters with $\mathcal{N} = 4$ and $\sigma_{\log M} = 0.6$ as shown in Figure 4.7b. The four plotted points with error bars are observational values taken from Martín et al. (2000), FM92, DM91 and Shatsky & Tokovinin (2002). The hashed box represents the extrapolated multiplicity of PMS stars (Patience et al. 2002). 85
- 5.7 The G-dwarf separation distribution resulting from the dissolution of clusters with radius (a) $R_c = 2.0$ pc, (b) $R_c = 1.0$ pc; all clusters have fractal dimension $D_f = 1.5$ and contain 100 cores. The dotted line represents the lognormal fit to the separation distribution for pre-Main sequence binaries with primary mass in the range $0.5 M_\odot \leq M \leq 5.0 M_\odot$, as collated by Patience et al. (2002). The dashed line represents the separation distribution of field G-dwarf binaries as observed by DM91. 86
- 5.8 The G-dwarf eccentricity distribution resulting from the dissolution of clusters with radius (a) $R_c = 2.0$ pc, (b) $R_c = 1.0$ pc; all clusters have fractal dimension $D_f = 1.5$ and contain 100 cores. The dot-dash histogram represents the observed G-dwarf binary eccentricity distribution for high-period binaries ($P > 10^3$ days; DM91). 87
- 5.9 The G-dwarf mass-ratio distribution resulting from the dissolution of clusters with radius (a) $R_c = 2.0$ pc, (b) $R_c = 1.0$ pc; all clusters have fractal dimension $D_f = 1.5$ and contain 100 cores. The dot-dash histogram represents the observed G-dwarf binary mass-ratio distribution for high-period binaries ($P > 10^3$ days; DM91). 88

6.1	Calculating properties in SPH. The properties of particle i are calculated as a weighted average of the properties of it's neighbours, i.e. all particles within a distance $2h_i$ (the grey particles).	94
6.2	(a) The unnormalised M4-kernel function, as given by Equation 6.18 (b) The unnormalised kernel gradient function. Plotted are both the exact derivative of the M4-kernel (Equation 6.19; solid line), and the modified derivative as proposed by Thomas & Couchman (1992; Equation 6.20; dashed line)	96
6.3	An example of how a tree organises the spatial domain into cells. In regions of low particle density, the size of a cell is relatively large, whereas in regions with high particle density, the cell size is small in order to populate the leaf cells with at most a few particles. Note that this is a 3-D simulation and so the cells also extend into the z-dimension	101
7.1	Results of the isothermal Sod test using standard artificial viscosity: (a) the density distribution after $T = 0.4$, and (b) the x-velocity distribution after $T = 0.4$	113
7.2	Results of the isothermal Sod test using artificial viscosity with the Balsara switch: (a) the density distribution after $T = 0.4$, (b) the x-velocity distribution after $T = 0.4$, and (c) the Balsara factor, f_b (Equation 6.30) over the shock region after $T = 0.4$	114
7.3	Results of the isothermal Sod test using time-dependent viscosity with $\alpha^* = 0.1$ and $\alpha_{\text{MAX}} = 1.0$: (a) the density distribution after $T = 0.4$, (b) the x-velocity distribution after $T = 0.4$, and (c) α for particles around the shock region after $T = 0.4$	115
7.4	Results of the isothermal Sod test using time-dependent viscosity with $\alpha^* = 0.1$ and $\alpha_{\text{MAX}} = 2.0$: (a) the density distribution after $T = 0.4$, (b) the x-velocity distribution after $T = 0.4$, and (c) α for particles around the shock region after $T = 0.4$	116
7.5	Results of simulations of colliding flows with $\mathcal{M}' = 4.0$ using standard viscosity: (a) the density distribution after $T = 0.4$, and (b) the x-velocity distribution after $T = 0.4$	117
7.6	Results of simulations of colliding flows with $\mathcal{M}' = 4.0$ using artificial viscosity with the Balsara switch: (a) the density distribution after $T = 0.4$, (b) the x-velocity distribution after $T = 0.4$, and (c) the Balsara factor (Equation 6.30) over the shock region after $T = 0.4$	118

- 7.7 Results of simulations of colliding flows with $\mathcal{M}' = 4.0$ using time-dependent artificial viscosity with $\alpha_{\text{MAX}} = 1.0$: (a) the density distribution after $T = 0.4$, (b) the x -velocity distribution after $T = 0.4$, and (c) α_i for particles around the shock region after $T = 0.4$ 119
- 7.8 Results of simulations of colliding flows with $\mathcal{M}' = 4.0$ using time-dependent artificial viscosity with $\alpha_{\text{MAX}} = 2.0$: (a) the density distribution after $T = 0.4$, (b) the x -velocity distribution after $T = 0.4$, and (c) α_i for particles around the shock region after $T = 0.4$ 120
- 7.9 Results of the shear flow test. The x -velocity profile is plotted as a function of y after a time $T = 1.0$ for (a) standard artificial viscosity, (b) artificial viscosity using the Balsara switch, (c) time-dependent viscosity using $\alpha_{\text{MAX}} = 1.0$, and (d) time-dependent viscosity using $\alpha_{\text{MAX}} = 2.0$. The solid line shows the initial velocity profile, as given by Equation 7.4. 122
- 7.10 The solid line represents one wavelength of the imposed sinusoidal plane-wave perturbation. The other lines represent the smoothing kernels used in the results displayed in Fig. 7.13: $\mathcal{R} = 0.5$ (dotted line) the very well resolved case; $\mathcal{R} = 1.0$ (dash-dot line) the marginally resolved case; and $\mathcal{R} = 2.0$ (dashed line) the under-resolved case. The kernels are all scaled so that the integrated area under the kernel is equal to the area under the perturbation. 128
- 7.11 The density distributions of the perturbation. Plotted in each panel are the analytical density curves (solid lines), the smoothed density as calculated by Equation 7.30 (dot-dashed lines) and the density calculated using Equation 6.21 in SPH (points). Perturbations with different resolutions are plotted (a) $\mathcal{R} = 0.5$ (b) $\mathcal{R} = 1.0$ (c) $\mathcal{R} = 2.0$ 129
- 7.12 The analytical and SPH forces exerted on the particles. Plotted in each are the analytical gravitational (solid lines) and analytical hydrodynamical (dashed lines) forces along with the SPH gravitational (dark points) and SPH hydrodynamical (light triangles) forces. The hydrodynamical forces are calculated for the case $\lambda/\lambda_j = 0.8$. Perturbations with different resolutions are plotted (a) $\mathcal{R} = 0.5$, (b) $\mathcal{R} = 1.0$ and (c) $\mathcal{R} = 2.0$ 130

- 7.13 Characteristic timescales for the evolution of plane-wave perturbations, as a function of wavelength. The ordinate is the wavelength in units of the Jeans length, and the abscissa is the timescale in units of $(G\rho_0)^{-1/2}$. For perturbations which oscillate (i.e. those with $\lambda < \lambda_j$) the oscillation period estimated from the SPH simulations is represented by an open circle. For perturbations which collapse (i.e. those with $\lambda > \lambda_j$) the time for the peak density in the SPH simulations to increase by a factor 1.54 (see text) is represented by an open star. The filled circles and stars represent results of simulations using the self-support correction term (See Section 7.5.5). For reference, the analytic timescales are given by solid curves. (a) The very well resolved case, $\mathcal{R} = 0.5$. (b) The marginally resolved case, $\mathcal{R} = 1.0$. (c) The under-resolved case, $\mathcal{R} = 2.0$ 132
- 8.1 The initial density profile of the prestellar cores used in simulations. The solid line shows the analytical density profile (i.e. Equation 8.1) and the points represent the SPH initial density profile. 141
- 8.2 The mass distribution, $dN/d \log_{10} M$, resulting from turbulent cores with masses (a) $2.17 M_\odot$, and (b) $4.34 M_\odot$. All cores have an initial turbulent virial ratio $\alpha_{\text{TURB}} = 0.2$ 148
- 8.3 The distribution of binary separations, $dN/d \log_{10} a$, resulting from turbulent cores with masses (a) $2.17 M_\odot$, and (b) $4.34 M_\odot$. All cores have an initial turbulent virial ratio $\alpha_{\text{TURB}} = 0.2$. The dashed line shows the separation distribution of PMS binaries (Patience et al. 2002). The curve and the histogram are normalised to contain unit area rather than to the multiplicity. 149

List of Tables

2.1	Summary of main observational surveys of field star binaries	18
2.2	Summary of main observational surveys of pre-Main Sequence binaries.	19
2.3	Summary of main observational surveys of binaries in open clusters.	20
3.1	Algorithms used in the NBODY codes	38
4.1	The numbers of different multiple systems produced in the dimensionless simulations; S - singles, B - binaries, T - triples and Q - quadruples. For each combination of $\sigma_{\log M}$ and N , we run an ensemble of $\sim 10^5/N$ simulations. Also shown are the three different multiplicity measures as defined in Section 2.2.	57
8.1	Parameters describing the initial conditions of turbulent-core simulations.	143
8.2	Systems formed in simulations of turbulent cores with mass $M_{\text{CORE}} = 2.17 M_{\odot}$ and with turbulent virial ratio $\alpha_{\text{TURB}} = 0.2$. Each set of initial conditions is simulated using the three different viscosities, Standard Viscosity (ST), the Balsara switch (BS), and time-dependent viscosity (TD).	145
8.3	Systems formed in simulations of turbulent cores with mass $M_{\text{CORE}} = 4.38 M_{\odot}$ and with turbulent virial ratio $\alpha_{\text{TURB}} = 0.2$. Each set of initial conditions is simulated using the three different viscosities, Standard Viscosity (ST), the Balsara switch (BS), and time-dependent viscosity (TD).	146
8.4	Summary of main results of turbulent core simulations. The columns from left to right: Run id - the parameter set id; M_{core} - the initial core mass; Viscosity - the viscosity used (ST - Standard, BS - Balsara switch, TD - time-dependent viscosity); N_{sims} - the total number of simulations in the ensemble; $\overline{N_{\text{obj}}} \pm \Delta \overline{N_{\text{obj}}}$ - the mean number of objects (plus uncertainty); σ_N - the standard deviation of the object number; $\overline{\log_{10} a} \pm \Delta \overline{\log_{10} a}$ - the mean of the logarithm of the separation (plus uncertainty); $\sigma_{\log a}$ - the standard deviation of $\log_{10} a$; \bar{e} - the mean eccentricity; \bar{q} - the mean mass-ratio.	147

Chapter 1

Introduction

1.1 Theoretical star formation

Stars appear to account for most of the visible dense baryonic matter in the Universe. They are therefore a fundamental constituent of the Universe, and of great importance in their own right. Moreover, astronomers also have to understand the life-cycles of stars before they can attempt to understand the structure and evolution of galaxies, the origin of the heavy elements, or the genesis of planetary systems. However, although the Main Sequence and post-Main Sequence phases of stellar evolution have been studied for over a hundred years, the field of star formation has a much shorter history, and only really developed in the last few decades, with the introduction of long-wavelength observing techniques (for example infrared and sub-millimetre telescopes) and the advent of powerful computers. These developments allowed observers to probe into the dark dense clouds where new stars are forming, and enabled theorists to start simulating the complex non-linear gas dynamics which converts interstellar gas into Main Sequence stars (a conversion which takes the gas through about twenty orders of magnitude in density and six orders of magnitude in temperature). A key feature of the stellar systems we see in the sky is that many (probably most) of them are actually binary – or higher order multiple – systems.

1.1.1 Binary and multiple systems

A binary system is a pair of stars in orbit around one another. Observational surveys of galactic field stars (e.g. Duquennoy & Mayor 1991, Fischer & Marcy 1992, Mayor et al. 1992) indicate that a significant number of nearby stellar systems are binary systems. In fact, approximately 60% of solar-mass Main Sequence primary stars are part of binary systems. This suggests that the final result of the star formation process is very often a binary star.

Star formation theory cannot explain the high frequency of binaries if we assume that stars form as single systems and are later on 'paired-up' to form binary systems. Stars must be born as part of a binary system; otherwise we cannot explain the high binarity of stars in the galactic field. Binary star formation is thus likely to be the dominant mechanism of star formation over single star formation.

1.1.2 The life cycle of stars

The life cycle of a star consists of a series of different evolutionary stages, of which some are not well understood. We briefly describe the main steps during star formation in order to appreciate which steps are relevant to this research.

The diffuse interstellar gas that pervades the disc of a galaxy provides the raw material from which stars form. By some mechanism, this gas assembles into dense clouds called *molecular clouds* (MCs). It is unclear how molecular clouds form, how they are supported, and how long they live for. At some point, a molecular cloud will fragment into a number of smaller self-gravitating gas clumps called *prestellar cores*. These prestellar cores evolve to become either young protostars or groups of protostars (e.g. young binary systems). These protostars will accrete extra mass and evolve to become Main-Sequence stars, like our Sun. The original molecular cloud has now become a young cluster of stars which may then disperse and populate the galactic field with newly-born stars. These stars will remain in the field during the Main-Sequence phase until they exhaust their fuel supply for nuclear fusion and die. Lower mass stars will cool and fade away as white dwarf stars or neutron stars whereas higher mass stars may explode as supernovae enriching the galaxy with heavy elements, and possibly triggering a new phase of star formation.

1.1.3 The goals of this thesis

The main aims of the work in this thesis are to gain insight into the origins of binary stars, and to explain the statistical distribution of binary properties. We look at the properties of very young (i.e. primordial) binary systems and also older, galactic-field binaries.

1.2 The main stages of star formation

Here we discuss each of the main stages of the star formation process in more detail describing how each stage could affect the properties of the resulting stars and binary systems. Understanding the different stages allows us to set up more realistic initial conditions for numerical simulations.

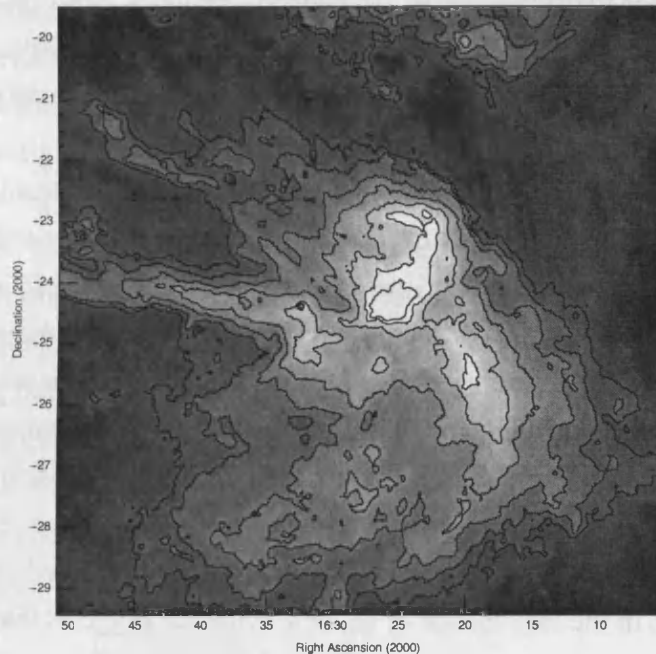


Figure 1.1: The Ophiuchus molecular cloud observed in the Infra-red using IRAS (Wheelock et al. 1991, IRAS Sky Survey Atlas Explanatory Supplement). The grey-scale shows the intensity of thermal emission from dust (dark - low emission, light - high emission). This image shows the filamentary structure of a molecular cloud.

1.2.1 Molecular clouds and star forming regions

Molecular clouds are large condensations of interstellar gas which are optically thick to dissociative UV photons, thereby allowing molecular hydrogen, H_2 , to form. Evidence of recent star formation, such as the presence of young stellar objects (YSOs), is only found in the vicinity of a molecular cloud. Figure 1.1 shows the Ophiuchus molecular cloud observed at infra-red wavelengths.

Molecular clouds have masses from $\sim 10^2 M_\odot$ up to $\sim 10^6 M_\odot$. Molecular clouds with masses greater than $10^4 M_\odot$ are usually called *Giant Molecular clouds* (GMCs). Figure 1.1 shows that molecular clouds are not single coherent structures (such as spheres) but are often observed to have a filamentary structure. Considerable sub-structure is present in the form of larger clumps (coherent regions of higher than average density) and smaller, higher-density prestellar cores which are believed to be the progenitors of individual stellar systems (i.e. either single systems or binary stars). Only a small fraction of observed clumps are gravitationally bound due to the high effective internal pressure which prevents gravitational collapse. Line-width observations of clumps and cores suggest suprathermal motions due to turbulence in molecular clouds (Larson 1981). The origin of turbulence in molecular clouds is unclear, but

is likely to be either hydrodynamical turbulence, feedback from protostellar jets or magneto-hydrodynamical waves (e.g. Ballesteros-Paredes et al. 2006). Turbulence is also important in binary star formation since simulations indicate that turbulence can promote fragmentation of molecular clouds and of prestellar cores.

Another possible indication of the effect of turbulence in molecular clouds is their filamentary sub-structure. This sub-structure can be quantified using fractals (e.g. Blitz & Williams 1999). A cloud is fractal if the perimeter of any region of the cloud, P , is related to its surface area, A , by the relation $P \propto A^{D_f/2}$ where D_f is the fractal dimension. For some molecular clouds, the observed fractal dimension is $D_f \sim 1.5$ (Blitz & Williams 1999).

For many years, it was believed that molecular clouds were long-lived structures with lifetimes of order 1 Gyr, i.e. much longer than their dynamical crossing times (e.g. Ballesteros-Paredes et al. 2006). Some form of support was presumed to balance gravity so that molecular clouds could survive for so long. Magnetic fields were identified as the likely source of this support. However, in the last decade or so, new evidence suggests that cloud lifetimes are much shorter than 1 Gyr and are of order a few free-fall times (e.g. Blitz & Williams 1999, Elmegreen 2000). Molecular clouds are now believed to be transient structures that are formed, make stars, and then disperse quickly. The formation mechanism of molecular clouds is not well understood, but they are probably destroyed by the luminous and mechanical output from high-mass stars formed within the molecular cloud. The typical lifetime of a Giant molecular cloud is believed to lie in the range $20 \text{ Myr} < t_{\text{GMC}} < 100 \text{ Myr}$ (e.g. Blitz & Williams 1999).

Two of the most well-known star forming regions are the Taurus-Auriga and the Orion molecular clouds. They are contrasting examples of the physical conditions in star forming regions. Orion is an example of a high-mass, ‘clustered’ star-forming region with a total mass of $10^5 M_\odot$ and is extended over a region of size 50 pc. Orion produces stars in dense clusters (such as the famous Trapezium cluster). Taurus is an example of a low-mass, ‘isolated’ star-forming region with only $10^4 M_\odot$ extended over a region of size 10 pc. Although the average density of the two regions is comparable, the young stars of Taurus are formed in small but relatively extended groups in contrast to the concentrated high-density regions in Orion like the Trapezium cluster.

1.2.2 Prestellar cores and Young stellar objects

Prestellar cores and young stellar objects are dense condensations of gas in molecular clouds which are gravitationally bound and represent the early stages of a star’s life. Prestellar cores are the youngest objects which are considered to be the progenitors of young stellar systems. Many are observed to be collapsing under gravity (e.g. André et al. 2000), but do not yet have a central protostar. A young stellar object represents the next stage of evolution where a prestellar core

has formed a central object (i.e. a protostar). YSOs radiate brightly due to accretion and due to the release of self-gravitational potential energy as they collapse. YSOs are usually located deep inside molecular clouds so any emission from them is obscured by the surrounding envelope of gas and dust. It is usually only possible to observe YSOs at long wavelengths such as the sub-millimetre ($\lambda \sim 10^{-4} - 10^{-3}m$) and infra-red ($\lambda \sim 10^{-6} - 10^{-4}m$). Observed YSOs belong to one of four defined classes, Class 0, I, II and III (e.g. Lada 1999, André et al. 2000). Each class is believed to represent a different stage in a young star's evolution; Class 0 is the youngest stage and Class III is the oldest.

Class 0 objects are believed to be the earliest phase of a protostar's life. The spectral energy distribution (SED) of a Class 0 source is very similar to that of a modified blackbody. The SED peaks at sub-millimetre or far-infrared wavelengths suggesting a temperature of $\approx 10 - 20$ K. Class 0 objects are almost always associated with highly energetic bipolar outflows which are jets of gas ejected from the central object along the poles (e.g. André, Ward-Thompson & Barsony 1993, 2000).

Class I sources have a SED that peaks at far-infrared wavelengths, and contain a relatively large infrared excess. The SED cannot be characterised by a simple blackbody (or greybody) curve, as with Class 0 sources, due to this excess. Modelling the SED as a composite of different temperature blackbody (or greybody) SEDs suggests that Class I objects contain a dense central object surrounded by an envelope of gas and dust. Class I objects are also associated with bipolar outflows (e.g. Bontemps et al. 1996, Lada 1999).

Class II sources represent the emergence of the central stellar object from the surrounding envelope and into the pre-Main Sequence phase of evolution. The SED is dominated by emission from the central object, but contains a relatively small infrared excess (compared to Class I objects) which is presumed to be emission from a circumstellar disk. The SED peaks at near-infrared or visible wavelengths. The SED also contains characteristic emission lines. Class II objects are known historically as Classical T-Tauri stars (e.g. Lada 1999)

Class III objects represent the last phase of the development of a YSO into a star. The SEDs of Class III objects have very little excess emission and can be fitted well with a blackbody spectrum which peaks in the near infrared or the visible. Class III objects are known historically as Weak-line T-Tauri stars (e.g. Lada 1999)

Using statistical arguments and models of pre-Main Sequence evolution, it is possible to infer ages and timescales for the various stages of a protostar's evolution. Approximate timescales for each stage are $t_{\text{Class 0}} : t_{\text{Class I}} : t_{\text{Class II}} : t_{\text{Class III}} = 10^4 \text{ yrs} : 10^5 \text{ yrs} : 10^6 \text{ yrs} : 10^7 \text{ yrs}$ (e.g. Lada 1999).

The distribution of clump and core masses has been measured by various authors (e.g. Motte et al. 1998, Testi & Sargent 1998, Johnstone et al. 2000, Motte et al. 2001). I will refer to the

core mass spectrum of Orion-B as observed by Motte et al. (2001) in this thesis which can be expressed as the following two-part power law,

$$\frac{dN_{\text{CORE}}}{dM_{\text{CORE}}} = \begin{cases} k_1 M_{\text{CORE}}^{-1.5}, & 0.5 M_{\odot} \leq M_{\text{CORE}} \leq 1.0 M_{\odot}; \\ k_2 M_{\text{CORE}}^{-2.5}, & 1.0 M_{\odot} \leq M_{\text{CORE}} \leq 10.0 M_{\odot}. \end{cases} \quad (1.1)$$

1.2.3 Embedded clusters

An embedded cluster is a cluster of young stars which is hidden deep within a molecular cloud by gas and dust that obscures visible light. Longer wavelengths (e.g. infrared) must be used to observe embedded clusters. Lada & Lada (2003) report that there are more than 100 embedded clusters in nearby molecular clouds (within 2 kpc). It is suggested by various authors that the majority of stars is formed within embedded clusters (Lada & Lada 1991, 2003, McCaughrean, Rayner & Zinnecker 1991). This is often referred to as the *dominant mode* of star formation. Statistical arguments based on number counts suggest that the vast majority of embedded clusters are destroyed when the molecular cloud is itself destroyed. The rapid loss of gas from a molecular cloud leaves the newly formed cluster gravitationally unbound and the constituent stars disperse into the field. It is rare that an embedded cluster remains bound after residual gas loss; in this case, the embedded cluster becomes an open cluster.

1.2.4 Open clusters and OB associations

An open cluster is a group of young stars, formed immediately after a molecular cloud is destroyed. Open clusters contain from as little as a few dozen stars (e.g. Ursa Major) to around a thousand members (e.g. the Pleiades). Open clusters represent the most advanced stage of the star formation process before stars join the galactic field. The oldest open clusters are nearly 1 Gyr old. Binaries in open clusters may be altered or destroyed due to many-body interactions.

OB associations are groups of O- ($M > 20 M_{\odot}$) and B- ($M > 4 M_{\odot}$) stars which are always found in the vicinity of molecular clouds. The largest OB association in the solar vicinity is that of Orion, which contains 9 O-stars and more than 300 B-stars. The significance of OB associations is that the O and B stars have very high luminosities and thus short lifetimes. There is little time for them to move very far away from their birthsite, and since most are found near molecular gas, their existence and location is good circumstantial evidence that molecular clouds are the sites of star formation. However we note the existence of high-velocity OB-stars outside of the galactic plane which may be due to dynamical ejections from dense protoclusters (e.g. Clarke & Pringle 1992).

1.2.5 The Main Sequence

A star will evolve from the pre-Main Sequence phase by continuing to collapse until it is dense and hot enough to begin nuclear burning. The star will reach an equilibrium state where the energy generated by nuclear reactions provides sufficient pressure support to prevent further collapse under gravity. This is the Main-Sequence phase where the star will remain for the majority of its life. Stars with masses less than $0.08 M_{\odot}$ do not reach the required temperature to burn hydrogen and become *Brown Dwarfs* (BDs) and thus do not reach the Main-Sequence phase.

The spectrum of stellar masses immediately after formation is called the initial mass function (IMF). The first determination of the IMF was made by Salpeter (1955) who showed that the distribution of stellar masses could be fitted with a simple power law between $0.4 M_{\odot}$ and $10 M_{\odot}$. More recent determinations have extended the IMF down to lower masses. We will refer to the IMF determined by Kroupa (2001); this IMF is a 4-part power law parameterized as

$$\frac{dN_{\star}}{dM_{\star}} \propto M_{\star}^{-\alpha} dM_{\star}, \quad (1.2)$$

where

$$\begin{aligned} \alpha_0 &= +0.3 \pm 0.7, & 0.01 M_{\odot} \leq M_{\star} < 0.08 M_{\odot}; \\ \alpha_1 &= +1.3 \pm 0.5, & 0.08 M_{\odot} \leq M_{\star} < 0.50 M_{\odot}; \\ \alpha_2 &= +2.3 \pm 0.3, & 0.50 M_{\odot} \leq M_{\star} < 1.00 M_{\odot}; \\ \alpha_3 &= +2.3 \pm 0.7, & 1.00 M_{\odot} \leq M_{\star}. \end{aligned} \quad (1.3)$$

1.3 Numerical star formation

The details of the star formation process are not very well understood. The main difficulty is that star formation converts low-density material from the interstellar medium ($\rho \leq 10^{-20} \text{ g cm}^{-3}$) into stars which have a much higher density ($\rho \gtrsim 1 \text{ g cm}^{-3}$). This range of density spans more than twenty orders of magnitude where the gas is subject to many different physical processes. Overall, this makes the construction of realistic models difficult. Until recent years, observations of star formation did not provide many physical constraints on the models, and often presented new problems (e.g. the origin of outflows from young protostars). Observations and theory appear to suggest that star formation is a non-linear process, rendering analytical methods inadequate and requiring the use of numerical methods. As the main paradigm of star formation has shifted from quiescent, isolated star formation towards a more dynamical picture of rapid, turbulence-controlled star formation, computers have become an important requirement to investigate theoretical models. Numerical star formation requires considerable

computing resources and due to the nature of the problems, the development of effective and efficient algorithms is difficult. We briefly discuss the numerical codes which I have used for the work in this thesis.

1.3.1 N-body simulations

Once most of the gas in a star forming region has been accreted by stars and/or evaporated from the cluster by high-energy photons emitted from O-stars, the dominant force in the system is gravity due to the protostars in the young cluster. The problem becomes one of stellar and cluster dynamics where gravity alone determines the fate of the cluster rather than hydrodynamics. At this point, N-body codes can be used to follow the ballistic evolution of the cluster. N-body codes solve the equation of motion assuming stars can be treated as point masses and interact only through gravity.

In this thesis, I have used N-body codes to model the evolution of small-N clusters to investigate the properties of primordial binaries, and also of large-N star clusters to investigate the disruption of binaries in dense star formation regions.

1.3.2 Hydrodynamical codes

Hydrodynamical codes are used to model star formation when most of the mass is still molecular gas in molecular clouds. Hydrodynamical codes are required to follow processes such as the fragmentation of molecular clouds into cores and into protostars. Such codes have become increasingly sophisticated in recent years allowing most of the main physical processes involved in star formation to be included in simulations. These include hydrodynamics, gravity, radiative transfer, magneto-hydrodynamics, thermal physics and chemistry.

The two numerical schemes most commonly used to treat star formation problems are Smoothed Particle Hydrodynamics (SPH) and Adaptive mesh refinement (AMR) finite difference codes. SPH is a Lagrangian code which uses particles to represent the fluid (Lucy 1977, Gingold & Monaghan 1977). SPH is particularly well suited to problems with large changes in density such as star formation, due to its Lagrangian nature. AMR is an Eulerian code which assumes a grid fixed in space where each cell represents a fluid element (e.g. Truelove et al. 1998). The resolution of the grid (i.e. number of grid points) can increase in localised regions where needed. Both numerical schemes have advantages and disadvantages depending on the details of the problem.

One concern about hydrodynamical codes that has been highlighted in recent years is that of resolution. If a simulation with SPH has an insufficient number of particles, or a simulation with AMR uses an insufficient number of grid points, then particular physical processes will not

be modelled correctly. In simulations of star formation, the critical process is fragmentation.

During my PhD, I have assisted in the design and coding of a SPH code, DRAGON, which was written as a tool to model certain stages of the star formation process. I have investigated the evolution of turbulent prestellar cores with particular focus on binary star formation following the work of Goodwin et al (2004a, 2004b). I have also developed a test of our SPH code to investigate the resolution of SPH simulations with respect to gravitational fragmentation.

1.4 Overview of thesis

The main focus of this thesis will be to investigate the formation of binary systems using numerical methods. Due to the non-linear nature of star formation, we will conduct our research using numerical N-body and hydrodynamical codes.

In Chapter 2, we discuss in detail the orbital properties of binary stars, observational techniques used to detect binary stars, the extent of observational surveys of binary stars, the main models of binary star formation, and discuss some of the main problems that need to be answered in this field.

In Chapter 3, we discuss the main algorithms and features of N-body codes, in particular with reference to Aarseth's NBODY series which we will use in this thesis.

In Chapter 4, we develop a simple binary formation model where cores fragment into small-N clusters. We then perform N-body simulations of these small-N clusters using Aarseth's NBODY3 and compare the results to the observations.

In Chapter 5, we investigate using N-body simulations, the effect of the larger cluster environment on the statistics of binary stars.

In Chapter 6, we discuss the main algorithms and features of Smoothed Particle Hydrodynamics, a Lagrangian hydrodynamics algorithm commonly used in numerical star formation problems.

In Chapter 7, we test our Smoothed Particle Hydrodynamics code, DRAGON, using various standard test cases, with particular focus on the effect of artificial viscosity in simulations. Also, we discuss a new test called the Jeans test, designed to test the ability of SPH to resolve gravitational fragmentation.

In Chapter 8, we perform simulations of turbulent star forming prestellar cores. This follows the work of Goodwin et al (2004a, 2004b).

Chapter 2

Binary Stars : Observations and Theory

In this chapter, we discuss the main properties of binary stars and higher-order multiple systems. First, we discuss the parameters that define the orbits of binary stars and higher-order multiple systems. Second, we review the main observational surveys of binary stars that have been performed in the last two decades and summarise the main statistical properties of field binaries, binaries in open clusters and pre-Main Sequence binaries in star-forming regions. Finally, we discuss the main theoretical models of binary star formation highlighting the strengths and weaknesses of these models, and which are the main questions of binary star formation that need to be answered.

2.1 Binary stars

A binary is a system of two stars which orbit their common centre of mass due to their mutual gravitational attraction. Observations show that a high fraction of the stars in the night sky are in fact binary systems. Higher-order multiple systems with three stars (triple systems) and four stars (quadruple systems) are also observed, although they are less abundant than binary systems. The distance between the two component stars of a binary system is generally much larger than the radii of the stars. We can therefore model the stars as point masses and use Newton's law of gravity to model the dynamics of the system. The only stable configuration which has an analytical solution for the orbit is a binary system. Higher-order multiples ($N \geq 3$) are generally unstable but since we have observed such systems, we know that quasi-stable configurations exist. These systems can be modelled numerically, or semi-analytically in special limiting cases.

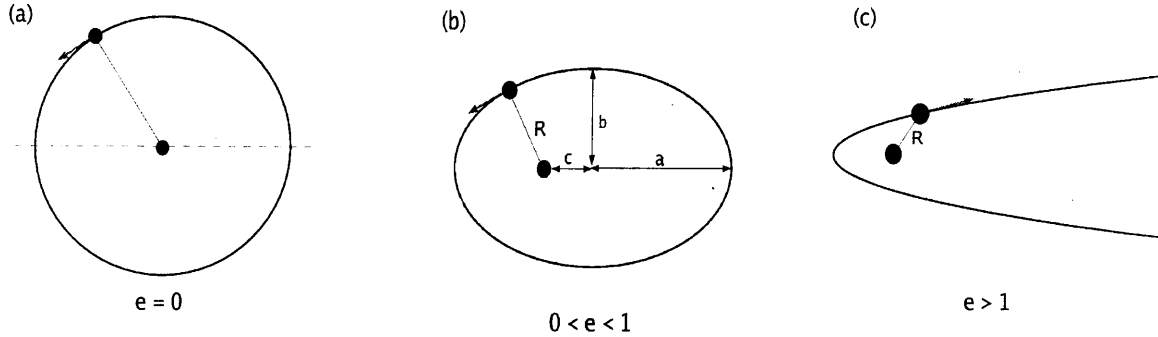


Figure 2.1: The possible orbits resulting from two-body interactions under gravity. (a) A circular orbit with eccentricity $e = 0$ for two bound objects. (b) An elliptical orbit with eccentricity $0 < e < 1$ for two bound objects. The main orbital parameters are shown: a - semi-major axis, b - semi-minor axis, c - distance between focus and centre of ellipse. (c) A parabolic (hyperbolic) orbit for 2 unbound objects with eccentricity $e = 1$ ($e \geq 1$).

2.1.1 Orbits of binary stars

An exact general analytical solution for the orbital motion of a system containing N gravitating bodies is only possible for the $N = 2$ case, using the reduced two-body problem. Consider two bodies with masses m_1 and m_2 (where $m_1 > m_2$), having relative separation vector $\mathbf{R} \equiv \mathbf{r}_2 - \mathbf{r}_1$, and assume that gravity is the only force. The equivalent reduced 2-body problem consists of a body of reduced mass $\mu = m_1 m_2 / (m_1 + m_2)$ orbiting a stationary body of effective gravitational mass $M = m_1 + m_2$. The equation of motion is

$$\frac{d^2 \mathbf{R}}{dt^2} = -\frac{G(m_1 + m_2)}{|\mathbf{R}|^3} \mathbf{R}. \quad (2.1)$$

The solution of this differential equation shows that the orbits follow conic sections. The separation between the two components, $R \equiv |\mathbf{R}|$, as the body moves around the orbit is given by

$$R = \frac{h^2 / (G(m_1 + m_2))}{1 + e \cos \theta} \quad (2.2)$$

where h is the specific angular momentum of the orbiting body, e is the eccentricity of the orbit and θ is the true anomaly (i.e. the angle between the long-axis of the ellipse and the vector \mathbf{R}). The eccentricity characterises the type of orbit:

- For $e = 0$, the orbit is circular (Figure 2.1a), i.e. $R = \text{const}$.
- For $0 < e < 1$, the orbit is elliptical. Figure 2.1b shows the main geometrical measures of an ellipse. The semi-major axis, a , is the length of the long axis of the ellipse, and the

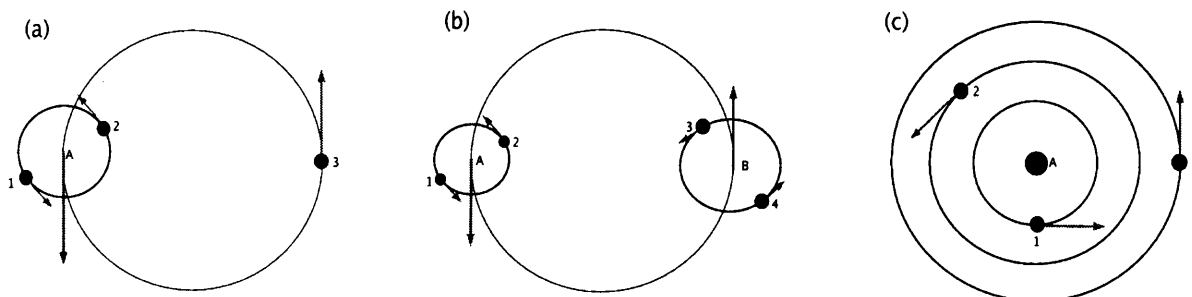


Figure 2.2: Examples of common multiple systems. Circular orbits are used here for simplicity, with each diagram in the centre of mass frame. (a) An hierarchical triple system; stars 1 and 2 are part of a bound binary, which is represented by its centre of mass, A. Binary A and star 3 orbit their centre of mass as would 2 single stars in a binary system. (b) An hierarchical quadruple system; stars 1 and 2 form a bound binary system, A, and stars 3 and 4 form a bound binary system, B; Binaries A and B orbit their centre of mass as would 2 single stars in a binary. (c) A planetary multiple system; The mass of the central star, A, is much greater than that of the other stars; Stars 1, 2 and 3 orbit around the star A.

semi-minor axis, b , measures the short axis of the ellipse. The central object is located at one of the foci of the ellipse, a distance c from the centre of the ellipse. In terms of geometrical quantities, the eccentricity is given by $e = c/a$.

- For $e \geq 1$, the orbit is not closed, following either a parabolic path ($e = 1$) or a hyperbolic path ($e > 1$; Figure 2.1c). For $e = 1$, the total energy of the system is exactly zero and the orbiting star moves asymptotically towards infinity, i.e. the star decelerates to zero speed as it approaches infinity. For $e > 1$, the total energy of the system is positive and the body decelerates towards a finite speed as it moves to infinity.

A binary star must have negative total energy to be a bound system, and thus only orbits with $0 \leq e < 1$ are bound orbits. Stars that travel on orbits with $e \geq 1$ are unbound.

2.1.2 Higher-order multiple systems

Although the dynamical motion of N-body systems with $N > 2$ is generally non-linear, some quasi-stable configurations exist. Higher-order multiple systems have been observed such as triple systems and quadruple systems. Figure 2.2 shows the configuration of common types of multiple systems (using circular orbits for simplicity).

1. *Hierarchical triple systems*

An hierarchical triple system (Figure 2.2a) consists of a hard binary system (i.e. a binary with small separation and high binding energy) which is orbiting a more distant single star (or more correctly the binary and the single star orbit their common centre of mass). If the single star is far enough away from the binary, the tidal perturbing force it exerts on the binary is negligible. The further apart the binary and the star, the more stable the system.

2. *Hierarchical quadruple systems*

An hierarchical quadruple system (Figure 2.2b) consists of two hard binary stars which are in orbit around their common centre of mass. If the distance between the binaries is much greater than the separation of the individual components, then the perturbing forces the binaries exert on each other will not be sufficient to disrupt the binaries.

3. *Planetary multiple systems*

A planetary multiple system (Figure 2.2c) consists of several relatively low-mass stars in orbit around one very massive star which dominates the gravitational potential of the system. This is analogous to the solar system where many planets have stable near-circular orbits due to the dominating gravitational attraction of the Sun.

2.2 Orbital parameters and statistics of binary stars

In both observational surveys and computer simulations, the binary parameters are usually presented as statistical distributions of the total ensemble. The main statistics used in the literature are stated here, and will be used in this thesis. It should be noted that there is no universal convention for the definition of some parameters (in particular the multiplicity); different publications use different definitions and different naming conventions which can make comparison difficult. The main statistics are:

- The masses of the binary components, m_1 and m_2 . Equivalently, we could use the primary mass, m_1 , and the mass-ratio of the binary components, $q \equiv m_2/m_1$ where m_2 is the secondary mass. In observational surveys, the latter convention is used since most surveys of visual binaries observe a range of primary masses.
- Measures of multiplicity - The multiplicity of stars gives a quantitative measure of how many binaries exist relative to the number of single stars. Several different definitions are used (some with different naming conventions) in the literature. We define S , B , T and Q as the number of single, binary, triple and quadruple systems respectively.

1. *Multiplicity frequency (mf)* - This is the fraction of systems that are multiple. This does not depend on the type of multiple system.

$$\mathbf{mf} = \frac{B + T + Q}{S + B + T + Q} \quad (2.3)$$

2. *Binary star fraction (bf)* - This is the fraction of stars that is in multiple systems.

$$\mathbf{bf} = \frac{2B + 3T + 4Q}{S + 2B + 3T + 4Q} \quad (2.4)$$

3. *Companion star fraction (csf)* - This is the average number of orbits per system, counting a binary as one orbit, a triple as two orbits, and quadruples as 3 orbits.

$$\mathbf{csf} = \frac{B + 2T + 3Q}{S + B + T + Q} \quad (2.5)$$

Observational surveys are usually restricted to a particular primary mass-range. Therefore it is meaningful to calculate the multiplicity for a particular primary mass (or mass-range), rather than all stars of all masses. The binary star fraction (**bf**) is thus difficult to calculate since it requires looking at all stars in that range, including secondaries, whereas the other two measures of multiplicity require only observing primaries of that mass.

- *Physical separation* - The separation of the binary components is characterised by the semi-major axis, a . Histograms of the separations usually use logarithmic binning, i.e. $\Delta N / \Delta \log_{10} a$ or $dN/d \log_{10} a$. The area under the histogram is usually normalised to equal the total multiplicity of the sample. In previous publications (e.g. Duquennoy & Mayor 1991, Patience et al. 2002), both the **mf** and the **csf** have been used.
- *Orbital period* - The orbital period of the binary system. If we know the total mass and semi-major axis of the binary, then we can use Kepler's third law to determine the period, i.e.

$$P^2 = \frac{4\pi^2 a^3}{G(m_1 + m_2)} \quad (2.6)$$

The period distribution is also presented in the form $\Delta N / \Delta \log_{10} P$ or $dN/d \log_{10} P$, i.e. using logarithmic binning.

- *Orbital eccentricity* - e

2.3 Observational techniques

Although binary stars were known about in the 19th century, the first complete statistical surveys were not conducted until the early 1990's. Such surveys have shown binary stars to be extremely common. Thus it is important to compile statistically robust distributions of the properties of binary stars in order to constrain binary star formation models, and indeed star formation models in general. Here, we briefly review the principal techniques used to detect binary stars.

1. *Common proper-motion pairs*

If two relatively close stars are observed to have a nearly identical proper-motion, it is inferred that they are part of a co-moving binary system. This technique is commonly used to detect very wide binaries where the period could be as long as 10^7 years making it impractical to follow the orbits for a complete period.

2. *Direct imaging of visual binaries*

Visual binaries are binary stars where both of the individual components are resolved and identifiable as two single stars in the optical, or in other wavelengths such as the infrared (IR). Both components can only be observed if the binary system is relatively nearby, or if the component separation is large. Long-term observations may reveal if the two stars are orbiting each other, or if it is just a chance alignment of two distant single stars. In statistical surveys, a proportion of the binaries will be unassociated stars in the same region of sky by chance (called 'apparent binaries'). Poisson statistics gives the probability of this occurring and thus allows a confidence level to be assigned to the identification of visual binaries, if the overall surface-density of stars in the region is known.

3. *Adaptive optics imaging*

The advent of adaptive optics (AO) systems has improved the resolution of telescopes towards their theoretical diffraction limits. Adaptive optics requires the use of a nearby bright reference star, which makes this method practical in young star clusters and star forming regions where reference stars are abundant.

4. *Lunar occultation*

Close binary systems (i.e. angular separation $\leq 1''$) cannot be resolved due to the seeing effects of the atmosphere. However, if the moon passes across an unresolved binary, the moon will block out the light from one of the stars, shortly followed by the second. This luminosity change can be recorded easily. This method can measure angular separations between the binary components projected along the normal to the moon's surface, but can

only be used for binaries in regions where the moon passes, i.e. between a declination of -30° and $+30^\circ$.

5. *Speckle interferometry*

Speckle interferometry attempts to de-convolve the effects of 'seeing' from the true diffraction limited image. Turbulent motions in the atmosphere cause light from a source to be diffracted with a particular point-spread function. If a short enough exposure is made, the effects of the diffraction can be de-convolved increasing the resolution of the image. Binaries with angular separations less than $1''$ can then be resolved. A derivative of this method, speckle holography, has also been adopted recently.

6. *Eclipsing binaries*

Eclipsing binaries have an orbital inclination close to the line of sight, such that the two stars eclipse each other at some point during the orbit. The total luminosity of the binary is reduced during an eclipse. If the luminosity is observed to vary periodically, then it is inferred that the star is part of an eclipsing binary system. This method cannot be used on its own as a tool for large statistical surveys since the percentage of systems with a small enough orbital inclination is very low. This method is only practical for very close binaries (e.g. such as interacting binaries) where the components cannot be resolved.

7. *Spectroscopic binaries*

The radial velocity of a star can be measured by calculating the Doppler shift of a known spectral line. If the Doppler shift (and hence radial velocity) is oscillating in time, we can infer that the star is orbiting another body, and hence is part of a binary system. If only one spectral line is seen to oscillate, then it is known as a single-line spectroscopic binary. If each spectral line has two components which oscillate in opposite directions, then it is known as a double-line spectroscopic binary. This is the same technique that is used to find planets orbiting around stars.

2.4 Surveys of Binary Stars

Observational surveys of binary stars have been conducted in many different environments using one or more of the techniques described in Section 2.3. Knowledge of the binary population at different stages of star formation (Main Sequence vs pre-Main Sequence) and in different star forming environments (clustered vs. isolated) provides important constraints on star formation theory. Many surveys have only been completed in specific limited samples e.g. volume-limited, magnitude-limited, resolution-limited. A complete description of binary parameters

Sample/Region	Author(s)	Detection method(s)	Survey limits	Separation/Period	Mass-ratio	Eccentricity	Sample size (S:B:T:Q)
Field G dwarfs	Duquennoy & Mayor (1991)	Spectroscopic, visual, CPM	All G-dwarf primaries within 22pc, $\delta \leq -15^\circ$.	$10^{-1} \leq P_d \leq 10^{10}$	Complete $q > 0.1$ and $P_d > 10^3$	Limited $P_d \leq 10^5$	164 : 62 : 7 : 2
	Mazeh et al. (1992)	Spectroscopic	All G-dwarf primaries within 22pc, $\delta \leq -15^\circ$.		Complete $P_d \leq 3000$		23 binaries
Field K dwarfs	Mayor et al. (1992)	Spectroscopic, visual, CPM	All K-dwarf primaries within 22pc, $\delta \leq -15^\circ$.	$1 \leq P_d \leq 10^{10}$		Limited $P_d \leq 10^{3.5}$	172 : 67
Field KG dwarfs	Halbwachs et al. (2003)	Spectroscopic	All KG-dwarf primaries within 22pc, $\delta \leq -15^\circ$				52 binaries
	Eggenberger et al. (2004)	Spectroscopic, Visual	All KG-dwarf primaries within 22pc, $\delta \leq -15^\circ$	$P_d < 2 \times 10^6$	Complete $q > 0.6$		570 : 51
Field M dwarfs	Fischer & Marcy (1992)	IR imaging, IR speckle interferometry, Spectroscopic, visual	All stars within 20pc	$0.04 \text{ AU} \leq a \leq 10^4 \text{ AU}$	Complete $q > 0.4$		Many samples - see paper
	Udry et al. (2000)	Spectroscopic	All M-dwarf primaries within 20pc, $\delta \leq -15^\circ$			Incomplete $P_d \leq 10^4$	31 binaries

Table 2.1: Summary of main observational surveys of field star binaries

Sample/Region	Author(s)	Detection method(s)	Survey limits	Separation/Period	Mass-ratio	Eccentricity	Sample size (S:B:T:Q)
Taurus	Simon et al. (1992)	IR imaging, IR lunar occultation	T-tauri stars in the northern Taurus star-forming region	$0.005'' \leq \theta \leq 10''$			28 : 11 : 2
	Leinert et al. (1993)	IR imaging, IR lunar occultation, IR speckle interferometry	T-tauri stars within Taurus star forming region, $3h 45 < \alpha < 5h 15$, $15^\circ < \delta < 35^\circ$	$0.13'' \leq \theta \leq 13''$			104 : 39 : 3 : 2
	Simon et al. (1995)	IR lunar occultation, IR imaging	T-tauri stars within Taurus star forming region	$0.005'' \leq \theta \leq 10''$			47 : 22 : 4
	Köhler & Leinert (1998)	IR imaging, IR lunar occultation, IR speckle interferometry, X-ray imaging	T-tauri stars within Taurus star forming region	$0.13'' \leq \theta \leq 13''$			178 : 68 : 9 : 3
	Torres et al. (2002)	Spectroscopic	X-ray selected sample of young stars in the Taurus-Auriga star-forming region	$P_y < 1$			43 binaries
	Duchêne et al. (2004)	IR imaging	Class I protostars in Taurus star forming region	$0.8'' \leq \theta \leq 30''$, $110\text{AU} \leq a \leq 4200\text{AU}$			22 : 5
Ophiuchus	Simon et al. (1995)	IR lunar occultation, IR imaging	T-tauri stars in Ophiuchus star forming region	$0.005'' \leq \theta \leq 10''$			35 : 10 : 2 : 1
	Barsony et al. (2003)	IR speckle interferometry	T-tauri stars in Ophiuchus star forming region	$0.1'' \leq \theta \leq 1.1''$			19 : 4 : 1
	Duchêne et al. (2004)	IR imaging	Class I protostars in Ophiuchus star forming region	$0.8'' \leq \theta \leq 10''$, $110\text{AU} \leq a \leq 1400\text{AU}$			41 : 12
	Ratzka et al. (2005)	Speckle interferometry	Ophiuchus star forming region	$0.13'' \leq \theta \leq 6.4''$			158 : 43 : 3
Orion	Prosser et al. (1994)	HST PC imaging	Trapezium cluster	$0.06'' \leq \theta \leq 1''$, $26\text{AU} \leq a \leq 440\text{AU}$			319:35
	Padgett et al. (1997)	HST WFPC2 imaging	NGC-2064, NGC-2068 & NGC2071	$0.3'' \leq \theta \leq 2.3''$, $138\text{AU} \leq a \leq 1050\text{AU}$			99:15
	Petr et al. (1998)	Speckle holography	Trapezium cluster	$0.14'' \leq \theta \leq 0.5''$, $63\text{AU} \leq a \leq 225\text{AU}$			35:4
	Simon et al. (1999)	Adaptive optics IR imaging	Orion Trapezium Cluster	$0.3'' \leq \theta \leq 0.6''$			292 : 17
	Scally et al. (1999)	CPM pairs	Orion Nebular Cluster	$1000\text{AU} \leq a \leq 5000\text{AU}$			894 : 3
	Köhler (2004)	AO imaging	0.7pc - 2.0pc from ONC	$0.13'' \leq \theta \leq 1.11''$, $60\text{AU} \leq a \leq 500\text{AU}$			See paper
Chamaeleon	Köhler (2001)	IR imaging, IR speckle interferometry, X-ray imaging	X-ray selected T-tauri stars in the Chamaeleon star-forming regions	$1'' \leq \theta \leq 12''$, $150\text{AU} \leq a \leq 1800\text{AU}$			80 : 19
Southern sky star forming regions	Reipurth & Zinnecker (1993)	IR imaging	Chamaeleon, Lupus, Ophiuchus, Corona Australis	$1'' \leq \theta \leq 12''$, $150\text{AU} \leq a \leq 1800\text{AU}$			238 : 37 : 1
	Ghez et al. (1997)	Speckle interferometry, imaging	T-tauri stars within Chamaeleon, Lupus and Corona Australis	$0.1 \leq \theta \leq 12$			43 : 25
	Melo et al. (2003)	Spectroscopic	Ophiuchus-Scorpius, Chamaeleon, Lupus, Corona Australis	$P_d < 10^2$			65 : 4

Table 2.2: Summary of main observational surveys of pre-Main Sequence binaries.

Sample/Region	Author(s)	Detection method(s)	Survey limits	Separation/Period	Mass-ratio	Eccentricity	Sample size (S:B:T:Q)
Hyades	Stefanik & Latham (1992)	Spectroscopic	Visible stars in Hyades cluster	$P_d < 10^5$		Limited $P_d < 10^5$	200 : 46
	Patience et al. (1998)	Speckle Interferometry	Visible stars in Hyades cluster	$0.044'' \leq \theta \leq 1.34''$		Complete $q > 0.2$	167:33
Pleiades	Mermilliod et al. (1992)	Spectroscopic, photometric	KG primaries in the Pleiades cluster	$P_d < 10^3$		Complete $q > 0.4$ for photometric binaries	Limited $P_d < 10^3$ 56:30:2
	Bouvier et al. (1997)	IR Adaptive optics imaging	KG primaries in the Pleiades cluster	$0.08'' \leq \theta \leq 6.9''$, $11\text{AU} \leq a \leq 910\text{AU}$			144 : 22 : 3
	Martin et al. (2000)	IR photometry and optical spectroscopy	Brown dwarfs in the Pleiades				
Praesepe	Mermilliod & Mayor (1999)	Spectroscopic, photometric	KG primaries in the Praesepe cluster	$P_d < 10^4$		Complete $q > 0.5$ for photometric binaries	Limited $P_d < 10^4$ 47:30:3
	Bouvier et al. (2001)	IR Adaptive optics imaging	KG primaries in the Praesepe cluster	$0.08'' \leq \theta \leq 3.3''$, $15\text{AU} \leq a \leq 600\text{AU}$			149 : 26
	Patience et al. (2002)	Speckle Interferometry, Near-IR HST	Praesepe cluster	$0.053'' \leq \theta \leq 7.28''$		Complete $q > 0.4$	100 : 12
Persei	Patience et al. (2002)	Speckle Interferometry, NIR HST NICMOS	Persei cluster	$0.053'' \leq \theta \leq 7.28''$		Complete $q > 0.4$	109 : 10
Scorpius	Brandner & Köhler (1998)	X-ray selected sample of weak-line T-auri stars in the Scorpius-Centaurus OB association	IR speckle interferometry, X-ray imaging	$0.1'' \leq \theta \leq 3''$			114 : 39
	Köhler et al. (2000)	X-ray selected sample of T-auri stars in the Scorpius-Centaurus OB association	IR speckle interferometry, IR imaging, X-ray imaging	$0.13'' \leq \theta \leq 6''$			104 : 36 : 5
	Shatsky & Tokovinin (2002)	Near-infrared adaptive optics	B-type stars in the Scorpius OB2 association	$0.3'' \leq \theta \leq 6.4''$			115 : 27
	Kouwenhoven et al. (2004)	Near-IR adaptive optics	Hipparcos selected A- and B-type stars of the Scorpius OB2 association	$0.22'' \leq \theta \leq 12.4''$			199 : 74

Table 2.3: Summary of main observational surveys of binaries in open clusters.

in star formation regions is not yet available, although on-going surveys like those performed using CORAVEL (e.g. Duquennoy & Mayor 1991) are likely to provide invaluable constraints on star formation theory in the future. Here we discuss the extent and results from existing surveys. Tables 2.1, 2.2 and 2.3 summarise the main surveys that have been performed of binary systems.

2.4.1 The galactic field

The galactic field represents the final destination for the majority of stars formed. While there are believed to be different star formation environments that form binaries with different properties (e.g. the difference between Taurus and Orion), the overall resultant binary distribution must be that of the field. Surveys of field star binaries provide the most complete and statistically robust observed binary distributions available. Table 2.1 summarises the main surveys performed of field stars, which binary parameters were measured, and the observational limits.

G-dwarfs

Duquennoy & Mayor (1991; hereafter DM91) published the first complete survey of the binary properties from a selected volume limited sample of stars. DM91 chose nearby (within 22 pc) field G-dwarf (F7 - G9) stars corresponding to Main-Sequence primary stars with masses in the range $0.84 M_{\odot} \leq M \leq 1.2 M_{\odot}$. This study was part of the ongoing CORAVEL spectroscopic survey to obtain the properties of short-period spectroscopic binaries. This survey was combined with published data on CPM and visual binaries within 22pc to provide a complete sample over the full binary separation range. This yielded a sample size of 164 G-dwarf primaries. The mass-ratio distribution for low-period ($P_d < 10^3$ days) systems was determined by Mazeh et al. (1992).

DM91 found that the period distribution of G-dwarf binary systems could be well fitted with a lognormal,

$$\frac{dN}{d \log P_d} = C_p \exp \left(\frac{-\left(\log P_d - \overline{\log P_d}\right)^2}{2\sigma_{\log P_d}^2} \right), \quad (2.7)$$

where P_d is the period in days. For G-dwarfs, $\overline{\log P_d} = 4.8$, $\sigma_{\log P_d} = 2.3$. We convert this period distribution into a separation distribution (c.f. FM92) using Kepler's third law. The separation distribution is also lognormal,

$$\frac{dN}{d \log a_{\text{AU}}} = C_a \exp \left(\frac{-\left(\log a_{\text{AU}} - \overline{\log a_{\text{AU}}}\right)^2}{2\sigma_{\log a}^2} \right), \quad (2.8)$$

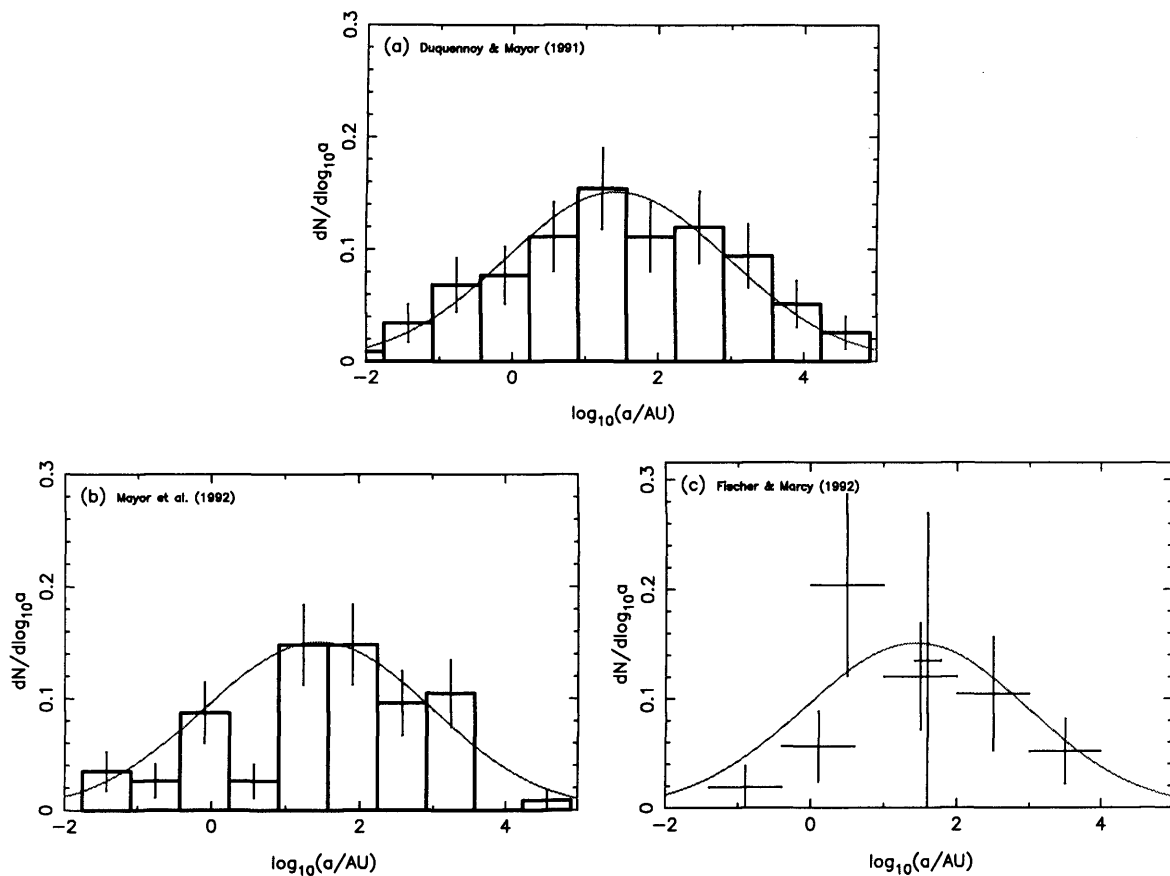


Figure 2.3: (a) The observed separation distribution of field G-dwarf binaries (Duquennoy & Mayor 1991), which is fitted with a lognormal function given by Equation 2.8. This lognormal is used in all other figures of binary separation as a reference curve. (b) The observed separation distribution of field K-dwarf binaries (Mayor et al. 1992). (c) The observed separation distribution of field M-dwarf binaries (Fischer & Marcy 1992)

where a_{AU} is separation in AU. For G-dwarfs, $\overline{\log a_{\text{AU}}} = 1.44$, $\sigma_{\log a} = 1.53$. This lognormal fit, along with the observational data, is plotted on Figure 2.3a. We also plot Equation 2.8 on all graphs showing the separation distribution as a reference curve. The total multiplicity of G-dwarfs over the full separation range is 0.57 ± 0.08 corrected for incompleteness.

K-dwarfs

The CORAVEL survey also looked at the binary properties of K-dwarf primaries. The sample included all K-dwarf (IV - VI) stars in the mass range $0.47 M_{\odot} \leq M \leq 0.84 M_{\odot}$ within 22pc with declination $\delta \leq -15^{\circ}$, comparable to the DM91 G-dwarf sample. This yielded a total sample size of 172 K-dwarf primaries. Mayor et al. (1992) published preliminary results of this survey. Eggenberger et al. (2004) and Halbwachs et al. (2005) published more recent results of the CORAVEL survey, but combined the K-dwarf and G-dwarf samples rather than keeping them separate.

Mayor et al (1992) found that the K-dwarf binary period distribution is lognormal, like the G-dwarf period distribution, with a similar width and mean; $\overline{\log P_d} = 4.9$, $\sigma_{\log P_d} = 1.9$. The equivalent separation distribution is plotted in Figure 2.3b. The multiplicity of K-dwarfs is 0.45 ± 0.07 .

M-dwarfs

Fischer & Marcy (1992; hereafter FM92) published a collation of known binary properties of M-dwarf stars (corresponding to Main-sequence stars with masses $0.08 M_{\odot} \leq M \leq 0.47 M_{\odot}$). FM92 selected a volume-limited sample of all M-dwarf primaries within 20 pc from the Gliese (1969) catalogue, similar to DM91. They used a wide range of techniques to detect binaries, such as radial velocity measurements, infra-red imaging, infra-red speckle interferometry, as well as visual binaries and common proper-motion binaries. FM92 measured binary periods over nearly the same wide range as DM91.

FM92 also found a roughly lognormal period/separation distribution for M-dwarf binaries (Figure 2.3c), consistent with the form of the G-dwarf distribution, although the height of the distribution is lower due to the lower multiplicity of M-dwarfs. The multiplicity of M-dwarfs is 0.42 ± 0.09 .

2.4.2 Star-forming regions

The pre-Main Sequence phase of a star's evolution represents the epoch between when young stars emerge from the core within which they formed and when they appear on the Main Sequence. Detailed observations of this early evolutionary stage can help to establish if binary

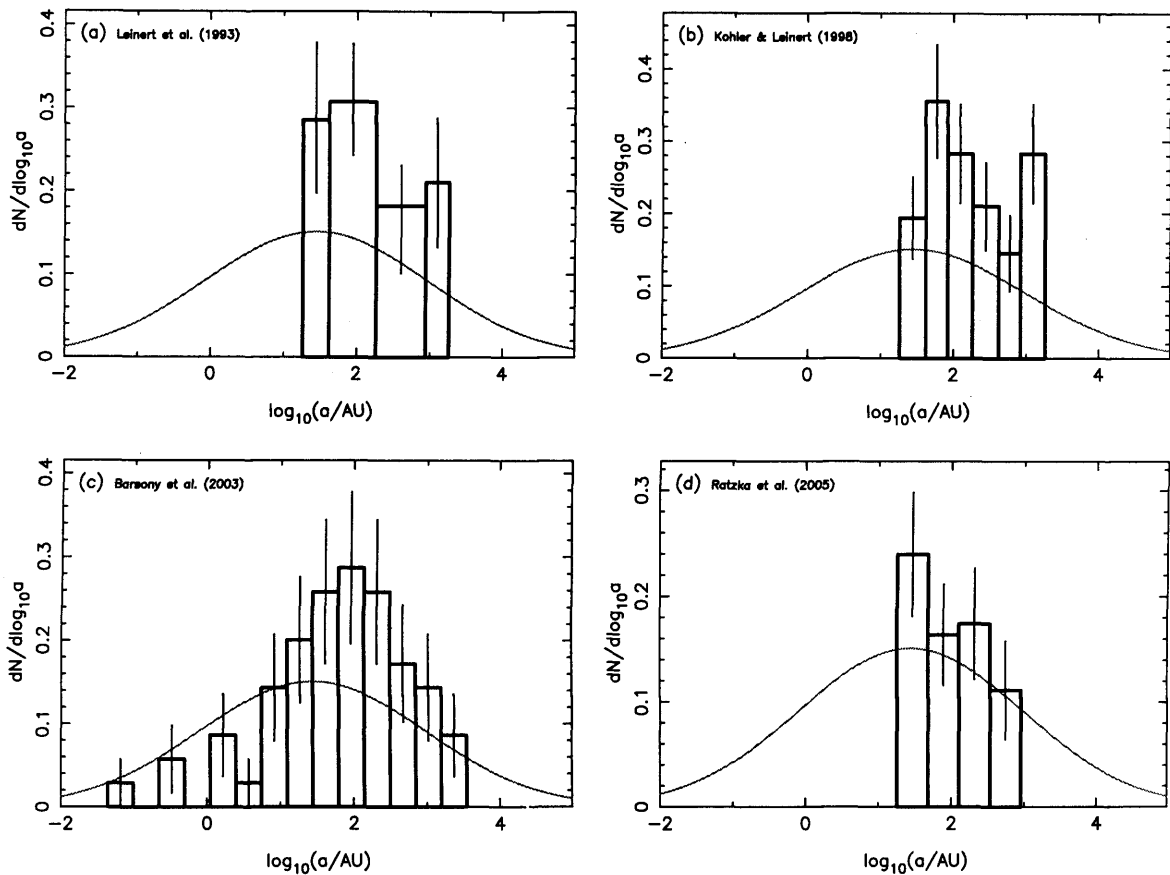


Figure 2.4: (a) Separation distribution of binaries in Taurus (Leinert et al. 1993) (b) Separation distribution of binaries in Taurus, including PMS binaries identified using the X-ray ROSAT survey (Köhler & Leinert 1998) (c) Separation distribution of binaries in ρ Ophiuchi (Barsony et al. 2003). (d) Separation distribution of binaries in ρ Ophiuchus (Ratzka et al. 2005). The DM91 lognormal fit to the separation distribution of G-dwarf field binaries is shown as a thin line for comparison.

properties are determined when the stars are formed, or if binary properties are determined later on in a star's life. Here, we discuss surveys made in the two decade of pre-Main Sequence binaries in well-observed nearby star forming regions. These surveys have helped to determine the multiplicity and separation distributions of binaries. Mass-ratios are difficult to calculate due to uncertainties in PMS evolutionary tracks.

Taurus

Taurus is the most studied star formation region due to its proximity (≈ 140 pc) and its low density (hence low extinction and lack of confusion). The properties of binary stars in Taurus have been investigated in various studies (Leinert et al. (1993), Simon et al. (1995), Köhler & Leinert (1998)) using techniques such as direct imaging, lunar occultation and speckle interferometry

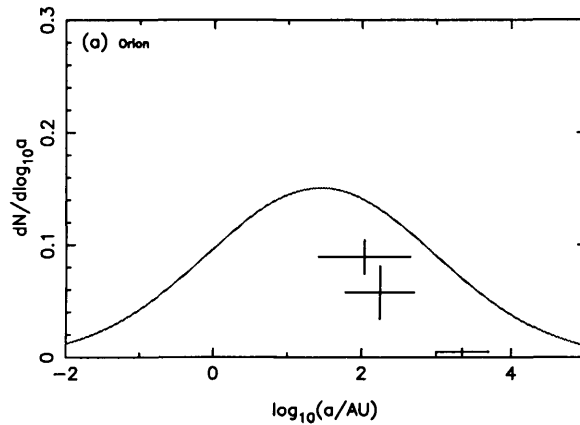


Figure 2.5: Observations of the multiplicity of low-mass PMS stars in the Trapezium cluster (Prosser et al. 1994; Padgett et al. 1997; Scally et al. 1999; Köhler 2004).

in the infra-red. Duchêne et al. (2004) performed the first survey of the binary properties of even younger class I protostars.

Figures 2.4a and b show the binary separation distributions in the Taurus star formation region as determined by Leinert et al. (1993) and Köhler & Leinert (1998). In the separation range $18.2 \text{ AU} \leq a \leq 1820 \text{ AU}$, the multiplicity of PMS stars in Taurus is about a factor of 2 higher than for field stars. If the form of the separation distribution of PMS stars is the same as for field stars and we extrapolate over the entire separation range, then this suggests that *all PMS stars in Taurus are part of multiple systems*. This is also suggested by earlier studies of Taurus (Simon et al. 1992, Ghez et al. 1993). Duchêne et al. (2004) found that the multiplicity of Class I sources in the separation range $110 \text{ AU} \leq a \leq 1400 \text{ AU}$ is about 0.23 ± 0.09 , which again is about twice the value of field stars.

Ophiuchus

The Ophiuchus star forming region has intermediate properties between the two extreme cases of Taurus and Orion (e.g. Duchêne et al. 2004). It is relatively nearby ($\approx 140 \text{ pc}$) and is thus well observed. Barsony et al. (2003) and Ratzka et al. (2005) have performed surveys of ρ -Ophiuchus using infra-red speckle interferometry techniques similar to those used to observe Taurus. Duchêne et al. (2004) also surveyed the binary properties of class I protostars in Ophiuchus, as well as Taurus.

Binary surveys of Ophiuchus (e.g. Barsony et al. 2003, Ratzka et al. 2005) reveal that the multiplicity of PMS stars in the separation range $10 \text{ AU} \leq a \leq 1000 \text{ AU}$ is greater than in the field, and similar to the multiplicity of Taurus. Barsony et al. (2003; Figure 2.4c) show that while there is an excess of binaries in the separation range $10 \text{ AU} \leq a \leq 1000 \text{ AU}$ relative to the field, the multiplicity in other separation ranges is roughly consistent with the field (although

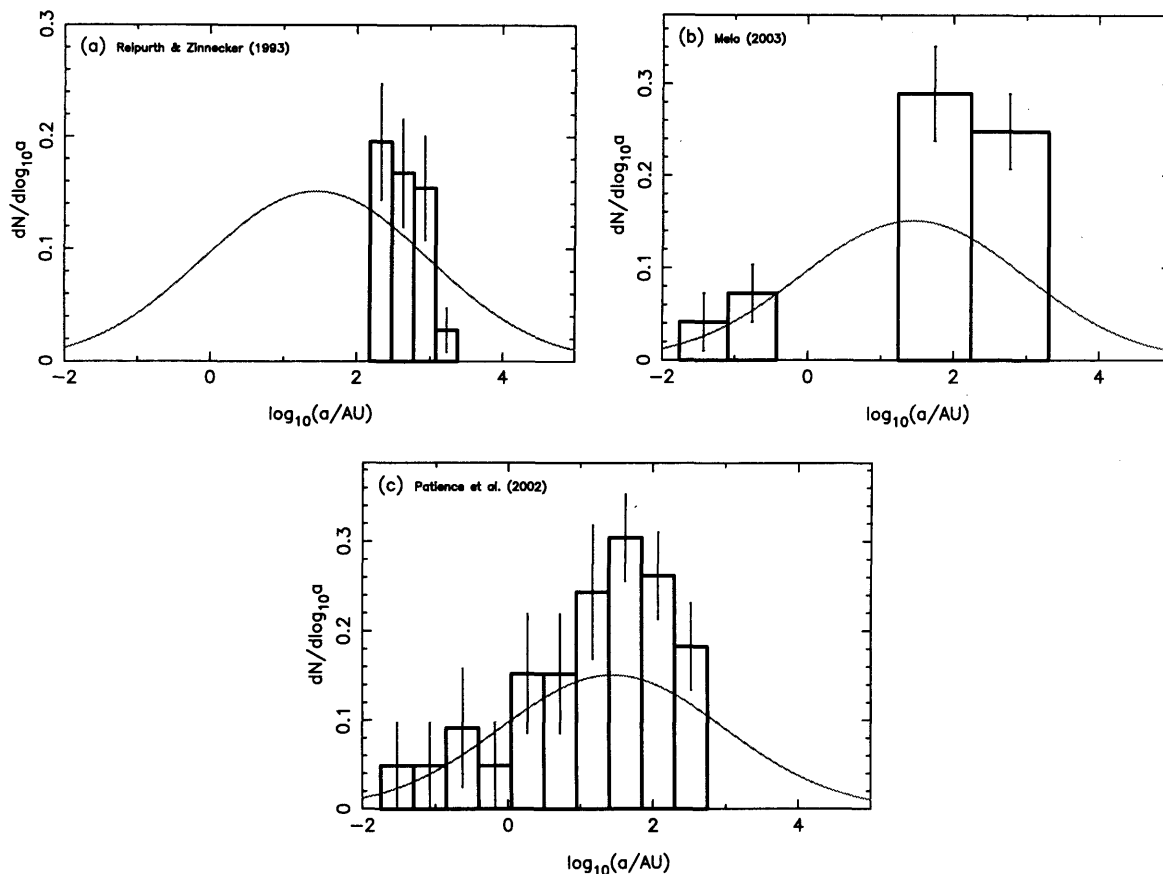


Figure 2.6: (a) Separation distribution of PMS binaries from the Ophiuchus, Lupus, Chamaeleon and Corona Australis star formation regions (Reipurth & Zinnecker 1993) (b) Observations of spectroscopic binaries in the Ophiuchus-Scorpius, Chamaeleon, Lupus and Corona Australis star formation regions (Melo 2003) combined with observations by Ghez et al. (1993) and Ghez et al. (1997) (c) Compilation of observations of the binary separation distribution for binaries in Taurus, Ophiuchus, Lupus, Chamaeleon and Corona Australis (Patience et al. 2002)

observations in these separation ranges are not necessarily complete). The form of the separation distribution for pre-Main Sequence stars is thus different to the Main Sequence distribution. Duchêne et al. (2004) found that the multiplicity of Class I sources in Ophiuchus within the separation range $110 \text{ AU} \leq a \leq 1400 \text{ AU}$ is about 0.29 ± 0.07 ; this is the same (within $\approx 1\sigma$) as the multiplicity of Class I sources in Taurus and again roughly twice that of the field.

Orion

The Orion star formation region is considered to be the archetypal example of the clustered mode of star formation. It is believed that the majority of stars are formed in such environments (e.g. Lada & Lada 2003), so constraining its binary properties is of particular importance. The Orion star forming region has several distinct sub-regions, such as OB associations, the

molecular cloud complex, embedded clusters and the famous Trapezium cluster. Observations of binary stars have concentrated on the Trapezium cluster (Petr et al. 1998, Padgett et al. 1997) and also the wider Orion Nebular Cluster (e.g. Scally et al. 1999)

The binary separation distribution in Orion is less well constrained due to its greater distance and higher stellar density. Figure 2.5 shows a compilation of various studies of the separation distribution in the dense Trapezium cluster. The observations suggest a deficit of binaries compared to the field for solar-mass stars. The **csf** in Orion for binaries with $a \sim 100\text{AU}$ is between $\sim \frac{1}{3}$ and $\sim \frac{2}{3}$ of the field value, although the statistical errors are large. There also appear to be no wide binaries present ($a > 1000\text{AU}$) in the Trapezium cluster (Scally et al. 1999). This suggests the overall **csf** of the Trapezium cluster is lower than the field, unless there is an excess of binaries at smaller separations. This is in contrast to less dense regions like Taurus where there is a clear excess of binaries at wider separations. However, Petr et al. (1998) found that the **csf** in the outer regions of the Trapezium, plus other parts of the ONC have a higher **csf** than the field, and comparable to Taurus and Ophiuchus.

Combined surveys

Reipurth & Zinnecker (1993) performed one of the first combined surveys of pre-Main Sequence binaries, including binaries from the Ophiuchus, Lupus, Chamaeleon and Corona Australis star formation regions. They found that the multiplicity in the separation range $150\text{AU} \leq a \leq 1800\text{AU}$ is approximately 0.16, 1.4 times larger than the field value (Figure 2.6a). Extrapolating over the full binary separation range, they suggest the multiplicity is at least 0.8.

Melo (2003) combined spectroscopic studies of pre-Main Sequence binaries in Ophiuchus-Scorpius, Chamaeleon, Lupus and Corona Australis with high-angular resolution studies of the same regions from Ghez et al. (1993) and Ghez et al. (1997). Figure 2.6b shows the resulting separation distribution. The **csf** of pre-Main Sequence spectroscopic binaries is larger than in the field, but is within the 1σ error bars and thus may not be statistically significant. The **csf** of larger-separation binaries ($15\text{AU} \leq a \leq 1800\text{AU}$) is 0.52 and is almost twice as large as the **csf** of Main Sequence binaries in the same separation range. Melo (2003) notices differences in the multiplicity of spectroscopic binaries between the different regions.

Figure 2.6c shows the separation distribution from a compilation of various star forming regions (Taurus, Ophiuchus, Chamaeleon, Corona Australis, Lupus) by Patience et al. (2002).

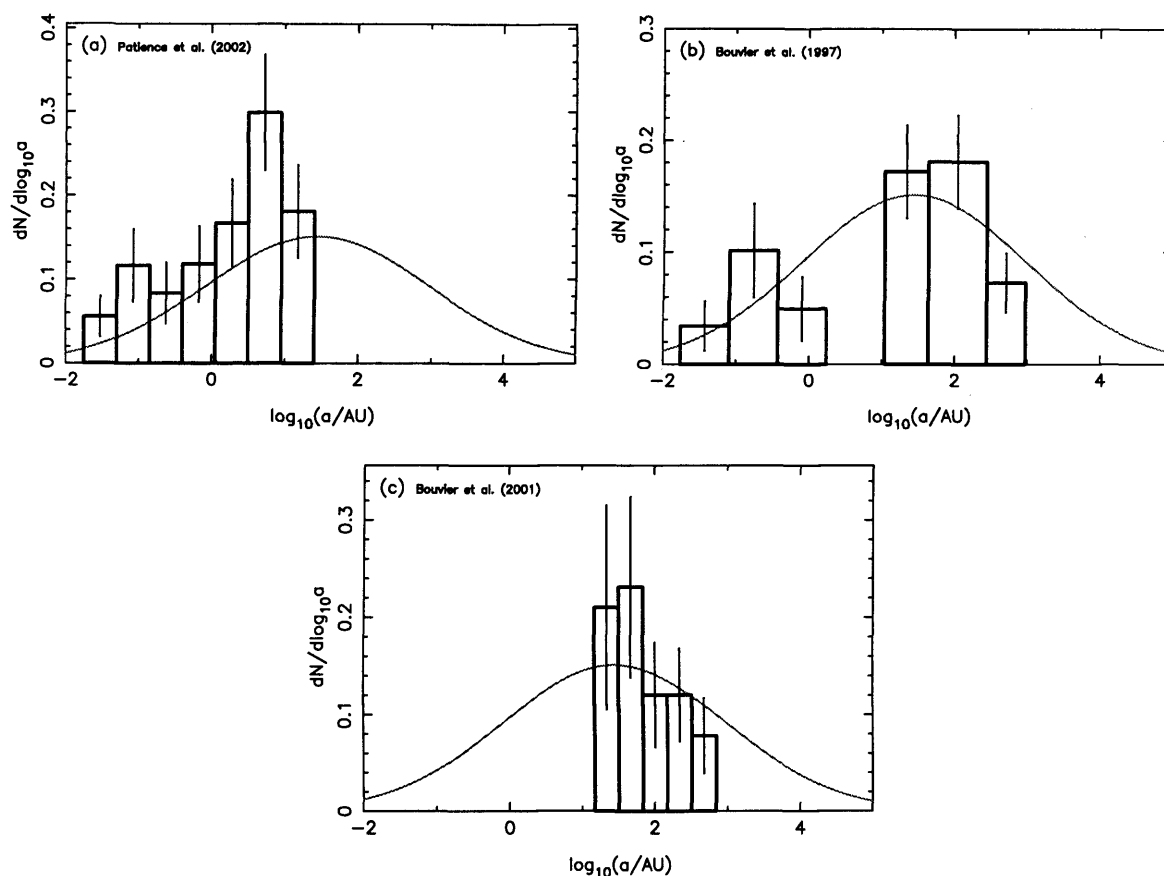


Figure 2.7: (a) Separation distribution of binaries in the Hyades cluster (Patience et al. 2002). (b) Separation distribution of spectroscopic and visual binaries in the Pleiades cluster (Bouvier et al. 1997). (c) Separation distribution of visual binaries in the Praesepe cluster (Bouvier et al. 2001).

2.4.3 Young open clusters

Young open clusters represent an intermediate state between star formation and when a star joins the Galactic field population. Observations at this stage of the evolution may provide another constraint on binary formation models.

Hyades

The Hyades is a nearby (≈ 46 pc) open cluster of estimated age 625 Myr (Perryman et al. 1998). It has been surveyed for binaries using spectroscopic methods (e.g. Griffin et al. 1988) and using infra-red speckle interferometry (Patience et al. 1998).

Figure 2.7a shows the separation distribution of Hyades binaries in the separation range $0.02 \text{ AU} \leq a \leq 25 \text{ AU}$ (Patience et al. 2002). The multiplicity at all separations in this range appear to be at least as high as the field. However, there is a noticeable peak in the separation distribution at around $a \sim 5 \text{ AU}$, i.e. at a significantly smaller separation than the peak of the

field G-dwarf binary separation distribution at $a \sim 50$ AU. This suggests that the separation distribution of clusters such as the Hyades is weighted towards smaller separation than the field, i.e. opposite to observations of some star forming regions such as Taurus which suggest a peak at larger separations than the field.

Pleiades

The Pleiades is one of the most well known star clusters. It is situated in the constellation of Taurus at a distance of ≈ 132 pc. The cluster has an estimated age of ≈ 100 Myr (Mazzei & Pigatte 1989). It has been surveyed for spectroscopic binaries (Mermilliod et al. 1992) and for visual binaries using Adaptive Optics (Bouvier et al. 1997). Surveys of brown dwarfs and brown-dwarf binaries have been conducted using optical and near infra-red photometry (e.g. Martín et al. 2000, Pinfield et al. 2003).

Figure 2.7b shows the observed separation distribution of the Pleiades combining the results of Bouvier et al. (1997) and Mermilliod et al. (1992). In the observed separation ranges ($a \leq 2$ AU for spectroscopic binaries; $11 \text{ AU} \leq a \leq 910$ AU for visual binaries), the multiplicity is similar (within the errors) to the field G-dwarf values.

Martín et al. (2000) find that the multiplicity of brown dwarfs in the Pleiades is low. Out of a sample of 34 brown dwarf candidates, they find 6 binaries with separations $a \leq 27$ AU, but none with $a > 27$ AU suggesting both a low overall multiplicity for brown dwarfs and a deficit of wide systems. However, Pinfield et al. (2003) suggest that the multiplicity of brown dwarfs in the Pleiades may be as high as 0.5.

Praesepe

Praesepe is an open cluster of age ≈ 700 Myr. Bouvier et al (2001) surveyed the cluster for G and K-type primaries and detected 26 binaries using Adaptive Optics. Patience et al. (2002) surveyed the cluster using speckle interferometry.

Figure 2.7c shows the separation distribution observed by Bouvier et al. (2001) in the range $15 \text{ AU} \leq a \leq 600$ AU. The separation distribution is consistent with the field G-dwarf distribution within the statistical errors. There is a suggestion that the multiplicity of binaries at larger separations is lower than the field but better statistics are required to confirm this trend.

Scorpius

Scorpius OB2 is an OB association near the Scorpius star formation region. Shatsky & Tokovinin (2002) searched for visual companions of B-type ($3.5 M_{\odot} - 20 M_{\odot}$) stars using near infra-red adaptive optics. They found the csf of B-type stars in the separation range $45 \text{ AU} \leq a \leq 900$ AU was 0.26 ± 0.05 compared to 0.16 for field G-dwarfs in the same range.

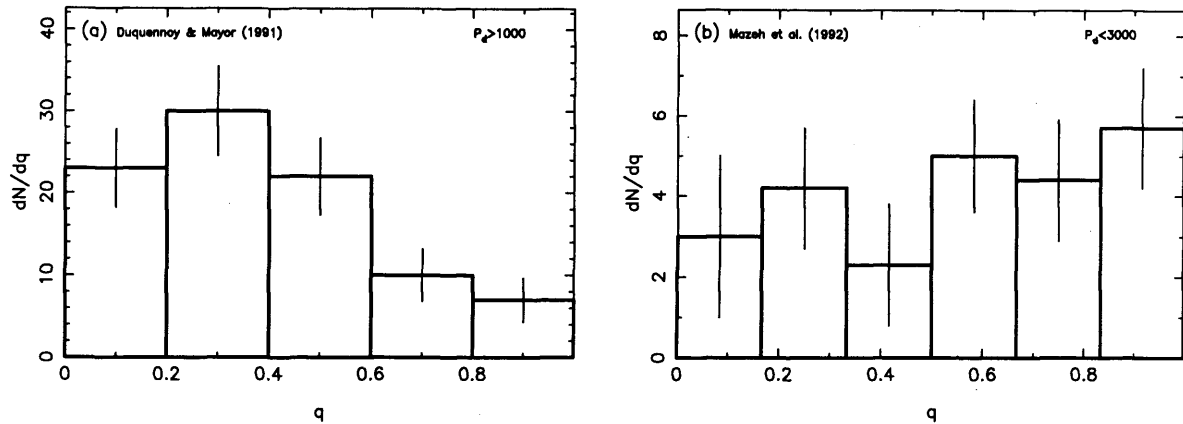


Figure 2.8: Observed mass-ratio distribution for (a) field G-dwarf binaries with periods $P_d > 10^3$ (Duquennoy & Mayor 1991), and (b) field G-dwarf binaries with periods $P_d < 10^3$ (Mazeh et al. 1992).

Kouwenhoven et al. (2004) conducted a survey of the multiplicity of stars of various spectral classes, focusing on A-type ($1.8 M_\odot - 3.4 M_\odot$) stars selected from HIPPARCOS data, again using near infra-red adaptive optics. They found a possible trend of multiplicity with mass in their limited sample; in general the multiplicity decreased with decreasing mass.

Köhler et al. (2000) have observed the multiplicity of T-tauri stars in the Scorpius-Centaurus OB association selected by X-ray observations using speckle interferometry and direct imaging. They find that the multiplicity of pre-Main Sequence stars in the separation range $17 \text{ AU} \leq a \leq 780 \text{ AU}$ is 1.6 times higher for field stars. They also compare the separation distribution of two subgroups in the association, Upper Scorpius A and B, and find the peak of the distribution is different.

2.4.4 Mass-ratios

DM91 find that for binaries having Main Sequence G-dwarf primaries, the distribution of q -values is dependent on the period. For long-period systems ($P_d > 10^3$), the q -distribution has a significant peak at around $q = 0.3$ (see Figure 2.8a). For short-period systems, a much flatter distribution is observed, gently rising towards $q = 1$ (Mazeh et al. 1992; Figure 2.8b).

Mass ratios have also been determined for binaries having Main Sequence M-dwarf primaries by FM92. However, there are too few systems to reveal any clear dependence on period, and the sample is incomplete for $q < 0.4$. For the whole sample, the distribution of mass ratios is consistent with being flat in the range $q \geq 0.5$, but there is the suggestion of a decrease for lower q -values. We note that for M-dwarf primaries these low q -values ($q \leq 0.5$) usually correspond to brown dwarf companions.

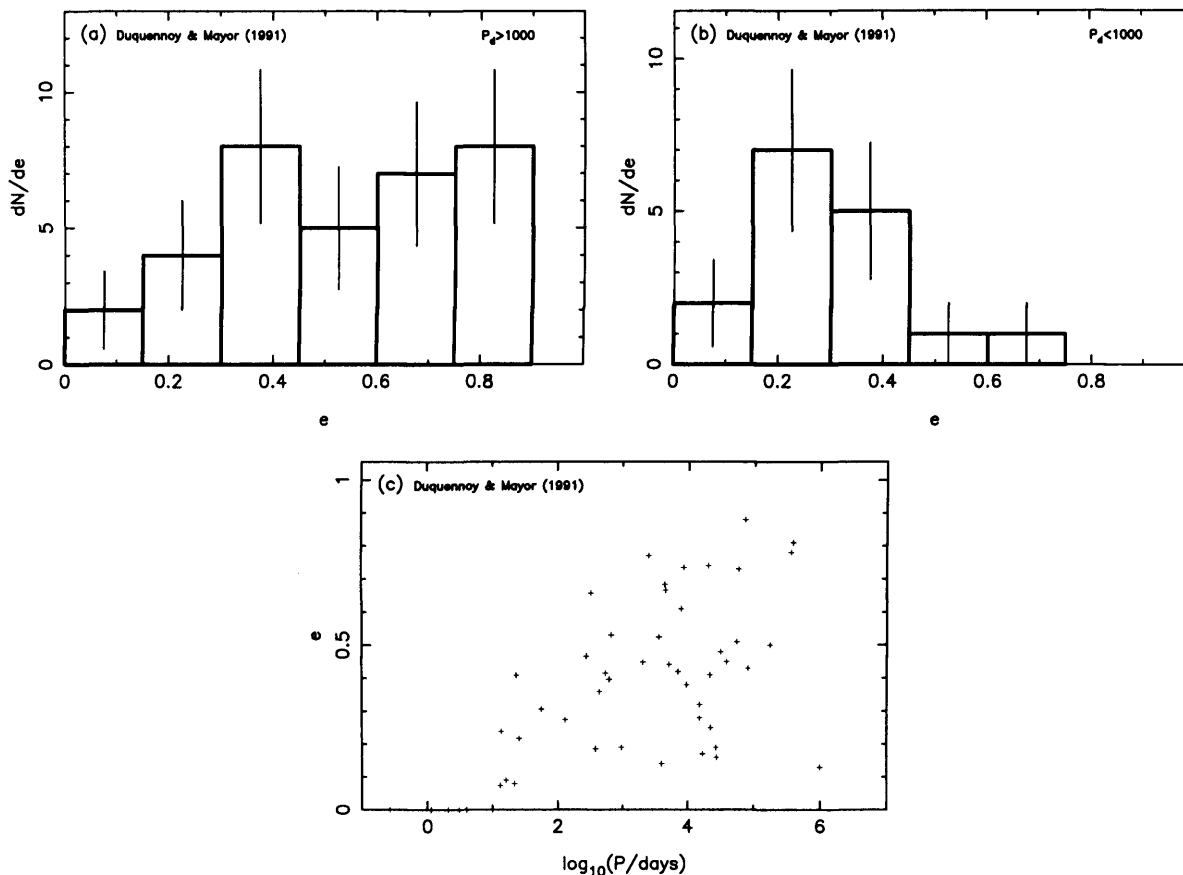


Figure 2.9: Observed eccentricity distribution for (a) field G-dwarf binaries with periods $P_d > 10^3$ (Duquennoy & Mayor 1991), and (b) field G-dwarf binaries with periods $P_d < 10^3$ (Duquennoy & Mayor 1991). (c) Period vs. eccentricity for G-dwarf binaries (Duquennoy & Mayor 1991); this graph shows the observed circularisation cut-off at around 10 days.

2.4.5 Eccentricity

DM91 find that for binaries with Main Sequence G-dwarf primaries, the eccentricity distribution depends on the period. For long-period systems ($P_d > 10^3$, $a > 10$ AU), the eccentricity distribution is approximately thermal (i.e. $dN/de = 2e$, Valtonen & Mikkola 1991); the DM91 results for long-period binaries are shown on Figure 2.9a. For short-period binaries with Main Sequence G-dwarf primaries ($P_d < 10^3$), the eccentricities tend to be significantly lower, with a distribution peaked around $e \approx 0.2$ (See Figure 2.9b). In addition, there appears to be an upper limit on the eccentricity, $e_{\text{MAX}}(P)$, which decreases with decreasing P and approaches zero for $P_d \leq 10$ (see Figure 2.9).

The data available for binaries with Main Sequence primaries of other spectral types (i.e. M-dwarfs and K-dwarfs) are limited, particularly for systems with long periods, but the overall distribution of eccentricity with period appears to be broadly similar to that for binaries with G-dwarf Main Sequence primaries. In particular, the upper limit on the eccentricity, $e_{\text{MAX}}(P)$,

decreasing with decreasing P and approaching zero for $P_d \leq 10$, appears to apply to all Main Sequence binaries (Mayor et al. 1992, Udry et al. 2000). This upper limit on e is normally attributed to tidal circularisation of close orbits.

For Pre-Main Sequence binaries the data on eccentricity is limited to short-period systems ($P_d < 10^4$). Again there appears to be an upper limit on the eccentricity, $e_{\text{MAX}}(P)$, which decreases with decreasing P (Mathieu 1994). However, this limit is somewhat larger than that for binaries with G-dwarf Main Sequence primaries, and it only approaches zero for $P_d \leq 3$. Again, this is consistent with a picture in which close systems are circularised tidally; in pre-Main Sequence systems there has been less time for the process to work.

2.5 Theories of Binary Star Formation

In this section, we discuss the various theories of binary star formation that have been proposed. We discuss older theories, explaining the reasons for their failure to explain the observations, and then discuss in greater detail theories which are currently being investigated by the star formation community (For further reading, see Tohline 2002 and Larson 2003).

2.5.1 Fission

Fission was proposed as early as the 19th century as a possible formation mechanism for binary stars. Fission occurs when a star-forming cloud with non-zero angular momentum forms a protostar and 'spins up' as it collapses. When the rotational velocities of the protostar become too high (i.e. greater than the break up speed), the protostar splits into two stars thus forming a binary star. This theory remained popular until the 1970's where increased computer power allowed numerical simulations to investigate fission thoroughly. Various numerical studies (e.g. Durisen et al. 1986) show that fission is unlikely to occur and is incapable of explaining the observed properties of binary systems. Simulations suggest that a rapidly rotating cloud will form spiral arms which transport angular momentum away from the star until it is stabilised rather than split into two bodies. When fission does occur, the mass-ratios are typically low (i.e. $q \ll 1$) contrary to observations.

2.5.2 Capture

The theory of capture assumes that a star forms as a single object in a cluster and then becomes bound to another star by dynamical encounters. Capture by purely dynamical (i.e. gravitational) interactions requires at least three stars. For two unbound stars to become bound as a binary system, a third star must remove some binding energy from the pair. This mechanism

has several failings in respect to the observations; (a) 3-body encounters are rare, both in the cluster environment and the field, so capture is too inefficient to produce the observed number of binaries (e.g. Kroupa 1995), (b) the ages of binary components would not be correlated in capture whereas observations suggest the ages of binary components are the same, suggesting that they form at the same time and presumably as a binary (Ghez & White 2000).

2.5.3 Disc capture

T-tauri stars are known, both indirectly (through their SEDs) and directly (from HST observations), to have significant discs. A variant on the capture model is that single pre-Main Sequence stars interact very early on before their discs have been accreted. Close interactions between discs or star-disc encounters may dissipate orbital energy. Disc interactions may therefore provide a mechanism for forming a binary system from two unbound stars. Disc capture only requires two-body interactions and thus may be more common than dynamical capture. However, simulations of star-disc encounters using realistic clusters suggests that the high relative velocities would result in the disc being destroyed rather than dissipating enough energy to leave the system bound.

2.5.4 Core fragmentation

The Shu (1977) model of star formation assumed that prestellar cores produce only a single star. However, binary star formation models that assume stars initially form as singles (such as capture and disc capture) cannot explain the high multiplicity of stars. We must assume stars are born in multiple systems. Prestellar cores are assumed to fragment into multiple protostars. There are several possible modes of fragmentation which we briefly discuss.

1. *Disc fragmentation*

Depending exactly on the initial conditions, disc fragmentation occurs when a core initially collapses to form a central star. Any material that has sufficient angular momentum forms a flattened accretion disc around the star. The remaining core material will become part of the disc. If the disc becomes sufficiently massive, and depending on the thermal properties of the disc, then the disc can become gravitationally unstable and fragment forming a second star.

2. *Rotational fragmentation*

Rotational fragmentation is when a core fragments directly after the first collapse phase forming multiple protostars. Unlike disc fragmentation, rotational fragmentation does not produce a central object first. In general, rotational fragmentation occurs when a slowly

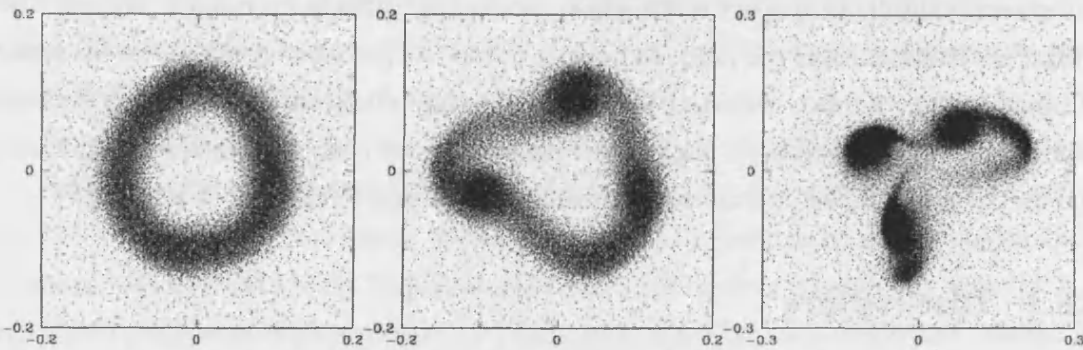


Figure 2.10: Example of ring fragmentation in numerical simulations of star formation (from Cha & Whitworth 2003b).

rotating core collapses due to gravity. The main parameter is β (\equiv rotational energy / gravitational energy). As a core collapses, β increases; when $\beta \approx 1$, the infalling material is rotating so fast that it exceeds centrifugal support and 'bounces' back outwards. This can form a dense ring of material which is unstable and fragments into multiple protostars (e.g. Bonnell & Bate 1994, Cha & Whitworth 2003b; see Figure 2.10). This mechanism is highly dependent on the density and velocity profiles. In particular, it seems to require a differentially rotating core to work effectively (e.g. Myhill & Koala 1992); otherwise a central object may form first.

3. Dynamically triggered fragmentation

Dynamically triggered star formation occurs when a particular star formation event is triggered by the motion of other material, such as clumps or protostars, in the star-forming region. Examples of dynamically triggered star formation include cloud-cloud collisions (e.g. Bhattal et al. 1998), interactions between protostars and protostellar discs (e.g. Boffin et al. 1998, Watkins et al. 1998a, 1998b). The increased density in turn increases the cooling rate such that the temperature is reduced thereby shortening the Jeans length. If the Jeans length is much shorter than the system size, then fragmentation can occur.

4. Turbulent fragmentation

Observations of star-forming regions suggest that turbulence plays an important role in determining the structure and evolution of molecular clouds (e.g. Larson 1981). Simulations of prestellar cores with turbulence show that turbulent motions can promote fragmentation. Turbulent motions can seed density perturbations in a core or create gravitationally unstable shock layers. Many recent studies of star formation have focused on the effects of turbulence (e.g. Bate, Bonnell & Bromm 2002a, 2002b, 2002c, Goodwin, Whitworth & Ward-Thomson 2004a, 2004b). Turbulent fragmentation can explain the

formation of brown dwarfs as an ejected population of protostellar 'seeds' that have not had sufficient time to accrete.

2.5.5 Problems involving binary star formation

Here we discuss some of the important questions that need answering in order to obtain a more complete understanding of the origin of binary stars and their statistical properties. Answering these questions is the main motivation for the work reported in this thesis. We distinguish here between the primordial binary population, which are binaries resulting directly from the fragmentation of individual cores (i.e. zero-age binaries), and the pre-Main Sequence binary population, which may have undergone internal or external evolution after a finite time.

1. *What are the main factors that determine the properties of primordial binaries?*

If we assume that an individual star-forming core produces an individual stellar system (i.e. a single, binary or higher-order multiple), then the properties of the stellar system are likely to be determined by the properties of the core. This includes the core mass, total angular momentum, the velocity profile (e.g. turbulent, bulk rotation, differential rotation etc.), the density profile, the temperature profile and the ionization fraction. External factors may also influence the core evolution (e.g. ambient magnetic-field, ambient pressure in the molecular cloud). The overall process is complicated with many different free parameters to choose if one wishes to perform simulations of star formation.

2. *Are the properties of primordial binaries the same in regions like Taurus and Orion?*

The properties of primordial binaries cannot be directly measured since they are deeply embedded in molecular clouds. Eventually young stars emerge from the cloud, but not before a finite amount of time during which significant evolution may have occurred (e.g. dynamical decay, tidal disruption). It is thus difficult to determine the actual primordial binary properties directly.

3. *What is the main reason for the difference between pre-Main Sequence binary properties in different regions?*

If the properties of primordial binaries are the same in different regions, then environmental factors are presumably responsible for any differences when young-stellar objects enter the pre-Main Sequence phase. The favoured mechanism is binary disruption due to binary-binary and binary-star encounters. Kroupa and co-workers (e.g. Kroupa 1995a, 1995b) have argued that primordial binary properties are universal and that the differences between regions are due to such disruptive interactions. In this picture, low-stellar density regions will have little binary disruption (hence explaining the high multiplicity

of Taurus) whereas higher-stellar density regions will have considerable binary disruption (hence explaining the apparent low multiplicity of Orion).

4. *Why are pre-Main Sequence binary properties different from the field? How do pre-Main Sequence properties evolve to become those of the field?*

The field binary properties are in effect a weighted average of the properties of pre-Main Sequence binaries from different regions. It has often been stated that the pre-Main Sequence multiplicity is higher than that of the Main Sequence. However, most studies have focused on low-density regions like Taurus, whereas the majority of stars probably form in denser clusters such as Orion (e.g. Lada & Lada 2003), where the observed statistics are not very robust. Better observations of the binary properties of regions such as Orion may be required before this question can be answered.

Chapter 3

N-body codes

In this chapter, we discuss the main principles and algorithms behind the design of N-body codes. In particular we focus on the NBODY series written by Sverre Aarseth, which we will use later in this thesis. We discuss the main integration schemes used, the principle algorithms used to improve accuracy, such as regularisation, and the output files produced by NBODY.

3.1 Newton's law of gravity

N-body codes compute the dynamical evolution of an ensemble of N particles, where gravity is the only or dominant force. The equation of motion for the i^{th} particle is given by Newton's law of gravitation

$$\mathbf{a}_i = - \sum_{j=1, j \neq i}^N \frac{Gm_j(\mathbf{r}_i - \mathbf{r}_j)}{|\mathbf{r}_i - \mathbf{r}_j|^3} \quad (3.1)$$

N-body codes are commonly used in astrophysics to model the motions of stars in clusters, and also the evolution of dark matter in cosmological and galaxy simulations. In this thesis, N-body codes will be used to model the evolution of small- N ($N \leq 6$) clusters, and of larger ($N = 400$) clusters.

3.2 The NBODY codes

A powerful series of N-body codes has been developed by Sverre Aarseth at the Institute of Astronomy, Cambridge, called NBODY. There are currently 6 main versions, entitled NBODY1 to NBODY6, with a variety of different features and each optimized for a particular problem. We have chosen to use these codes to model cluster evolution, due to their robustness, sophistication and accuracy after more than forty years of development. Table 3.1 shows the different

	NBODY1	NBODY2	NBODY3	NBODY4	NBODY5	NBODY6
Force Polynomials	•	•	•	•	•	
Hermite Scheme		•				•
Gravity softening	•	•				
KS regularisation			•	•	•	•
3/4 body regularisation			•		•	•
Chain regularisation			•			•
Stumpff KS method						•
Ahmad-Cohen scheme		•			•	•
Co-moving co-ordinates				•		
Stellar evolution				•		•

Table 3.1: Algorithms used in the NBODY codes

features available in the NBODY series, which we will discuss in this chapter.

3.3 Integration scheme

N-body codes require an accurate and stable integration scheme due to both the non-linear nature of motion under gravity, and the singular form of Newton's law of gravity (i.e. $|\mathbf{a}_i| \rightarrow \infty$ as $|\mathbf{r}_i - \mathbf{r}_j| \rightarrow 0$). Simple Euler and Runge-Kutta methods are not accurate enough and can be numerically unstable, therefore more advanced schemes such as high-order predictor-corrector schemes are required. A predictor-corrector scheme uses information from previous steps to form a 'prediction' of the solution. This new information is used to form a corrector step which improves the accuracy of the final solution.

3.3.1 Force Polynomials

A common predictor-corrector integration scheme used in earlier versions of the NBODY codes is the Force Polynomial scheme developed by Aarseth (1963), and improved upon by Ahmad & Cohen (1973). This scheme records the acceleration vector, \mathbf{a} , for each particle at four previous times, t_0, t_1, t_2, t_3 , with t_0 being the most recent. Using this information, we can fit \mathbf{a} with a fourth-order polynomial using a Taylor series

$$\mathbf{a}_t = \mathbf{a}_0 + \mathbf{a}^{(1)}(\Delta t) + \frac{\mathbf{a}^{(2)}}{2!}(\Delta t)^2 + \frac{\mathbf{a}^{(3)}}{3!}(\Delta t)^3 + \frac{\mathbf{a}^{(4)}}{4!}(\Delta t)^4 \quad (3.2)$$

where $\mathbf{a}^{(n)}$ is the n^{th} derivative of the acceleration with respect to time, i.e. $d^n \mathbf{a} / dt^n$, and $\Delta t \equiv t - t_0$. In order to construct the various terms in the Taylor series, we use the divided differences, \mathbf{D}^k (Ahmad & Cohen 1973). These are constructed using the values of \mathbf{a} from the 4 previous

times. Mathematically,

$$\mathbf{D}^k[t_0, t_k] = \frac{\mathbf{D}^{k-1}[t_0, t_{k-1}] - \mathbf{D}^{k-1}[t_1, t_k]}{t_0 - t_k} \quad (3.3)$$

where $\mathbf{D}^0 \equiv \mathbf{a}$. The square brackets indicate the time intervals between which each divided difference is constructed. Note that apart from \mathbf{D}^0 , this is a recursive definition. First we calculate the values of \mathbf{D}^1 from $\mathbf{D}^0 (\equiv \mathbf{a})$, then the values of \mathbf{D}^2 from \mathbf{D}^1 , and so on. The Force Polynomial (Equation 3.2) can then be written in terms of divided differences:

$$\mathbf{a}_t = (((\mathbf{D}^4(t - t_3) + \mathbf{D}^3)(t - t_2) + \mathbf{D}^2)(t - t_1) + \mathbf{D}^1)(t - t_0) + \mathbf{F}_0. \quad (3.4)$$

Expanding Equation 3.4 and comparing terms containing Δt , Δt^2 , Δt^3 and Δt^4 with Eq. 3.2 gives the acceleration derivatives in terms of divided differences.

$$\begin{aligned} \mathbf{a}^{(1)} &= ((\mathbf{D}^4 t'_3 + \mathbf{D}^3) t'_2 + \mathbf{D}^2) t'_1 + \mathbf{D}^1 \\ \mathbf{a}^{(2)} &= 2!(\mathbf{D}^4(t'_1 t'_2 + t'_2 t'_3 + t'_1 t'_3) + \mathbf{D}^3(t'_1 + t'_2) + \mathbf{D}^2) \\ \mathbf{a}^{(3)} &= 3!(\mathbf{D}^4(t'_1 + t'_2 + t'_3) + \mathbf{D}^3) \\ \mathbf{a}^{(4)} &= 4! \mathbf{D}^4 \end{aligned} \quad (3.5)$$

where $t'_k = t_0 - t_k$. To proceed, we first evaluate the first 3 divided differences, \mathbf{D}^1 , \mathbf{D}^2 and \mathbf{D}^3 from the previous acceleration information and form the first 3 force derivatives using Equation 3.5 (ignoring any terms involving \mathbf{D}^4) which yields the preliminary (i.e. predictor) solution. The preliminary solution is then used to calculate \mathbf{D}^4 . To form the corrector step, we include all terms with \mathbf{D}^4 (and $\mathbf{a}^{(4)}$) in the Force Polynomial.

No previous information is known at the first step, so special starting conditions are required (e.g. Aarseth 2001b). It is possible to include higher order terms in the Taylor series, but each successive term needs even earlier acceleration information, and thus becomes less and less accurate but increasingly expensive computationally. A fourth-order scheme is found to be the optimum order for this type of integration scheme (Makino 1991).

3.3.2 Hermite scheme

A more recent integration scheme used in N-body codes is the Hermite integration scheme developed by Makino & Aarseth (1992). Hermite interpolation allows us to fit a function with a 4th-order polynomial between two points if we know the value of the function and its first derivative at those two points. As with the Force Polynomial scheme, we can fit \mathbf{a} with a fourth-order polynomial. To use Hermite interpolation in N-body codes, we need to calculate \mathbf{a} and

$\mathbf{a}^{(1)}$ at the beginning and end of the timestep. The acceleration of a particle is given by

$$\mathbf{a}_i = - \sum_{j=1, j \neq i}^N \frac{Gm_j(\mathbf{r}_i - \mathbf{r}_j)}{|\mathbf{r}_i - \mathbf{r}_j|^3} \quad (3.6)$$

and we are able to calculate its first derivative explicitly by differentiating Eq. 3.6 to obtain

$$\mathbf{a}_i^{(1)} = - \sum_{j=1, j \neq i}^N \frac{Gm_j(\mathbf{v}_i - \mathbf{v}_j)}{|\mathbf{r}_i - \mathbf{r}_j|^3} + 3 \sum_{j=1, j \neq i}^N \frac{(\mathbf{r}_i - \mathbf{r}_j) \cdot (\mathbf{v}_i - \mathbf{v}_j) \mathbf{a}_{ij}}{|\mathbf{r}_i - \mathbf{r}_j|^2}. \quad (3.7)$$

First we calculate \mathbf{a}_0 and $\mathbf{a}_0^{(1)}$ at the beginning of the timestep. Using this information, we predict the position and velocity of the particles at the end of the step,

$$\begin{aligned} \mathbf{r} &= \mathbf{r}_0 + \mathbf{v}_0 \Delta t + \frac{1}{2} \mathbf{a}_0 \Delta t^2 + \frac{1}{6} \mathbf{a}_0^{(1)} \Delta t^3, \\ \mathbf{v} &= \mathbf{v}_0 + \mathbf{a}_0 \Delta t + \frac{1}{2} \mathbf{a}_0^{(1)} \Delta t^2. \end{aligned} \quad (3.8)$$

Next, we calculate the acceleration and its first derivative at the end of the step, i.e. \mathbf{a} and $\mathbf{a}^{(1)}$. To form the corrector term, we consider a Taylor series for both the acceleration and its first derivative up to order $\mathbf{a}^{(3)}$, i.e.

$$\begin{aligned} \mathbf{a} &= \mathbf{a}_0 + \mathbf{a}_0^{(1)} \Delta t + \frac{1}{2} \mathbf{a}_0^{(2)} \Delta t^2 + \frac{1}{6} \mathbf{a}_0^{(3)} \Delta t^3, \\ \mathbf{a}^{(1)} &= \mathbf{a}_0^{(1)} + \mathbf{a}_0^{(2)} \Delta t + \frac{1}{2} \mathbf{a}_0^{(3)} \Delta t^2. \end{aligned} \quad (3.9)$$

Solving these two equations simultaneously gives $\mathbf{a}^{(2)}$ and $\mathbf{a}^{(3)}$,

$$\begin{aligned} \mathbf{a}_0^{(2)} &= 2(-3(\mathbf{a}_0 - \mathbf{a}) - (2\mathbf{a}_0^{(1)} + \mathbf{a}^{(1)})\Delta t)/\Delta t^2, \\ \mathbf{a}_0^{(3)} &= 6(2(\mathbf{a}_0 - \mathbf{a}) + (\mathbf{a}_0^{(1)} + \mathbf{a}^{(1)})\Delta t)/\Delta t^3. \end{aligned} \quad (3.10)$$

We can now add the higher order correction terms to Eq. 3.8,

$$\begin{aligned} \mathbf{r} &= \mathbf{r} + \frac{1}{24} \mathbf{a}_0^{(2)} \Delta t^4 + \frac{1}{120} \mathbf{a}_0^{(3)} \Delta t^5, \\ \mathbf{v} &= \mathbf{v} + \frac{1}{6} \mathbf{a}_0^{(2)} \Delta t^3 + \frac{1}{24} \mathbf{a}_0^{(3)} \Delta t^4. \end{aligned} \quad (3.11)$$

The main benefit of the Hermite scheme over the Force Polynomial scheme is that the first derivative is exactly determined and hence it is more accurate and stable. The Hermite scheme can use larger timesteps than the Force Polynomial scheme and achieve the same level of accuracy. It is different from other predictor-corrector schemes in that you don't re-use past information to predict, but you use all the information you have at the beginning of the step. This scheme has been incorporated into NBODY2, NBODY4, NBODY5 and NBODY6.

3.4 Timesteps

The timestep, Δt , controls the accuracy and efficiency of the integration. We use the notation $\Delta t \equiv t - t_0$. The error in the fourth-order Force Polynomial is of order $O(\Delta t^5)$ and hence reducing the stepsize increases the accuracy of the calculation. On the other hand, reducing the stepsize increases the number of force calculations required over the course of the simulation and hence the computational effort. The optimum stepsize can be calculated using the current acceleration and acceleration derivative information. One simple form of the timestep uses the acceleration and its second derivative

$$\Delta t = \sqrt{\frac{\eta|\mathbf{a}|}{|\mathbf{a}^{(2)}|}} \quad (3.12)$$

where η is a dimensionless number that controls the accuracy. This is similar to the Courant condition (Courant et al. 1967), but may fail in certain special situations (e.g. when $|\mathbf{a}| \sim 0$), so a more sophisticated timestep criterion of the form

$$\Delta t = \sqrt{\frac{\eta(|\mathbf{a}||\mathbf{a}^{(2)}| + |\mathbf{a}^{(1)}|^2)}{|\mathbf{a}^{(1)}||\mathbf{a}^{(3)}| + |\mathbf{a}^{(2)}|^2}} \quad (3.13)$$

is used in the NBODY codes (Aarseth 2001b). This prescription uses all the acceleration derivatives to ensure an appropriate timestep. The suggested value of η for optimum performance is 0.2 in the NBODY codes (e.g. Aarseth 2001b).

3.4.1 Multiple particle timesteps

Applying Equation 3.13 to all the particles typically gives a wide range of timesteps. Although it is possible to use a single global timestep (usually equal to the minimum value of Δt of all the particles), this would only be efficient for a small number of particles. For a large number of particles, it would require many more force polynomial calculations than is deemed optimum by Equation 3.13. A more efficient approach is to use multiple particle timesteps in place of a global timestep. In order to achieve this in practice, a hierarchy of discrete timesteps Δt_n is used, where

$$\Delta t_n = t_{\min} 2^n \quad \text{and} \quad n = 0, 1, \dots, n_{\max}. \quad (3.14)$$

Note therefore that t_{\max} must equal $t_{\min} 2^{n_{\max}}$.

All particles are synchronised at the beginning of the simulation. Particles with the smallest timestep are calculated first and at the end of the timestep the force is recalculated, and the timestep for the next step is determined. When calculating the force for the particles with small

timesteps, the positions of the other particles are calculated to low-order using a Taylor series

$$\mathbf{r}_j = \mathbf{r}_0 + \mathbf{v}_0(t - t_j) + \frac{\mathbf{a}}{2!}(t - t_j)^2 + \frac{\mathbf{a}^{(1)}}{3!}(t - t_j)^3 \quad (3.15)$$

where t_j is the time of the last force polynomial calculation of particle j . Particles with larger timesteps have their positions predicted using Equation 3.15 until they reach the end of their timesteps, where the force polynomial is fully calculated as described in section 3.3.1. Once the maximum timestep, t_{max} , is reached, all the particles have gone through at least one of their timesteps and the particles are all synchronised again. The procedure is repeated again beginning with recalculating all the timesteps using Equation 3.13.

3.5 N-body units

The NBODY codes use the standard set of N-body units (Heggie & Mathieu 1986). In these units, we set the gravitational constant, $G = 1$, the total mass, $M_{tot} = 1$, and the total energy, $E_{tot} = -1/4$ (for bound systems). In these units, the virial radius is equal to $R_v = 1$, the rms velocity is $V_{rms} = 2\sqrt{2}$ and the crossing time is $t_{cr} = 1\sqrt{2}$. NBODY automatically scales using these units, although they can be adjusted using one of the switch options. The procedure of standard N-body units is described in Aarseth (2001).

3.6 Regularisation

3.6.1 The 2-body singularity and gravity softening

Due to the form of Newton's law of gravity, the force between two bodies becomes infinitely large as the separation approaches zero. Even when two stars do not 'collide', the asymptotic behaviour of the force near the singularity can cause large errors in the numerical integration, both for the Force Polynomial and Hermite schemes. Early N-body codes (and some modern ones) used gravity softening to counter this problem. Gravity softening adds an extra term to the denominator in the usual inverse square law, i.e.

$$\mathbf{a}_{ij} = -\frac{Gm_j(\mathbf{r}_i - \mathbf{r}_j)}{(|\mathbf{r}_i - \mathbf{r}_j|^2 + \epsilon^2)^{3/2}}. \quad (3.16)$$

The denominator can never equal zero, and as the numerator tends to zero, then $|\mathbf{a}| \rightarrow 0$. Although this form of gravity reduces numerical errors and prevents singularities, the motion is not modelled correctly for small separations, i.e. $|\mathbf{r}_i - \mathbf{r}_j| \lesssim \epsilon$

3.6.2 KS regularisation

An alternative solution is to *regularise* the equations of motion. For a 2-body interaction, a co-ordinate transformation can be performed so that the new equations of motion do not become singular at any point, unlike Newton's law. These new equations can be integrated much more accurately, and can be transformed back to physical co-ordinates at any point.

The NBODY codes use Kustaanheimo-Stiefel (hereafter KS) 2-body regularisation (Stiefel & Scheifele 1971, Aarseth 2001a). In a 2-body interaction, the relative acceleration between the 2 bodies is given by

$$\mathbf{a}_{ij} = -\frac{M_{ij}}{R_{ij}^3}\mathbf{R}_{ij} + \mathbf{P} \quad (3.17)$$

where $\mathbf{R}_{ij} = \mathbf{r}_i - \mathbf{r}_j$, $R_{ij} = |\mathbf{R}_{ij}|$, $M_{ij} = m_i + m_j$ and \mathbf{P} is the tidal perturbing force per unit mass due to other stars (using N-body units with $G = 1$). In this form, the dependent and independent variables are R and t respectively.

In KS regularisation, we transform both the displacement and time into new co-ordinates. First, we transform the position 3-vector, \mathbf{R}_{ij} , into the 4-vector \mathbf{u} . \mathbf{R}_{ij} and \mathbf{u} are related by the matrix transformation

$$\mathbf{R}_{ij} = \mathbf{L}(\mathbf{u})\mathbf{u} \quad (3.18)$$

where

$$\mathbf{L}(\mathbf{u}) = \begin{pmatrix} u_1 & -u_2 & -u_3 & u_4 \\ u_2 & u_1 & -u_4 & -u_3 \\ u_3 & u_4 & u_1 & u_2 \\ u_4 & -u_3 & u_2 & -u_1 \end{pmatrix} \quad (3.19)$$

is the KS transformation matrix. u_1, u_2, u_3 and u_4 are the four components of the 4-vector \mathbf{u} . Note that now we must define \mathbf{R}_{ij} as a 4-vector and set the fourth component equal to zero in order for Equation 3.18 to be valid. Also the time is transformed to a fictional time τ by the differential relation $dt = R_{ij} d\tau$. τ is not linearly related to t since R_{ij} in general changes with time (except for circular orbits). The regularised equations of motion (in the new co-ordinates) become

$$\begin{aligned} \mathbf{u}'' &= \frac{1}{2}h\mathbf{u} + \frac{1}{2}R\mathbf{L}^T\mathbf{P} \\ h' &= 2\mathbf{u}' \cdot \mathbf{L}^T\mathbf{P} \\ t' &= \mathbf{u} \cdot \mathbf{u} \end{aligned} \quad (3.20)$$

(See Aarseth 2001a for a complete description). These new equations of motion describe the relative motion of 2 particles (in the new co-ordinates). In the context of the overall cluster, the KS pair is replaced by one particle representing their mutual centre of mass and its motion is

integrated as a regular single particle.

The relative perturbation, γ , is defined as the ratio of the perturbing force to the mutual 2-body gravitational force, i.e.

$$\gamma = \frac{|\mathbf{P}|R_{ij}^2}{M_{ij}} \quad (3.21)$$

For no perturbation or a very weak ($\gamma \ll 1$) perturbations, the equations of motion reduce to the simpler forms

$$\begin{aligned} \mathbf{u}'' &= \frac{1}{2}h\mathbf{u} \\ h' &= 0 \\ t' &= \mathbf{u} \cdot \mathbf{u} \end{aligned} \quad (3.22)$$

Equation 3.22 is similar to the equation of SHM, and solutions correspond to bound elliptical, or unbound hyperbolic, orbits in real space. For larger perturbations, the extra terms are included as in Equation 3.20 and must be solved numerically.

3.6.3 Higher-order regularisation schemes

For close interactions with more than two particles, either 3-body, 4-body or chain regularisation must be used. 3-body regularisation extends the principles of 2-body regularisation by choosing a reference body, and solving two coupled KS-regularised differential equations for the relative motions of the other bodies (Aarseth & Zare 1974). The reference body is chosen with the criterion that the distance between the other 2 bodies is not the smallest distance in the system.

Chain regularisation further extends the principle of solving many coupled KS differential equations (Mikkola & Aarseth 1993). In practice, it is used for interactions involving up to ten stars, but in principle, it could be extended to more stars. An inter-particle chain is created connecting all the stars involved in the many-body interaction. Analogous to 3-body regularisation, the criterion is that the smallest distance between stars not along the chain, is larger than the smallest distance between stars in the chain. For a chain of m stars, we need to solve $m - 1$ coupled KS differential equations. In NBODY, the differential equations are solved using the Bulirsch-Stoer method (Press et al 1992).

3.7 Ahmad-Cohen Neighbour scheme

Ahmad & Cohen (1973) devised a scheme to reduce the computational cost of N-body simulations with large N . One complete timestep typically requires $\sim N^2$ force polynomial calculations. To reduce this expense, they split the force polynomial into 2 contributions, an irregular

and regular component, i.e.

$$\mathbf{F} = \mathbf{F}_{irr} + \mathbf{F}_{reg} \quad (3.23)$$

The irregular component contains the force contribution from all neighbouring particles within a sphere of radius R_s (defined in Aarseth 1999). All particles outside the sphere are included in the regular force calculation. Since these particles are more distant, their force contribution changes more slowly and can be calculated with a longer timestep. This can decrease the number of force calculation (from $O(N^2)$ to $O(N^{3/2})$), speeding up the simulation without much loss in accuracy.

3.8 Co-moving co-ordinates

Larger-scale simulations such as those investigating the dynamics of galaxy clusters (e.g. Aarseth 1963) must take account of the expansion of the universe. To do this, a term that takes account of the Hubble flow is included in the equations of motion. This has been incorporated into NBODY4.

3.9 Stellar evolution

In realistic star clusters, a star's lifetime may become comparable with, or even shorter than, the cluster lifetime. This is particularly important for high-mass stars. Stellar evolution should be modelled so that the effect on the overall morphology and appearance of the cluster can be considered. NBODY6 includes an option to model stellar evolution for a star of given mass and metallicity. It uses fast look-up tables to follow the evolution of its mass, luminosity and temperature. Also, this allows theoretical HR diagrams of the cluster to be generated.

3.10 Binary identification

The NBODY codes contain various subroutines to identify binaries and higher order multiples, and output the relevant binary parameters. Although a large number of configurations are possible, the more stars there are in a system, the greater the chance of the system decaying. We limit ourselves to detecting binaries, and heirarchical triples and quadruples, which are more stable.

- *KS binaries*

Any bound pair of stars that is regularised is automatically detected as a binary. All the binary parameters are easily calculated using the information already obtained during

regularisation. NBODY6 allows the various binary parameters to be output to the file OUT9. For each KS-regularised binary, the following parameters are output:

E_b - binding energy of the binary	P - period of the binary in days
e - eccentricity	\mathcal{N}_i - identifier of i th body
E_{CM} - centre-of-mass energy	\mathcal{N}_j - identifier of j th body
r - separation	k_i^* - stellar type of i th body
m_i - mass of the i th body	k_j^* - stellar type of j th body
m_j - mass of the j th body	

- *Wide binaries*

Wide binaries which are not regularised can be identified by following the 2-body energies of all possible candidates. If a pair is bound for more than one Kepler period, it is identified as a wide binary.

- *Hierarchical systems*

Hierarchical systems can either have a tight binary in orbit around a single star (a hierarchical triple), or two tight binaries orbiting each other (a hierarchical quadruple). Such systems can be identified by comparing the energies of the centre of mass 'particles', similar to the method of identifying wide binaries. Since systems with more than 2 stars are generally unstable to decay, extra stability criteria are used to check if the hierarchy is stable, or likely to decay in the future.

Chapter 4

Ring Fragmentation

In this chapter, we develop a simple model of isolated binary star formation based on the hypothesis that all prestellar cores are rotating, and that they fragment due to rotational instabilities. Each core is assumed to form a ring or disc and fragment into a small- N cluster containing N protostars (where $N \leq 6$). Each cluster is expected to dissolve, due to N -body interactions, into an ensemble of stable systems including binary stars, higher-order multiple systems and ejected single stars. We model each protostar as a point-mass, follow the dynamical evolution of the cluster using an N -body code (NBODY3), and determine the resultant binary statistics.

Using observed core properties and an appropriate choice of input parameters, our model can successfully generate IMFs, eccentricity and mass-ratio distributions which are consistent with the observations. The multiplicity in our model is consistent with the multiplicity of stars in PMS stars in low-mass star forming regions like Taurus. It is presumed, in the context of our model, that interactions in a clustered star forming environment like Orion will evolve the binary statistics towards the field distribution.

*The work in this chapter has been published in *Astronomy & Astrophysics* (Hubber & Whitworth 2005).*

4.1 Introduction

A prestellar core is presumed to collapse and fragment producing a dense ensemble of protostars. Interactions between these protostars and the ambient gas then determine their final masses, which ones end up in multiple systems, and their orbital parameters. Understanding how cores fragment and how many objects are produced requires 3-D hydrodynamical simulations, which are (a) very computer intensive, and (b) highly dependent on the input physics and initial conditions of the cores (e.g. Tohline 2002). Few simulations can be performed, and the statistical properties of the resulting protostars are therefore poorly constrained. Also, such

simulations are not able to follow star formation to completion, so the final fate of a star-forming core and the stars it produces is not completely resolved. In particular, the orbital parameters of the resulting multiple systems are unlikely to have reached their final values when a 3-D hydrodynamic simulation is terminated.

The problem can be simplified by ignoring complicated gas-dynamical processes like fragmentation, merger and accretion and modelling protostars as point masses in a small- N clusters. The ballistic evolution of the protostars can then be followed using an N -body code (as described in Chapter 3). Gravitational interactions alone determine the resulting single and multiple-system properties.

4.1.1 Previous N-body work

Since the early 1990's when detailed surveys of binary statistics for both Main Sequence and pre-Main Sequence stars were published, detailed N-body simulations have been performed with a view to exploring the observed statistics. This approach has been pioneered by Kroupa and co-workers (Kroupa 1995a, 1995b; Kroupa & Bouvier 2003a, 2003b; Kroupa et al. 2003), and by Sterzik & Durisen (1998, 2003). Sterzik & Durisen have considered the origin of primordial binaries in small- N clusters of protostars. In Kroupa's work the emphasis is more on how these primordial binary properties are altered by subsequent dynamical interactions with other multiple systems and single stars in a wider cluster environment; this is with the aim of explaining the difference between pre-Main Sequence and Main Sequence binary properties.

Sterzik & Durisen (1998) investigate the binary statistics resulting from the dynamical dissolution of small- N clusters. They pick cluster masses from a power-law core mass spectrum, and calculate cluster radii from a scaling law of the form $R_{\text{CLUSTER}} \propto M_{\text{CLUSTER}}^{\xi}$ ($\xi = 0, 1$ or 2). Each cluster contains N stars ($N = 3, 4$ or 5) with masses picked from a prescribed stellar mass spectrum. Initially the stars are positioned randomly in the cluster volume, with zero velocity. Their ballistic evolution is then followed for many crossing times, using an N-body code, and the properties of the resulting multiple systems are recorded. However, this model is unable to reproduce the broad distribution of binary separations as observed in the field or in star forming regions (as discussed in Chapter 2).

In a second paper Sterzik & Durisen (2003) repeat these experiments, but now with clusters which initially are oblate and have some rotation about their short axis (specifically, $\beta = 0.1$, where β is the ratio of rotational to gravitational energy). In addition, they relax the assumption of constant N . Instead stars are chosen from a prescribed mass distribution until their total mass adds up to the preordained mass of the cluster, and this then determines N for that cluster. They are able to reproduce the dependence of multiplicity frequency on primary mass, but the distribution of separations is still much narrower than that observed.

A variation on this type of N-body approach has been explored by Delgado Donate et al. (2003) with a view to capturing hydrodynamic effects. They model a uniform-density core of isothermal gas using Smoothed Particle Hydrodynamics, and place five sink particles (representing protostellar embryos) at random positions within the core. Initially each sink contains only 2% of the total mass, but subsequently the sinks grow by competitive accretion and interact dynamically with one another, to generate a mass function which is a good fit to the observed Initial Mass Function. The resulting binary systems also have the right distribution of eccentricities. However, the distribution of separations is again much narrower than that observed by DM91, and is more similar to that observed in open clusters (Patience et al. 2002).

The work of Kroupa and collaborators is discussed in detail in Chapter 5. One important result highlighted here is that the binary separation distribution is not broadened significantly by dynamical interactions in a dense cluster (e.g. Kroupa & Burkert 2001). This supports the notion that the observed separation distribution originates from the properties of primordial binaries.

4.1.2 Ring fragmentation

Simulations of binary formation have investigated the various modes of fragmentation of pre-stellar cores. Such simulations use a wide variety of input physics (e.g. magnetic fields, radiative transfer, the equation of state, etc..) with a wide range of initial and boundary conditions. This results in a wide variety of final states and binary properties. In simulations of core collapse which include rotation (e.g. Bonnell & Bate 1994, Cha & Whitworth 2003b, Hennebelle et al. 2004), in particular those where instability against collapse is triggered impulsively, the core may overshoot centrifugal balance and then bounce to form a dense ring, which subsequently fragments into multiple protostars. For example, Cha & Whitworth (2003b) consider differentially rotating cores and model these with hydrodynamical simulations. Figure 2.10 shows the results from one of their simulations. The cloud forms a flattened ring (Figure 2.10a) which then fragments into a few protostars. This small-N cluster then breaks up due to the chaotic nature of motion under gravity.

We investigate the consequences of assuming that this is the dominant mechanism by which a core breaks up into individual protostars. Specifically, we use an N-body code to follow the ballistic evolution of protostars which are initially distributed on a ring, and record their final binary statistics. We scale the mass and radius of the ring to match the observed distributions of core mass, core radius, and core rotation, and we compare the resulting binary statistics with observations.

4.2 Observations of cores

We review briefly the observations of cores which provide the input parameters for our model, namely the distribution of core masses (Section 4.2.1), the mass-radius relation for cores (Section 4.2.2), and the distribution of core rotation rates (Section 4.2.3).

4.2.1 Core masses

Motte et al. (2001) have measured the core-mass spectrum in Orion B and fitted it with a two part power law:

$$\frac{dN_{\text{CORE}}}{dM_{\text{CORE}}} = \begin{cases} k_1 M_{\text{CORE}}^{-1.5}, & M_{\text{MIN}} \leq M_{\text{CORE}} \leq M_{\text{KNEE}}; \\ k_2 M_{\text{CORE}}^{-2.5}, & M_{\text{KNEE}} \leq M_{\text{CORE}} \leq M_{\text{MAX}}. \end{cases} \quad (4.1)$$

where $M_{\text{MIN}} = 0.5 M_{\odot}$, $M_{\text{KNEE}} = 1.0 M_{\odot}$ and $M_{\text{MAX}} = 10.0 M_{\odot}$. Similar results have been reported by Johnstone et al. (2001) for Orion B, by Motte, André & Neri (1998) and Johnstone et al. (2000) for ρ Ophiuchus, and by Testi & Sargent (1998) for Serpens. More recent observations have begun to constrain the lower mass end of the CMS (e.g. Lada, Alves & Lombardi 2006, Nutter et al. in prep). We shall use Equation 4.1 in our model but we extend the core mass spectrum up to $M_{\text{MAX}} = 20.0 M_{\odot}$.

4.2.2 Core radii

We shall assume that the initial core radii are given by the scaling relations

$$R_{\text{CORE}}(M_{\text{CORE}}) = \begin{cases} 0.1 \text{ pc } (M_{\text{CORE}}/M_{\odot}), & M_{\text{CORE}} < M_{\odot}; \\ 0.1 \text{ pc } (M_{\text{CORE}}/M_{\odot})^{1/2}, & M_{\text{CORE}} > M_{\odot}; \end{cases} \quad (4.2)$$

(cf. Larson 1981, Myers 1983). Here, the low-mass regime applies to cores whose support is dominated by thermal pressure, and the high-mass regime applies to cores whose support is primarily from turbulence. Strictly speaking there is a range of core radii at any given core mass, but we neglect this to restrict the number of free parameters.

4.2.3 Core rotation

Goodman et al. (1993; hereafter G93) have measured the velocity profiles across a sample of 43 prestellar cores. They find statistically significant velocity gradients across 24 of the cores they observe, and from these velocity gradients they calculate the ratio of rotational to gravitational

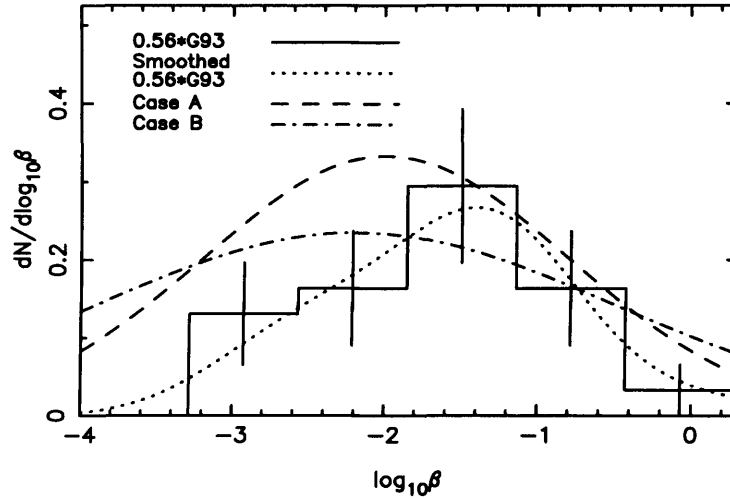


Figure 4.1: The histogram and the dotted curve represent the distribution of observed β -values from Goodman et al. (1993), scaled to 56% (since they only measured rotation for 24 out of 43 cores). The dashed line represents the log-normal distributions of Case A ($\overline{\log \beta} = -2.0$, $\sigma_{\log \beta} = 1.2$) and the dash-dot line represents the log-normal distribution of Case B ($\overline{\log \beta} = -2.2$, $\sigma_{\log \beta} = 1.7$).

potential energy, β , on the assumption of uniform solid-body rotation. The distribution of these β -values, normalized to $24/43 \approx 56\%$, is represented by the histogram on Figure 4.1, and also by the dotted line. The dotted line is obtained by smoothing the individual β values with a gaussian kernel having $\sigma_{\log \beta} = 0.5$,

$$\left. \frac{dN_{\text{CORE}}}{d \log \beta} \right|_{\text{OBS}} = \sum_i \left\{ \frac{1}{(2\pi)^{1/2} \sigma_{\log \beta}} \exp \left[-\frac{(\log \beta_i - \log \beta)^2}{2\sigma_{\log \beta}^2} \right] \right\} \quad (4.3)$$

and is intended to mitigate the effects of arbitrarily binning a very small number of data points. However, due to low number statistics and the fact that only large projected velocity gradients can be measured, the full distribution of β -values is not well constrained by the observations of G93.

Burkert & Bodenheimer (2000) have pointed out that the velocity gradients observed by G93 can also be explained by turbulent motions in cores, rather than solid-body rotation. By modelling the turbulence as a Gaussian random velocity field with power spectrum $P(k) \propto k^{-n}$ with $3 \leq n \leq 4$, they show that the resulting distribution of β -values fits the G93 observations well, and is approximately lognormal (see their Figure 3, lower left panel).

In our model, we assume a log-normal distribution of β -values:

$$\frac{dN_{\text{CORE}}}{d \log \beta} \propto \exp \left(\frac{-(\log \beta - \overline{\log \beta})^2}{2\sigma_{\log \beta}^2} \right). \quad (4.4)$$

Since G93 only determined β for 24 of the 43 pre-stellar cores they observed, the observed β distribution on Figure 4.1 represents only 56% of all the cores, and we therefore have some freedom in choosing the parameters $\overline{\log\beta}$ and $\sigma_{\log\beta}$ for the full distribution in Eqn. (4.4). We presume that some of the cores for which β could not be determined were observed with inadequate resolution and/or from an unhelpful viewing direction (i.e. close to the angular momentum vector). However, this cannot account for all the non-determinations, and we assume that the majority of the non-determinations have β values lower than those that are determined. Therefore we must invoke an overall distribution which contains the observed distribution, but extends to lower β values. We consider two possibilities.

In Case A we adopt $\overline{\log\beta} = -2.0$ and $\sigma_{\log\beta} = 1.2$ (dashed curve on Figure 4.1). This is the less extreme possibility, in the sense that (a) it is easily compatible with the constraint of containing the observed distribution, and (b) it has most of the remaining 44% of β values below, but only just below, the observed ones. It is therefore also our preferred possibility. In Section 4.6 we show that it yields a distribution of separations similar to that of the pre-Main Sequence binaries collated by Patience et al. (2002).

In Case B we adopt $\overline{\log\beta} = -2.2$ and $\sigma_{\log\beta} = 1.7$ (dot-dash curve on Figure 4.1). This is the more extreme possibility, in the sense that (a) it is only just compatible with the constraint of containing the observed distribution and (b) it has most of the remaining 44% of β values not just below, but well below, the observed ones. In Section 4.6 we show that it yields a distribution of separations similar to that of the Main Sequence G-dwarf binaries in the field.

We assume that β is not correlated with core mass, as indicated by G93 (their Fig. 13(b)).

4.3 Outline of model

4.3.1 Assumptions and aims

Our model of binary star formation is based on the assumption that all cores are rotating, that they collapse and fragment via ring formation, and that the resulting protostars then interact ballistically to form multiple systems. We aim to investigate whether this simple model can explain the observed multiplicity of stars and their distributions of period, separation, eccentricity and mass-ratio.

4.3.2 The model

Consider a rotating prestellar core of mass M_{CORE} which initially has radius R_{CORE} and ratio of rotational to gravitational energy

$$\beta = \frac{R_{\text{CORE}}^3 \Omega_{\text{CORE}}^2}{3 G M_{\text{CORE}}} = \frac{25 H_0^2}{12 G M_{\text{CORE}}^3 R_{\text{CORE}}} \ll 1. \quad (4.5)$$

If the core collapses conserving its angular momentum, H_0 , and then bounces to form a centrifugally supported ring, the ring has radius

$$R_{\text{RING}} \simeq \beta R_{\text{CORE}}. \quad (4.6)$$

Suppose further that the ring is formed with approximately uniform line-density, but then fragments into \mathcal{N} protostars (where we expect \mathcal{N} to be small). Assume (i) that the \mathcal{N} protostars formed from a single core have masses M_n ($n = 1, 2, \dots, \mathcal{N}$) drawn from a log-normal distribution with standard deviation $\sigma_{\log M}$, and normalized so that

$$\sum_{n=1}^{n=\mathcal{N}} \{M_n\} = f M_{\text{CORE}}, \quad (4.7)$$

where f is the fraction of the core mass which is converted into stars (for simplicity we set $f = 1$ here); (ii) that the protostars are initially distributed round the ring so that each protostar occupies a fraction of the circumference proportional to the protostar's mass; and (iii) that the protostars condense out sufficiently fast that we can follow their subsequent dynamics using pure N-body methods.

For fixed \mathcal{N} and $\sigma_{\log M}$, we first formulate the dynamical evolution in dimensionless form and simulate a large number of cases to obtain statistically robust distributions of (a) multiplicity, (b) orbital eccentricity, e , (c) component mass-ratio, $q \equiv M_2/M_1$, and (d) ratio of orbital separation to ring radius, a/R_{RING} .

Then we convolve, *first* with the distribution of core masses, to obtain the overall stellar initial mass function (IMF) and the distributions of multiplicity, eccentricity and mass-ratio as a function of primary mass; and *second* with the distribution of core β -values to obtain the distribution of separations as a function of primary mass M_1 .

The core mass spectrum is fairly tightly constrained by observation (Motte et al. 1998, Testi & Sargent 1998, Johnstone et al. 2000, Motte et al. 2001, Johnstone et al. 2001), and therefore we do not adjust it (Section 4.2.1). Likewise the relation between core mass and core initial radius is constrained by observations, and we do not adjust it (Section 4.2.2). However,

the distribution of β -values is less well constrained, and we consider two possible distributions (Section 4.2.3). \mathcal{N} and $\sigma_{\log M}$ are treated as free parameters.

4.4 Dimensionless simulations

The first stage in constructing the model is to perform dimensionless simulations of low- \mathcal{N} star clusters. The results of these simulations can later be scaled up to any mass and size depending on the given parameters of the core, i.e. M_{CORE} and β .

4.4.1 Initial Conditions

We assume that a collapsing core forms a centrifugally supported ring having radius R_{RING} given by Equation 4.6. However, for the dimensionless simulations we set $R_{\text{RING}} = 1$. Two free parameters remain which must be explored in the dimensionless simulations. First, we must specify the number of stars in the ring, \mathcal{N} . Second, as posited in Section 4.3.2, the stellar masses must be drawn at random from a lognormal distribution having standard deviation $\sigma_{\log M}$,

$$\frac{dN_{\star}}{d \log M} = \frac{\mathcal{N}}{(2\pi)^{\frac{1}{2}} \sigma_{\log M}} \exp\left(-\frac{(\log M)^2}{2\sigma_{\log M}^2}\right), \quad (4.8)$$

and therefore we must specify $\sigma_{\log M}$. Strictly the mass distribution extends from $-\infty$ to $+\infty$ but for computational convenience we choose to curtail it at $\pm 3 \sigma_{\log M}$. Once the \mathcal{N} stellar masses M_n ($n = 1$ to \mathcal{N}) have been drawn randomly from this distribution, they are re-scaled by a factor g , $M_n \rightarrow \mu_n = gM_n$, so that the total system mass is equal to unity, i.e.

$$\sum_{n=1}^{n=\mathcal{N}} \{\mu_n\} = 1. \quad (4.9)$$

We note that scaling the stellar masses in this way skews the overall distribution of masses slightly; it is no longer precisely lognormal. This is not a critical element of the model. The asymmetry arises because we are invoking a finite – indeed small – number of stars. For simplicity consider the case $\mathcal{N} = 2$, and assume that the two stars do not have equal mass. If the more massive star is initially (pre re-scaling) exceptionally massive, it has to be reduced to achieve $\sum \{\mu_n\} = 1$, and this inevitably decreases the mass of the lower mass star, even if it was already quite small. Conversely, if the less massive star is initially of exceptionally low-mass, this has little or no influence on the re-scaling, which is mainly influenced by the more massive star. It is this asymmetry between the effects of exceptionally high-mass and exceptionally low-mass stars on the re-scaling that causes the re-scaled distribution to be skewed, particularly for

small \mathcal{N} . The effect disappears as $\mathcal{N} \rightarrow \infty$.

Next, we must specify the initial positions and velocities of the stars on the ring. If a ring having uniform line-density fragments into \mathcal{N} stars, then each star n forms from material in an ‘angular segment’, $\Delta\theta_n$, proportional to it’s mass, i.e.

$$\Delta\theta_n = 2\pi\mu_n. \quad (4.10)$$

Thus in circular polar co-ordinates, we put $\theta_1 = 0$ and

$$\theta_n = \theta_{n-1} + \frac{1}{2}(\Delta\theta_{n-1} + \Delta\theta_n), \quad n = 2, 3, \dots, \mathcal{N}. \quad (4.11)$$

In order to ensure conservation of linear momentum, each star n must be placed at the centre of mass of the material from which it forms, i.e. at radius

$$r_n = \frac{\sin(\mu_n \pi)}{\mu_n \pi}; \quad (4.12)$$

and then it must be given a circular speed

$$v_n = V \frac{\sin(\mu_n \pi)}{\mu_n \pi}, \quad (4.13)$$

where V is chosen so that the system is virialized. Only part of the angular momentum of the initial ring goes into the orbital motion of the stars in the cluster. The remaining angular momentum goes into spin of the individual stars and their attendant discs, which are not modelled here.

4.4.2 Numerical method

The ring is then evolved ballistically using an adapted version of NBODY3, supplied by Sverre Aarseth (e.g. Aarseth 1999). The main features of NBODY3 are described in Chapter 3.

4.4.3 Parameters

Simulations are performed for all possible combinations of $\mathcal{N} = 3, 4, 5$ and 6 , and $\sigma_{\log M} = 0.2, 0.4$ and 0.6 , and the distributions of multiplicity, semi-major axis (as a fraction of the radius of the ring), eccentricity, and mass-ratio are recorded.

For each set of parameters (i.e. each pair of \mathcal{N} and $\sigma_{\log M}$ values), a large number of runs is required to obtain statistically significant distributions. Each set of runs treats 10^5 stars in total (e.g. for $\mathcal{N}=4$, 2.5×10^4 runs are performed). Small- \mathcal{N} systems usually dissolve in a few

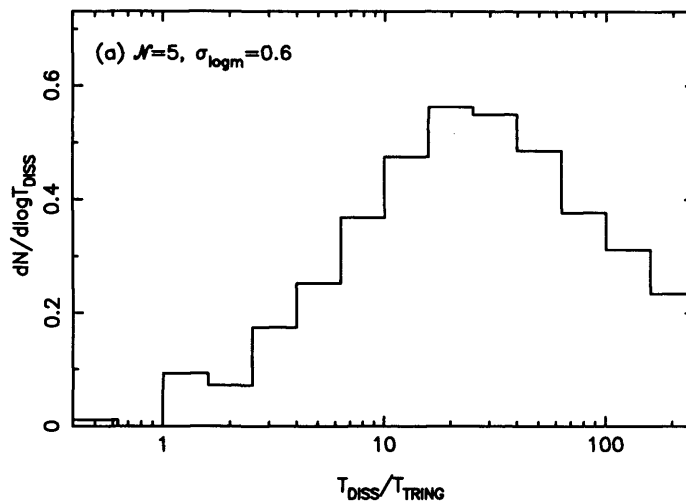


Figure 4.2: Dimensionless lifetimes of small- \mathcal{N} rings for $\mathcal{N} = 5$ and $\sigma_{\log M} = 0.6$.

tens of crossing times (e.g. Van Albada 1968, Sterzik & Durisen 1998), so, to ensure that the majority of systems have dissolved at the end of a simulation, each realisation is run for about 1000 crossing times. We choose a conservative tolerance parameter for the time step, to ensure accurate integration. Specifically we require that energy is conserved to 1 part in 10^5 over the entire integration.

4.4.4 Dissolution timescale

Typically a cluster dissolves after a few tens of dynamical times (e.g. Van Albada 1968) leaving ejected singles and a variety of multiple systems, i.e. binaries, triples and quadruples. In the present context, we define the dynamical timescale of the initial ring to be $T_{\text{RING}} = 2\pi(R_{\text{RING}}^3/GM_{\text{CORE}})^{1/2}$; this is roughly equivalent to the crossing time for a cluster with isotropic velocity dispersion. We measure the dissolution time of a cluster, T_{DISS} , as the time when the membership of binaries and multiple systems becomes fixed and there are no further exchanges or energy transfers. Only stable and quasi-stable systems will remain. Figure 4.2 shows the dissolution times, T_{DISS} , as a function of T_{RING} , for the case $\mathcal{N} = 5$ and $\sigma_{\log M} = 0.6$. About half of the rings have dissolved after $20 T_{\text{RING}}$, in agreement with previous numerical work.

4.4.5 Multiplicity

Table 4.1 shows the total numbers of singles, binaries, triples and quadruples produced and the various measures of multiplicity for different values of \mathcal{N} and $\sigma_{\log M}$. As \mathcal{N} is increased, \mathbf{mf} decreases. The reason for this is that a small cluster relaxes by dynamically ejecting stars, leaving a stable multiple system. For higher \mathcal{N} , more stars need to be ejected as singles before the

		$\mathcal{N} = 3$	$\mathcal{N} = 4$	$\mathcal{N} = 5$	$\mathcal{N} = 6$
$\sigma_{\log M} = 0.2$	S	33253	39711	43873	46567
	B	33241	22506	20207	19306
	T	88	5091	5014	4394
	Q	0	1	168	409
	mf	0.500	0.410	0.367	0.341
	csf	0.502	0.486	0.444	0.415
	bf	0.668	0.603	0.561	0.534
$\sigma_{\log M} = 0.4$	S	33231	41883	45534	48053
	B	33228	22073	18033	16670
	T	104	4657	5764	5389
	Q	0	0	277	609
	mf	0.501	0.390	0.346	0.321
	csf	0.502	0.457	0.437	0.414
	bf	0.668	0.581	0.545	0.519
$\sigma_{\log M} = 0.6$	S	33161	40950	41598	47707
	B	33155	23098	16955	16378
	T	176	4282	5645	5726
	Q	0	1	333	589
	mf	0.501	0.401	0.355	0.322
	csf	0.504	0.463	0.453	0.420
	bf	0.668	0.591	0.522	0.523

Table 4.1: The numbers of different multiple systems produced in the dimensionless simulations; S - singles, B - binaries, T - triples and Q - quadruples. For each combination of $\sigma_{\log M}$ and \mathcal{N} , we run an ensemble of $\sim 10^5/\mathcal{N}$ simulations. Also shown are the three different multiplicity measures as defined in Section 2.2.

cluster stabilizes, increasing S and thereby reducing **mf**. We do not consider systems with very large \mathcal{N} , since such systems are found to produce too many singles to match the observations. Also hydrodynamical simulations suggest that ring fragmentation produces only a small number of fragments (e.g. Cha & Whitworth 2003b). The effect of changing $\sigma_{\log M}$ is quite small compared with changing \mathcal{N} , and is not monotonic.

4.4.6 The dimensionless separation distribution

In Figures 4.3a, b, c and d, we see that the separation distribution has an approximately log-normal form. The widths of the lognormals are all in the range $\sigma_{\log a} \lesssim 0.5$ and are thus much narrower than the observed separation distribution (e.g. $\sigma_{\log a} = 1.53$ for G-dwarfs; DM91). We notice two main trends as we vary \mathcal{N} and $\sigma_{\log M}$.

If we fix $\sigma_{\log M}$ and increase \mathcal{N} , the peak separation shifts to smaller values and the overall distribution becomes broader. Increasing \mathcal{N} tends to increase the number of 3-body interactions

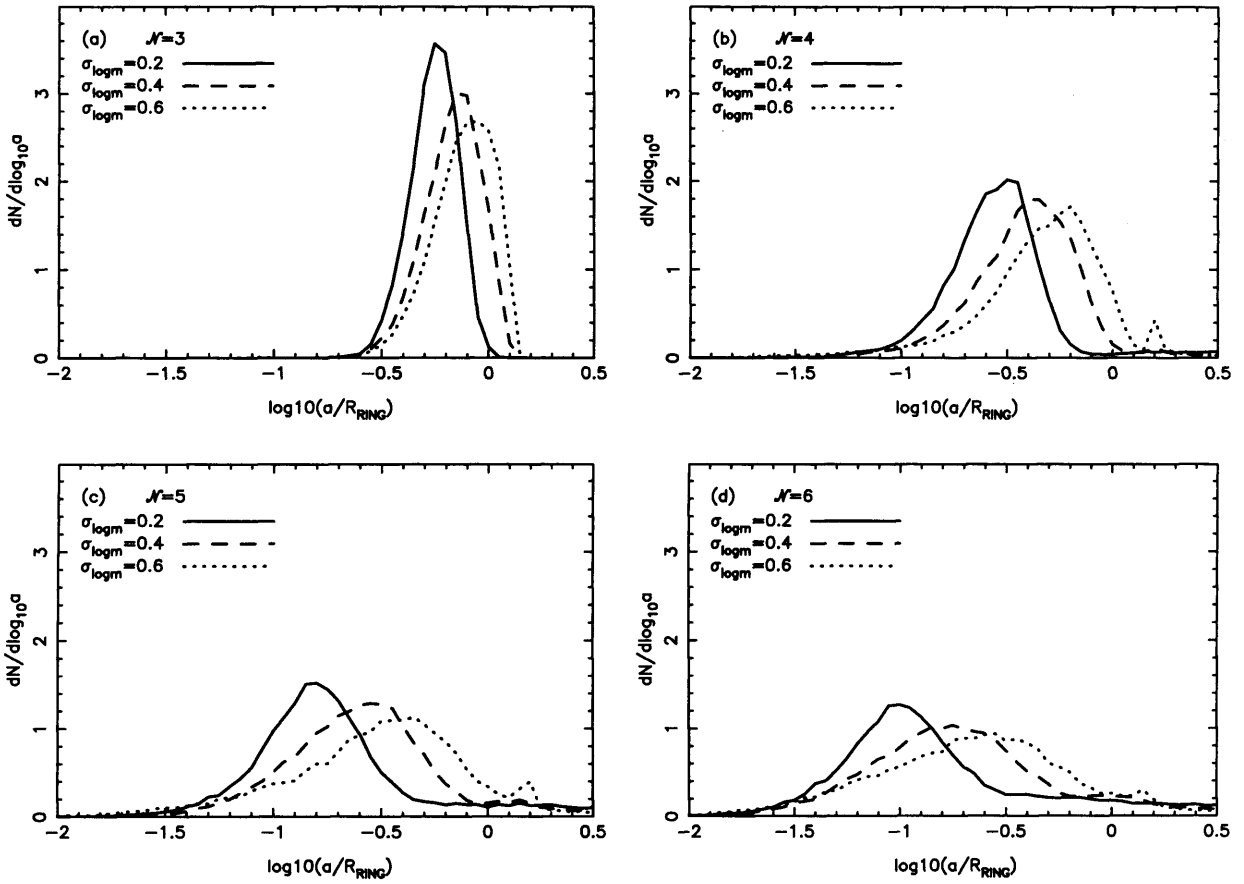


Figure 4.3: The dimensionless separation distribution, $dN/d \log_{10} a$, resulting from simulations with parameters $\sigma_{\log M} = 0.2$ (solid line), $\sigma_{\log M} = 0.4$ (dashed line) and $\sigma_{\log M} = 0.6$ (dotted line), and (a) $\mathcal{N} = 3$, (b) $\mathcal{N} = 4$, (c) $\mathcal{N} = 5$ and (d) $\mathcal{N} = 6$.

which must occur before a stable multiple is formed, and therefore it tends to increase the binding energy of the surviving multiple system, i.e. to decrease its separation. The greater number of 3-body interactions also produces a wider logarithmic range of final separations because it is a stochastic process (i.e. one binary system may be stabilized by just two mild interactions and another by four violent interactions). Also, for high- \mathcal{N} , there is an asymmetric tail stretching to large separations.

If we now fix \mathcal{N} and increase $\sigma_{\log M}$, the separation distribution shifts to larger separations and becomes somewhat broader. This is because the number of 3-body interactions which occur before a stable multiple is formed is fixed by \mathcal{N} and is therefore the same. However, for large $\sigma_{\log M}$, the two most massive stars which form the final binary contain almost all the mass, and the remaining stars are so lightweight, that their ejection does not harden the binary much. Conversely, for small $\sigma_{\log M}$ the two stars which form the final binary are of comparable mass to those which get ejected, and so their ejection hardens the remaining binary considerably.

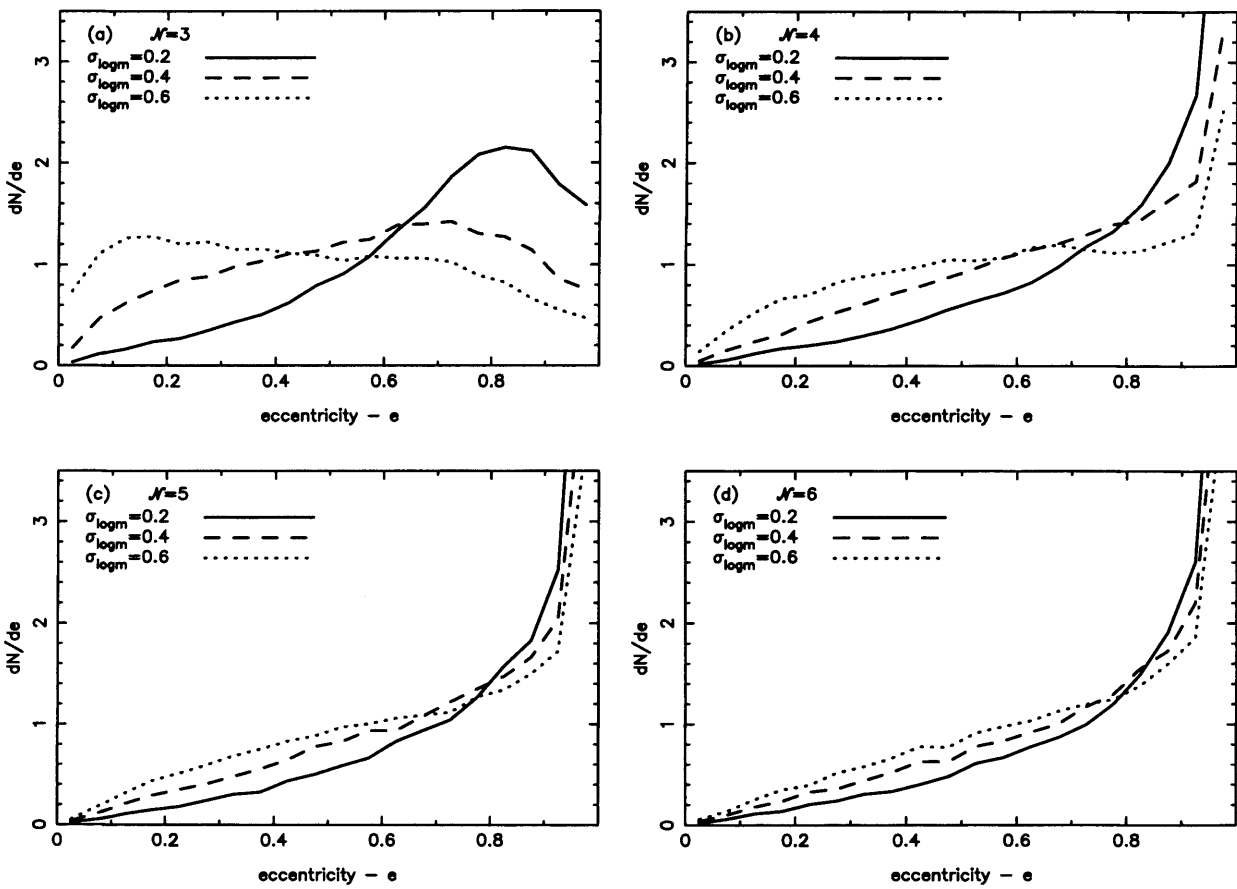


Figure 4.4: The total eccentricity distribution, dN/de , resulting from simulations with parameters $\sigma_{\log M} = 0.2$ (solid line), $\sigma_{\log M} = 0.4$ (dashed line) and $\sigma_{\log M} = 0.6$ (dotted line), and (a) $N = 3$, (b) $N = 4$, (c) $N = 5$ and (d) $N = 6$.

4.4.7 Eccentricities

The distribution of eccentricities depends strongly on the value of $\sigma_{\log M}$, and somewhat on the value of \mathcal{N} . For $\mathcal{N} = 3$, there are considerable differences between the distributions for $\sigma_{\log M} = 0.2$, $\sigma_{\log M} = 0.4$ and $\sigma_{\log M} = 0.6$ (Figure 4.4a). For $\sigma_{\log M} = 0.2$, the eccentricity distribution, dN/de , rises monotonically (until about $e \approx 0.8$). As $\sigma_{\log M}$ is increased, dN/de becomes more and more flat. For high- $\sigma_{\log M}$, the lowest mass component is likely to be easily ejected, within a few dynamical times, leaving behind a highly circularised binary. With so few interactions, the eccentricity distribution is highly unlikely to become thermalised (i.e. the thermal distribution; Valtonen & Mikkola 1992). For higher- \mathcal{N} (≥ 4), there are more N-body interactions before the cluster dissolves which allows the eccentricity distribution to become more thermalised. For low $\sigma_{\log M}$, there are few low-eccentricity binaries, and the numbers increase monotonically with increasing eccentricity, rising rapidly for very high eccentricities ($e > 0.9$). The rise at high eccentricities is characteristic of the dissolution of 2D planar systems; in contrast, the dissolution of 3D systems results in a thermal distribution of eccentricities ($dN/de = 2e$, e.g. Valtonen & Mikkola 1991). As we increase $\sigma_{\log M}$, the number of high-eccentricity binaries decreases and the distribution becomes a little flatter (but not flat, see Figures 4.4b, c & d).

4.4.8 Mass-ratios

The distribution of mass-ratio, dN/dq , is found to be strongly dependent on $\sigma_{\log M}$, and only lightly dependent on \mathcal{N} (Figures 4.5a, b, c and d). $\sigma_{\log M}$ controls the range of masses possible in a single core and thus the possible masses of components in a binary. If there is a low range of masses available, q cannot differ greatly from unity. For any \mathcal{N} , Figures 4.5a, b, c and d show that for low $\sigma_{\log M} = 0.2$, most of the binaries have mass-ratios greater than 0.5 with a peak at around $q \sim 0.8$. As $\sigma_{\log M}$ is increased, there are more binaries with lower mass-ratios and the peak moves to a lower value of q .

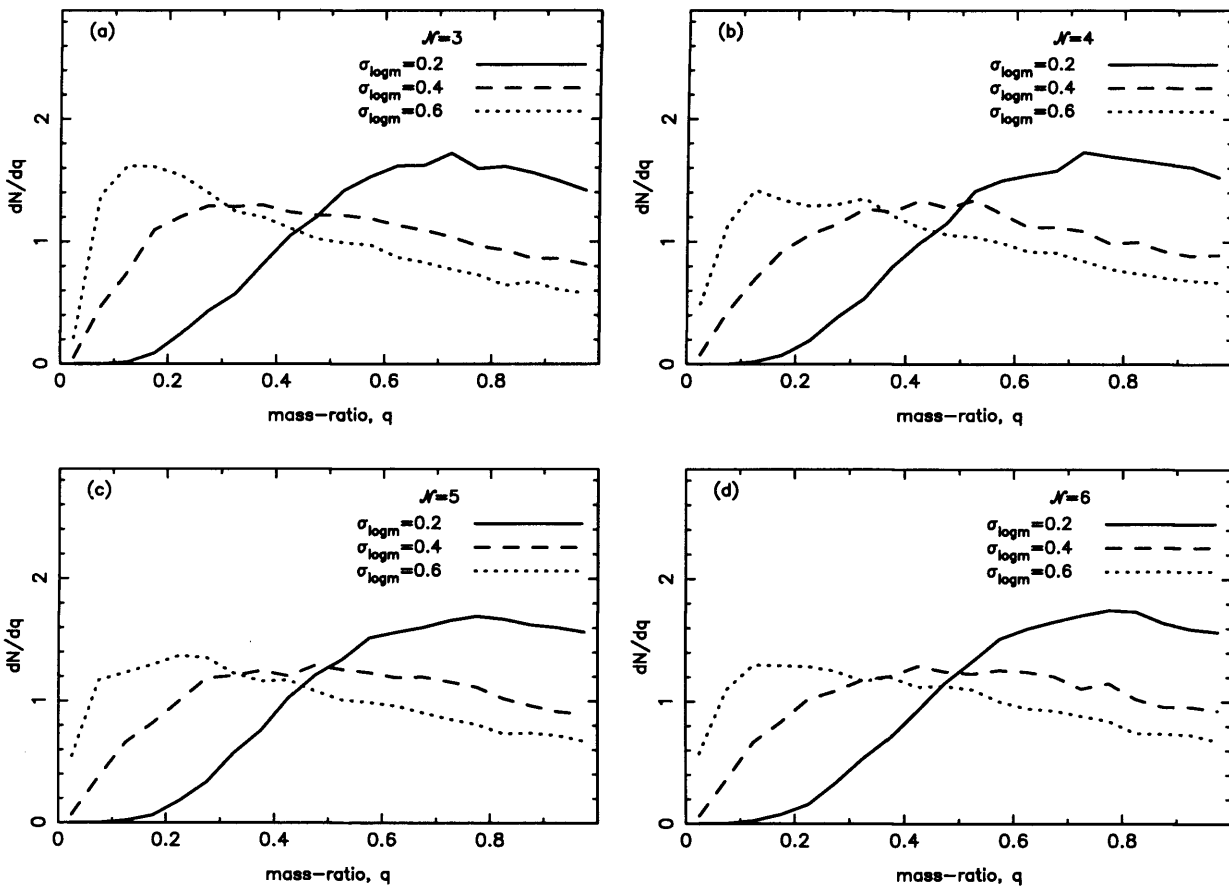


Figure 4.5: The total mass-ratio distribution, dN/dq , resulting from simulations with parameters $\sigma_{\log M} = 0.2$ (solid line), $\sigma_{\log M} = 0.4$ (dashed line) and $\sigma_{\log M} = 0.6$ (dotted line), and (a) $N = 3$, (b) $N = 4$, (c) $N = 5$ and (d) $N = 6$.

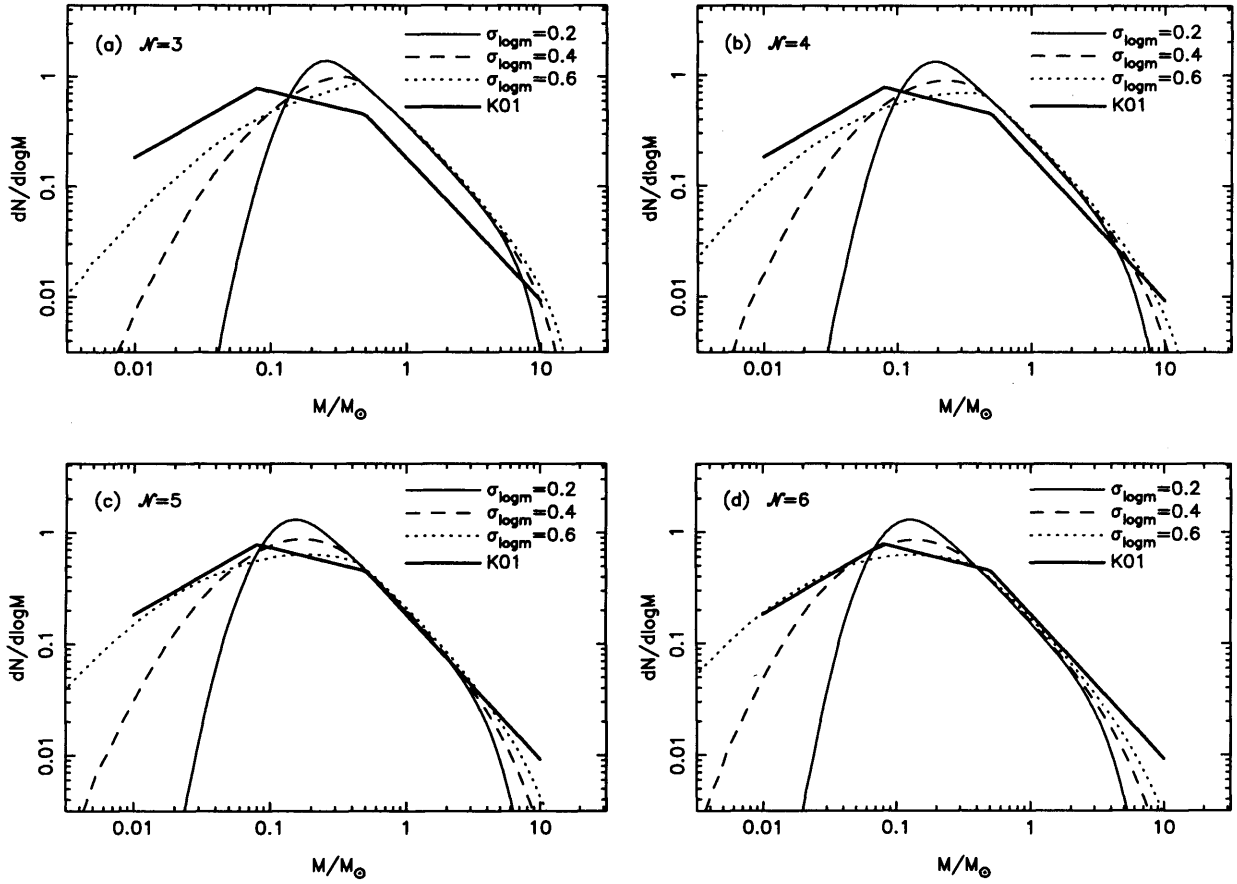


Figure 4.6: (a) The model IMF for $\mathcal{N} = 3$ with $\sigma_{\log M} = 0.2$ (thin solid line), $\sigma_{\log M} = 0.4$ (dashed line) and $\sigma_{\log M} = 0.6$ (dotted line). (b) as (a) but for $\mathcal{N} = 4$. (c) as (a) but for $\mathcal{N} = 5$. (d) as (a) but for $\mathcal{N} = 6$. The observed IMF (Kroupa, 2001) is shown as a heavy solid line on each panel.

4.5 Convolution with the core-mass spectrum

We can now convolve the dimensionless simulations with the core mass spectrum to produce an overall distribution of stellar masses (i.e. an IMF), the multiplicity as a function of primary mass M_1 , and the distributions of eccentricity e and mass-ratio q , as functions of M_1 .

4.5.1 The resultant IMF

The model IMFs, dN_\star/dM_\star , are given by convolving the core mass function, $dN_{\text{CORE}}/dM_{\text{CORE}}$ (Equation 4.1), and the dimensionless stellar mass spectrum, $dN_\mu/d\mu$, as defined in section 4.4.1,

$$\frac{dN_\star}{dM_\star} = \int_{M_{\text{CORE,MIN}}}^{M_{\text{CORE,MAX}}} \frac{dN_\mu}{d\mu} \left(\mu = \frac{M_\star}{M_{\text{CORE}}} \right) \frac{dN_{\text{CORE}}}{dM_{\text{CORE}}} \frac{dM_{\text{CORE}}}{M_{\text{CORE}}}. \quad (4.14)$$

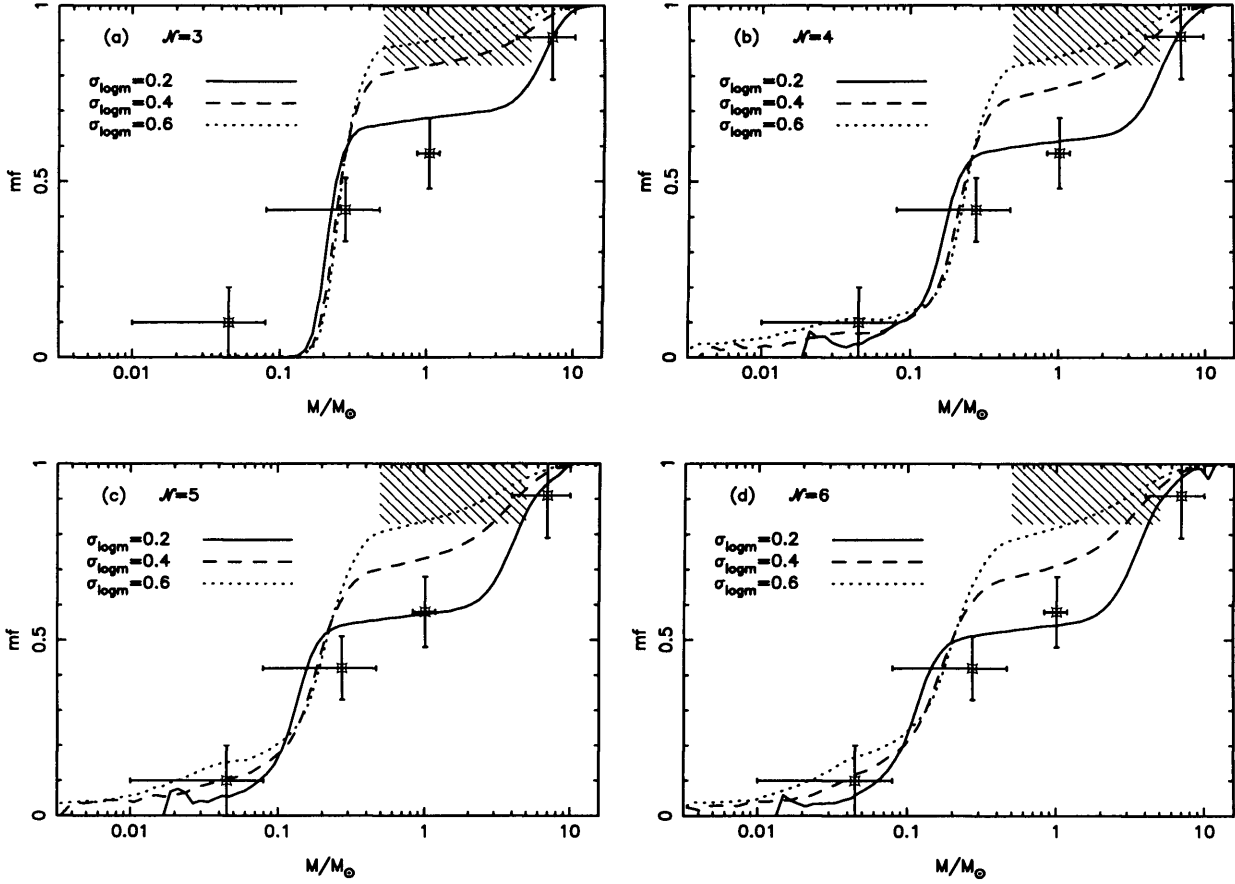


Figure 4.7: The multiplicity frequency as a function of primary mass for (a) $\mathcal{N} = 3$, (b) $\mathcal{N} = 4$, (c) $\mathcal{N} = 5$, and (d) $\mathcal{N} = 6$, all with $\sigma_{\log M} = 0.2, 0.4$ and 0.6 . The four plotted points with error bars are observational values taken from Martín et al. (2000), FM92, DM91 and Shatsky & Tokovinin (2002). The hashed box represents the extrapolated multiplicity of PMS stars (Patience et al. 2002)

Figure 4.6 shows the IMFs for all combination of $\mathcal{N} = 3, 4, 5$ and 6 and $\sigma_{\log M} = 0.2, 0.4$ and 0.6 , together with the observed IMF (Kroupa 2001). The shape of the IMF is highly dependent on $\sigma_{\log M}$. If we were to choose equal-mass stars (i.e. effectively $\sigma_{\log M} = 0.0$), the IMF would exactly mimic the shape of the core mass spectrum. As we increase $\sigma_{\log M}$, the IMF becomes broader. The lowest mass core has mass $0.5 M_{\odot}$, so a large value of $\sigma_{\log M}$ is required to produce the large observed numbers of low-mass stars and brown-dwarfs. \mathcal{N} has little effect on the shape of the IMF, but affects the position of the peak. If we keep $\sigma_{\log M}$ constant and increase \mathcal{N} , the overall shape of the IMF is roughly constant, but the peak moves to smaller mass. We can fit the Kroupa IMF well with $\mathcal{N} = 5$ and $\sigma_{\log M} \sim 0.6$; the ratio of brown dwarfs to stars is then ~ 0.5 . The main source of the agreement between the model IMF and the observed IMF is the similarity between the slope of the employed CMS and observed IMF at high masses. How well the model IMF agrees with observations at the low-mass end is determined mainly by $\sigma_{\log M}$.

4.5.2 Multiplicity

Figure 4.7 shows the multiplicity frequency as a function of stellar mass, $\mathbf{mf}(M_1)$, for all combination of $\mathcal{N} = 3, 4, 5$ and 6 and $\sigma_{\log M} = 0.2, 0.4$ and 0.6 . Overall, the model results have a similar trend to the observations, with \mathbf{mf} increasing from near zero at the lowest masses to near unity at the highest masses.

As $\sigma_{\log M}$ is increased, \mathbf{mf} increases at all masses above the peak in the initial mass function. This is because, as $\sigma_{\log M}$ is increased, these masses are increasingly likely to be the most massive star in the ring, and hence increasingly likely to form part of a multiple system due to dynamical biasing (McDonald & Clarke 1993).

As \mathcal{N} is increased, \mathbf{mf} decreases at all masses. This is because a small cluster evolves to a stable state (i.e. a binary), or a quasi-stable configuration (i.e. an hierarchical multiple), by ejecting stars. For higher \mathcal{N} , it is necessary to eject more stars before stability, or quasi-stability, is reached, and this decreases the overall multiplicity. If there is a range of masses, the lower mass stars are ejected preferentially.

Figure 4.7 shows that for intermediate stellar masses ($0.4 M_{\odot} \lesssim M_{\star} \lesssim 4 M_{\odot}$) \mathbf{mf} is almost independent of primary mass M_1 . This is a direct consequence of using a simple power-law core mass function and convolving with a dimensionless distribution. For stars of given mass M_{\star} in the range $0.4 M_{\odot}$ to $4 M_{\odot}$, there is an approximately constant ratio between the number of stars which have formed in a relatively low-mass core (and are therefore probably the most massive stars in that core and likely to end up as the primary in a multiple system) and the number of stars which have formed in a relatively high-mass core (and are therefore probably one of the less massive stars in that core and unlikely to end up as a primary). This approximately constant ratio translates into an approximately constant \mathbf{mf} .

For low masses ($M \lesssim 0.2 M_{\odot}$), \mathbf{mf} decreases rapidly with decreasing M . Low mass stars and brown dwarfs are therefore seldom found as primaries in binary systems, in agreement with observations. This decrease of \mathbf{mf} below $\sim 0.2 M_{\odot}$ would be less severe if the core mass spectrum were not cut off abruptly below $M_{\text{MIN}} = 0.5 M_{\odot}$ (see Eqn. 4.1).

If we consider the multiplicity of pre-Main Sequence stars, a high multiplicity (> 0.8) in the mass range $0.5 M_{\odot} < M_1 < 5.0 M_{\odot}$ can only be realised in our model if $\sigma_{\log M}$ is large (~ 0.6). To obtain a good fit to the IMF, we require $\mathcal{N} = 5$ and $\sigma_{\log M} = 0.6$ (see Section 4.5.1). Therefore we can obtain a good fit to *both* the observed IMF, *and* the observed high \mathbf{mf} for PMS stars, with $\mathcal{N} = 5$ and $\sigma_{\log M} = 0.6$.

However, there exists no parameter set that results in a satisfactory fit to the observed IMF, and reproduces the \mathbf{mf} of mature field stars. For example, to obtain a \mathbf{mf} of about 0.6 for G-dwarf primaries requires a low $\sigma_{\log M} \simeq 0.2$, but this produces a poor IMF which has too few brown dwarfs. This inconsistency can be resolved, if we retain $\sigma_{\log M} = 0.6$ and the \mathbf{mf} for

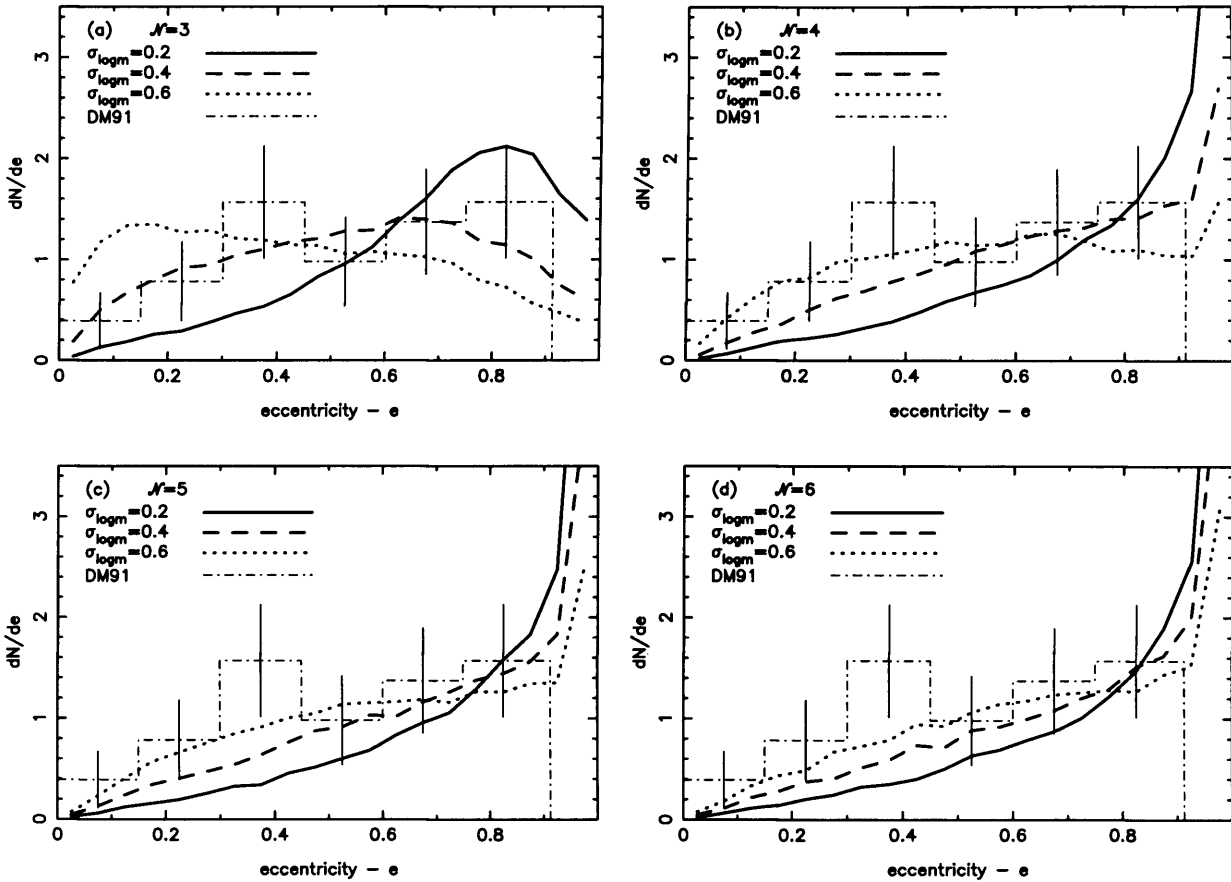


Figure 4.8: The G-dwarf eccentricity distribution resulting from convolving the dimensionless results with the observed core-mass spectrum (Equation 4.1) for parameters $\sigma_{\log M} = 0.2$ (solid line), $\sigma_{\log M} = 0.4$ (dashed line) and $\sigma_{\log M} = 0.6$ (dotted line), and (a) $\mathcal{N} = 3$, (b) $\mathcal{N} = 4$, (c) $\mathcal{N} = 5$ and (d) $\mathcal{N} = 6$. Also plotted in all panels is the observed G-dwarf binary eccentricity distribution for high-period binaries ($P_d > 10^3$ days; DM91).

G-dwarf primaries is reduced, after ring dissolution, by the interactions which occur between binary systems formed in different rings. This is essentially what Kroupa (1995a) calls *stimulated evolution*, and we will explore this possibility in Chapter 5.

4.5.3 Eccentricity

The eccentricity distribution of G-dwarfs in our model is consistent with the observed eccentricity distribution for long-period systems (DM91; Figure 4.8). We expect that the eccentricities of short-period systems are modified by tidal forces between the two components and/or mass equalization by accretion (e.g. Whitworth et al., 1995; Bate, 2000), neither of which processes is modelled in this work. Therefore we only compare our model to the observed eccentricity distribution for long-period systems. The observations are fitted best by $\mathcal{N} = 4$ or 5 and $\sigma_{\log M} = 0.4$ or 0.6 (see Figure 4.8b).

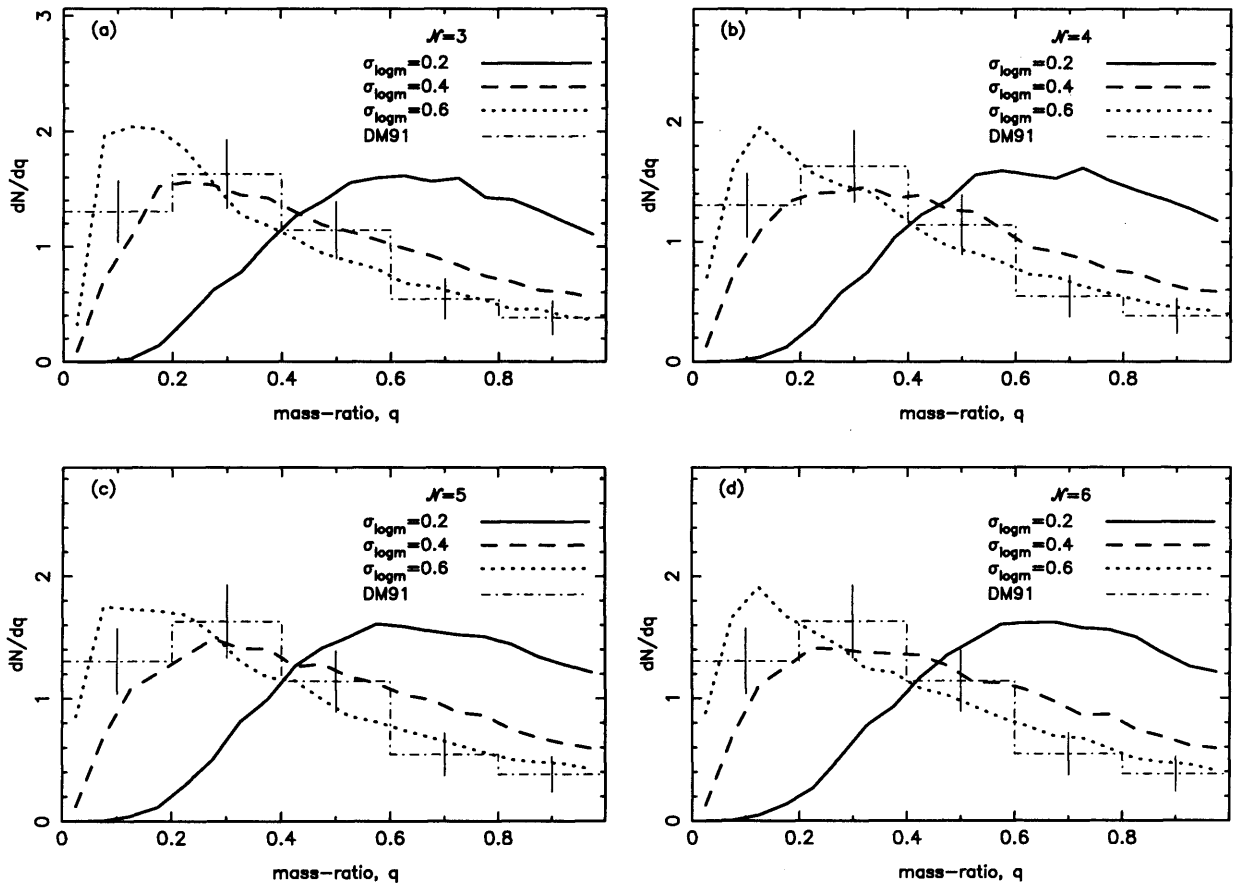


Figure 4.9: The G-dwarf mass-ratio distribution resulting from convolving the dimensionless results with the observed core-mass spectrum (Equation 4.1) for parameters $\sigma_{\log M} = 0.2$ (solid line), $\sigma_{\log M} = 0.4$ (dashed line) and $\sigma_{\log M} = 0.6$ (dotted line), and (a) $\mathcal{N} = 3$, (b) $\mathcal{N} = 4$, (c) $\mathcal{N} = 5$ and (d) $\mathcal{N} = 6$. Also plotted in all panels is the observed G-dwarf binary mass-ratio distribution for high-period binaries ($P_d > 10^3$ days; DM91).

For all cases, there is an excess of binaries with very high eccentricity ($e > 0.9$) compared to the observations. The simulations of Delgado et al. (2003) show that these systems would migrate to lower eccentricities if proper account were taken of gas dynamical processes at periastron during the protostellar stage (tidal interactions, mass exchange, etc.). High-eccentricity systems may also be more susceptible to tidal disruption, as noted by Kroupa (1995b), although this is a small effect.

4.5.4 Mass-ratio

The mass-ratio distribution from our model, with $\mathcal{N} = 4$ or 5 and $\sigma_{\log M} = 0.4$ or 0.6, is very similar to the mass-ratio distribution for G-dwarfs observed by DM91 (as illustrated on Figure 4.9b), but somewhat different from the mass ratio distribution observed in Taurus by Woitas et al. (2001). This difference may be attributable to Taurus having an unusual IMF, and in

particular a paucity of brown dwarfs (Briceño et al. 2002; Luhman et al. 2003). However, more recent observations suggest the IMF in Taurus may not be considerably different from the field IMF (Luhman 2004; Kroupa et al. 2003).

4.6 Convolving with the distribution of core rotation rates

4.6.1 The binary separation distribution

In order to obtain the distribution of separations, we must convolve the dimensionless results with both the distribution of core masses M_{CORE} , and the distribution of core β -values. M_{CORE} gives the core radius R_{CORE} through Equation (4.2), and β gives the ring radius R_{RING} through Equation (4.6). Knowing M_{CORE} and R_{RING} , the dimensionless simulations can be scaled to give the distributions of a and P , as a function of primary mass M_1 . As explained in Section 4.2.3 we consider two different β distributions.

Using Case A ($\overline{\log\beta} = -2.0$, $\sigma_{\log\beta} = 1.2$), our model gives the distribution of separations illustrated in Figure 4.10a (dotted line), where it is compared with the observations of pre-Main Sequence binaries having primary mass in the range $0.5 M_{\odot} \lesssim M_1 \lesssim 5.0 M_{\odot}$, as collated by Patience et al. (2002; dashed line and histogram). We see that there is close correspondence between these two distributions. The implication is that, if cores have a distribution of rotation rates similar to the one adopted in Case A, then the dynamical dissolution of small rings of protostars is able to reproduce the distribution of binary periods observed for pre-Main Sequence stars like those in Taurus and Ophiuchus.

Using Case B ($\overline{\log\beta} = -2.2$, $\sigma_{\log\beta} = 1.7$), our model gives the distribution of separations illustrated in Figure 4.10b (dotted line), where it is compared with the observations of G Dwarf binaries in the field by DM91 (dotted line and histogram). We see that there is a very close correspondence between the two distributions. The implication is that, if cores have a distribution of rotation rates similar to the one adopted in Case B, then the dynamical dissolution of small rings of protostars is able to reproduce the distribution of binary periods observed for G-Dwarf binaries in the field by DM91. The problem is that if we persist with the parameters $\mathcal{N} = 5$ and $\sigma_{\log M} = 0.6$, the resulting multiplicity fraction for G-dwarf binaries is much higher than observed, as noted in Section 4.5.2.

However, if most of the stars in the field are formed in populous clusters, we must allow that their binary statistics continue to evolve dynamically after the dissolution of the rings in which they are formed. The cause of further dynamical evolution is that, following dissolution of the individual rings, the stars and binary systems formed in one ring interact with the stars and binary systems formed in other neighbouring rings. In other words, the individual rings are just

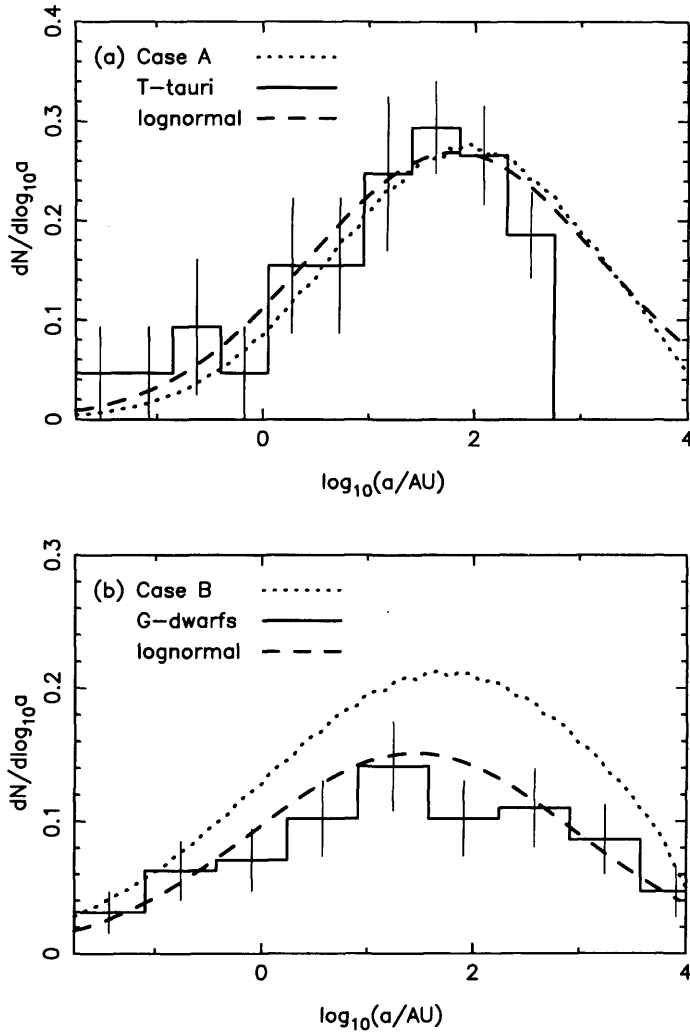


Figure 4.10: (a) The histogram shows the observed distribution of semi-major axes for pre-Main Sequence binaries in Taurus, as collated by Patience et al. (2002), and the dashed line is their best fit to this distribution. The dotted line shows the predictions of our model for Case A ($\log\beta = -2.0$ and $\sigma_{\log\beta} = 1.2$) with parameters $\mathcal{N} = 5$ and $\sigma_{\log M} = 0.6$. The peak and width of the model predictions are fairly close to the observations, with a similarly high overall multiplicity. (b) The histogram shows the observed distribution of semi-major axes for binaries with G-dwarf primaries in the field from DM91, and the dashed line is their log-normal fit to this distribution. The dotted line shows the predictions of our model for Case B ($\log\beta = -2.2$ and $\sigma_{\log\beta} = 1.7$) with parameters $\mathcal{N} = 5$ and $\sigma_{\log M} = 0.6$. The peak and width of the model predictions are similar to the observations, but the overall multiplicity is higher.

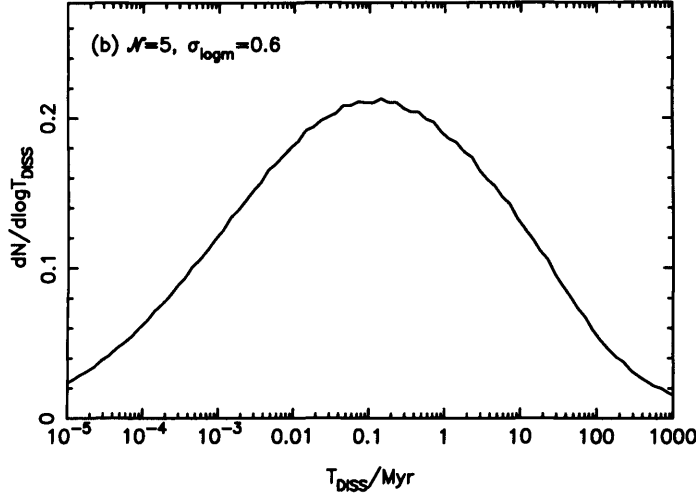


Figure 4.11: Lifetimes of all clusters with $\mathcal{N} = 5$ and $\sigma_{\log M} = 0.6$ when convolved over the core mass spectrum and the β distribution in Myrs.

subclusters within the larger cluster, and interactions on the scale of the cluster also influence the final binary statistics. Kroupa (1995a) has shown that interactions between binaries in clusters can widen the distribution of binary separations somewhat, and reduce the multiplicity from near unity to that observed in the field.

4.6.2 Dissolution timescales

The dimensionless ring dissolution times, $T_{\text{DISS}}/T_{\text{RING}}$, derived in Section 4.4.4, can be converted into physical times by combining Eqns. 4.2 and 4.6 with T_{RING} (Section 4.4.4) to obtain

$$\left(\frac{T_{\text{DISS}}}{\text{Myr}}\right) = \begin{cases} 2.8 \left(\frac{T_{\text{DISS}}}{T_{\text{RING}}}\right) \left(\frac{M_{\text{CORE}}}{M_{\odot}}\right) \beta^{3/2}, & M_{\text{CORE}} \leq M_{\odot}; \\ 2.8 \left(\frac{T_{\text{DISS}}}{T_{\text{RING}}}\right) \left(\frac{M_{\text{CORE}}}{M_{\odot}}\right)^{1/4} \beta^{3/2}, & M_{\text{CORE}} \geq M_{\odot}. \end{cases} \quad (4.15)$$

Hence by convolving the distribution of $T_{\text{DISS}}/T_{\text{RING}}$ (Figure 4.11) with the core mass spectrum (Equation 4.1) and the β -distribution (Equation 4.4), we obtain the overall distribution of dissolution times for the ring-clusters invoked in our model (Figure 4.11). The distribution peaks at around ~ 0.2 Myr, the majority of the ring-clusters has dissolved by 1 Myr, and only a handful ($< 3\%$) remains after 100 Myr.

4.7 Summary

We have developed a model of binary star formation in which cores collapse and bounce to produce rings, and the rings then fragment into protostars. The only free parameters describing core fragmentation are the number of stars spawned by a single core, \mathcal{N} , and the spread of masses produced by a single core, $\sigma_{\log M}$. The dynamical evolution of the protostars is followed using Aarseth's NBODY3 code, for many different realizations, and the properties of the resulting multiple systems are recorded. The main results of this chapter are summarised below.

1. Dimensionless N-body simulations of ring evolution show that rings dissolve typically after a few tens of dynamical times (Figure 4.2a), in agreement with previous numerical work (e.g. Van Albada 1968). The decaying cluster produces binary stars, multiple stars and ejected singles (Table 4.1).
2. The dimensionless binary separation distribution is approximately lognormal (Figures 4.3a - d). The widths of the curves are much narrower than those observed in the field (e.g DM91). If we increase the number of stars in a cluster, the width of the lognormal is increased. Increasing $\sigma_{\log M}$ shifts the position of the peak to larger values of $\log a$, and also increases the width of the lognormal a little.
3. The results of the dimensionless simulations must be convolved with a core-mass spectrum (CMS) and a distribution of core- β (i.e. the ratio of rotational to gravitational energy), or equivalently a distribution of core angular momenta, to produce scaled results that can be compared to observations.
4. *Irrespective of the distribution of core rotation rates*, our model reproduces the observed IMF (Figure 4.6), and the distributions of eccentricity and mass ratio in *long-period* binary systems (Figure 4.8 & 4.9), provided only that (a) each ring spawns $\mathcal{N} \sim 4 - 5$ protostars, and (b) the protostars have a lognormal mass-distribution with standard deviation $\sigma_{\log M} \sim 0.6$. Thus $\mathcal{N} \sim 4 - 5$ and $\sigma_{\log M} \sim 0.6$ are our preferred choices for these free parameters.
5. The distributions of eccentricity and mass ratio for *short-period* binary systems are not reproduced by our model, but we presume that this is because our model does not include tidal circularization or mass equalization by accretion.
6. The model reproduces the observed variation of multiplicity with primary mass for mature field stars (Figure 4.7), but only if $\sigma_{\log M} \sim 0.2$. With our preferred values, $\mathcal{N} \sim 4 - 5$ and $\sigma_{\log M} \sim 0.6$, the model produces multiplicities which are higher than those observed for mature field stars, but are very similar to those observed for pre-Main Sequence stars,

in the mass range 0.5 to $5 M_{\odot}$ (this is the only mass range for which reliable pre-Main Sequence multiplicities are available). We conclude that the multiplicities resulting from ring dissolution represent the observed pre-Main Sequence population well, and that the pre-Main Sequence population then evolves into the observed Main Sequence population through interactions between stars and binary systems from different rings in the same cluster.

7. In a somewhat different context, Kroupa (1995a) has shown that such interactions can reduce the overall multiplicity from ~ 1.0 to ~ 0.6 . Our model only requires such interactions to destroy $\sim 25\%$ of pre-Main Sequence binaries. A concern with the model would be that binaries with low mass-ratio will be destroyed preferentially (although not exclusively). This will skew the distribution of mass-ratios somewhat, and may thereby degrade the agreement with observations of mature G-dwarfs in the field (See Chapter 5 for discussion).
8. In order to predict the distribution of binary separations, we have to consider the distribution of core rotation rates. We assume that the distribution of β follows a lognormal, and we consider 2 cases. If we adopt Case A, our results match closely the distribution of semi-major axes obtained by Patience et al. (2002) for pre-Main Sequence stars (Fig. 4.10a), and we conclude that further dynamical evolution takes place – presumably involving interactions with protostars from other neighbouring rings – to convert this distribution into the one observed in the field. Conversely, if we adopt Case B, our results match closely the peak and width of the separation distribution obtained by DM91 for field G Dwarfs (Fig. 4.10a). However, our results do not match the observed multiplicity frequency for field G-dwarfs, in the sense that our predicted \mathbf{mf} -value is too high. It is unlikely that further dynamical evolution, following ring dissolution, can rectify this, since to preserve the peak and width of the separation distribution would require dynamical processes which destroy, with equal efficiency, binary systems having widely different separations. Therefore Case A is our preferred option.
9. Most rings have dissolved after 1 Myr and fewer than 3 % remain after 100 Myr (Figure 4.11).

Chapter 5

The evolution of binary properties in young clusters

In this chapter, we develop a simple model of clustered binary star formation. Observations show that young stars are usually found in clusters containing from 30 to 1000 members or more (Lada & Lada 2003). We assume that a molecular cloud fragments into a large ($N = 100$) number of prestellar cores which are clustered with fractal dimension D_f . Each core fragments into a small- N cluster, in the same way as we modelled cores in Chapter 4 (i.e. they collapse, bounce to form rings and fragment to form N stars). We follow the dynamical evolution of the larger cluster using an N -body code (NBODY6) and determine the effect the larger cluster has on the binary statistics. We follow the evolution for 20 Myr which is of order the lifetime of a cluster.

We find that dynamical interactions between binaries and other members of the cluster are successful in destroying some binaries, principally with large separations, and thereby reducing the multiplicity. The binary destruction efficiency is strongly dependent on the stellar density of the cluster. We find that for a cluster containing 100 cores (400 stars when $N = 4$), a cluster radius of ≤ 1.0 pc is sufficient to destroy a significant fraction of binaries after 20 Myr so the binary statistics tend towards that of the field. Clusters with more sub-structure (i.e. lower D_f) can reproduce some of the observed binary statistics better than models with uniform density.

5.1 Introduction

The majority of stellar systems form in clusters rather than in isolation (Lada & Lada 1991, 2003, McCaughrean, Rayner & Zinnecker 1991). Realistic models of binary star formation should consider how young stellar systems evolve in larger clusters, rather than as isolated entities, so as to include any dynamical effects on the orbital properties of the binaries. Weakly-

bound (i.e. soft) binaries may be easily disrupted by tidal forces due to the cluster or by 3-body interactions with other cluster members. This can reduce the overall multiplicity and alter the distribution of binary separations and other orbital parameters.

Simulations of small-N clusters, such as those performed in Chapter 4, investigate the formation and statistical properties of primordial binaries in isolation. In this chapter, we extend our model from Chapter 4 by placing many small-N clusters in a larger cluster environment; in particular, we model fractal clusters. We investigate how the binary properties differ from those generated by isolated cores, as predicted in Chapter 4, and we also compare the results with the observed statistics.

5.2 Observations of young clusters

5.2.1 Embedded clusters

Embedded clusters are young stellar clusters which have formed deep inside a molecular cloud; they are obscured from view at optical wavelengths by dust extinction and are only visible at infra-red and sub-mm wavelengths. Embedded clusters typically contain between 50 and 200 objects and have a spatial extent of order 1 pc (Lada & Lada 2003).

Lada & Lada (2003) suggest that the majority of young clusters are dissolved within 10 Myr of their formation. Only about $\sim 4\%$ of young clusters reach the age of 100 Myr and survive to become open clusters such as the Pleiades. All other young clusters are destroyed shortly after they have formed. A possible mechanism for cluster destruction is that a sufficiently massive proto-cluster will form an O star which outputs a huge luminosity; this radiation can ionise, evaporate and disperse all of the gas from the cluster. If the gas contributes significantly to the gravitational potential of the cluster and the gas removal timescale is shorter than the cluster crossing time, then its rapid removal can unbind the cluster. If the gas removal timescale is much longer than the crossing time and/or the total gas mass is a relatively small fraction of the total cluster mass, then the cluster can slowly adjust and remain bound and approximately virialised.

5.2.2 The fractal properties of young clusters

Observations of young clusters reveal some sub-structure (other than the presence of binaries), suggesting that they are fractal. If clusters are indeed fractal, this is likely to be related to the fractal structure of molecular clouds, i.e. the fractal structure of the cloud seeds the fractal structure of the cluster. Cartwright & Whitworth (2004) have developed a new method for calculating the fractal dimension of clusters, D_f , and applied this method to clusters in Taurus,

ρ -Ophiuchus and Chamaeleon among others. They calculate the fractal dimension of Taurus to be $D_{f,TAURUS} = 1.55 \pm 0.25$ suggesting considerable sub-structure. They also calculate a fractal dimension for older clusters like Chamaeleon, which has a fractal dimension of $D_{f,CHAM} = 2.25 \pm 0.25$. Other clusters such as ρ -Ophiuchus do not have noticeable fractal sub-clustering, instead having a simple radial density gradient. Lada & Lada (2003) comment that some young embedded clusters also appear to have sub-structure. This may possibly be an evolutionary effect, where substructure is slowly smoothed-out over time due to dynamical evolution and the cluster relaxes to a more uniform, spherically symmetric density distribution.

5.3 Previous work on cluster dissolution

The dynamical evolution of binaries in clusters has received considerable attention from Kroupa and co-workers (e.g. Kroupa 1995a, 1995b; Kroupa, Aarseth & Hurley 2001; Kroupa & Bouvier 2003a, 2003b).

Kroupa (1995a) explores the evolution of a cluster of binary systems, and concludes that the properties of binaries in the field can be reproduced by dynamical interactions between binaries in a young cluster. He identifies a *dominant mode cluster*, which contains 200 binaries initially distributed within a Plummer sphere of half-mass radius $R_{0.5} = 0.8$ pc. The binary component masses are formed by random pairings from the field IMF, and have periods drawn randomly from a distribution covering 1 day to 10^9 days and having no correlation with primary mass. Interactions amongst the binaries (termed *stimulated evolution*) reduce the multiplicity by selectively removing low-mass companions (i.e. dynamical biasing), and thereby reproduce the distributions of period and mass ratio observed in field G Dwarf binaries by DM91.

In Kroupa (1995b), this model is extended to include the *eigenevolution* (i.e. internal binary evolution) of short-period systems (for example, their tidal circularization). He shows that stimulated evolution does not change the distribution of orbital eccentricities significantly (so the observed distribution must be essentially primordial). In addition, stimulated evolution does not generate sufficient higher multiples by capture to match the observed numbers of triples and quadruples. However, it does produce a distribution of mass ratios for G Dwarf primaries which is in good agreement with the observations of DM91. Kroupa (1995b) also suggests that long-period binaries with large eccentricities are somewhat more likely to be disrupted tidally than long-period binaries with low eccentricities.

In contrast to the above works, Kroupa & Burkert (2001) investigate the ballistic evolution of clusters comprising 100 or 1000 primordial binaries, but with a narrow range of initial separations compared to the observations. They find that even under the most favourable conditions, dynamical interactions between binaries cannot produce a distribution of separations as broad as

that observed by DM91. The observed separation distribution must therefore be set principally by the properties of primordial binaries.

Kroupa, Aarseth & Hurley (2001) show that the Pleiades may have evolved from a cluster like the Orion Nebula Cluster (ONC), following loss of residual gas and simultaneous stimulated evolution. They point out that the primordial binary population in the ONC could have been very similar to the pre-Main Sequence binary population that is currently observed in Taurus-Auriga. Subsequent dynamical interactions in the dense cluster environment then changed it into what we see today.

Goodwin & Whitworth (2004) investigated the dynamical evolution of fractal clusters, in contrast to Plummer spheres which are commonly used (such as in the work by Kroupa discussed above). They find that for virialised or super-virial clusters ($Q > 0.5$ where Q is the ratio of kinetic to gravitational potential energy), the sub-structure is not destroyed for at least several crossing times. In sub-virial clusters ($Q < 0.5$), the sub-structure is rapidly destroyed within a few crossing times. Goodwin & Whitworth (2004) only consider fractal sub-structure of systems and do not consider binaries or other hierarchical multiple systems.

5.4 Model

5.4.1 Assumptions and Aims

We assume that molecular clouds fragment to produce a fractal distribution of star-forming cores. Each core is rotating and thus contains some angular momentum. As a core collapses, rotationally induced fragmentation occurs producing a ring of N stars, as modelled in Chapter 4. These small- N clusters dissolve due to both internal dynamical evolution and external forces, to produce single stars, binaries and higher-order multiples. We aim to investigate to what degree the cluster environment can affect the overall multiplicity of the cluster and the binary properties of the multiple systems within it, and to compare these results to the observations.

5.4.2 Initial conditions

First, we set up the fractal distribution of core positions and velocities within the cluster as follows. The computational domain consists of a cube with side-length $2R_c$. First, we divide this cube d times in each dimension, therefore into d^3 equal volumes. Each volume is called a child cell. For each child cell, the probability P that it contains a core is related to the fractal dimension by $P = d^{(D_f-3)}$. We pick a random number, \mathcal{R} , for each core; if $\mathcal{R} < P$, then the cell contains a core. After we have populated all of the volumes, if the total number of cores is less than the required number of cores, then we continue to sub-divide the computational

domain. Any cell with a ‘core’ is sub-divided into a further d^3 volumes and populated with cores using the method described above; the original parent core is removed. Any cell which is not populated is considered a dead cell and is removed from the computational domain. This process is continued until more than enough cores have been selected. We only include cores which are less than a distance R_c from the center to produce a spherical-fractal cluster. If too many cores remain, we remove cores at random until we have the required number, N_{CORES} . This does not affect the fractal dimension of the cluster.

We determine the velocity of each core as we determine its position in the cluster. The first time we divide the computational domain, the selected cores are given a random velocity. Each time we divide a cell into child cells, the velocity of each child cell is equal to the sum of the velocity of its parent cell plus an additional random component. The velocity of a core is thus linked to its parent’s velocity and to the fractal structure of the cloud, as opposed to being purely random.

Second, we select core masses at random from a core mass spectrum. We use the core mass spectrum observed by Motte et al. (2001), which we also use in Chapter 4, i.e. Equation 4.1.

Third, we scale the velocities of all the cores in the cluster to obtain the required virial parameter, Q . We calculate the total kinetic energy of the cores, T , and the total gravitational potential energy, Ω . The velocity of each core is then scaled by

$$v_i \rightarrow v_i \left(\frac{|\Omega| \times Q}{T} \right)^{1/2}.$$

Finally, we replace each core with a small-N cluster ring. In addition to M_{CORE} , we must specify a value for β , the ratio of rotational to gravitational energy. We use the lognormal prescription used in Chapter 4, i.e. Equation 4.4 and draw out a random value of β . We can then construct a small-N cluster following the procedure described in Section 4.4.1 for dimensionless rings using chosen values of \mathcal{N} and $\sigma_{\log M}$. These are then scaled using the selected values of M_{CORE} and β for that core. Each ring is rotated to face a randomly selected direction so there is no preferred orientation of rings in the cluster. Each ring is positioned so that its centre lies at the position of its parent core. The total velocity of each star is equal to its velocity in the ring plus the velocity of its parent core in the cluster. Figure 5.1 shows the spatial configuration of stars in clusters with fractal dimension $D_f = 2.5$ and $D_f = 1.5$.

5.4.3 Numerical method

The cluster is evolved using an adapted version of NBODY6, supplied by Sverre Aarseth (e.g. Aarseth 1999). The main features of the NBODY codes, including NBODY6 are described

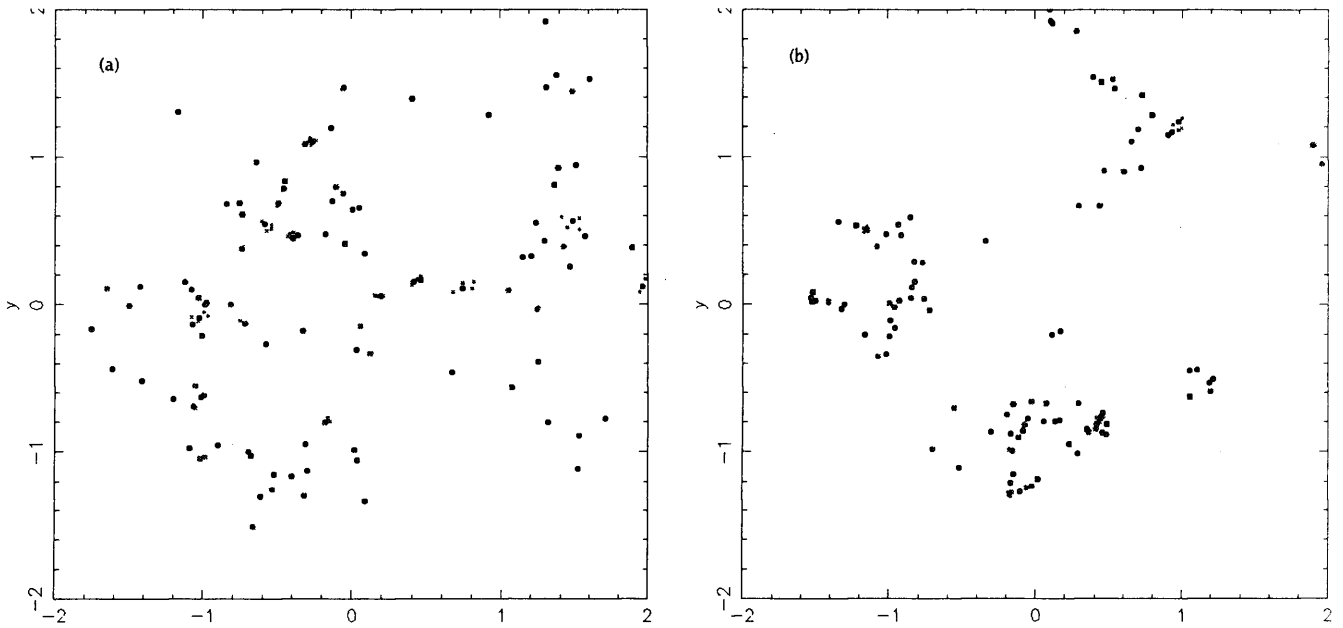


Figure 5.1: Fractal clusters. (a) A fractal cluster with fractal dimension $D_f = 2.5$ containing 100 cores (400 stars), (b) a fractal cluster with fractal dimension $D_f = 1.5$ containing 100 cores.

in Chapter 3. The main difference between NBODY6 and NBODY3 (used in Chapter 4 to model small-N clusters) is that NBODY6 includes the Ahmad-Cohen neighbour scheme which increases the efficiency of calculations with large numbers of particles.

5.4.4 Parameters

This simple model already provides a large number of parameters that can be investigated. Some of these have been investigated for isolated small-N clusters in Chapter 4 and we select values for them based on that work. The total parameter set is:

1. *The fractal dimension of the cluster, D_f*

For our base parameter set, we select a fractal dimension of $D_f = 2.5$. We can vary D_f to test how the fractal dimension of a cluster can affect its binary properties. We also test $D_f = 1.5$.

2. *The number of cores in the cluster, N_{CORES}*

For our base parameter set, we select $N_{\text{CORES}} = 100$ which is of order the number of systems observed in young embedded clusters.

3. *The radius of the cluster, R_c*

The radii of young, embedded clusters is of order 1.0 pc. We investigate clusters with radii 0.5 pc, 1.0 pc and 2.0 pc.

4. *The virial ratio, Q*

The virial parameter of the cluster is important in determining the survival rate of primordial binaries. A sub-virial cluster will contract before evaporating whereas a super-virial cluster will expand and may have little effect on the binary population. Realistic young clusters may be born either in a sub-virial, virialised or super-virial state depending on the conditions of the parent molecular cloud. For example, if OB stars are switched on early in a clusters life, the molecular cloud gas evaporates quickly leaving the young cluster in a super-virial state.

We select the virial ratio $Q = 0.5$ for our base simulations, corresponding to a virialised cloud.

5. *The number of stars per core, \mathcal{N}*

We investigate cores with $\mathcal{N} = 4$ stars. This choice is based on the results from the dissolution of small- \mathcal{N} clusters in Chapter 4.

6. *The lognormal mass-function of stars in the core, i.e. $\sigma_{\log M}$*

After selecting a total core mass, M_{CORE} , from the core-mass spectrum (i.e. Equation 4.1), we select the masses of stars in that core by sampling from a lognormal distribution with width $\sigma_{\log M} = 0.6$. The masses are then scaled so that $\sum_1^{\mathcal{N}} m_i = M_{\text{CORE}}$. As with our choice of \mathcal{N} , $\sigma_{\log M}$ is selected based on the results of Chapter 4.

7. *The β distribution for cores*

We select the β -distribution such that we obtain the pre-Main Sequence separation distribution observed in low-density regions like Taurus. Based on the results of Chapter 4, we select values of β from a lognormal β distribution with $\sigma_{\log \beta} = 1.2$ and $\overline{\log \beta} = -2.0$.

5.5 Results

Here we present results of simulations using a variety of different parameter sets. First, we consider the standard parameter set and present the various binary distributions and compare to observations and previous work. We focus in particular on the results after 20 Myr which can be taken as a representative age of clusters before they are destroyed (e.g. Lada & Lada 2003).

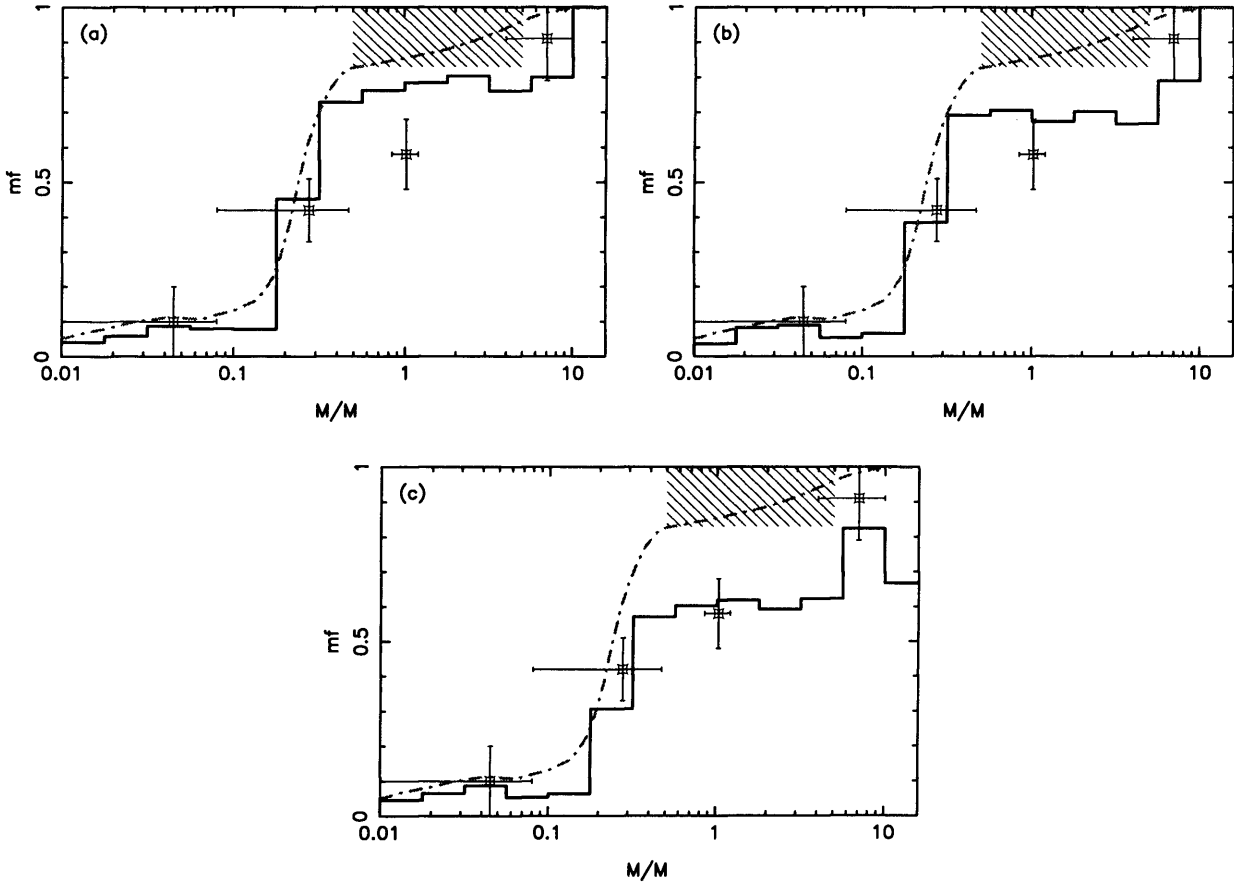


Figure 5.2: The multiplicity frequency as a function of primary mass resulting from the dissolution of clusters $D_f = 2.5$ containing 100 cores with radius (a) $R_c = 2.0$ pc, (b) $R_c = 1.0$ pc, (c) $R_c = 0.5$ pc; all clusters have fractal dimension $D_f = 2.5$ and contain 100 cores. The dotted line represents the multiplicity frequency resulting from the dissolution of isolated ring clusters with $\mathcal{N} = 4$ and $\sigma_{\log M} = 0.6$ as shown in Figure 4.7b. The four plotted points with error bars are observational values taken from Martín et al. (2000), FM92, DM91 and Shatsky & Tokovinin (2002). The hashed box represents the extrapolated multiplicity of PMS stars (Patience et al. 2002).

5.5.1 Standard runs : $N_{\text{CORES}} = 100$, $D_f = 2.5$, $R_c = 0.5$ pc, 1.0 pc, 2.0 pc

Multiplicity

Figure 5.2 shows the multiplicity frequency as a function of primary mass, $\mathbf{mf}(M_1)$, for runs with the base parameter set after 20 Myr. Also plotted are four observational values (see caption) and the multiplicity frequency resulting from the dissolution of isolated rings for the $N = 4$, $\sigma_{\log m} = 0.6$ case (dot-dashed line; see Section 4.5.2).

Figure 5.2 shows that the cluster environment is effective at disrupting and destroying binaries and thereby reducing the multiplicity frequency. In most mass ranges, the multiplicity frequency for stars in large clusters after 20 Myr (solid histogram) is lower than that obtained for isolated small-N clusters (dot-dashed line). For the largest and least dense clusters ($R_c = 2$ pc, Figure 5.2a), the multiplicity frequency is only reduced by a relatively small amount ($\sim 0.05 - 0.1$ for stars with masses $0.5 M_\odot \leq M \leq 5.0 M_\odot$). For the smallest and most dense clusters ($R_c = 0.5$ pc, Figure 5.2b), the multiplicity frequency is reduced substantially (~ 0.3 for stars with masses $0.5 M_\odot \leq M \leq 5.0 M_\odot$). This is in agreement with the trend found by Kroupa (1995a); he found that the overall multiplicity frequency was reduced in clusters by binary encounters and that the final multiplicity decreased with decreasing cluster radius, or equivalently increasing stellar density. An encounter between a binary and a perturbing body needs to be sufficiently close to disrupt the binary. Denser clusters have a higher close encounter rate and therefore a higher binary disruption rate. Kroupa (1995a) suggests that the dominant mode cluster has $N_{\text{BIN}} = 200$ and a half-mass radius $R_{0.5} = 0.8$ pc. Although we use different initial conditions to Kroupa (1995a), the main trends are the same and our results suggest that a cluster with radius ≤ 1 pc can disrupt binaries efficiently within the required timescale (< 100 Myr).

The multiplicity in the mass range $0.5 M_\odot \leq M \leq 5.0 M_\odot$ is reduced to an approximately constant value (Figure ??). This compares to the observations which suggest a systematic increase of multiplicity with increasing mass in this range (although more observational points are required to confirm this trend).

The binary separation distribution

Figure 5.3 shows the binary separation distribution, $dN/d \log_{10} a$, for runs with the base parameter set (histogram). The field G-dwarf separation distribution (dashed line; DM91) and the pre-Main Sequence separation distribution (dot-dash line; Patience et al. 2002) are shown for comparison.

The binary separation distribution for G-dwarf primaries is strongly affected by the stellar density of the cluster. For the isolated model, the separation distribution is approximately the

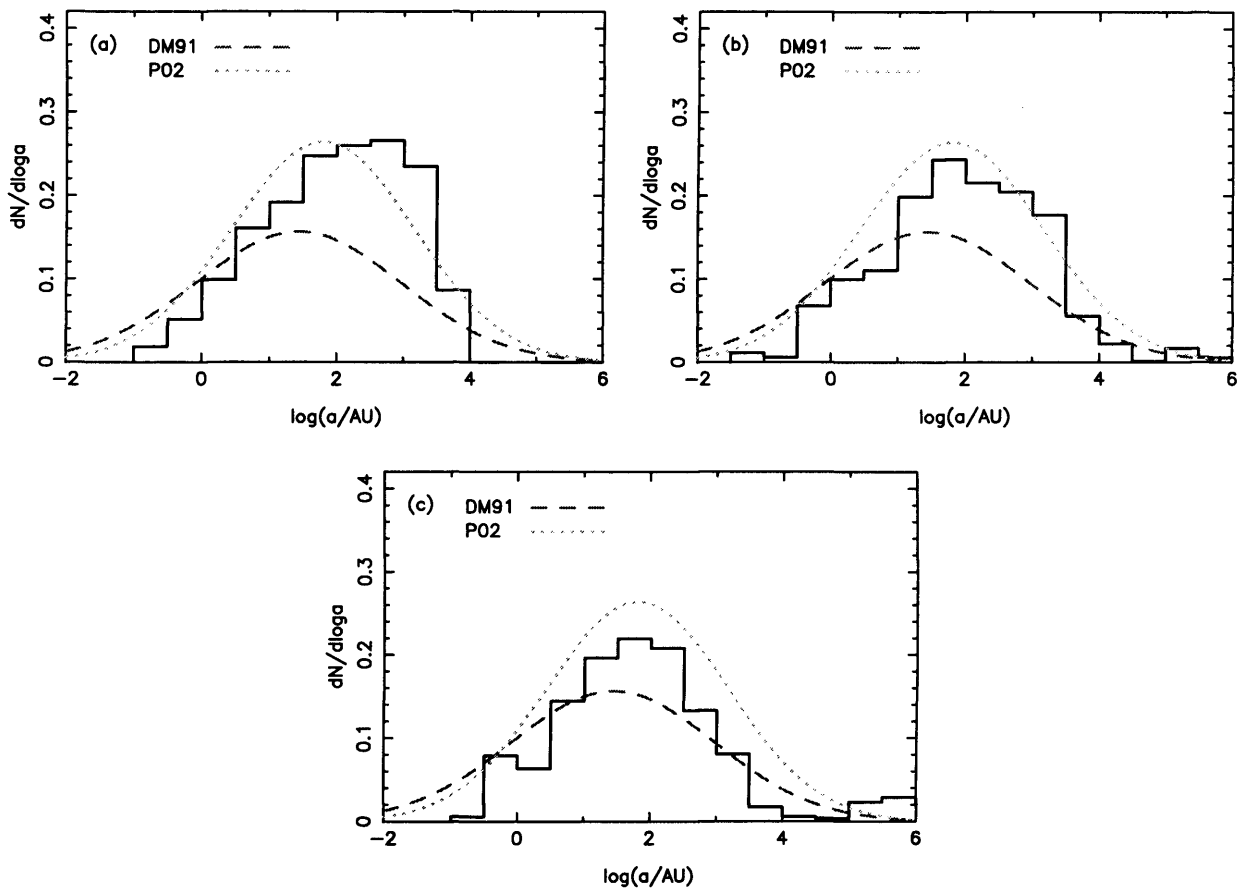


Figure 5.3: The G-dwarf separation distribution resulting from the dissolution of clusters (histogram) with radius (a) $R_c = 2.0$ pc, (b) $R_c = 1.0$ pc, (c) $R_c = 0.5$ pc; all clusters have fractal dimension $D_f = 2.5$ and contain 100 cores. The dotted line represents the lognormal fit to the separation distribution for pre-Main sequence binaries with primary mass in the range $0.5 M_\odot \leq M \leq 5.0 M_\odot$, as collated by Patience et al. (2002); this is also the separation distribution resulting from the dissolution of isolated cores in our model (See Chapter 4). The dashed line represents the separation distribution of field G-dwarf binaries as observed by DM91.

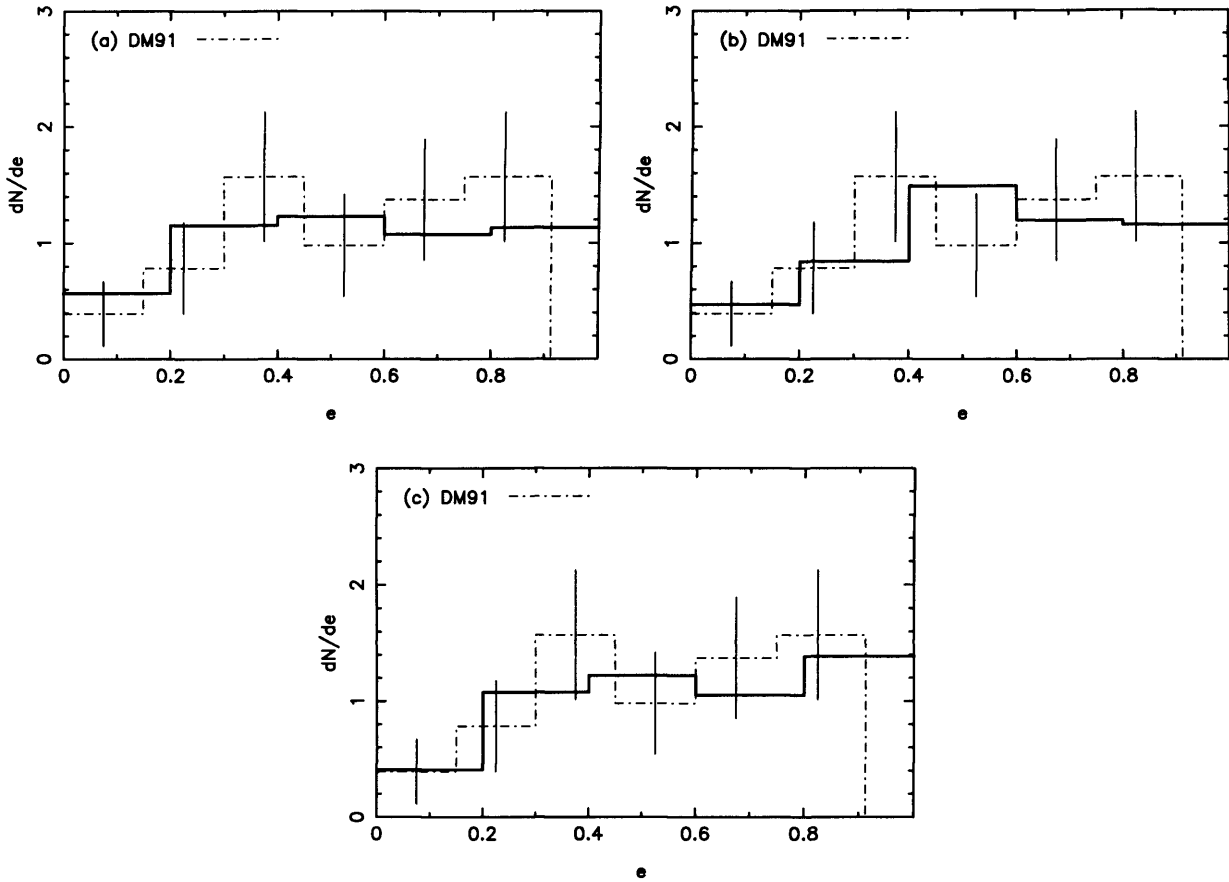


Figure 5.4: The G-dwarf eccentricity distribution resulting from the dissolution of clusters with radius (a) $R_c = 2.0$ pc, (b) $R_c = 1.0$ pc, (c) $R_c = 0.5$ pc; all clusters have fractal dimension $D_f = 2.5$ and contain 100 cores. The dot-dash histogram represents the observed G-dwarf binary eccentricity distribution for high-period binaries ($P > 10^3$ days; DM91).

same as the pre-Main Sequence separation distribution of Patience et al. (2002) (See Figure 4.10a). For the least dense cluster ($R_c = 2$ pc), Figure 5.3a shows that the separation distribution has evolved little from the pre-Main Sequence distribution (dotted line, Patience et al. 2002). As we decrease the radius of the cluster (and increase the stellar density), we see in Figures 5.3b & c that the number of binaries, in particular the number of wide binaries with $a > 100$ AU, decreases. The dynamical disruption of binaries in a cluster tends to alter the separation distribution as well as the overall multiplicity. As the radius of the cluster is reduced, the peak shifts to smaller separations. This is also the trend found by Kroupa (1995a, 1995b). We also notice that some very wide binaries ($a > 10^5$ AU) have been formed for the most dense clusters (Figure 5.3c). These binaries are likely to be transient systems (i.e. systems which are very weakly bound) formed by capture and are readily disrupted as the cluster dissolves.

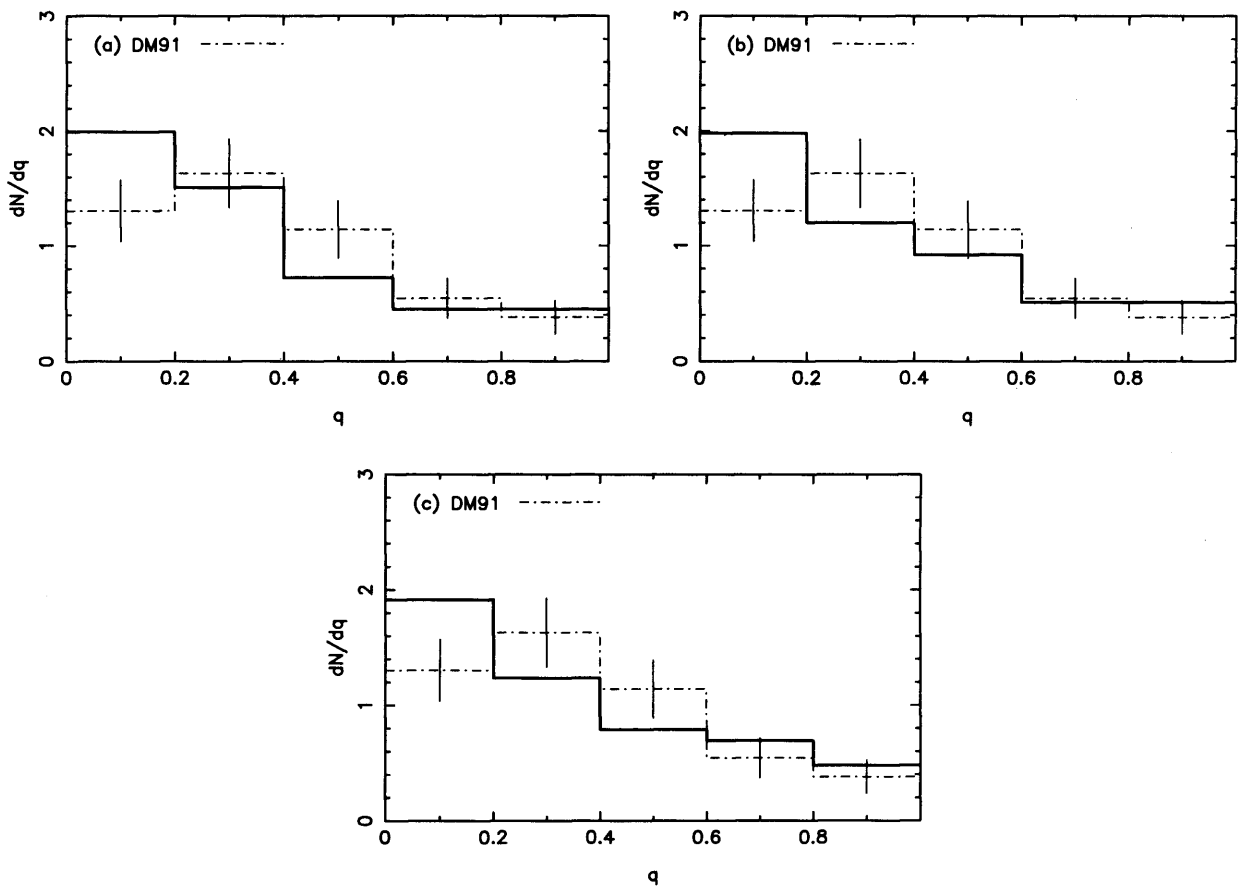


Figure 5.5: The G-dwarf mass-ratio distribution resulting from the dissolution of clusters with radius (a) $R_c = 2.0$ pc, (b) $R_c = 1.0$ pc, (c) $R_c = 0.5$ pc; all clusters have fractal dimension $D_f = 2.5$ and contain 100 cores. The dot-dash histogram represents the observed G-dwarf binary mass-ratio distribution for high-period binaries ($P > 10^3$ days; DM91).

Eccentricity

Figure 5.4 shows the distribution of orbital eccentricity for the binaries after 20 Myr. Comparing with the final eccentricity distributions for isolated clusters (Figure 4.8b - dotted line), we can see that there is little difference between the isolated model and the clustered model. The isolated cluster model using the chosen parameters ($\mathcal{N} = 4$, $\sigma_{\log M} = 0.6$) fits the observed distribution of DM91 reasonably well (i.e. the model passes through the error bars of the observations). The cluster model is largely unaffected by dynamical interactions. We note that due to the smaller number of simulations performed, we use fewer histogram bins to represent the data, but the overall trend is still the same.

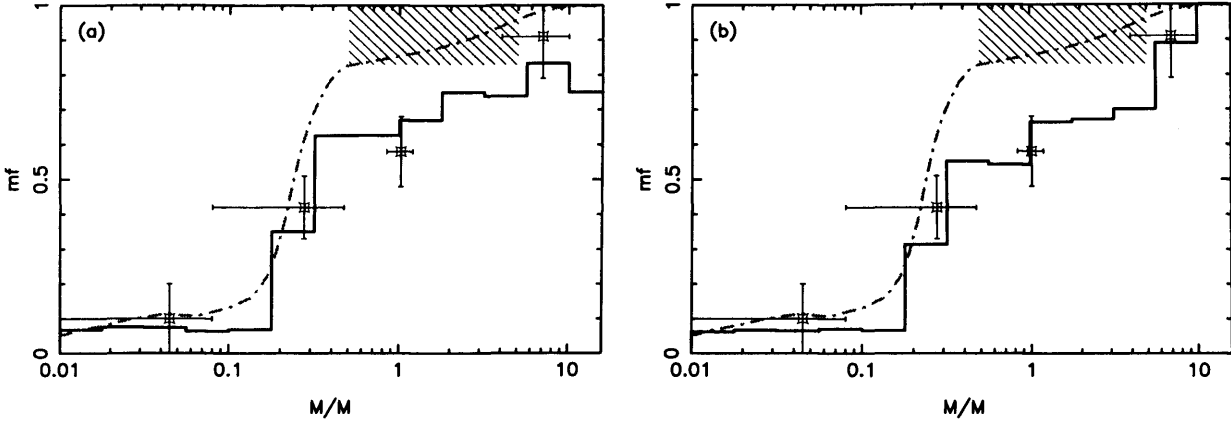


Figure 5.6: The multiplicity frequency as a function of primary mass resulting from the dissolution of clusters with radius (a) $R_c = 2.0$ pc, (b) $R_c = 1.0$ pc. all clusters have fractal dimension $D_f = 1.5$ and contain 100 cores. The dotted line represents the multiplicity frequency resulting from the dissolution of isolated ring clusters with $\mathcal{N} = 4$ and $\sigma_{\log M} = 0.6$ as shown in Figure 4.7b. The four plotted points with error bars are observational values taken from Martín et al. (2000), FM92, DM91 and Shatsky & Tokovinin (2002). The hashed box represents the extrapolated multiplicity of PMS stars (Patience et al. 2002).

Mass-ratio

Figure 5.5 shows the distribution of mass-ratios for the binaries after 20 Myr. There is a small difference between the mass-ratio distributions from the isolated model (Figure 4.9b - dotted line) and the clustered model. There is a deficiency of binaries in the range $0.2 < q < 0.6$ relative to the isolated model, and to the observations of G-dwarf binaries (DM91). It might be expected that the number of low- q binaries would be reduced, since these binaries have the lowest binding energies. The lower mass component can easily be ejected in a 3-body exchange process where a more massive single replaces the low-mass secondary. This is another example of dynamical biasing. However it has little apparent effect in this case.

5.5.2 Changing the fractal dimension : $N_{\text{CORES}} = 100$, $D_f = 1.5$, $R_c = 1.0$ pc, 2.0 pc

We now perform simulations using the same parameters as our base parameter set, but we change the fractal dimension. Here we consider clusters with fractal dimension $D_f = 1.5$. As with the $D_f = 2.5$ case, we follow the simulations for 20 Myr.

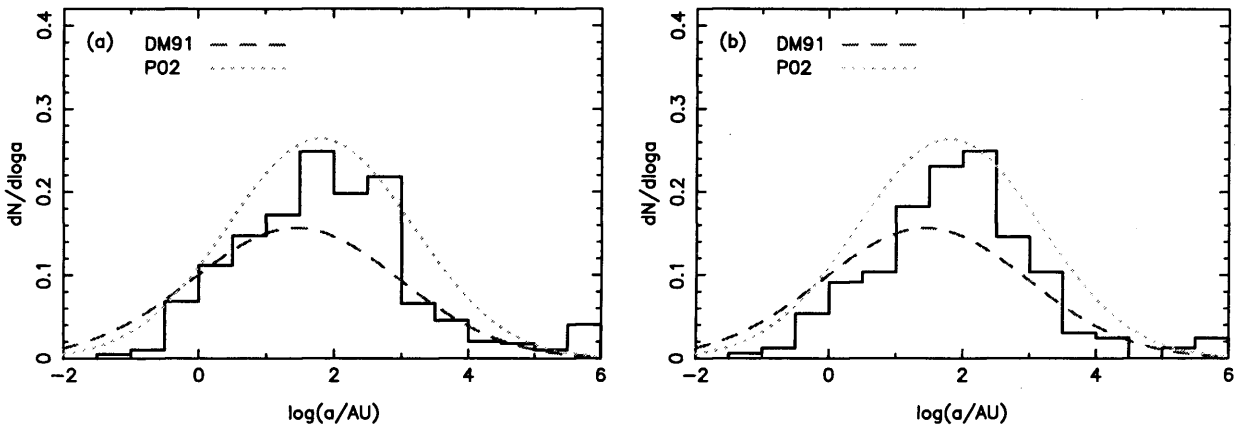


Figure 5.7: The G-dwarf separation distribution resulting from the dissolution of clusters with radius (a) $R_c = 2.0$ pc, (b) $R_c = 1.0$ pc; all clusters have fractal dimension $D_f = 1.5$ and contain 100 cores. The dotted line represents the lognormal fit to the separation distribution for pre-Main sequence binaries with primary mass in the range $0.5 M_\odot \leq M \leq 5.0 M_\odot$, as collated by Patience et al. (2002). The dashed line represents the separation distribution of field G-dwarf binaries as observed by DM91.

Multiplicity

Figure 5.6 shows the multiplicity frequency as a function of primary mass, $\mathbf{mf}(M_1)$, for clusters with fractal dimension $D_f = 1.5$ after 20 Myr. We again plot the four observational values (see caption) and the multiplicity frequency resulting from the dissolution of isolated rings for the $\mathcal{N} = 4$, $\sigma_{\log m} = 0.6$ case (dot-dashed line).

We can see that, as with the $D_f = 2.5$ case, the multiplicity frequency is reduced or retains the same value, but does not increase with respect to the isolated model, at all mass ranges plotted. This again is due to destruction of binaries by dynamical encounters. The overall multiplicity for the $D_f = 1.5$ case is smaller than for the $D_f = 2.5$ case because the stellar density in the regions of the clusters is higher due to the higher clustering of fractal clusters, i.e. the efficiency of binary disruption is determined by the local stellar density and not the average stellar density of the cluster.

There is also a noticeable difference in the form of the multiplicity frequency distribution between the $D_f = 2.5$ case (Figure 5.2) and the $D_f = 1.5$ case (Figure 5.6). For the $D_f = 1.5$ case, \mathbf{mf} is more strongly dependent on mass and is a monotonically increasing function of mass (except for $M < 0.1 M_\odot$ where $\mathbf{mf} \approx 0.05$). For the $R_c = 1$ pc case, \mathbf{mf} has an approximately linear gradient with respect to $\log M$ rising from less than 0.1 for $0.1 M_\odot$ up to approximately unity at $10 M_\odot$. The plotted observational points suggest a linear gradient with respect to $\log M$ which may support this choice of parameters.

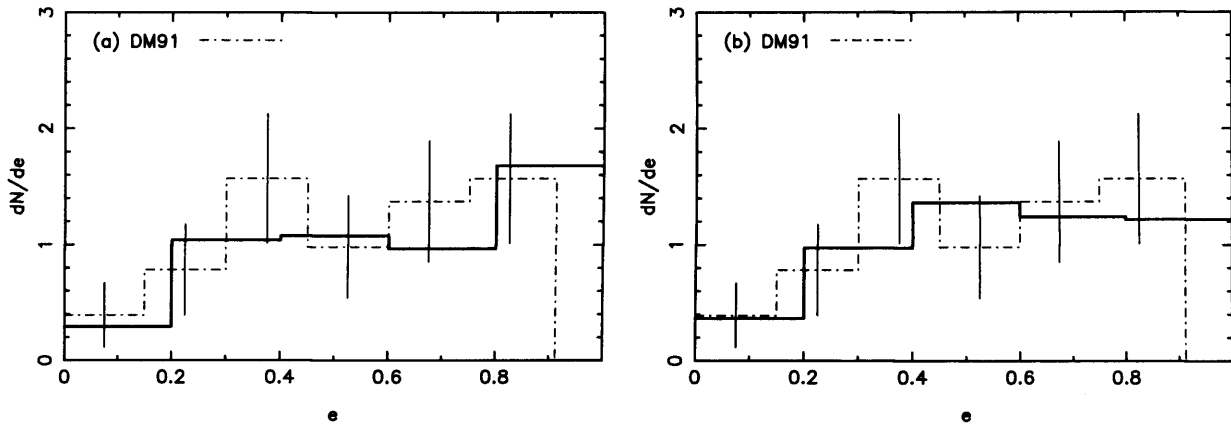


Figure 5.8: The G-dwarf eccentricity distribution resulting from the dissolution of clusters with radius (a) $R_c = 2.0$ pc, (b) $R_c = 1.0$ pc; all clusters have fractal dimension $D_f = 1.5$ and contain 100 cores. The dot-dash histogram represents the observed G-dwarf binary eccentricity distribution for high-period binaries ($P > 10^3$ days; DM91).

The binary separation distribution

Figure 5.7 shows the binary separation distribution, $dN/d \log_{10} a$, for the $D_f = 1.5$ case. The field G-dwarf separation distribution (dashed line; DM91) and the pre-Main sequence separation distribution (dot-dash line; Patience et al. 2002) are shown for comparison.

The binary separation distribution for the $D_f = 1.5$ cluster is affected in a similar way to the $D_f = 2.5$ cluster. Wide binaries are readily disrupted by dynamical interactions; the binary disruption efficiency is enhanced in the $D_f = 1.5$ clusters by the higher stellar density caused by greater sub-clustering. The $D_f = 1.5$ separation distribution has a prominent peak at $a \approx 100$ AU, which is not consistent with the field binary distribution (DM91).

Eccentricity

Figure 5.8 shows the distribution of orbital eccentricity for the binaries after 20 Myr from clusters with $D_f = 1.5$. As with the $D_f = 2.5$ case, the model is consistent with the observations (i.e. the $D_f = 1.5$ eccentricity distribution passes through the error bars of the observations). There is no significant difference between the $D_f = 1.5$ case and the $D_f = 2.5$ case.

Mass-ratio

Figure 5.9 shows the distribution of mass-ratios for the binaries after 20 Myr. There is a small difference between the mass-ratio distribution from the isolated model (Figure 4.9b - dotted line) and the $D_f = 1.5$ case for $R_c = 2.0$ pc. Again there is a deficiency of binaries in the range $0.2 < q < 0.6$ relative to the isolated model, and to the observations of G-dwarf binaries

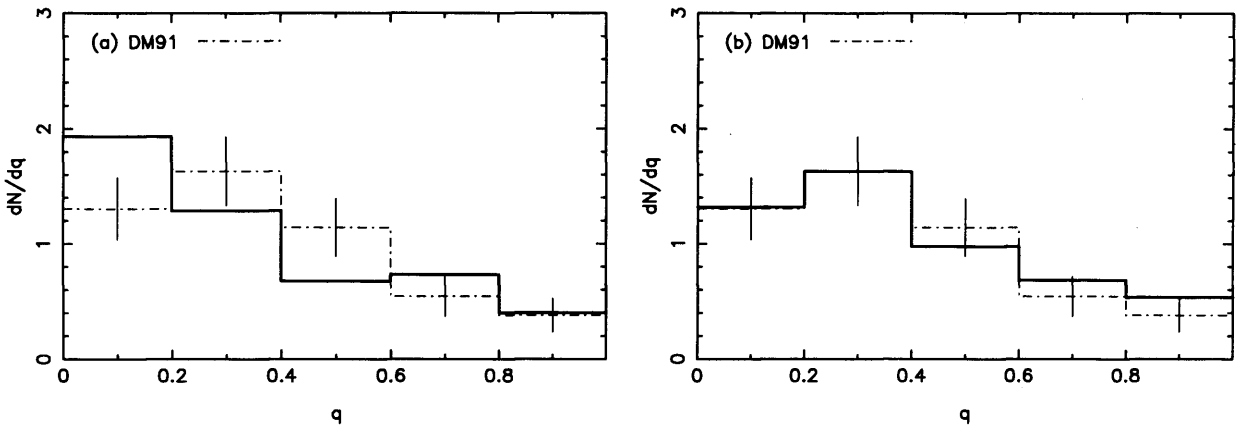


Figure 5.9: The G-dwarf mass-ratio distribution resulting from the dissolution of clusters with radius (a) $R_c = 2.0$ pc, (b) $R_c = 1.0$ pc; all clusters have fractal dimension $D_f = 1.5$ and contain 100 cores. The dot-dash histogram represents the observed G-dwarf binary mass-ratio distribution for high-period binaries ($P > 10^3$ days; DM91).

(DM91). There is a noticeable difference between the $R_c = 2.0$ pc case and the $R_c = 1.0$ pc case. The mass-ratio distribution peaks at $0.2 < q < 0.4$ for the $R_c = 1.0$ case, as do the observations. Low-mass ratio binaries have been disrupted here due to dynamical biasing.

5.6 Summary and Discussion

Following on from the work in Chapter 4 where we developed a model of isolated binary star formation, we consider the more common scenario where stellar systems form in clusters and dynamical interactions can have a significant effect on the binary population. We consider fractal clusters, which may be a more realistic configuration than the commonly used Plummer sphere. We evolve the clusters for 20 Myr which is a representative lifetime for a young cluster before it is dispersed. The main results from our simulations are summarised and discussed below.

1. The main effect of modelling binary formation in a cluster is that binaries are disrupted by dynamical interactions thereby reducing the overall multiplicity of the cluster. This is evident in all of the simulations that we have undertaken, for all cluster sizes and all fractal dimensions (Figures 5.2 and 5.6). The main trend is that the stellar multiplicity decreases as the radius of the cluster decreases (or equivalently, as the stellar density increases). This agrees with the results of Kroupa (1995a; 1995b).
2. The simulations of isolated clusters in Chapter 4 produced a multiplicity frequency distribution that is consistent with the multiplicity of pre-Main Sequence binaries in star

forming regions like Taurus (Figure 4.7b - dotted line). In order for a region like Taurus to retain a high multiplicity frequency near unity after 20 Myr, it must have a relatively low stellar density so that dynamical interactions are not strong enough. For the lowest stellar density simulations ($R_c = 2$ pc), the multiplicity is only reduced by a small fraction ($\sim 0.05 - 0.1$). Since Taurus is of order tens of parsecs in diameter, the binaries in Taurus should not be affected by dynamical evolution and thus the observed binary distributions are presumably primordial.

3. Dynamical interactions within the cluster destroy soft (i.e. large separation) binaries more efficiently than hard (i.e. small separation) binaries. This is evident from the resultant binary separation distributions in Figure 5.3. Figure 5.3a is the resultant binary separation distribution for the largest (lowest density) cluster where the binary disruption efficiency is low and the multiplicity frequency is similar to that obtained for isolated cores. The separation distribution has a large excess of binaries at large separations ($a > 100$ AU) relative to the field. As we increase the stellar density, the fraction of wide binaries decreases (Figures 5.3b and c). In contrast, the fraction of hard binaries is affected very little. There is no observed decrease due to disruption, or increase due to hardening of wider binaries. The peak of the separation distribution moves towards smaller values as R_c is decreased.
4. The eccentricity distribution is not affected strongly by dynamical evolution in the cluster, although the distributions are noisy due to relatively poor statistics. A larger number of simulations would be desirable to clarify this result.
5. The mass-ratio distribution is affected slightly by dynamical evolution. The number of binaries in the mass-ratio range $0.2 < q < 0.6$ is slightly reduced, relative to the isolated cluster model.
6. The initial fractal dimension of the cluster can affect the final distribution of multiplicity frequency as a function of mass and the final binary separation distribution. For the $D_f = 2.5$ case, Figure 5.2 shows that the multiplicity frequency in the mass range $0.5 M_\odot < M < 5.0 M_\odot$ is roughly constant, i.e. for a roughly uniform density cluster, there is little obvious dynamical biasing of binary disruption. For the $D_f = 1.5$ case, Figure 5.6 shows that the multiplicity frequency is more strongly dependent on mass. The multiplicity frequency has a gradient with respect to mass; the **mf** is less than 0.1 for $0.1 M_\odot$ with an approximately linear gradient with respect to $\log M$ up to approximately 1 at $10 M_\odot$. There is also a difference between the separation distributions for the $D_f = 1.5$ and $D_f = 2.5$ cases; wide binaries are discriminated against even more in $D_f = 1.5$ clusters producing

a sharper peak in the separation distribution.

7. The binary separation distribution of the Hyades (e.g. Patience et al. 2002; Figure 2.7a) is observed to have a peak at relatively small separations ($a \approx 5$ AU). The multiplicity of this peak is higher than that of the field or other observed star-formation regions. The simulations in this chapter show that significant hardening of binaries does not occur. Therefore the origin of this peak (if indeed it is real) must be due to the properties of the primordial binaries in the Hyades rather than due to dynamical evolution, or possibly other mechanisms such as secondary fragmentation (Whitworth & Stamatellos 2006).
8. A cluster of radius 1.0 pc with fractal dimension $D_f = 1.5$ containing 100 cores each spawning 4 stars, initially in virial equilibrium and dynamically evolved for 20 Myr is the model most consistent with observations of field G-dwarf binaries (Duquennoy & Mayor 1991). This model gives distributions consistent with the observations of eccentricity, mass-ratio and the multiplicity as a function of mass. However, there is an excess of binaries near 100 pc relative to field G-dwarf stars.

Chapter 6

Smoothed Particle Hydrodynamics

In this chapter, we will discuss Smoothed Particle Hydrodynamics (SPH). This algorithm solves the equations of self-gravitating hydrodynamics using particles to represent the fluid rather than using a grid as with finite-difference numerical schemes. It is well suited to gravitational collapse problems such as star formation, since as a region condenses to higher densities, the spatial resolution is adjusted automatically. We discuss the fundamental principles of SPH, the equations of hydrodynamics in this formalism, and additional features which improve the performance of the code. Finally, we discuss issues specific to star formation.

6.1 Numerical Hydrodynamics

Numerical hydrodynamics is a powerful tool for studying the evolution of star forming gas clouds. In general, interstellar clouds are influenced by a combination of hydrodynamical, gravitational, magnetic and viscous forces, the relative strengths of which depend on properties such as the temperature and ionization fraction of the gas. The evolution of the cloud is embodied in the equations of hydrodynamics. If we consider only hydrodynamical forces, these equations are

$$\frac{d\rho}{dt} \equiv \frac{\partial\rho}{\partial t} + \mathbf{v} \cdot \nabla\rho = -\rho\nabla \cdot \mathbf{v}, \quad \text{Continuity equation;} \quad (6.1)$$

$$\rho \frac{d\mathbf{v}}{dt} \equiv \rho \frac{\partial\mathbf{v}}{\partial t} + \rho\mathbf{v} \cdot \nabla\mathbf{v} = -\nabla P, \quad \text{Momentum equation;} \quad (6.2)$$

$$\frac{du}{dt} \equiv \frac{\partial u}{\partial t} + \mathbf{v} \cdot \nabla u = -\frac{P}{\rho} \nabla \cdot \mathbf{v}, \quad \text{Energy equation.} \quad (6.3)$$

These equations describe the evolution of the density, ρ , velocity, \mathbf{v} , and specific internal energy, u , at all points in the cloud. A fourth equation known as the equation of state is required to

compute the pressure and temperature of the fluid as a function of the other local state variables, i.e. $P \equiv P(\rho, u)$, $T \equiv T(\rho, u)$.

The equations of hydrodynamics can be presented using two different formulations. First, in the Eulerian formulation, we assume a static reference frame against which the fluid moves and evolves. In this reference frame, we must calculate the Eulerian derivatives, i.e. the partial derivatives $\partial\rho/\partial t$, $\partial\rho\mathbf{v}/\partial t$ and $\partial u/\partial t$ which give the rates of change of the properties at a particular spatial point. Computing the properties of the fluid requires a grid of fixed points in space. Equations 6.1 - 6.3 are then solved numerically at each point. Traditionally, computational models of fluid flow are solved using this method.

Alternatively, in the Lagrangian formulation, we adopt a reference frame comoving with the fluid. We then compute the Lagrangian derivatives, $d\rho/dt$, $\rho d\mathbf{v}/dt$ and du/dt which give the rates of change of the properties of a particular fluid element. Computing the properties of the fluid numerically requires dividing the fluid into a number of small mass elements and solving Equations 6.1 - 6.3 for each element. Both schemes have advantages and disadvantages depending on the exact physics and initial conditions used.

6.2 Basic principles of Smoothed Particle Hydrodynamics

Smoothed particle hydrodynamics (SPH) is a numerical method used to solve the Lagrangian equations of hydrodynamics. It was invented independently by Lucy (1977) and Gingold & Monaghan (1977) to simulate non-axisymmetric self-gravitating hydrodynamical problems in astrophysics. It is particularly well-suited to gravitational collapse problems such as star formation. The principles of SPH are reviewed by Monaghan (1992).

In SPH, the fluid is represented by N particles, each with mass m . The properties of each particle such as its mass are distributed (i.e. ‘smoothed’) over a finite volume, so the fluid is still continuous over all regions of space despite being represented by a finite number of discrete points. Particles are smoothed over a typical length scale, h , which is called the *smoothing length*, using a weighting function $W(\mathbf{r}, h)$, called the *smoothing kernel*. The smoothed value of any physical property A at position \mathbf{r} is a weighted average over the surrounding fluid, and is calculated by integrating A convolved with the smoothing kernel, i.e.

$$\langle A(\mathbf{r}) \rangle = \int_V A(\mathbf{r}') W(\mathbf{r} - \mathbf{r}', h) d^3\mathbf{r}'. \quad (6.4)$$

We are free to choose any kernel function provided it satisfies the following two conditions.

First, the smoothing kernel must be normalised,

$$\int_{\mathcal{V}} W(\mathbf{r} - \mathbf{r}', h) d^3\mathbf{r}' = 1. \quad (6.5)$$

Secondly, the kernel function must tend to a Dirac delta function as the smoothing length tends to zero, i.e.

$$\lim_{h \rightarrow 0} W(\mathbf{r} - \mathbf{r}', h) = \delta(\mathbf{r} - \mathbf{r}'). \quad (6.6)$$

This is equivalent to saying that as the kernel width becomes infinitesimally small, the smoothed property $\langle A \rangle$ at a point \mathbf{r} must be equal to the true value of A at point \mathbf{r} . This is apparent if W is replaced by the Dirac delta function in Equation 6.4, where we obtain $\langle A(\mathbf{r}) \rangle = A(\mathbf{r})$ (This is the definition of the Dirac delta function).

In general, the kernel function is not a delta function, and this causes a difference between the smoothed value, $\langle A(\mathbf{r}) \rangle$ and the actual value, $A(\mathbf{r})$. The form of the kernel function and the size of the smoothing length are important in determining this error. This can be seen if we first expand $A(\mathbf{r}')$ as a Taylor series about \mathbf{r} , i.e.

$$A(\mathbf{r}') = A(\mathbf{r}) + \frac{\partial A}{\partial r_\alpha}(\mathbf{r})\Delta r_\alpha + \frac{1}{2} \frac{\partial^2 A}{\partial r_\beta \partial r_\gamma}(\mathbf{r})\Delta r_\beta \Delta r_\gamma + O(\Delta \mathbf{r}^3), \quad (6.7)$$

where $\Delta \mathbf{r} \equiv \mathbf{r}' - \mathbf{r}$; α, β and γ are component suffices, and repeated suffices imply summation. We then substitute for $A(\mathbf{r}')$ in Equation 6.4 to evaluate the smoothed average $\langle A(\mathbf{r}) \rangle$, i.e.

$$\begin{aligned} \langle A(\mathbf{r}) \rangle &= A(\mathbf{r}) \int_{\mathcal{V}} W(\mathbf{r} - \mathbf{r}', h) d^3\mathbf{r}' + \frac{\partial A}{\partial r_\alpha}(\mathbf{r}) \int_{\mathcal{V}} \Delta r_\alpha W(\mathbf{r} - \mathbf{r}', h) d^3\mathbf{r}' \\ &\quad + \frac{1}{2} \frac{\partial^2 A}{\partial r_\beta \partial r_\gamma}(\mathbf{r}) \int_{\mathcal{V}} \Delta r_\beta \Delta r_\gamma W(\mathbf{r} - \mathbf{r}', h) d^3\mathbf{r}' + O(\Delta \mathbf{r}^3). \end{aligned} \quad (6.8)$$

The first term in Equation 6.8 is simply equal to $A(\mathbf{r})$ since the first integral is equal to unity from Equation 6.5. If the kernel is an even function (i.e. if $W(\mathbf{r} - \mathbf{r}') = W(\mathbf{r}' - \mathbf{r})$), then the second integrand is antisymmetric in space around \mathbf{r} . Thus if we integrate over all space, the second term becomes zero, as does every odd term in the Taylor series. Thus the dominant error term when evaluating $\langle A(\mathbf{r}) \rangle$ is of second order (e.g. Monaghan 1992, Price 2004; PhD thesis).

In SPH, the continuum of the gas is replaced by a series of discrete particles (e.g. Figure 6.1), and we replace the integral in Equation 6.4 with a summation. By convention, the smoothed

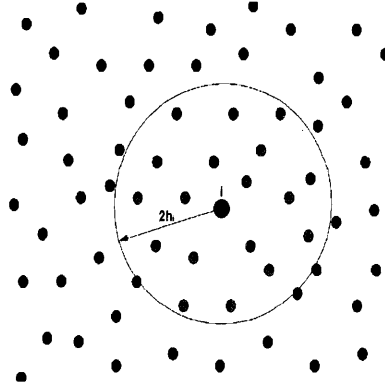


Figure 6.1: Calculating properties in SPH. The properties of particle i are calculated as a weighted average of the properties of its neighbours, i.e. all particles within a distance $2h_i$ (the grey particles).

value of A at the position of particle i is then

$$\langle A \rangle_i = \sum_{j=1}^N m_j \frac{A_j}{\rho_j} W(\mathbf{r}_i - \mathbf{r}_j, h). \quad (6.9)$$

where j is the particle index, m_j is the particle's mass, ρ_j is the density at the position of particle j , and A_j is the physical parameter A of particle j . Equation 6.9 is the fundamental equation for calculating all quantities in SPH. Using Equation 6.9 introduces additional errors into evaluating $\langle A \rangle$ such as discretisation noise (e.g. poisson noise).

6.3 Calculating vector properties in SPH

It is also possible to calculate vector quantities using this formulation. The gradient of any scalar property A can be estimated using

$$\langle \nabla A(\mathbf{r}) \rangle = \int_V A(\mathbf{r}') \nabla W(\mathbf{r} - \mathbf{r}', h) d^3 \mathbf{r}' \quad (6.10)$$

or using the summation approximation,

$$\langle \nabla A \rangle_i = \sum_{j=1}^N m_j \frac{A_j}{\rho_j} \nabla W(\mathbf{r}_i - \mathbf{r}_j, h). \quad (6.11)$$

This formulation has the advantage that we don't need to calculate individual values of ∇A_j , which would require setting up a grid and therefore additional computational expense. Instead, we use the gradient of the smoothing kernel, ∇W , which can be a well-known analytical function

and thus easily calculated.

This approximation can be improved by expanding Equation 6.11 as a Taylor series and subtracting the first order error terms. This gives

$$\langle \nabla A \rangle_i = \sum_{j=1}^N m_j \frac{(A_j - A_i)}{\rho_j} \nabla W(\mathbf{r}_i - \mathbf{r}_j, h). \quad (6.12)$$

Another useful alternative is to use the vector identity $\nabla \left(\frac{A}{\rho} \right) = \frac{\nabla A}{\rho} - \frac{A}{\rho^2} \nabla \rho$. Rearranging and using Equation 6.10, we obtain

$$\langle \nabla A \rangle_i = \rho_i \sum_{j=1}^N m_j \left(\frac{A_i}{\rho_i^2} + \frac{A_j}{\rho_j^2} \right) \nabla W(\mathbf{r}_i - \mathbf{r}_j, h). \quad (6.13)$$

Equation 6.4 can also be used to calculate the divergence and curl of any vector property \mathbf{A} . Substituting $\nabla \cdot \mathbf{A}$ and $\nabla \times \mathbf{A}$ into Equation 6.4 gives

$$\langle \nabla \cdot \mathbf{A}(\mathbf{r}) \rangle = \int_V \mathbf{A}(\mathbf{r}') \cdot \nabla W(\mathbf{r} - \mathbf{r}', h) d^3 \mathbf{r}', \quad (6.14)$$

$$\langle \nabla \times \mathbf{A}(\mathbf{r}) \rangle = \int_V \mathbf{A}(\mathbf{r}') \times \nabla W(\mathbf{r} - \mathbf{r}', h) d^3 \mathbf{r}', \quad (6.15)$$

or using the summation approximation,

$$\langle \nabla \cdot \mathbf{A} \rangle_i = \sum_{j=1}^N m_j \frac{\mathbf{A}_j}{\rho_j} \cdot \nabla W(\mathbf{r}_i - \mathbf{r}_j, h), \quad (6.16)$$

$$\langle \nabla \times \mathbf{A} \rangle_i = \sum_{j=1}^N m_j \frac{\mathbf{A}_j}{\rho_j} \times \nabla W(\mathbf{r}_i - \mathbf{r}_j, h). \quad (6.17)$$

6.4 The kernel function

Various kernels have been used since the conception of SPH, for example, the Gaussian kernel (Gingold & Monaghan 1977), the exponential kernel (Wood 1981), and the super-gaussian kernel (Gingold & Monaghan 1982). The most widely used kernel is the M4 spline kernel



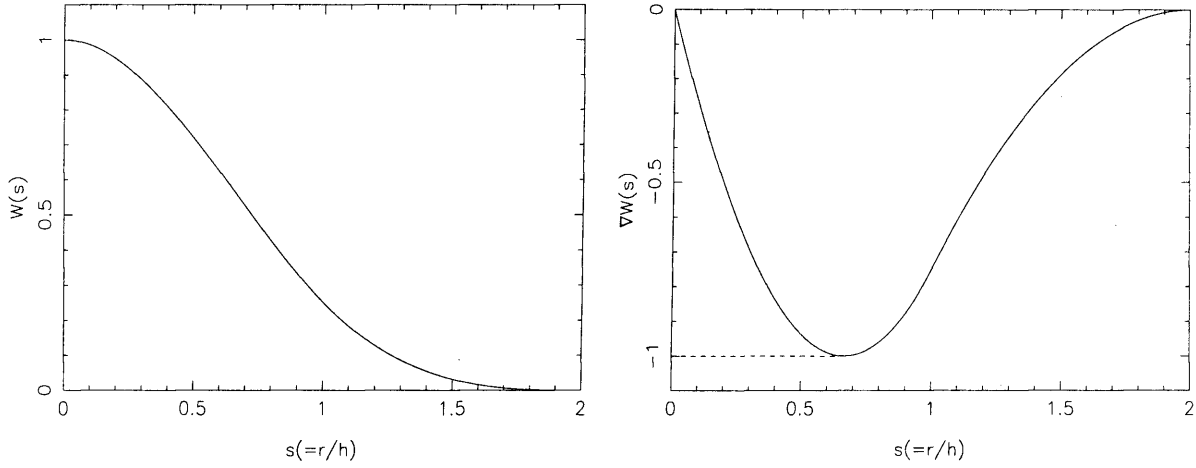


Figure 6.2: (a) The unnormalised M4-kernel function, as given by Equation 6.18 (b) The unnormalised kernel gradient function. Plotted are both the exact derivative of the M4-kernel (Equation 6.19; solid line), and the modified derivative as proposed by Thomas & Couchman (1992; Equation 6.20; dashed line)

(Monaghan & Lattanzio 1985),

$$W(s) = \frac{1}{\pi h^3} \begin{cases} 1 - \frac{3}{2}s^2 + \frac{3}{4}s^3 & \text{if } 0 \leq s \leq 1; \\ \frac{1}{4}(2-s)^3 & \text{if } 1 \leq s \leq 2; \\ 0 & \text{if } s > 2. \end{cases} \quad (6.18)$$

where $s \equiv r/h$ (Figure 6.18a). This kernel is spherically symmetric and only a function of r/h . The first spatial derivative (i.e. dW/dr) of the M4 kernel is

$$\frac{dW}{dr}(s) = -\frac{1}{\pi h^4} \begin{cases} 3s - \frac{9}{4}s^2 & \text{if } 0 \leq s \leq 1; \\ \frac{3}{4}(2-s)^2 & \text{if } 1 \leq s \leq 2; \\ 0 & \text{if } s > 2. \end{cases} \quad (6.19)$$

This particular kernel has a number of desirable features which have made it popular. Firstly, the kernel function only has non-zero values out to a radius of $2h$, thus it cannot interact with particles further than $2h$ away (Figure 6.2a). This is an improvement on some kernels (For example, the Gaussian kernel has infinite extent, and this means every particle interacts with every other particle in the simulation, which is unphysical since microscopically, gas particles interact with and therefore exert pressure forces on particles that are on average within one mean-free path). Secondly, the first derivative (Figure 6.2b) and second derivatives of this kernel are continuous everywhere which means calculating particle properties is less sensitive to particle noise.

Despite its advantages, a slightly modified kernel is often used in SPH codes with self-

gravity. The kernel function in Equation 6.18 is used, but with a modified 1st derivative (Thomas & Couchman 1992; see Figure 6.2b),

$$\frac{dW}{dr}(s) = -\frac{1}{\pi h^4} \begin{cases} 1 & \text{if } 0 \leq s \leq \frac{2}{3}; \\ 3s - \frac{9}{4}s^2 & \text{if } \frac{2}{3} \leq s \leq 1; \\ \frac{3}{4}(2-s)^2 & \text{if } 1 \leq s \leq 2; \\ 0 & \text{if } s > 2. \end{cases} \quad (6.20)$$

6.5 The smoothing length

Choosing an appropriate smoothing length is important since h controls both the resolution and accuracy of SPH. In general, any features smaller than the smoothing length are diluted by the smoothing and are lost. Thus the smoothing length is effectively the resolution length in SPH. Since SPH uses particles rather than a continuum, noise affects the accuracy of calculated properties. A larger smoothing length means a particle has more ‘neighbours’ (i.e. particles within the smoothing kernel) thereby reducing noise. As more particles are used, the summation (Equation 6.9) becomes a better approximation to the integral (Equation 6.4). Choosing a suitable value for h thus becomes a compromise between having enough neighbours (to reduce poisson noise and increase accuracy) and having enough resolution (to resolve density structures).

A satisfactory approach is to allow the particles to have individual smoothing lengths, rather than a single global smoothing length. We choose each value of h such that all the particles have approximately a constant number of neighbours, N_{NEIB} . This approach means the fractional error incurred in calculating the various properties is about the same for all particles. Also the resolution length ($\sim h$) becomes smaller for denser regions where more resolution is needed. Most SPH simulations use $N_{\text{NEIB}} \sim 50$.

Using individual smoothing lengths can cause ambiguity as to whether a particle is another’s neighbour or not. Two approaches are possible in choosing neighbours, the ‘gather’ approach and the ‘scatter’ approach. Consider a particle i with a potential neighbour, particle j . In the ‘gather’ approach, particle j is a neighbour of particle i if the position of j lies within the smoothing kernel of i , i.e. $r_{ij} < 2h_i$. Alternatively in the scatter approach, particle j is a neighbour of particle i if the smoothing kernel of particle j encompasses particle i , i.e. $r_{ij} < 2h_j$. If a constant smoothing length is employed, both interpretations are equivalent. However, if a variable smoothing length is used as suggested above, it is possible for particle i to be a neighbour of particle j , but for particle j not to be a neighbour of particle i , or vice versa. This is unsatisfactory for particle-pair hydrodynamical interactions since Newton’s third law would be violated. To ensure all particle pairs are always each others neighbours, the criterion for

particles i and j to be neighbours is that their distance apart is less than twice their average smoothing length i.e. $r_{ij} < 2h_{ij} = 2\left(\frac{h_i+h_j}{2}\right) = h_i + h_j$.

6.6 The hydrodynamical equations in SPH

In the SPH formulation, Equations 6.2 and 6.3 must be converted into their 'smoothed' forms. An SPH equivalent of the continuity equation (Equation 6.1) is unnecessary since SPH automatically conserves mass through its particle nature, although using Equation 6.1 can be useful in certain situations. However, it is necessary to calculate the density of all the particles before computing other quantities. Using Equation 6.9 and setting $A = \rho$, the density of particle i is given by

$$\rho_i = \sum_{j=1}^N m_j W(\mathbf{r}_i - \mathbf{r}_j, h_{ij}). \quad (6.21)$$

For the momentum and energy equations, it is desirable to have equations in 'symmetrised' form, i.e. so that particle pair forces are equal and opposite and momentum and energy are conserved. In order to calculate the pressure gradient (as required in Equation 6.2), we choose to use Equation 6.13 which is symmetrized, rather than Equations 6.11 and 6.12, and substitute $A = P$. A symmetrised form of the energy equation can also be formed. The SPH versions of the hydrodynamical equations become

$$\frac{d\mathbf{v}_i}{dt} = - \sum_{j=1}^N m_j \left(\frac{P_i}{\rho_i^2} + \frac{P_j}{\rho_j^2} \right) \nabla_i W(\mathbf{r}_i - \mathbf{r}_j, h_{ij}) \quad (6.22)$$

$$\frac{du_i}{dt} = - \frac{1}{2} \sum_{j=1}^N m_j \left(\frac{P_i}{\rho_i^2} + \frac{P_j}{\rho_j^2} \right) (\mathbf{v}_i - \mathbf{v}_j) \cdot \nabla_i W(\mathbf{r}_i - \mathbf{r}_j, h_{ij}) \quad (6.23)$$

6.7 Artificial Viscosity

SPH requires artificial viscosity to ensure that shocks are captured adequately. Without any viscous term, post-shock oscillations may occur rather than a well defined shock front. Also with high Mach-number converging flows, particle streams may penetrate each other and pass through the shock, rather than decelerating at the shock front. An extra term involving artificial

viscosity is added to Equations 6.22 and 6.23 in SPH

$$\frac{d\mathbf{v}_i}{dt} = - \sum_{j=1}^N m_j \left(\frac{P_i}{\rho_j^2} + \frac{P_j}{\rho_i^2} + \Pi_{ij} \right) \nabla_i W(\mathbf{r}_i - \mathbf{r}_j, h_{ij}) \quad (6.24)$$

$$\frac{du_i}{dt} = - \frac{1}{2} \sum_{j=1}^N m_j \left(\frac{P_i}{\rho_i^2} + \frac{P_j}{\rho_j^2} + \Pi_{ij} \right) (\mathbf{v}_i - \mathbf{v}_j) \cdot \nabla_i W(\mathbf{r}_i - \mathbf{r}_j, h_{ij}) \quad (6.25)$$

where

$$\Pi_{ij} = \begin{cases} \frac{-\alpha c_{ij} \mu_{ij} + \beta \mu_{ij}^2}{\rho_{ij}} & \mathbf{v}_{ij} \cdot \mathbf{r}_{ij} < 0 \\ 0 & \mathbf{v}_{ij} \cdot \mathbf{r}_{ij} > 0 \end{cases} \quad (6.26)$$

and

$$\mu_{ij} = \frac{h_{ij} \mathbf{v}_{ij} \cdot \mathbf{r}_{ij}}{\mathbf{r}_{ij}^2 + \eta^2}. \quad (6.27)$$

This contains two terms ($-\alpha c_{ij} \mu_{ij} / \rho_{ij}$ and $\beta \mu_{ij}^2 / \rho_{ij}$) which handle low- and high-Mach number shocks respectively. Suggested values to ensure shocks are captured well are $\alpha = 1$, $\beta = 2$ and $\eta^2 = 0.01 h^2$ (Monaghan 1992). This viscosity term is only non-zero for approaching particle pairs (as required for shocks) and vanishes for receding particle pairs. It produces good results for planar shocks (e.g. Chapter 7), but also generates artificial shear viscosity, which can transport angular momentum unphysically. This is important in simulations which involve shearing motions for example circumstellar discs. Alternative forms of artificial viscosity have been proposed with the aim of reducing the amount of shear viscosity, but maintaining a high level of bulk viscosity in order to capture shocks (see below).

6.7.1 The Balsara switch

Balsara (1995) suggested a switch designed to turn on viscosity for converging flows (such as shocks) and to turn off viscosity for shear flows. Balsara used the divergence and the curl of the velocity as indicators of local inflow or shear. Using Equations 6.16 and 6.17 and $\mathbf{A} = \mathbf{v}$, then

$$\langle \nabla \cdot \mathbf{v} \rangle_i = - \frac{1}{\rho_i} \sum_{j=1}^N m_j \mathbf{v}_{ij} \cdot \nabla W(\mathbf{r} - \mathbf{r}_j, h), \quad (6.28)$$

$$\langle \nabla \times \mathbf{v} \rangle_i = - \frac{1}{\rho_i} \sum_{j=1}^N m_j \mathbf{v}_{ij} \times \nabla W(\mathbf{r} - \mathbf{r}_j, h). \quad (6.29)$$

For each particle, we define a dimensionless factor, f_i which represents the fraction of local

motion that is inflow,

$$f_i = \frac{|\nabla \cdot \mathbf{v}|_i}{|\nabla \cdot \mathbf{v}|_i + |\nabla \times \mathbf{v}|_i + 0.0001 \frac{c_i}{h_i}}. \quad (6.30)$$

The viscosity term for each particle pair interaction, Π_{ij} , is multiplied by $f_{ij} = \frac{1}{2}(f_i + f_j)$. For large values of local shear, $|\nabla \times \mathbf{v}| \gg |\nabla \cdot \mathbf{v}|$, and $f_{ij} \ll 1$ thereby effectively switching off the viscosity term. For large values of local inflow, then $|\nabla \cdot \mathbf{v}| \gg |\nabla \times \mathbf{v}|$ and $f_{ij} \rightarrow 1$, thereby turning the viscosity fully on.

6.7.2 Time-dependent viscosity

Morris & Monaghan (1997) introduced another approach to the problem of large shear viscosity. They suggested each particle has its own viscosity parameter, α_i , instead of a global value of $\alpha = 1$. For each particle, α_i evolves according to the differential equation

$$\frac{d\alpha_i}{dt} = -\frac{\alpha_i - \alpha^*}{\tau_i} + S_i \quad (6.31)$$

where α^* is the minimum and initial value of α , S_i is the source term and τ is the e-folding time. The source term, S_i controls the rate of increase of α_i . Following the prescription of Rosswog et al. (2000), we use the source term

$$S_i = \max(-\langle \nabla \cdot \mathbf{v} \rangle_i, 0)(\alpha_{\text{MAX}} - \alpha_i) \quad (6.32)$$

where α_{MAX} is the maximum value of α . α_i will therefore increase in regions of strong inflow up to a steady state value of α_{MAX} . The first term in Equation 6.31 is the decay term. In the absence of any source term, the value of α decays exponentially towards α^* on an e-folding time τ . τ is chosen to be of order the sound crossing time over a smoothing length, i.e. $\tau_i = h_i/(C c_i)$. Morris & Monaghan (1997) suggest $C = 0.2$.

6.8 Gravity in SPH

In self-gravitating fluids, an extra term must be added to the momentum equation (Equation 6.2), \mathbf{a}_{grav} , which is the total gravitational acceleration due to all other particles, i.e.

$$\mathbf{a}_{grav,i} = - \sum_{j=1, j \neq i}^N \frac{G m_j (\mathbf{r}_i - \mathbf{r}_j)}{|\mathbf{r}_i - \mathbf{r}_j|^3}. \quad (6.33)$$

This is the same as the gravitational N-body problem, as discussed in Chapter 3. Since the SPH equations give 2nd-order accuracy, there is little to be gained from using a 4th-order integration

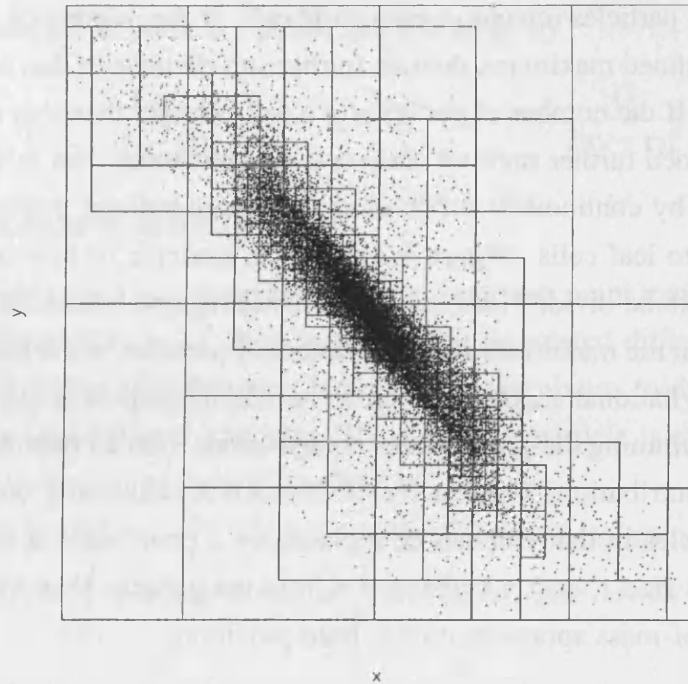


Figure 6.3: An example of how a tree organises the spatial domain into cells. In regions of low particle density, the size of a cell is relatively large, whereas in regions with high particle density, the cell size is small in order to populate the leaf cells with at most a few particles. Note that this is a 3-D simulation and so the cells also extend into the z -dimension

scheme or techniques such as regularisation for gravity with SPH. SPH codes calculate the total gravitational acceleration using kernel-softened gravity (when $r_{ij} < 2h_{ij}$) and tree-gravity (for all other particles).

6.8.1 Tree-gravity

SPH codes commonly use the Barnes-Hut octal tree (Barnes & Hut 1986) to calculate the gravitational acceleration efficiently (as opposed to N -body codes which use the Ahmad-Cohen (1973) scheme). Using a tree becomes more efficient than direct summation of Equation 6.33 for a sufficiently large number of particles ($N \gtrsim 4000$). The total computational cost of calculating \mathbf{a}_{grav} reduces from $O(N^2)$ calculations to $O(N \log N)$ calculations.

Trees are used to divide the computational domain into smaller spatial units in order to ease the computational expense of calculating \mathbf{a}_{grav} . They also record which particles are in a selected region of space and therefore can be used in identifying neighbours.

A tree is created by continuously dividing the computational domain into smaller and smaller sections. The entire computational domain forms the *root cell* of the tree. The root cell is divided into 8 octants which form the child cells. Everytime a cell is divided, a check is made

to see how many particles remain in each child cell. If the number of particles in a cell is less than some pre-defined maximum, then no further sub-division of that cell is required; these are called leaf cells. If the number of particles in a cell is larger than this maximum, then this cell must be sub-divided further until no child cell contains more than this maximum. The tree is thus constructed by continuously subdividing the computational domain in space until all the particles belong to leaf cells. Figure 6.3 shows an example of how a region filled with SPH particles (dots) can be divided into cells. The dense regions have smaller cell sizes in order to have no more than the maximum allowed number of particles in the leaf cells.

The total gravitational acceleration on an individual particle is calculated by 'walking' the tree. Instead of summing the gravitational contributions from all particles (as in Equation 6.33), we look at the contributions from each cell. If a cell is sufficiently far away from the particle, then all the particles in that cell can be replaced by a point mass at the centre-of-mass of the cell. If a cell has size s , and is a distance d from the particle, then the cell subtends an angle s/d . The centre-of-mass approximation is used providing

$$\frac{s}{d} \leq \theta_{\text{MAX}} \quad (6.34)$$

where θ_{MAX} is the maximum allowed angular size of a cell. If the cell does not meet this criterion, then it must be opened and the child cells must be traversed. This process is repeated until either a child cell satisfies Equation 6.34 or we reach a leaf cell which has no further child cells.

We can improve on the center-of-mass approximation by adding higher-order correction terms that take into account the distribution of mass within a cell (e.g. Pfalzner & Gibbon 1996). We calculate the quadrupole moment of the cell using

$$Q_{ab,k} = \sum_{p=1}^N m_p (3x_{a,p} x_{b,p} - r_p^2 \delta_{ab}). \quad (6.35)$$

If a cell also contains child cells, then the quadrupole moment of the cell is given by

$$Q_{ab,k} = \sum_{p=1}^{N_{\text{child}}} Q_{ab,p} + \sum_{p=1}^N m_p (3x_{a,p} x_{b,p} - r_p^2 \delta_{ab}). \quad (6.36)$$

The gravitational acceleration of particle i due to cell k is thus

$$\mathbf{a}_{\text{grav},ik} = -Gm_k \frac{(\mathbf{r}_i - \mathbf{r}_k)}{|\mathbf{r}_i - \mathbf{r}_k|^3} + G \frac{\mathbf{Q}_k \cdot (\mathbf{r}_i - \mathbf{r}_k)}{|\mathbf{r}_i - \mathbf{r}_k|^5} - \frac{5G}{2} \frac{((\mathbf{r}_i - \mathbf{r}_k) \cdot \mathbf{Q}_k \cdot (\mathbf{r}_i - \mathbf{r}_k)) (\mathbf{r}_i - \mathbf{r}_k)}{|\mathbf{r}_i - \mathbf{r}_k|^7}. \quad (6.37)$$

The gravitational potential of particle j due to cell k is given by

$$\phi_{ik} = -\frac{Gm_k}{|\mathbf{r}_i - \mathbf{r}_k|} - ((\mathbf{r}_i - \mathbf{r}_k) \cdot \mathbf{Q}_k \cdot (\mathbf{r}_i - \mathbf{r}_k)) \frac{G}{2|\mathbf{r}_i - \mathbf{r}_k|^5}. \quad (6.38)$$

6.8.2 Kernel-softened gravity

For interactions where $r_{ij} > 2h_{ij}$, the particles can be treated as point masses. For particles that are also SPH neighbours (i.e. $r_{ij} < 2h_{ij}$), gravity must be treated differently to take account of smoothing. Specifically, only the mass interior to r contributes to the gravitational force, according to Gauss's Gravitational Theorem. The mass of a particle is extended over a sphere of radius $2h$. The mass interior to radius r is given by

$$M(< r) = \int_0^r 4\pi r'^2 \rho(r') dr' = m \int_0^r 4\pi r'^2 W(r', h) dr' = mW^*(r/h). \quad (6.39)$$

For the M4 spline kernel (Equation 6.18), $W^*(r, h)$ is

$$W^*(s) = \begin{cases} \frac{4}{3}s^3 - \frac{6}{5}s^5 + \frac{1}{2}s^6 & \text{if } 0 \leq s \leq 1; \\ \frac{8}{3}s^3 - 3s^4 + \frac{6}{5}s^5 - \frac{1}{6}s^6 - \frac{1}{15} & \text{if } 1 \leq s \leq 2; \\ 1 & \text{if } s > 2. \end{cases} \quad (6.40)$$

where $s = r/h$. The gravitational acceleration of particle i due to particle j is thus

$$\mathbf{a}_{grav,ij} = -Gm_i W^*(r_{ij}, h_{ij}) \frac{\mathbf{r}_{ij}}{|\mathbf{r}_{ij}|^3} \quad (6.41)$$

The mutual gravitational potential energy of particles i and j can be evaluated using Equation 6.41,

$$\begin{aligned} \phi_{grav,ij} &= - \int_{\infty}^r \mathbf{a}_{grav,ij} \cdot d\mathbf{r}' \\ &= -Gm_i m_j \int_{\infty}^r \frac{W^*(r', h)}{r'^2} dr' \\ &= -\frac{Gm_i m_j}{r} \left[W^*(r, h) + r \int_{\infty}^r \frac{1}{r'} \frac{dW^*}{dr'} dr' \right] \\ &= -\frac{Gm_i m_j}{r_{ij}} \{ W^*(r_{ij}/h_{ij}) + W^{**}(r_{ij}/h_{ij}) \}. \end{aligned} \quad (6.42)$$

For the M4 spline kernel (Equation 6.18), $W^{**}(r, h)$ is

$$W^{**}(s) = \begin{cases} \frac{7}{5}s - 2s^3 + \frac{3}{2}s^5 - \frac{3}{5}s^6 & \text{if } 0 \leq s \leq 1; \\ \frac{s}{10}(2s+1)(2-s)^4 & \text{if } 1 \leq s \leq 2; \\ 0 & \text{if } s > 2. \end{cases} \quad (6.43)$$

6.8.3 Periodic gravity

Periodic boundary conditions are used to simulate an infinitely extended medium with a finite number of particles and finite computational domain. The boundaries are ‘wrapped around’ so that any particle that passes the extremity of the box will appear at the other side e.g. If the box size is L , then any particle that moves to a position $x = L + \epsilon$ is replaced at $x = \epsilon$, and similarly for the y and z dimensions.

In effect, the main box of particles is replicated as a 3-D array of boxes in space, and so particles near an extremity interact hydrodynamically with particles on the other side of the box. For an infinitely extending self-gravitating medium, an infinite number of replicas must be considered to correctly calculate the force.

One of the most efficient techniques used is the Ewald method (Hernquist et al. 1991; Klessen 1997). Consider a cubic box with sides of length L , and containing N particles. The total gravitational force exerted on particle i by particle j and all of its infinitely extending replicas is given by

$$\mathbf{F}_{ij} = Gm_i m_j \mathbf{f}(\mathbf{r}_{ij}) \quad (6.44)$$

where

$$\begin{aligned} \mathbf{f}(\mathbf{r}_{ij}) = & - \sum_{\mathbf{n}} \frac{\mathbf{r}_{ij} - \mathbf{n}L}{|\mathbf{r}_{ij} - \mathbf{n}L|^3} \left[\operatorname{erfc}(\alpha|\mathbf{r}_{ij} - \mathbf{n}L|) + \frac{2\alpha}{\sqrt{\pi}} |\mathbf{r}_{ij} - \mathbf{n}L| \exp(-\alpha^2|\mathbf{r}_{ij} - \mathbf{n}L|^2) \right] \\ & - \frac{1}{L^3} \sum_{\mathbf{k}} \frac{4\pi\mathbf{k}}{k^2} \exp\left(-\frac{k^2}{4\alpha^2}\right) \sin(\mathbf{k} \cdot \mathbf{r}_{ij}) \end{aligned} \quad (6.45)$$

Suggested values for good accuracy are $\alpha = 2/L$, $|\mathbf{r} - \mathbf{n}L| < 3.6L$ and $|k|^2 < 40\pi^2/L^2$ (Hernquist et al. 1991). For better accuracy and also to make full use of the tree structure in SPH, it is best to compute the correction force on the particle due to the replicas, i.e.

$$\mathbf{F}_{corr,ij} = Gm_i m_j \left(\mathbf{f}(\mathbf{r}_{ij}) + \frac{\mathbf{r}_{ij}}{|\mathbf{r}_{ij}|^3} \right) \quad (6.46)$$

and add this correction to the particle-pair force that is calculated using the tree. In practice, we set-up a 3 dimensional grid where the correction forces, $\mathbf{f}(\mathbf{r}_{ij})$, are calculated and stored. When the gravitational force between two particles (or a particle and a cell) is being calculated,

the correction force is obtained by interpolating from this grid. We note that no quadrupole moment correction term is added; this force is $\propto r^{-4}$ and thus quickly becomes negligible for distant particles.

6.9 Integration scheme

In SPH, the hydrodynamical equations are usually solved using a second-order Runge-Kutta scheme, although alternative schemes such as predictor-corrector methods are also used. Since SPH computes hydrodynamical forces to only second-order accuracy in space, there is little advantage in using better than a second-order integration scheme.

First, we must calculate appropriate timesteps for each particle:

$$\Delta t_i = \gamma \text{MIN} \left\{ \frac{h_i}{|\mathbf{v}_i| + c_i}, \left(\frac{h_i}{|\mathbf{a}_i| + \eta} \right)^{-\frac{1}{2}}, \frac{h_i}{c_i + 1.2\alpha c_i + 1.2\beta \text{MAX}\{\mu\}} \right\} \quad (6.47)$$

The first term inside the bracket is the Courant condition; the second ensures that the speed does not change significantly between timesteps; the third is a modified Courant condition that also accounts for artificial viscosity. SPH codes use multiple particle timesteps in exactly the same way as N-body codes do. This is discussed in full in Section 3.4.

Once the timesteps are computed, we can proceed with solving the hydrodynamical equations. First, the accelerations are computed at the beginning of the timestep, i.e. $\mathbf{a}(t_0)$. Then the positions, velocities and internal energies at the half timestep are computed, i.e.

$$\mathbf{r}(t_0 + \frac{1}{2}\Delta t) = \mathbf{r}(t_0) + \frac{1}{2}\mathbf{v}(t_0)\Delta t, \quad (6.48)$$

$$\mathbf{v}(t_0 + \frac{1}{2}\Delta t) = \mathbf{v}(t_0) + \frac{1}{2}\mathbf{a}(t_0)\Delta t, \quad (6.49)$$

$$u(t_0 + \frac{1}{2}\Delta t) = u(t_0) + \frac{1}{2}\frac{du}{dt}(t_0)\Delta t. \quad (6.50)$$

Next we recompute the acceleration and heating rate with the half timestep positions and velocities, i.e. $\mathbf{a}(t_0 + \frac{1}{2}\Delta t)$ and $\frac{du}{dt}(t_0 + \frac{1}{2}\Delta t)$. Finally using the half timestep velocities, accelerations and heating rates, we compute the full timestep positions, velocities and internal energies, i.e.

$$\mathbf{r}(t_0 + \Delta t) = \mathbf{r}(t_0) + \mathbf{v}(t_0 + \frac{1}{2}\Delta t)\Delta t, \quad (6.51)$$

$$\mathbf{v}(t_0 + \Delta t) = \mathbf{v}(t_0) + \mathbf{a}(t_0 + \frac{1}{2}\Delta t)\Delta t, \quad (6.52)$$

$$u(t_0 + \Delta t) = u(t_0) + \frac{du}{dt}(t_0 + \frac{1}{2}\Delta t)\Delta t. \quad (6.53)$$

6.10 Simulating star formation using SPH

We will be using SPH to investigate problems in star formation. SPH is well-suited to simulating problems involving gravitational collapse. Its Lagrangian nature allows SPH to follow simulations with large density contrasts without the need for complicated regridding algorithms such as in AMR codes. Despite its suitability, there are still some issues relating specifically to star formation which must be considered. We also discuss some extra features which can be incorporated into SPH to improve its efficiency in star formation simulations.

6.10.1 The Equation of State

Any true simulation of star formation should include a treatment of the radiation transport in a star forming region. Radiation sources include background interstellar radiation (including the CMB), emission from newly born young stars and re-emission/scattering of radiation from molecular cloud material. Modelling radiation transport can however be computationally very expensive and can increase the simulation run-time considerably.

Fortunately, this problem can be simplified avoiding the need for including radiation transport. Molecular gas is optically thin at low densities. The gas has an equilibrium temperature of about 10K, which is set by the background radiation and the emission properties of the gas and dust. For a large range of densities, the gas is approximately isothermal, i.e. $T \approx \text{const} \approx 10\text{K}$. As a clump of gas begins to collapse under its self-gravity, gravitational potential energy is converted into kinetic and thermal energy. When the gas is optically thin, the extra thermal energy is radiated away rapidly so that the clump remains at 10K. As the density of the gas increases, it eventually becomes optically thick. The gas can no longer radiate freely, and therefore becomes approximately adiabatic. This is known as the opacity limit (e.g. Rees 1976). The density at which a fragment becomes adiabatic depends on its mass. However it can be difficult to measure the mass of a fragment using local variables. To simplify this, we assume the density where the gas switches from isothermal to adiabatic behaviour is that of a $1M_{\odot}$ fragment (i.e. $\rho_{AD} = 10^{-13}\text{g cm}^{-3}$). The pressure of the gas is given by the following barotropic equation of state

$$P = \rho c_0^2 \left[1 + \left(\frac{\rho}{\rho_{AD}} \right)^{2/3} \right]. \quad (6.54)$$

where c_0 is the isothermal sound speed, which for molecular gas at 10K is equal to 0.19 km s^{-1} .

6.10.2 Resolution criterion of SPH

A computer code must have an appropriate resolution limit to ensure the key physical processes are well resolved and thus modelled correctly. In star formation, arguably the most important physical process is the Jeans instability (e.g. Jeans 1929). There are no simple analytical tests of the Jeans instability which can be applied to test codes (however see Chapter 7 and Hubber, Goodwin & Whitworth 2006). Instead, both AMR and SPH codes have used the configuration first proposed by Boss & Bodenheimer (1979) to test the convergence and resolution of hydrodynamical codes. Burkert & Bodenheimer (1993) have subsequently proposed a variant of this configuration which provides a more stringent test of a code's limits. The initial configuration involves a spherical cloud with mass $M = 1M_{\odot}$, radius $R = 5 \times 10^{16}$ cm, uniform density $\rho = 3.8 \times 10^{-18}$ g cm $^{-3}$, uniform temperature $T = 10$ K and uniform angular speed $\Omega = 7.2 \times 10^{-13}$ rad s $^{-1}$ (hence ratio of thermal to gravitational energy $\alpha = 0.26$ and ratio of rotational to gravitational energy $\beta = 0.16$). An azimuthal $m = 2$ density perturbation with fractional amplitude $A = 0.1$ is then imposed and the subsequent isothermal evolution is followed. Truelove et al. (1997) have used this configuration to show that in AMR codes, fragmentation is only modelled correctly if the grid spacing, d , satisfies the condition $d < \lambda_J/4$ (where λ_J is the local Jeans length). If this condition (known as the Jeans condition) is not met in AMR simulations, artificial fragmentation can occur, i.e. clumps of gas which should be Jeans stable are liable to fragment due to numerical effects rather than physical effects.

Bate & Burkert (1997) have investigated the resolution limits of SPH using the same initial conditions as Burkert & Bodenheimer (1993). They suggest that the minimum mass that can be resolved by SPH is given by $M_{\text{MIN}} = \beta N_{\text{NEIB}} m$, where $N_{\text{NEIB}} \sim 50$ is the mean number of neighbours, β is a numerical factor of order unity and m is the mass of a single SPH particle (here assumed to be universal). The Jeans condition then requires that the Jeans mass be greater than the minimum resolvable mass, i.e.

$$M_{\text{MIN}} = \beta N_{\text{NEIB}} m \leq M_J = \frac{4\pi (\lambda_J/2)^3 \rho}{3} = \frac{\pi^{3/2} c^3}{6 G^{3/2} \rho^{1/2}}. \quad (6.55)$$

In terms of the Jeans length, λ_J , and the smoothing length, h , this condition becomes

$$\lambda_J \geq 4\beta^{1/3} h, \quad (6.56)$$

Bate & Burkert (1997) suggest $\beta = 2$ so that $\lambda_J \geq 5h$. In a subsequent paper (Bate, Bonnell & Bromm 2002a), this limit was revised down to $\beta = 1.5$.

6.10.3 Particle splitting

Particle splitting is a technique used to increase the number of particles “on the fly” (i.e. during a simulation) where and when more resolution is required. In relation to star formation, particle splitting can be used in simulations to ensure that the Jeans condition (Bate & Burkert 1997) is not violated. The Jeans mass is resolved if the density is less than the critical density, i.e.

$$\rho \leq \rho_{crit} = \left(\frac{\pi c^2}{G} \right)^3 \left(\frac{\pi}{12 N_{NEIB} m} \right)^2. \quad (6.57)$$

If the density approaches the critical density, particle splitting must be used to ensure the Jeans condition is obeyed.

The method of Kitsionas & Whitworth (2002) suggests splitting a particle into 13 new particles, each with mass $m_{new} = m_{old}/13$. The particles are arranged into an hexagonal close-packed array, i.e. 1 particle placed at the position of the old particle with the other 12 placed in an array around the central particle at a radius of $1.5h_{old}$. One problem with particle splitting is that the simulation now contains particles with different masses, which can cause numerical problems. Kitsionas & Whitworth (2002) show that good results are obtained if the smoothing lengths are chosen so that a particle’s smoothing kernel contains 50 times its own mass, rather than containing 50 particles.

6.10.4 Sink particles

In simulations of gravitational collapse such as star formation, the timestep becomes progressively shorter as the gas collapses to higher densities. At higher densities, the smoothing lengths become smaller to retain a constant number of neighbours. According to Equation 6.47, the timestep is reduced. Thus simulations slow down in terms of physical time elapsed. Bate et al. (1995) introduced the concept of sink particles into SPH simulations in order to alleviate this problem and allow simulations to be followed for longer.

Once a region of gas has reached a high-enough density ($\rho > 10^{-11} \text{g cm}^{-3}$), it is assumed gravity is dominant and the formation of a star is inevitable. The high-density region is therefore replaced by a sink particle. Any material that approaches the sink particle and falls within a certain radius (known as the sink radius) is assumed to be accreted by the sink particle and is absorbed. The mass of the absorbed particle is added to that of the sink and the particle is then removed from the simulation. As particles are accreted by the sink, the total number of particles in the simulation decreases and thus the number of force calculations per timestep is reduced. The sinks can interact gravitationally with all other particles in the simulation, but not hydrodynamically. This can cause some unphysical effects where particles near the

sink boundary are pushed into the sink by neighbouring gas particles because there is no gas pressure force to counter this. Particles are thus accreted more rapidly than they should be. More advanced sinks have been developed (Boyd 2003; PhD Thesis) which model the collapsing protostar more realistically so that the sink can also interact hydrodynamically with nearby particles.

6.10.5 Correcting for the self-gravity of an individual SPH particle

In standard self-gravitating SPH, the mutual gravitational force between two different SPH particles is included in the equation of motion, but the self-gravity of an individual particle is not. We can improve the performance of the code, particularly when the Jeans condition is only just satisfied, by correcting for the fact that part of the pressure of an SPH particle must be used to support the particle against its own self-gravity. To formulate this correction, consider particle i in isolation. If its mass is m_i and its sound speed is c_i , then

$$3 \int P dV = 3 m_i c_i^2, \quad (6.58)$$

where the integral is over the volume of the SPH particle. The Virial Theorem tells us that, if the particle is to be in hydrostatic equilibrium, this integral must equal the magnitude of its self-gravitational potential energy, which is

$$\begin{aligned} |\Omega| &= - \int_0^{M_{\text{tot}}} \frac{GM(< r) dM}{r(M)} \\ &= - \int_0^{M_{\text{tot}}} 4\pi G M(< r) \rho(r) r dr \\ &= - \frac{G m_i^2}{h_i} \int_{s=0}^{s=2} \int_{s'=0}^{s'=s} W(s') 4\pi s'^2 ds' \cdot W(s) 4\pi s ds \\ &= - \frac{G m_i^2}{h_i} [W^{***}(s)]_0^2. \end{aligned} \quad (6.59)$$

For the M4 kernel, $W^{***}(r, h)$ is

$$W^{***}(s) = \begin{cases} 16\left(\frac{s^5}{15} - \frac{4s^7}{35} + \frac{3s^8}{64} + \frac{s^9}{20} - \frac{33s^{10}}{800} + \frac{3s^{11}}{352}\right) & \text{if } 0 \leq s \leq 1; \\ 16\left(-\frac{s^2}{60} + \frac{s^3}{60} - \frac{s^4}{160} + \frac{107s^5}{400} - \frac{7s^6}{12} + \frac{11s^7}{20} \right. \\ \left. - \frac{91s^8}{320} + \frac{61s^9}{720} - \frac{11s^{10}}{800} + \frac{s^{11}}{1056} + \frac{2449}{9900} + \frac{6109}{23100}\right) & \text{if } 1 \leq s \leq 2. \end{cases} \quad (6.60)$$

Therefore, $W^{**}(2) = 0.505$. The total self-gravitating potential energy becomes

$$|\Omega| = 0.505 \frac{G m_i^2}{h_i}. \quad (6.61)$$

With reference to the virial theorem (Equation 6.58), the sound speed squared, c_i^2 , must be reduced by a factor f_i , i.e. $c_i^2 \rightarrow c_i^2(1 - f_i)$ to correct for the self-support, where

$$f_i = \frac{0.505 G m_i}{3 h_i c_i^2}. \quad (6.62)$$

Chapter 7

Tests of SPH

In this chapter, we will discuss a variety of tests performed on our SPH code, DRAGON. Firstly, we perform two different shock-tube tests, the isothermal Sod test and the colliding inflow test, which determine how well the various prescriptions of artificial viscosity presented in Chapter 6 capture shocks in SPH. Secondly, we perform a shear flow test to investigate the problem of shear viscosity in SPH. Thirdly, we perform a new test, called the Jeans test, which is designed to investigate how well SPH resolves gravitational fragmentation.

7.1 Introduction

Tests of a numerical code are required (a) to demonstrate that it can model the physics correctly, by reproducing the results of problems with known analytical solutions; and (b) to verify that the program has been correctly coded (i.e. test for programming bugs). We implement a variety of tests on the Cardiff star formation group SPH code DRAGON. These include

- The isothermal Sod test (hydrodynamics & artificial viscosity),
- The colliding isothermal flows (hydrodynamics & artificial viscosity),
- The shear-flow test (shear viscosity),
- The Jeans test (gravity & hydrodynamics - fragmentation) .

These tests have been chosen to investigate how well DRAGON models physical processes that are important in star formation, such as the formation of shocks and gravitational fragmentation. DRAGON uses a barotropic equation of state (Section 6.10.1) which avoids the need for computationally expensive radiative transfer calculations; the energy equation need not be solved either. For all the tests listed above, we use an isothermal equation of state.

7.2 The isothermal Sod test

The Sod test is one of the standard tests of a numerical scheme's ability to capture shocks correctly. Sod (1978) proposed setting up a 1-D Riemann shock tube consisting of two uniform density regions with differing properties (i.e. temperature, density and pressure) in contact. At the contact area between the two regions ($x = 0$), there is a pressure discontinuity. A shock forms and propagates into the lower-pressure region; also a rarefaction wave propagates into the higher-pressure region.

The initial conditions we use are described as follows. The density is given as

$$\rho(x, t = 0) = \begin{cases} 1.0 & x < 0.0, \\ 0.25 & x > 0.0. \end{cases} \quad (7.1)$$

The left-hand side (LHS) is constructed from a $2x1x1$ box containing 6112 particles. The right-hand side (RHS) is constructed from a $2x1x1$ box containing 1528 particles. The velocity is zero everywhere, i.e. $\mathbf{v}(x, y, z, t = 0) = \mathbf{0}$. An isothermal equation of state is used, i.e. $P = c_0^2 \rho$. We use dimensionless units setting $c_0 = 1.0$. We follow the simulation until a dimensionless time $T = 0.4$. The exact analytical solution can be compared to the numerical results and is shown as a solid line in all figures (Figures 7.1 - 7.8). The shock tube test is particularly important for testing how well the artificial viscosity prescription used captures shocks. We test three different prescriptions for viscosity; standard artificial viscosity (Section 6.7), artificial viscosity with the Balsara switch (Section 6.7.1) and time-dependent artificial viscosity (Section 6.7.2) using both $\alpha_{\text{MAX}} = 1.0$ and $\alpha_{\text{MAX}} = 2.0$. For reference, the average smoothing lengths in the high and low density regions are $\bar{h} = 0.07874$ and $\bar{h} = 0.125$ respectively.

7.2.1 Standard artificial viscosity

Figure 7.1 shows the results from the Sod test using standard artificial viscosity together with the analytical solution (solid line) after $T = 0.4$. The SPH results agree very well with the analytical solution, except in the regions around the discontinuity and the steep rarefaction wave. SPH cannot resolve features smaller than a length scale of $\approx 2h$. Therefore any discontinuities are broadened by at least this much. The velocity profile (Figure 7.1b) shows that the shock moves in the positive x direction (i.e. into the low-density region) with a flat profile over the shock, and a rarefaction wave propagating behind it. The SPH results reproduce these features, again with the effects of smoothing. There are signs of post-shock oscillations in the velocity profile over the flat region. However the artificial viscosity has damped these somewhat.

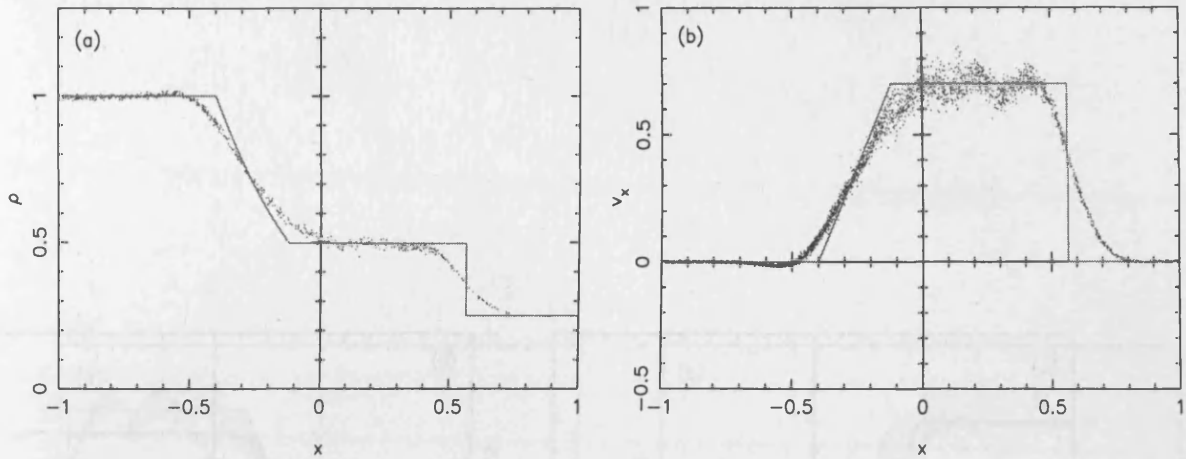


Figure 7.1: Results of the isothermal Sod test using standard artificial viscosity: (a) the density distribution after $T = 0.4$, and (b) the x-velocity distribution after $T = 0.4$.

7.2.2 Artificial viscosity with the Balsara switch

Figure 7.2 shows the results from the Sod test using artificial viscosity with the Balsara switch, after $T = 0.4$. The density profile (Figure 7.2a) agrees well with the analytical solution. The velocity profile (Figure 7.2b) is also very similar to the results when using standard artificial viscosity (Figure 7.1b). The post-shock oscillations in the velocity profile are a little more pronounced when using the Balsara switch, although again absent in the density profile. This form of viscosity is also sufficient to dampen these oscillations somewhat. Figure 7.2c shows the values of the Balsara factor, f_i (Equation 6.30), around the shock region after $T = 0.4$. f_i takes values between 0.9 and 1.0 in regions of strong divergence (i.e. the shock front and the rarefaction wave). Thus artificial viscosity is switched on only where it is needed (as the Balsara switch is designed to do). In all other regions where there is either zero or constant velocity, f_i is very noisy taking values between 0.0 and about 0.8. As there is no strong divergence or vorticity in these regions, the values of $|\nabla \cdot \mathbf{v}|$ and $|\nabla \times \mathbf{v}|$ calculated using Equations 6.28 and 6.29 are dominated by numerical noise, which are approximately of the same order of magnitude. Hence Equation 6.30 is also dominated by noise and results in a large range of values.

7.2.3 Time-dependent artificial viscosity

Figure 7.3 shows the results from the Sod test using time-dependent artificial viscosity with parameters $\alpha_{\text{MAX}} = 1.0$, $\alpha^* = 0.1$ and $C = 0.2$. Figure 7.3a shows that the density profile agrees well with the analytical solution, but not quite as well as when using standard viscosity or the Balsara switch. The density profile shows evidence of post-shock oscillations. This can also be seen in the velocity profile (Figure 7.3b). The post-shock oscillations are similar to those seen

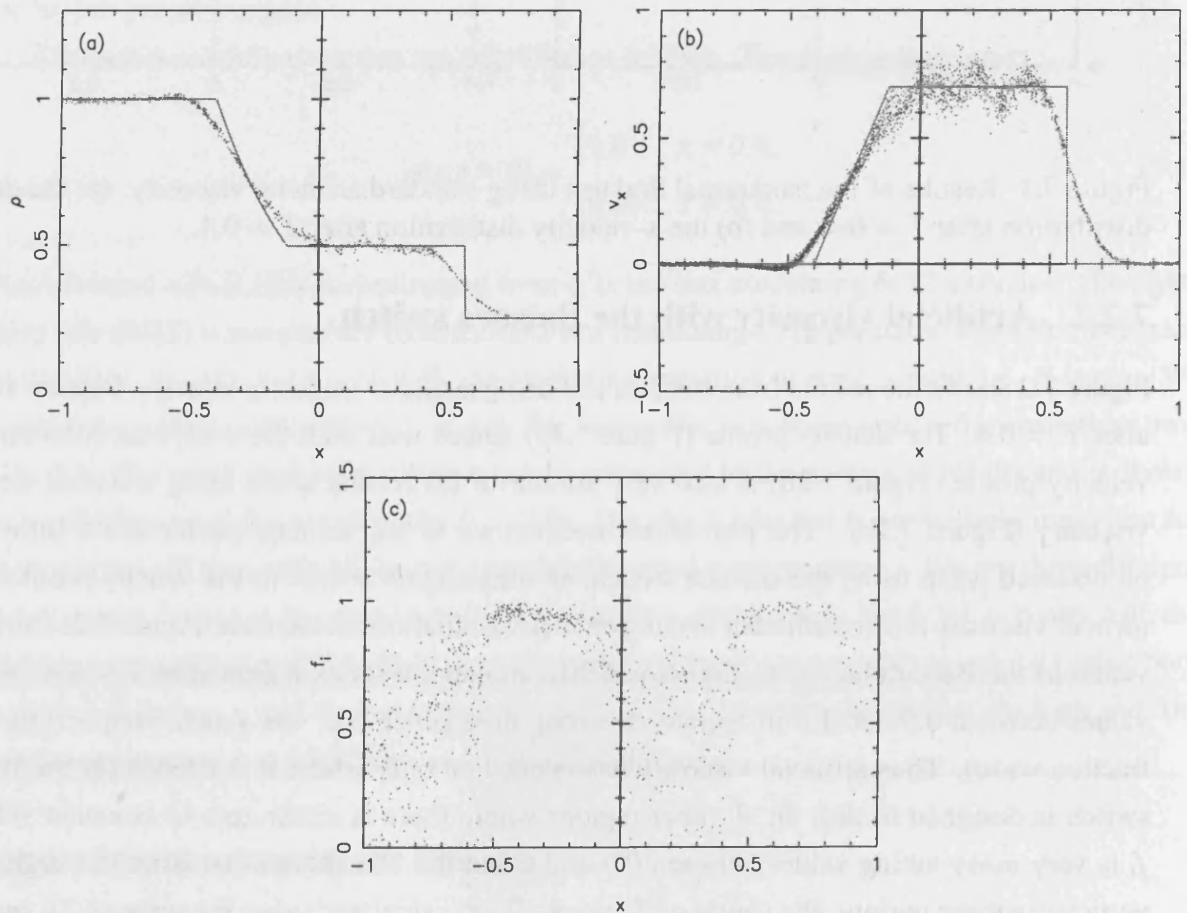


Figure 7.2: Results of the isothermal Sod test using artificial viscosity with the Balsara switch: (a) the density distribution after $T = 0.4$, (b) the x-velocity distribution after $T = 0.4$, and (c) the Balsara factor, f_b (Equation 6.30) over the shock region after $T = 0.4$.

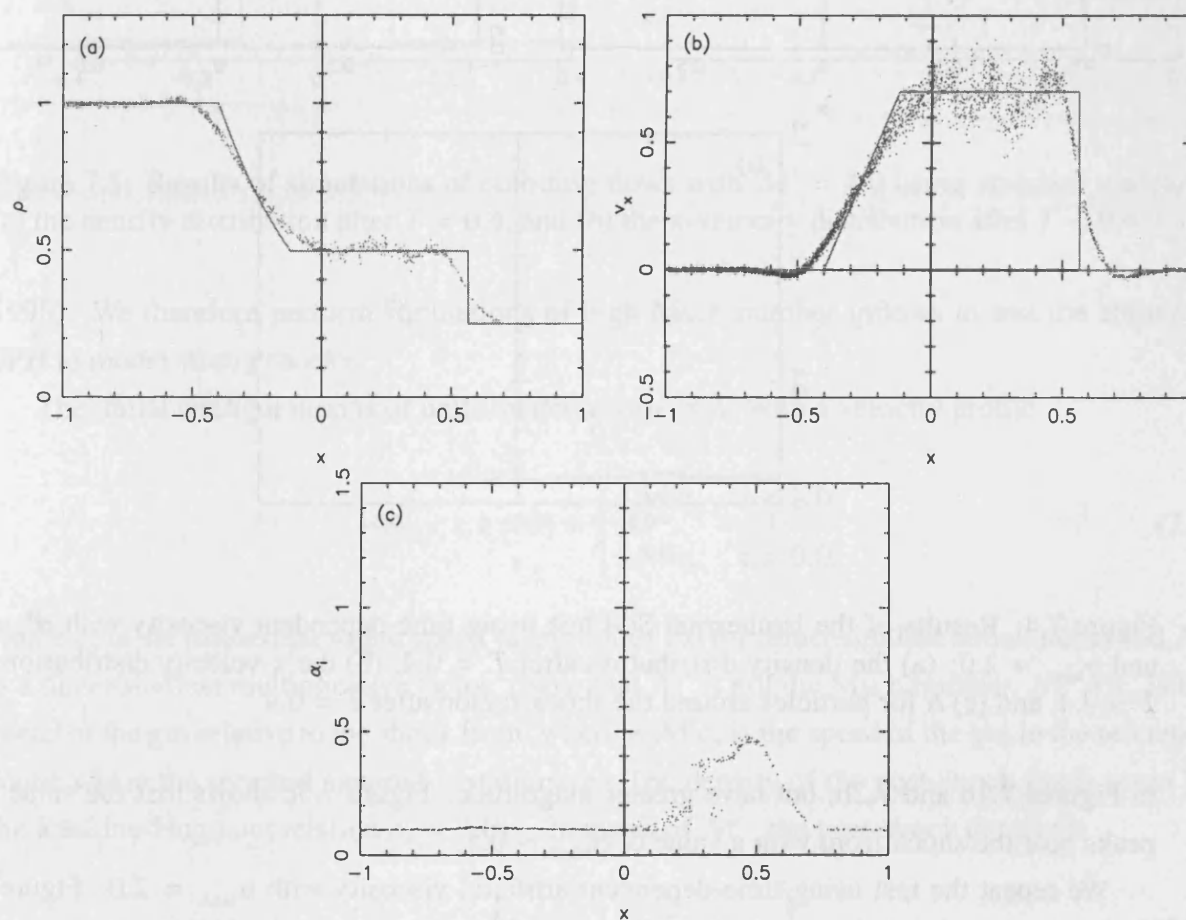


Figure 7.3: Results of the isothermal Sod test using time-dependent viscosity with $\alpha^* = 0.1$ and $\alpha_{\text{MAX}} = 1.0$: (a) the density distribution after $T = 0.4$, (b) the x-velocity distribution after $T = 0.4$, and (c) α for particles around the shock region after $T = 0.4$

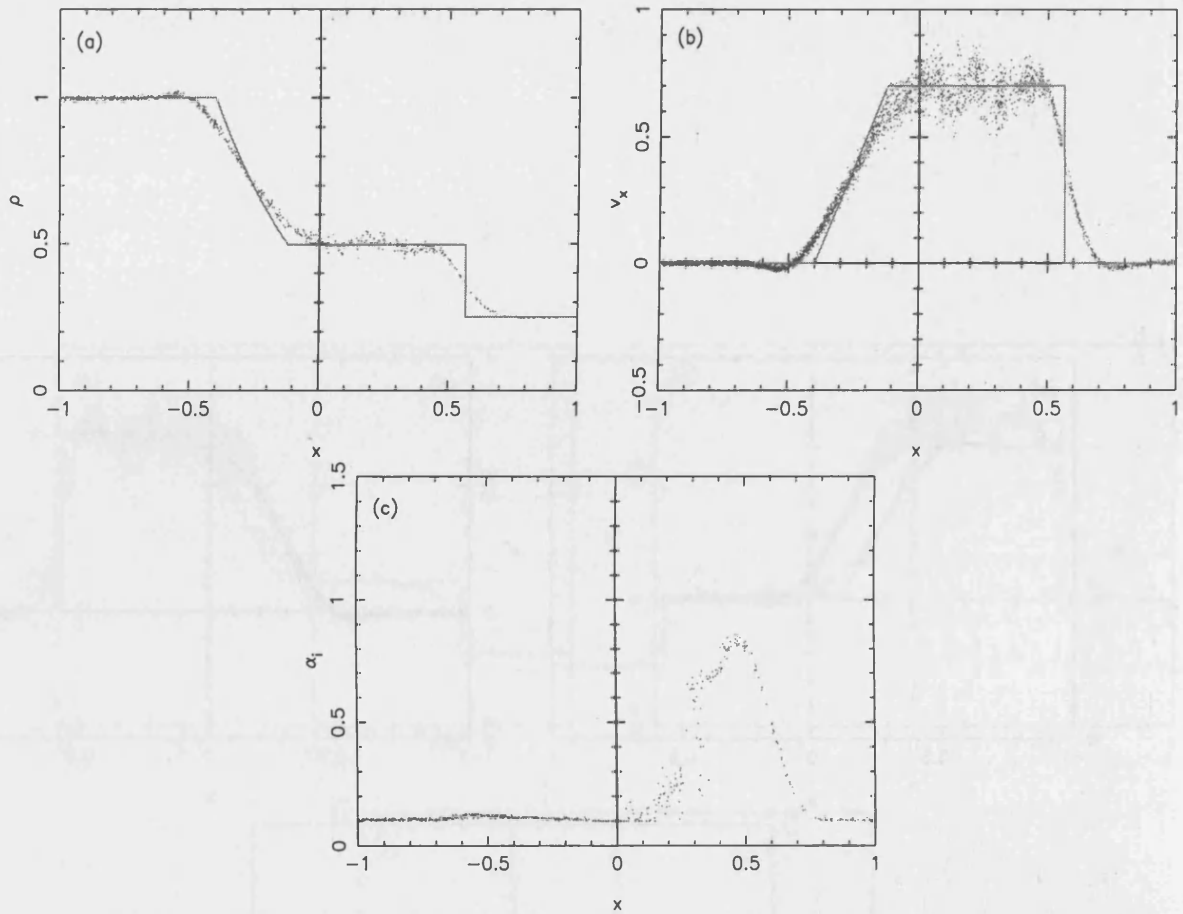


Figure 7.4: Results of the isothermal Sod test using time-dependent viscosity with $\alpha^* = 0.1$ and $\alpha_{\text{MAX}} = 2.0$: (a) the density distribution after $T = 0.4$, (b) the x -velocity distribution after $T = 0.4$, and (c) α for particles around the shock region after $T = 0.4$

in Figures 7.1b and 7.2b, but have greater magnitude. Figure 7.3c shows that the value of α_i peaks near the shock front with a value of $\alpha_{\text{PEAK}} \sim 0.5$.

We repeat the test using time-dependent artificial viscosity with $\alpha_{\text{MAX}} = 2.0$. Figure 7.4c shows that α_i peaks at a higher value of $\alpha_{\text{PEAK}} \approx 0.85$. Figures 7.4a and b show that increasing α_{MAX} has only a small effect in reducing post-shock oscillations in the density and velocity profiles.

7.3 Colliding isothermal flows

A more demanding test of the hydrodynamics and artificial viscosity is to simulate two colliding inflows of gas. Some simulations of star formation model turbulent clouds which generate colliding inflows and shocks (e.g. Bate et al. 2002a, 2002b & 2002c, Goodwin et al. 2004a, 2004b & 2004c), and others simulate collisions of molecular gas clouds (e.g. Bhattal et al.

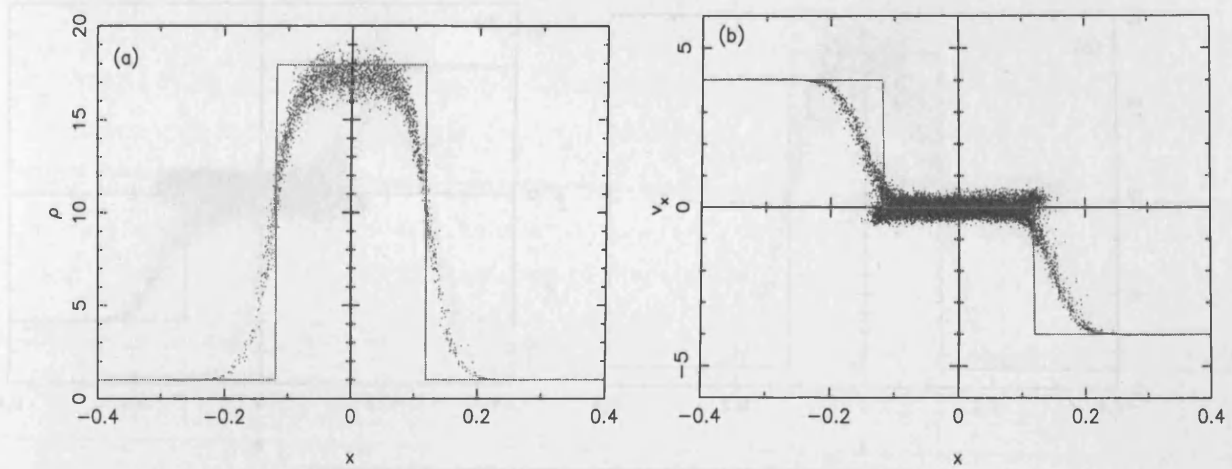


Figure 7.5: Results of simulations of colliding flows with $\mathcal{M}' = 4.0$ using standard viscosity: (a) the density distribution after $T = 0.4$, and (b) the x -velocity distribution after $T = 0.4$.

1998). We therefore perform simulations of high Mach number inflows to test the ability of SPH to model strong shocks.

The initial configuration is of uniform density ($\rho_0 = 1$) with a velocity profile

$$v_x(x, y, z, t = 0) = \begin{cases} +\mathcal{M}'c_0 & x < 0.0, \\ -\mathcal{M}'c_0 & x > 0.0, \end{cases} \quad (7.2)$$

where c_0 is the isothermal sound speed (again set to 1.0 for dimensionless simulations) and \mathcal{M}' is a dimensionless multiplicative factor. (Note that \mathcal{M}' is not the Mach number, \mathcal{M} . $\mathcal{M}c_0$ is the speed of the gas relative to the shock front, whereas $\mathcal{M}'c_0$ is the speed of the gas in the reference frame where the shocked material is stationary.) The density of the post-shock gas is given by the Rankine-Hugoniot relation $\rho_s = \mathcal{M}^2\rho_0$. In terms of \mathcal{M}' , the post-shock density is

$$\rho_s = \rho_0 \left(1 + \frac{2}{\sqrt{1 + 4/\mathcal{M}'^2 - 1}} \right). \quad (7.3)$$

We simulate relatively strong shocks with $\mathcal{M}' = 4.0$ and test the different artificial viscosity prescriptions. For reference, the post-shock density is $\rho_s = 17.94$ and the Mach number is $\mathcal{M} = 4.24$. The pre-shock smoothing length is $h = 0.0625$ and the post-shock smoothing length is $h = 0.0239$.

7.3.1 Standard artificial viscosity

Figure 7.5 shows the results of simulations of colliding flows with $\mathcal{M}' = 4.0$, using standard artificial viscosity with $\mathcal{M}' = 4.0$ after $T = 0.4$, along with the analytical solution (solid line). Fig-

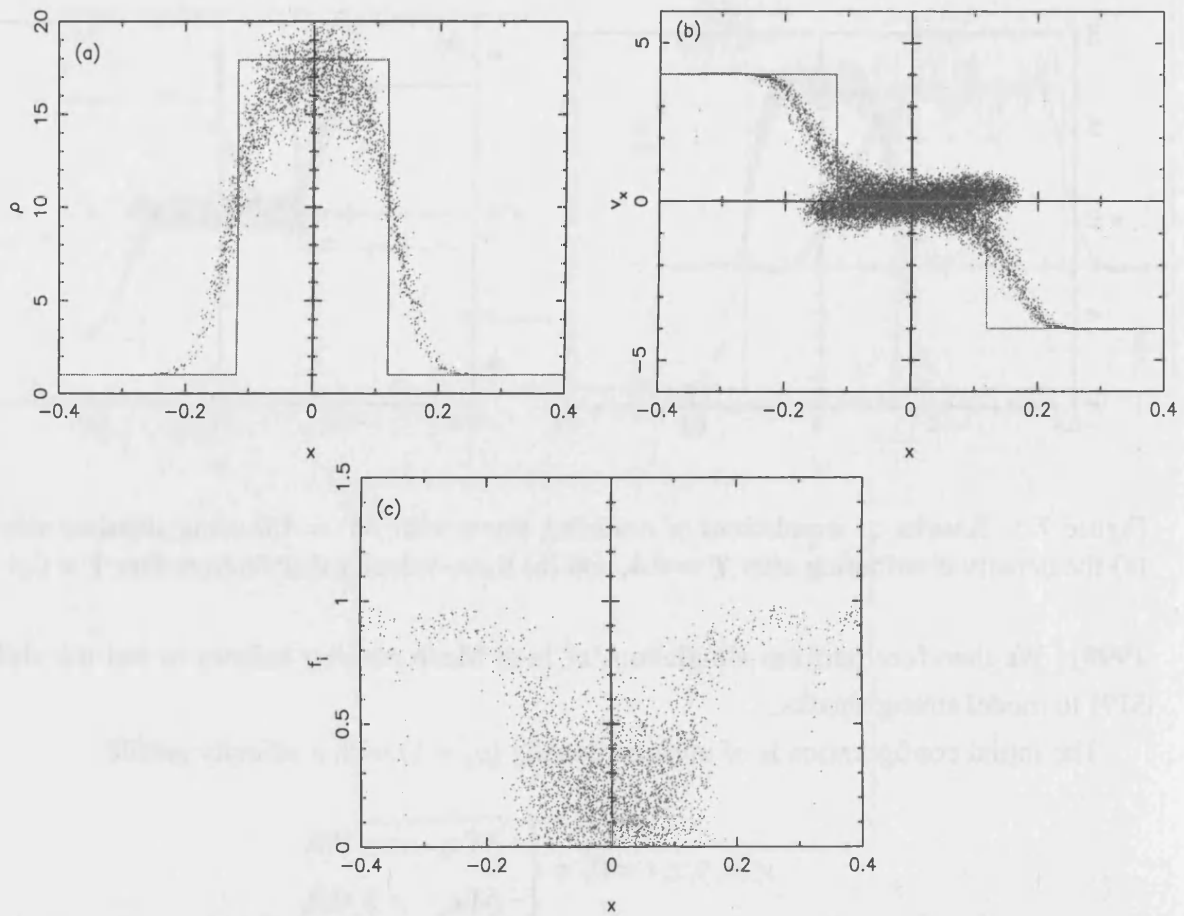


Figure 7.6: Results of simulations of colliding flows with $\mathcal{M}' = 4.0$ using artificial viscosity with the Balsara switch: (a) the density distribution after $T = 0.4$, (b) the x-velocity distribution after $T = 0.4$, and (c) the Balsara factor (Equation 6.30) over the shock region after $T = 0.4$.

Figure 7.5a shows that the density profile resulting from the simulation is in good agreement with the analytical solution except around the discontinuities which are broadened due to smoothing over $\sim 2h$ (as seen also in the Sod test; Section 7.2). The simulations show a broad, roughly flat high-density shock region with a small amount of dispersion; the height and width of the density profile of the shock agrees well with theory. The velocity profile of the shock (Figure 7.5b) shows that standard viscosity is successful in decelerating the inflowing material from supersonic speeds to approximately zero in the simulation co-ordinate frame. There is some dispersion in the velocity profile of the shock.

7.3.2 Artificial viscosity with the Balsara switch

Here we consider simulations of colliding flows with $\mathcal{M}' = 4.0$ using the Balsara switch. Figures 7.6a and b show the density and x-velocity distributions of particles around the shock, with

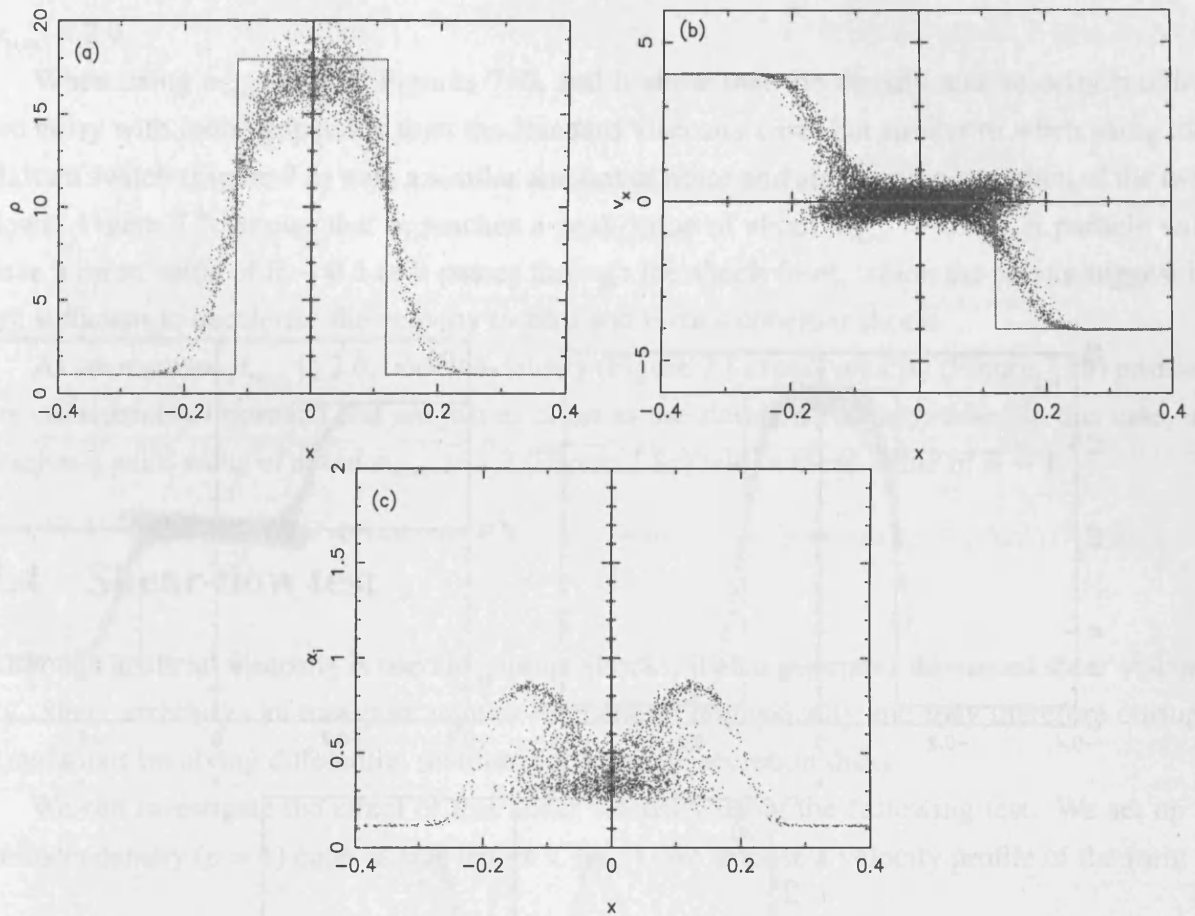


Figure 7.7: Results of simulations of colliding flows with $\mathcal{M}' = 4.0$ using time-dependent artificial viscosity with $\alpha_{\text{MAX}} = 1.0$: (a) the density distribution after $T = 0.4$, (b) the x -velocity distribution after $T = 0.4$, and (c) α_i for particles around the shock region after $T = 0.4$

Figure 7.6c showing the values of the Balsara factor (c.f. Equation 6.30). Figure 7.6c shows that the Balsara factor, f_i takes values $0.8 - 1.0$ in the regions of strong divergence (i.e. the shock fronts) and thus switches on the artificial viscosity where needed. f_i is again very noisy in regions where the divergence is low. The density profile (Figure 7.6a) is notably worse and less clean than the case with standard viscosity (Figure 7.5a). There is a larger dispersion in the SPH densities around the peak, although the average peak density agrees with the standard viscosity case. The velocity profile (Figure 7.6b) has considerable dispersion (almost supersonic). It also shows that the two flows almost penetrate each other.

7.3.3 Time-dependent artificial viscosity

Here we consider simulations of colliding flows $\mathcal{M}' = 4.0$ with time-dependent artificial viscosity with parameters $\alpha^* = 0.1$, $C = 0.2$. As with the Sod test, we use both $\alpha_{\text{MAX}} = 1.0$ and

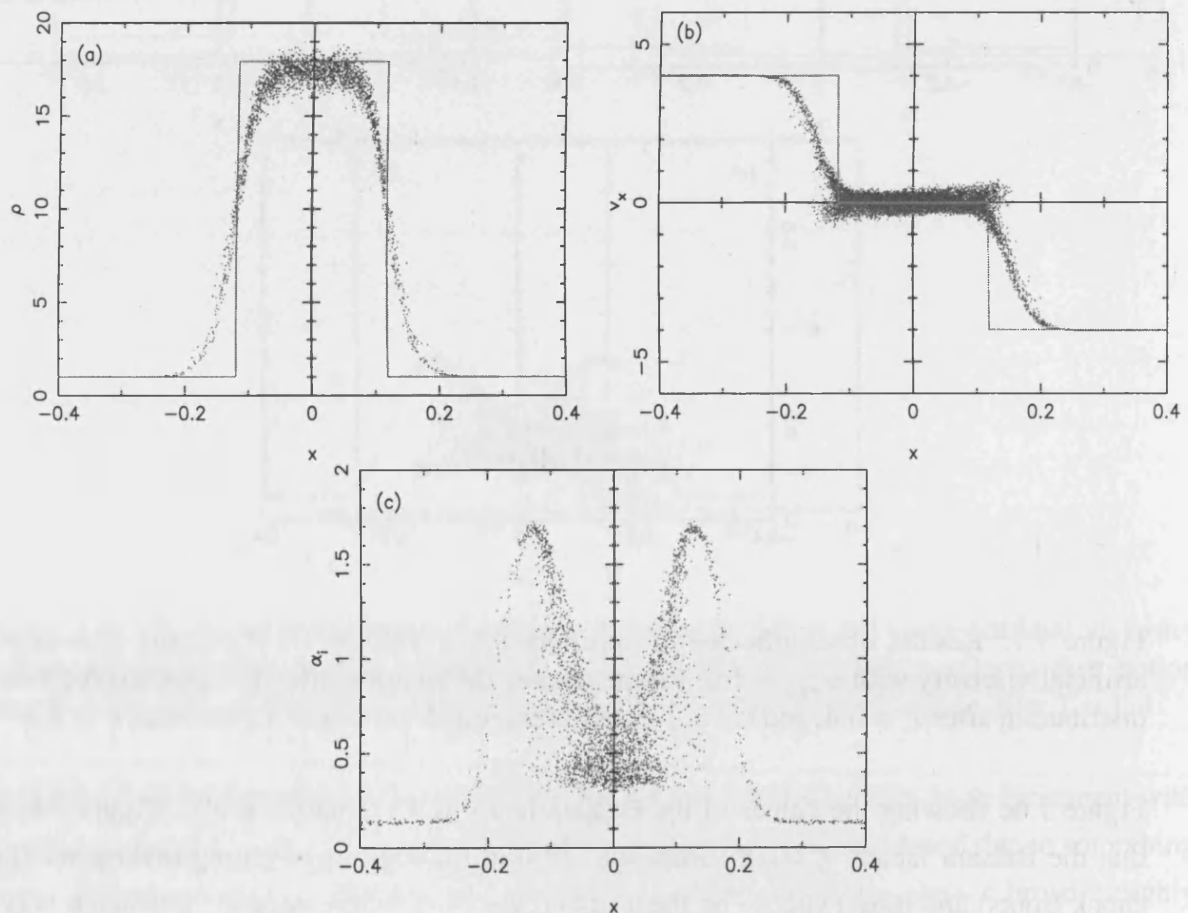


Figure 7.8: Results of simulations of colliding flows with $M' = 4.0$ using time-dependent artificial viscosity with $\alpha_{\text{MAX}} = 2.0$: (a) the density distribution after $T = 0.4$, (b) the x-velocity distribution after $T = 0.4$, and (c) α_i for particles around the shock region after $T = 0.4$

$\alpha_{\text{MAX}} = 2.0$.

When using $\alpha_{\text{MAX}} = 1.0$, Figures 7.7a and b show that the density and velocity profiles are noisy with more dispersion than the standard viscosity case, but similar to when using the Balsara switch (Figure 7.6) with a similar amount of noise and also some penetration of the two flows. Figure 7.7c shows that α_i reaches a peak value of about $\alpha_{\text{PEAK}} = 0.85$. A particle will have a mean value of $\bar{\alpha} \sim 0.5$ as it passes through the shock front, which the results suggest is not sufficient to decelerate the velocity to zero and form a coherent shock.

As we increase α_{MAX} to 2.0, both the density (Figure 7.8a) and velocity (Figure 7.8b) profiles are considerably improved and are just as clean as the standard viscosity case. In this case, α_i reaches a peak-value of about $\alpha_{\text{PEAK}} = 1.7$ (Figure 7.8c) with a mean value of $\bar{\alpha} \sim 1$.

7.4 Shear-flow test

Although artificial viscosity is used to capture shocks, it also generates unwanted shear viscosity. Shear viscosity can transport angular momentum unphysically and may therefore corrupt simulations involving differential rotation, for example accretion disks.

We can investigate the effect of this shear viscosity using the following test. We set up a uniform density ($\rho = 1$) cube of side length $L (= 1)$. We impose a velocity profile of the form

$$v_x(x, y, z, t = 0) = c_0 \sin\left(\frac{2\pi y}{L}\right), \quad (7.4)$$

and $v_y = v_z = 0$. We use periodic boundary conditions in all 3 dimensions. In the absence of shear viscosity, the profile should remain unchanged. Any shear viscosity opposes the shearing and tend to equalise the velocities. We allow the simulation to evolve until $T = 1.0$.

7.4.1 Standard artificial viscosity

Figure 7.9 shows the velocity profile after $T = 1.0$ when using standard artificial viscosity. The velocity profile clearly has been damped by the effect of shear viscosity. The velocity at all points is tending towards zero as expected so that $\partial v_x / \partial y \rightarrow 0$. $v_x(y)$ still has a roughly sinusoidal form, but with reduced amplitude (approximately 60% the initial amplitude). There is a small spread in the velocity profile due to particle noise.

7.4.2 Artificial viscosity with the Balsara switch

For the case of using the Balsara switch, the velocity profile (Figure 7.9b) is affected less by shear flows than when using standard artificial viscosity. $v_x(y)$ again retains a sinusoidal form

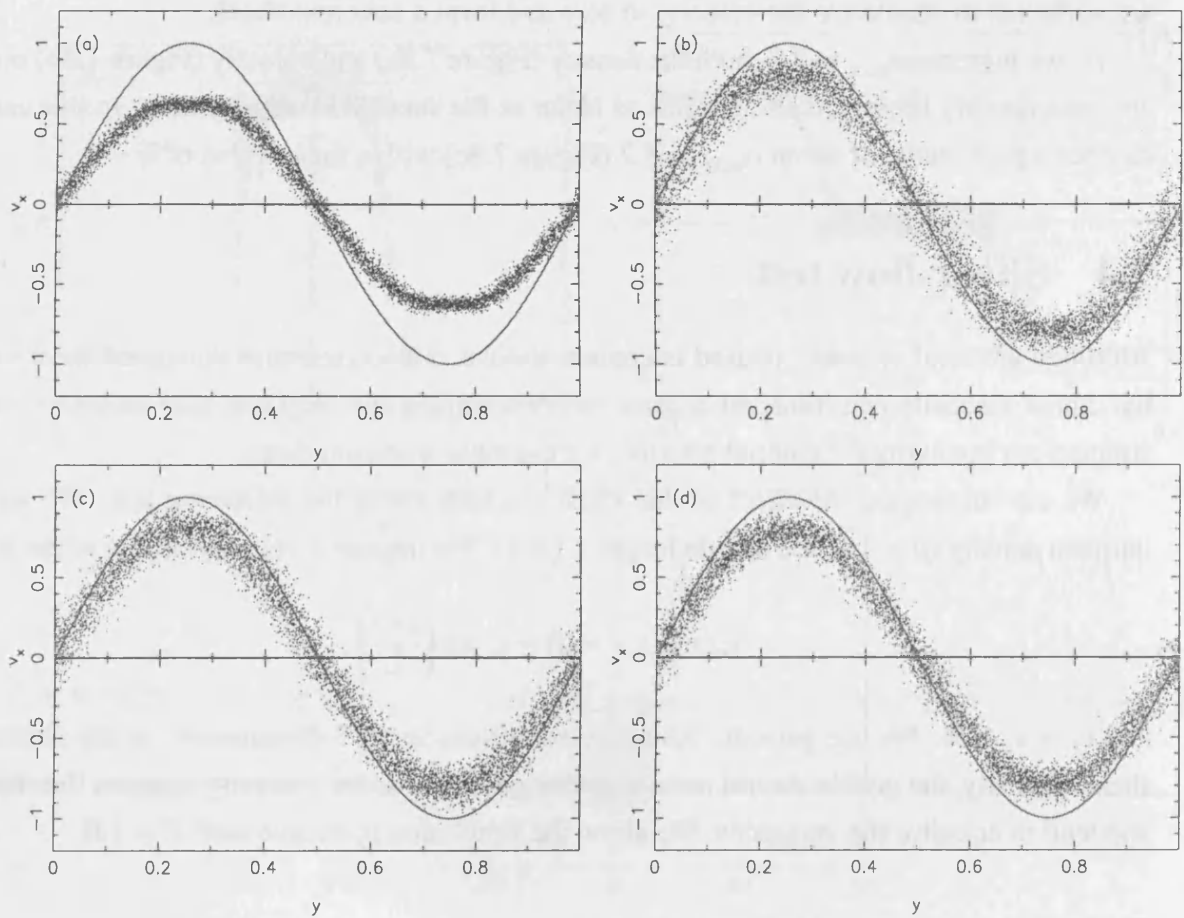


Figure 7.9: Results of the shear flow test. The x -velocity profile is plotted as a function of y after a time $T = 1.0$ for (a) standard artificial viscosity, (b) artificial viscosity using the Balsara switch, (c) time-dependent viscosity using $\alpha_{\text{MAX}} = 1.0$, and (d) time-dependent viscosity using $\alpha_{\text{MAX}} = 2.0$. The solid line shows the initial velocity profile, as given by Equation 7.4.

and has reduced magnitude, about 80% rather than 60%. The velocity spread is greater than with standard artificial viscosity. This is due to the lower average value of α and also the inherent noise when calculating f_i using Equation 6.30.

7.4.3 Time-dependent artificial viscosity

Figures 7.9c & d show the velocity profile using time dependent viscosity with $\alpha_{\text{MAX}} = 1.0$ and $\alpha_{\text{MAX}} = 2.0$ respectively, and $\alpha^* = 0.1$, after $T = 1.0$. Both profiles are similar to the velocity profile when using the Balsara switch (Figure 7.9b); $v_x(y)$ again retains its sinusoidal form with reduced amplitude ($\sim 80\%$). Varying α_{MAX} has little effect on the velocity profile since $\nabla \cdot \mathbf{v} \sim 0$ (plus noise) and therefore $\alpha_i \sim \alpha^*$ (plus noise). As with the Balsara switch, the noise in calculating $\nabla \cdot \mathbf{v}$ contributes to the noise in the velocity profile.

7.5 Jeans instability test

We introduce a new test which investigates the ability of SPH to model gravitational fragmentation correctly. This test is designed (a) to show that fragmentation is modelled correctly in SPH when well-resolved, (b) to determine the resolution required for SPH to achieve acceptable results, and (c) to demonstrate the consequences of performing simulations using SPH with poor resolution.

The resolution of self-gravitating hydrodynamics has been determined previously using the standard configuration first explored by Boss & Bodenheimer (1979). However, this test does not have an analytical solution. The resolution limit is inferred from the convergence of results from different simulations (e.g Bate & Burkert (1997)). Previous work on the resolution requirements of SPH is discussed in Section 6.10.2.

We use the classical analysis first performed by Jeans (1929) as the basis of our test. We consider a stationary self-gravitating, infinitely extended medium, with uniform density ρ_0 and constant isothermal sound speed c_0 . We assume that this medium is in static equilibrium. (This assumption is known as the Jeans swindle since an infinitely extended self-gravitating medium can only be in equilibrium if $\rho_0 = 0$. See Binney & Tremaine for a discussion.)

We impose a small density perturbation, ρ_1 , and velocity perturbation, \mathbf{v}_1 on top of the background medium so that $\rho = \rho_0 + \rho_1$ and $\mathbf{v} = \mathbf{v}_0 + \mathbf{v}_1 = \mathbf{v}_1$ (since $\mathbf{v}_0 = 0$). The evolution of the perturbation is described by the equations of self-gravitating fluid dynamics (c.f. Binney & Tremaine 1987). For suitably small perturbations (i.e. $|\rho_1| \ll |\rho_0|$), the equations simplify to the

linearised forms

$$\frac{\partial \rho_1}{\partial t} = -\rho_0 \nabla \cdot \mathbf{v}_1, \quad (7.5)$$

$$\frac{\partial \mathbf{v}_1}{\partial t} = -\frac{c_0^2 \nabla \rho_1}{\rho_1} - \nabla \phi_1, \quad (7.6)$$

$$\nabla^2 \phi_1 = 4\pi G \rho_1, \quad (7.7)$$

where ϕ_1 is the gravitational potential due to the perturbed density (e.g. Binney & Tremaine, 1987). Eliminating \mathbf{v}_1 and ϕ_1 from Eqns. (7.5) to (7.7) then yields

$$\frac{\partial^2 \rho_1}{\partial t^2} - c_0^2 \nabla^2 \rho_1 - 4\pi G \rho_0 \rho_1 = 0. \quad (7.8)$$

Substituting a plane wave of the form $\rho_1(\mathbf{r}, t) = A \rho_0 e^{i(kx \pm \omega t)}$ in Eqn. (7.8) gives the dispersion relation

$$\omega_k^2 = c_0^2 k^2 - 4\pi G \rho_0. \quad (7.9)$$

From Equation 7.9 we can identify a critical wave-number,

$$k_j = \frac{(4\pi G \rho_0)^{1/2}}{c_0}, \quad (7.10)$$

and correspondingly a critical wavelength, called the Jeans length

$$\lambda_j = \frac{2\pi}{k_j} = \left(\frac{\pi c_0^2}{G \rho_0} \right)^{1/2}. \quad (7.11)$$

For short wavelength perturbations (i.e. $\lambda < \lambda_j$, $k > k_j$), the density perturbations oscillate as sound waves, i.e. $\rho_1 \propto e^{i(kx)} e^{i(\pm \omega t)}$. For long wavelength perturbations (i.e. $\lambda > \lambda_j$, $k < k_j$), the density perturbations either grow or decay, i.e. $\rho_1 \propto e^{i(kx)} e^{\pm \gamma t}$ with a velocity $\mathbf{v}_1 \propto e^{i(kx)} e^{\pm \gamma t} \hat{\mathbf{e}}_x$.

However, we wish to set up an initially static perturbation ($\mathbf{v}(t=0) = \mathbf{0}$) This ensures that the factor that determines whether the perturbation oscillates or grows is how well the code models the physics rather than any imposed velocity perturbation. Since the fluid equations (Equations 7.5 - 7.7) are linear, a superposition of 2 planar waves is also a valid solution. To set up an initially stationary plane-wave perturbation, we superimpose two plane waves of equal

amplitude and wavelength, travelling in opposite directions:

$$\rho_1(\mathbf{r}, t) = \frac{A\rho_0}{2} \left\{ e^{i(kx - \omega_k t)} + e^{i(kx + \omega_k t)} \right\}, \quad (7.12)$$

$$\mathbf{v}_1(\mathbf{r}, t) = \frac{A\omega}{2k} \left\{ e^{i(kx - \omega_k t)} - e^{i(kx + \omega_k t)} \right\} \hat{\mathbf{e}}_x. \quad (7.13)$$

For short wavelength perturbations ($\lambda < \lambda_j$, $k > k_j$), the dispersion relation (Eqn. 7.9) indicates that ω^2 is positive, and therefore (switching from k to λ),

$$\omega_\lambda = 2\pi c_0 \left(\frac{1}{\lambda^2} - \frac{1}{\lambda_j^2} \right)^{1/2}, \quad (7.14)$$

is real and the perturbation oscillates. Taking the real parts of Eqns. (7.12) and (7.13),

$$\rho_1(\mathbf{r}, t) = A\rho_0 \cos\left(\frac{2\pi x}{\lambda}\right) \cos(\omega_\lambda t), \quad (7.15)$$

$$\mathbf{v}_1(\mathbf{r}, t) = \frac{A\omega_\lambda}{k} \sin\left(\frac{2\pi x}{\lambda}\right) \sin(\omega_\lambda t) \hat{\mathbf{e}}_x. \quad (7.16)$$

and the oscillation period is

$$T_\lambda = \frac{2\pi}{\omega_\lambda} = \left(\frac{\pi}{G\rho_0} \right)^{1/2} \left(\frac{\lambda_j^2}{\lambda^2} - 1 \right)^{-1/2}. \quad (7.17)$$

For long wavelength perturbations ($\lambda > \lambda_j$, $k < k_j$), the dispersion relation (Eqn. 7.9) indicates that ω^2 is negative, and therefore ω_λ is imaginary. Defining

$$\gamma_\lambda = 2\pi c_0 \left(\frac{1}{\lambda^2} - \frac{1}{\lambda_j^2} \right)^{1/2}, \quad (7.18)$$

we can put $\omega_\lambda = i\gamma_\lambda$. Then, taking the real parts of Eqns. (7.12) and (7.13), we have

$$\rho_1(\mathbf{r}, t) = A\rho_0 \cos\left(\frac{2\pi x}{\lambda}\right) \cosh(\gamma_\lambda t), \quad (7.19)$$

$$\mathbf{v}_1(\mathbf{r}, t) = \frac{A\gamma_\lambda}{k} \sin\left(\frac{2\pi x}{\lambda}\right) \sinh(\gamma_\lambda t) \hat{\mathbf{e}}_x. \quad (7.20)$$

The time for the perturbed density on the plane $x = 0$ to grow from $A\rho_0$ to $\cosh(1)A\rho_0 \approx 1.54A\rho_0$ is

$$T'_\lambda = \frac{1}{\gamma_\lambda} = \left(\frac{1}{4\pi G\rho_0} \right)^{1/2} \left(1 - \frac{\lambda_j^2}{\lambda^2} \right)^{-1/2}. \quad (7.21)$$

7.5.1 Initial conditions

Since in both situations (short wavelength perturbations that oscillate and long wavelength perturbations that grow) the initial state is

$$\rho(\mathbf{r}, t) = \rho_0 \left\{ 1 + A \cos\left(\frac{2\pi x}{\lambda}\right) \right\}, \quad (7.22)$$

$$\mathbf{v}(\mathbf{r}, t) = \mathbf{0}, \quad (7.23)$$

we set up the initial conditions as follows.

First, N_{TOTAL} particles are distributed randomly within a unit cube and settled using non-self-gravitating SPH and periodic boundary conditions. This reduces the Poissonian density fluctuations, and produces an approximately uniform, but non-crystalline, density distribution. The mean smoothing length of a particle is given by

$$\bar{h} = \left(\frac{3 N_{\text{NEIB}}}{32 \pi N_{\text{TOTAL}}} \right)^{1/3} \approx 1.1427 N_{\text{TOTAL}}^{-1/3}, \quad (7.24)$$

where we have substituted $N_{\text{NEIB}} = 50$, and implicitly the unit of length is the length of the edges of the cube.

Second, a sinusoidal density perturbation is imposed by adjusting the unperturbed x -coordinate, x_i , of each particle i to a perturbed value, x'_i , satisfying

$$x'_i + \frac{A \lambda}{2\pi} \sin\left(\frac{2\pi x'_i}{\lambda}\right) = x_i. \quad (7.25)$$

This equation must be solved numerically for $x'_i = x'(x_i)$. We use a perturbation with fractional amplitude $A = 0.1$.

Since periodic boundary conditions are being invoked, we can only apply perturbations which fit an integer number of wavelengths into the side of the unit cube, i.e.

$$\lambda = n_\lambda^{-1}, \quad (7.26)$$

where $n_\lambda = 1, 2, 3$, etc..

A convenient measure of the resolution is the ratio of the mean diameter of an SPH particle, $\bar{d} = 4\bar{h}$, to the wavelength of the perturbation, $\lambda = n_\lambda^{-1}$, i.e.

$$\mathcal{R} = \frac{\bar{d}}{\lambda} = n_\lambda 4\bar{h} = n_\lambda \left(\frac{6 N_{\text{NEIB}}}{\pi N_{\text{TOTAL}}} \right). \quad (7.27)$$

Thus a small value of \mathcal{R} corresponds to good resolution. Equation 6.56 suggests that we must

ensure the Jeans length is well resolved. Taking $\lambda = \lambda_j$, the Jeans condition (Bate & Burkert 1997; See Section 6.10.2) becomes

$$\mathcal{R} \leq 0.8. \quad (7.28)$$

The number of SPH particles in one Jeans mass is then

$$N_j = \frac{M_j}{m} = \frac{N_{\text{NEIB}}}{\mathcal{R}^3}. \quad (7.29)$$

In principle, we could investigate any resolution using boxes with different numbers of particles. Here we discuss perturbations with resolutions (a) $\mathcal{R} = 0.5$, i.e. very well resolved with $N_j = 8N_{\text{NEIB}} = 400$ SPH particles in one Jeans mass; (b) $\mathcal{R} = 1.0$, marginally resolved, with $N_j = N_{\text{NEIB}} = 50$ SPH particles in one Jeans mass; and (c) $\mathcal{R} = 2.0$, under-resolved, with just $N_j = N_{\text{NEIB}}/8 \simeq 6$ SPH particles in one Jeans mass. The initial conditions are constructed using boxes with 764 particles with $n_i = 1, 2, \text{ and } 4$ respectively. For each resolution, we evolve the perturbation with different values of the Jeans length. The Jeans wavelength can be varied arbitrarily by changing the isothermal sound speed, c_0 .

7.5.2 Results

Calculating smoothed averages in SPH is highly dependent on the form of the smoothing kernel; the size of a feature, λ , compared to the smoothing length, h , determines how accurately Equation 6.4 calculates $A(\mathbf{r})$. Figure 7.10 compares the sinusoidal perturbation with the smoothing kernel for the resolutions $\mathcal{R} = 0.5, 1.0$ and 2.0 . We will now discuss how well SPH resolves the density distribution, the hydrodynamical and gravitational forces in the Jeans test with reference to Figure 7.10.

7.5.3 Density and forces

For perturbations with $\mathcal{R} = 0.5, 1.0$ and 2.0 , the SPH density is plotted in Figures 7.11a, b and c respectively along with the exact analytical density (solid line, Equation 7.22). Also plotted in each case is the smoothed analytical density distribution (dot-dashed lines) using Equation 6.4 with $A(\mathbf{r}) = \rho(\mathbf{r})$, i.e.

$$\langle \rho(\mathbf{r}) \rangle = \int_V \rho(\mathbf{r}') W(\mathbf{r} - \mathbf{r}', h) d^3 \mathbf{r}'. \quad (7.30)$$

For the $\mathcal{R} = 0.5$ perturbation, Figure 7.10 shows that the kernel function is narrower than the perturbation; consequently the density does not vary considerably over a smoothing length.

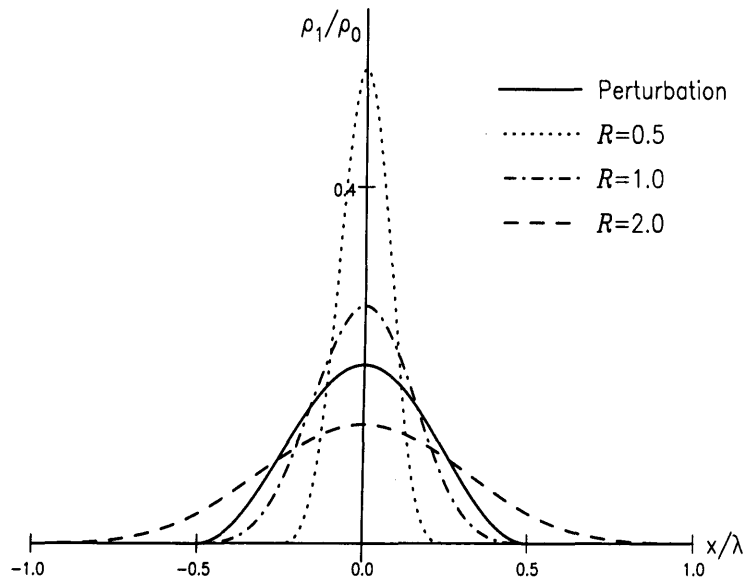


Figure 7.10: The solid line represents one wavelength of the imposed sinusoidal plane-wave perturbation. The other lines represent the smoothing kernels used in the results displayed in Fig. 7.13: $\mathcal{R} = 0.5$ (dotted line) the very well resolved case; $\mathcal{R} = 1.0$ (dash-dot line) the marginally resolved case; and $\mathcal{R} = 2.0$ (dashed line) the under-resolved case. The kernels are all scaled so that the integrated area under the kernel is equal to the area under the perturbation.

The effects of smoothing (i.e. using Equation 7.30) are therefore quite small in this case. Figure 7.11a shows that the smoothed density distribution is a very close approximation to the actual density distribution with a slightly lower peak value. Any peak is underestimated by Equation 7.30 since the value of the smoothed average is always pulled down by contributions from lower-density neighbouring particles. The SPH density (plotted as points) follows the smoothed analytical density distribution well with a small amount of scatter due to particle noise.

For the $\mathcal{R} = 1.0$ perturbation, Figure 7.10 shows that the smoothing kernel is of order the same size as the perturbation ($\lambda = 4h$). In this case, the density does vary considerably over the extent of a smoothing kernel, so the effects of smoothing become significant. Figure 7.11b shows that the smoothed density distribution, both from Equation 7.30 and as calculated by SPH deviates noticeably from the actual distribution.

For the worst resolved perturbation ($\mathcal{R} = 2.0$), Figure 7.10 shows that the smoothing kernel extends well beyond the perturbation wavelength. The smoothed density, $\langle \rho(\mathbf{r}) \rangle$, near the peak now includes contributions from the entire perturbation (and even weakly weighted contributions from neighbouring perturbations). Figure 7.11c shows that the smoothed density is a bad approximation to the actual density perturbation, as is the SPH density distribution.

Resolving the hydrodynamical and gravitational forces in SPH is crucial to modelling the Jeans instability since the relative strengths of these two opposing forces determine whether a perturbation will collapse or oscillate. For perturbations with $\mathcal{R} = 0.5, 1.0$ and 2.0 , the

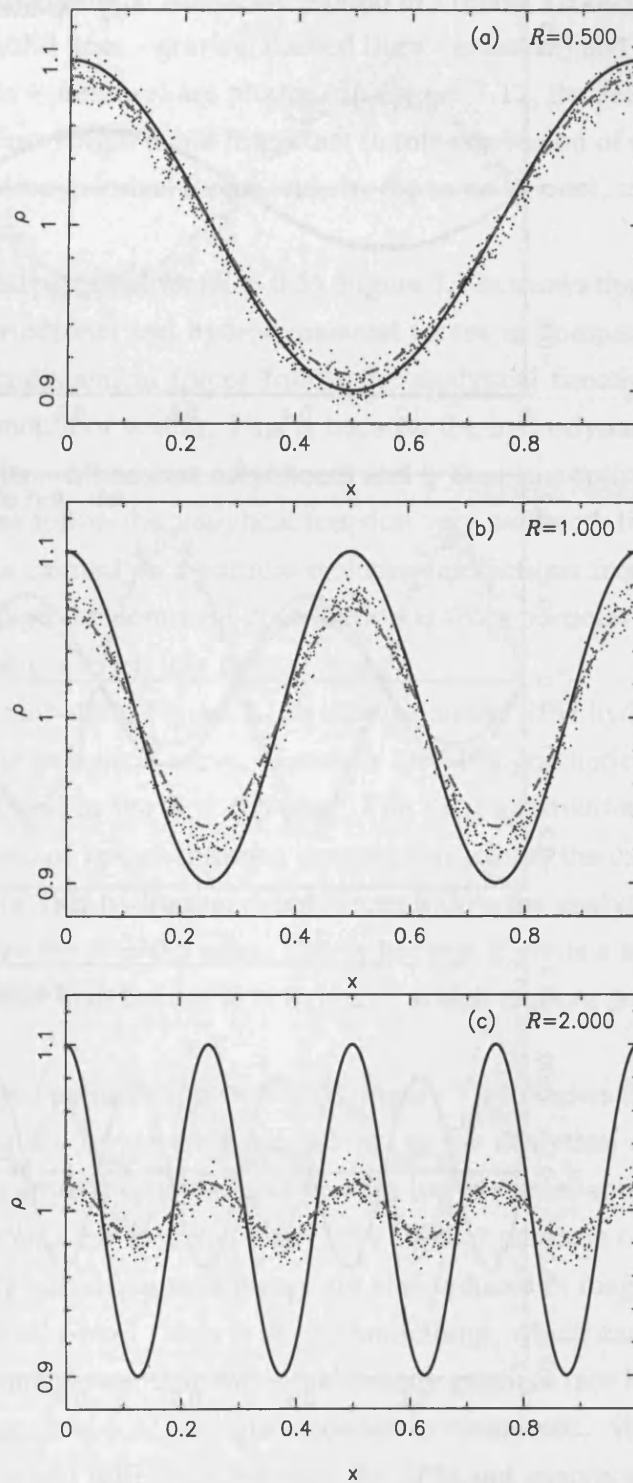


Figure 7.11: The density distributions of the perturbation. Plotted in each panel are the analytical density curves (solid lines), the smoothed density as calculated by Equation 7.30 (dot-dashed lines) and the density calculated using Equation 6.21 in SPH (points). Perturbations with different resolutions are plotted (a) $\mathcal{R} = 0.5$ (b) $\mathcal{R} = 1.0$ (c) $\mathcal{R} = 2.0$.

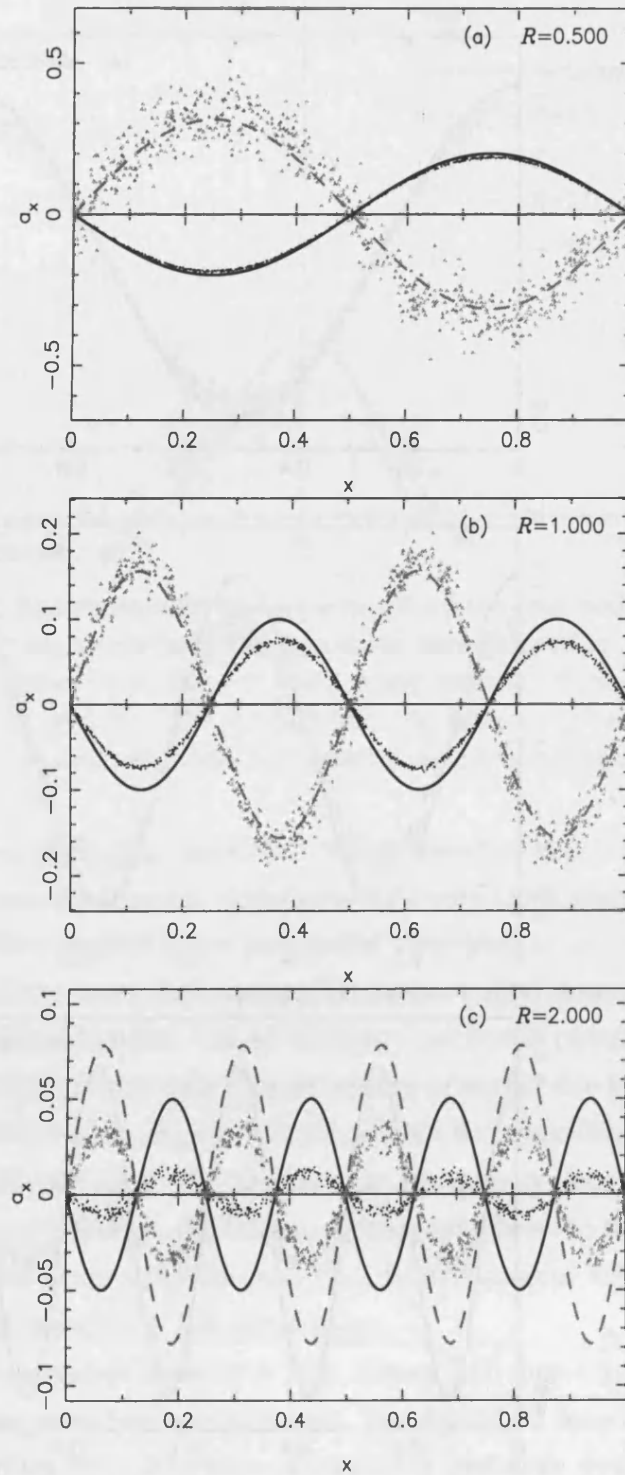


Figure 7.12: The analytical and SPH forces exerted on the particles. Plotted in each are the analytical gravitational (solid lines) and analytical hydrodynamical (dashed lines) forces along with the SPH gravitational (dark points) and SPH hydrodynamical (light triangles) forces. The hydrodynamical forces are calculated for the case $\lambda/\lambda_j = 0.8$. Perturbations with different resolutions are plotted (a) $\mathcal{R} = 0.5$, (b) $\mathcal{R} = 1.0$ and (c) $\mathcal{R} = 2.0$.

hydrodynamical and gravitational forces are plotted in Figures 7.12a, b & c respectively. Both the analytical forces (solid lines - gravity; dashed lines - pressure) and SPH forces (dark points - gravity, grey triangles - pressure) are plotted. In Figure 7.12, the Jeans length is $\lambda_j = 0.8 \lambda$. The exact choice of Jeans length is not important in this discussion of the forces since both the analytical and SPH hydrodynamical forces scale by the same amount, so the fractional deviation is the same.

For the well resolved perturbation ($\mathcal{R} = 0.5$), Figure 7.12a shows that SPH calculates to good accuracy both the gravitational and hydrodynamical forces in comparison with the analytical forms. The SPH hydrodynamical forces follow the analytical function well on average, but there is a noticeable amount of scatter. This is because the hydrodynamical force exerted on a particle is only due to its ~ 50 nearest neighbours and is thus susceptible to particle noise. The SPH gravitational forces follow the analytical function very well with little obvious scatter. The total gravitational force exerted on a particle includes interactions from all the other particles in the simulation although the dominant contribution is from particles within λ . For $\mathcal{R} = 0.5$, $N_j \approx 400$ and hence there is much less particle noise.

For the $\mathcal{R} = 1.0$ perturbation, Figure 7.12b shows that the SPH hydrodynamical forces still provide a good fit to the analytical curve. However the SPH gravitational forces do not match the analytical curve as well as the $\mathcal{R} = 0.5$ case. The SPH gravitational forces are reduced in magnitude due to the use of kernel-softened gravity; this affects the calculation of \mathbf{a}_{grav} for all particles within $\frac{1}{2}\lambda$. The SPH hydrodynamical forces follow the analytical curve well and also have less scatter than for the $\mathcal{R} = 0.5$ case. This is because there is a stronger density gradient over the smoothing kernel than for the $\mathcal{R} = 0.5$ case, which is more prominent than numerical noise.

For the worst resolved perturbation ($\mathcal{R} = 2.0$), Figure 7.12c shows that both the SPH hydrodynamical and gravitational forces are poor matches to the analytical curves. The SPH gravitational forces are even more severely affected by the use of kernel-softened gravity than in the $\mathcal{R} = 1.0$ case. There is noticeable scatter due to the smaller numbers of particles per perturbation volume. The SPH hydrodynamical forces are also reduced in magnitude considerably (on average $\sim \frac{1}{2}$ the analytical force). This is due to smoothing, which causes the calculated SPH density gradient to be much lower than the actual density gradient (see Figure 7.11c), and hence the pressure forces (Equation 6.22) are also reduced in magnitude. We note that in this case, as in all cases, the fractional difference between the SPH and analytical gravitational forces is greater than the fractional difference between the SPH and analytical hydrodynamical forces.

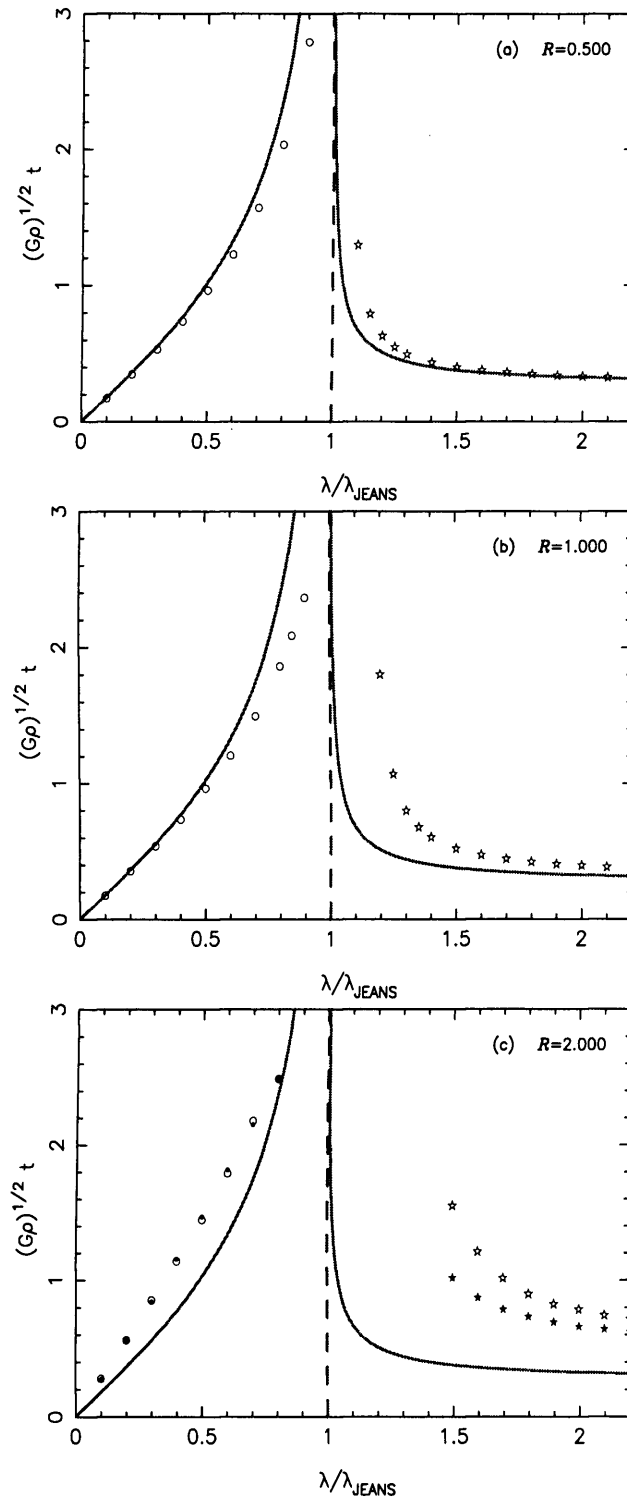


Figure 7.13: Characteristic timescales for the evolution of plane-wave perturbations, as a function of wavelength. The ordinate is the wavelength in units of the Jeans length, and the abscissa is the timescale in units of $(G\rho_0)^{-1/2}$. For perturbations which oscillate (i.e. those with $\lambda < \lambda_J$) the oscillation period estimated from the SPH simulations is represented by an open circle. For perturbations which collapse (i.e. those with $\lambda > \lambda_J$) the time for the peak density in the SPH simulations to increase by a factor 1.54 (see text) is represented by an open star. The filled circles and stars represent results of simulations using the self-support correction term (See Section 7.5.5). For reference, the analytic timescales are given by solid curves. (a) The very well resolved case, $\mathcal{R} = 0.5$. (b) The marginally resolved case, $\mathcal{R} = 1.0$. (c) The under-resolved case, $\mathcal{R} = 2.0$.

7.5.4 Timescales

In Figure 7.13, we plot the results of the Jeans test using various values of λ/λ_j between 0.1 and 2.4 and for different resolutions. Each panel of Fig. 7.13 corresponds to a different resolution, \mathcal{R} , viz. (a) $\mathcal{R} = 0.5$, (b) $\mathcal{R} = 1.0$, and (c) $\mathcal{R} = 2.0$. If the perturbation oscillates, we plot with an open circle the oscillation period. If the perturbation grows, we plot as an open star the time required for the amplitude to increase by a factor $\cosh(1) = 1.54$. The analytic predictions for these times (Eqns. 7.17 and 7.21) are shown as solid lines. (The solid stars and circles are discussed in Section 7.5.5).

The results for $\mathcal{R} = 0.5$ perturbations (Figure 7.13a) show excellent agreement with the analytical predictions. All perturbations that should oscillate ($\lambda < \lambda_j$) do oscillate, and all perturbations that should grow ($\lambda > \lambda_j$) do grow. There is good agreement between the theoretical timescales and the SPH timescales since the forces are well resolved (Figure 7.12a). There is a small discrepancy between theory and SPH for timescales near the $\lambda/\lambda_j = 1$ asymptote.

For the $\mathcal{R} = 1.0$ perturbations, the timescales are still in reasonably good agreement with the theory (see Figure 7.13b). However since the SPH gravitational forces are reduced in magnitude due to smoothing (see Figure 7.12b), the effective Jeans length is greater than that calculated using Equation 7.11. The asymptote (where $T \rightarrow \infty$) appears to move a greater value of λ/λ_j . Since the magnitude of \mathbf{a}_{grav} is reduced, the overall acceleration is smaller and the timescale for collapsing modes increases, i.e. the time it takes for the perturbed density to increase by a factor of $\cosh(1)$ is slightly increased.

For the $\mathcal{R} = 2.0$ perturbations, the SPH timescales for collapsing modes are in poor agreement with the theory (Figure 7.13c). The forces at this resolution are both severely under-resolved and reduced in magnitude; The overall acceleration is lower than it should be and the perturbation grows more slowly than predicted by theory. As with the $\mathcal{R} = 1.0$ case, the use of kernel-softened gravity increases the effective Jeans length so the asymptote moves to higher values of λ/λ_j . There is disagreement between the theoretical and SPH oscillating modes, although not as great a disparity as the growing modes. Note that there are no points in the region $\lambda/\lambda_j = 1.0 - 1.4$. This is because these very slowly evolving perturbations are corrupted by noise in the simulations and thus make computing an exact timescale difficult.

7.5.5 Including the correction term

We have implemented the self-support correction term discussed in Section 6.10.5 into DRAGON and have repeated some simulations of the Jeans test. We use the worst resolved case ($\mathcal{R} = 2.0$) where self-support is expected to be most significant. Figure 7.13c shows the timescales for the $\mathcal{R} = 2.0$ perturbations with the correction term (closed circles and stars). It can be seen that

including the correction term does improve the timescales of collapsing modes in the sense that they are closer to the analytical solution. However they are still considerably longer than the analytical solution, showing that the under-resolution of forces as discussed in Section 7.5.3 is the main reason for the discrepancy of the timescales. The timescales of oscillating modes are not affected by the correction term.

7.6 Discussion

7.6.1 Artificial viscosity

The isothermal Sod test (Section 7.2), the colliding flows test (Section 7.3) and the shear flow test (Section 7.4) were performed to test how well the different artificial viscosity prescriptions worked in various scenarios.

Standard artificial viscosity has been shown, in both the Sod test and the colliding flows test, to capture shocks and reproduce the analytical results reasonably well. The Balsara switch captures the main features of the shocks in both test cases. However, these tests reveal that even in the most controlled test case, the Balsara factor, f_i is very noisy and this noise can transfer to the density and velocity profiles. This is most clearly seen in the colliding flows test with the Balsara switch (Figures 7.6a and b). This noise is due to the inability of SPH to calculate gradients accurately. This problem can be minimised by using more neighbours in SPH simulations, although clearly this increases the computational cost and/or reduces the resolution. Time-dependent viscosity also successfully reproduces the main features of the shock tube tests. For $\alpha_{\text{MAX}} = 1.0$, the results of the colliding flows test are similar to the Balsara switch. Increasing α_{MAX} to 2.0 improves the results considerably, and they are as good as those with standard artificial viscosity. This suggests that in simulations where strong shocks are expected, we should use $\alpha_{\text{MAX}} = 2.0$ to ensure shocks are captured as accurately as is possible.

The shear flow test clearly shows the problem of shear viscosity in SPH. The standard viscosity case shows that the velocity profile is distorted significantly by shear viscosity. Both the Balsara switch and time-dependent viscosity help to reduce the amount of shear viscosity present, although they do also introduce some noise into the system.

7.6.2 Fragmentation

Simulations of star formation usually consider gas clouds or prestellar cores which are liable to fragment into multiple protostars. Bate & Burkert (1997) showed that self-gravitating SPH codes which use kernel-softened gravity should suppress fragmentation when under-resolved. Whitworth (1998) also showed using analytical arguments that artificial fragmentation will not

occur if the Jeans condition is met. The test presented here reinforces these results showing that at no point does a Jeans-stable perturbation collapse, no matter how poor the resolution. Instead, it is shown that as the resolution decreases, Jeans unstable perturbations become stable and do not collapse. The effective Jeans length increases causing density perturbations which should collapse to be stabilised. This confounds the claims by Klein, Fisher & McKee (2004) that self-gravitating gas clouds will fragment artificially in SPH simulations when under-resolved.

An appropriate resolution limit can be identified from these results if one specifies a maximum tolerance in the timescale error. For example, the Bate & Burkert (1997) condition ($\mathcal{R} \sim 0.8$) gives a typical timescale error of 10% for the growing modes. If a smaller error is preferred, the resolution must be increased.

Chapter 8

Binary formation from turbulent prestellar cores

In this chapter, we present preliminary results from hydrodynamical simulations of turbulent prestellar cores performed using Smoothed Particle Hydrodynamics. We investigate the effect of turbulence on the properties of the stars formed and on the statistical distributions of binary parameters.

Goodwin et al. (2004a, 2004b) perform simulations of prestellar cores with mass $M = 5.4 M_{\odot}$ and with turbulent virial ratio (i.e. the ratio of turbulent kinetic energy to gravitational potential energy) $\alpha_{\text{TURB}} = 0.01, 0.025, 0.05, 0.1$ and 0.25 . We expand this parameter space by performing ensembles of simulations of turbulent prestellar cores with different masses but keeping the turbulent virial ratio constant. We perform 10 simulations for each set of parameters, in order to obtain statistical distributions of the resultant properties. We simulate cores with masses $M = 2.17 M_{\odot}$ and $4.34 M_{\odot}$, and use $\alpha_{\text{TURB}} = 0.2$.

We find that cores of all masses almost always fragment producing a multiple system for simulations with $\alpha_{\text{TURB}} = 0.2$. The average number of objects produced is dependent on the core mass. The ensemble of $2.17 M_{\odot}$ cores produce on average 2.0 ± 0.2 objects per core and the ensemble of $4.34 M_{\odot}$ cores produce on average 2.6 ± 0.3 objects per core. The binary separation distribution for the $2.17 M_{\odot}$ and $4.34 M_{\odot}$ cores is narrower than that found by Goodwin et al. (2004b), and thus also much narrower than the observed distribution. Binaries tend to have nearly-equal mass components ($\bar{q} \approx 0.9$). The average eccentricity of the binaries is also very high ($\bar{e} \approx 0.9$). Overall, the binary statistics from these simulations do not provide a good match with the observations of binary stars, either for young or mature field binaries.

We also use these simulations as a test case to investigate how the different viscosity prescriptions affect realistic simulations of star formation. We find that there are no significant differences between the results using either standard viscosity, the Balsara switch, or time-

dependent viscosity.

We intend to perform further simulations with different values of α_{TURB} for $2.17 M_{\odot}$ and $4.34 M_{\odot}$ cores to extend the parameter space further for this class of simulation.

8.1 Introduction

The fragmentation of a prestellar core into a multiple system is generally accepted as being the dominant formation mechanism for binary stars (see Section 2.5). It is not clear exactly what factors control the fragmentation process or what is the main mode of fragmentation. Possibilities include rotational fragmentation (as considered in Chapter 4; Cha & Whitworth 2003), turbulent fragmentation (e.g. Bate et al. 2002a, Goodwin et al. 2004a, 2004b), collision-induced fragmentation (e.g. Bhattal et al. 1998) and externally-triggered fragmentation (e.g. Hennebelle et al. 2003, 2004) etc. In much of the star formation community, turbulent fragmentation has become the favoured mechanism and has been extensively studied by various authors for all stages of star formation.

Turbulence is a non-linear regime of fluid dynamics where highly complex motions of a fluid are set up due to instabilities within the fluid itself (e.g. the Kelvin-Helmholtz instability). Initially a fluid may move as a uniform flow with constant velocity (called laminar motion), but the instabilities can transfer energy to smaller scales setting up a series of eddy currents; this is referred to as a *turbulent cascade*. Therefore turbulence can be thought of as a process that transfers energy from large scale ordered motion to many smaller-scale motions.

Observations of molecular clouds are highly indicative of turbulent motions. The observed velocity dispersion, Δv , of any region of a molecular cloud is correlated with the size of the region, L , by the simple relation $\Delta v \propto L^{\alpha}$ where $\alpha \approx 0.38$ (Larson 1981; see also Myers 1983). This relation is similar to that expected of turbulent motions in fluids suggesting that turbulence exists in molecular clouds (Larson 1981).

8.1.1 Previous work on turbulent star formation

Numerical investigations into turbulent star formation has been ongoing for the past decade. AMR is well suited to modelling turbulence in fluids whereas SPH is better suited to gravitational collapse problems, so both have been used to model turbulent star formation. Here we summarise the main work that has been performed using SPH, which is our algorithm of choice.

Klessen and collaborators (e.g. Klessen et al. 2000) have investigated the evolution of molecular clouds by driving turbulence throughout the cloud. Driven turbulence requires inputting energy into the molecular cloud. Physically, the energy source may be from magnet-

hydrodynamical waves or possibly due to feedback from stars (for example, by bipolar outflows e.g. Bally et al. 2006). Turbulence is found to support larger regions of the molecular cloud against gravitational collapse while allowing smaller regions (such as prestellar cores) to collapse and form stars.

Bate, Bonnell and collaborators (e.g. Bate et al. 2002a) have investigated the evolution of larger cores ($50 M_{\odot}$ and greater) which are supported by thermal pressure and turbulence. In their simulations, they impose an initial turbulent velocity field but do not include a continuous source of turbulence, as do Klessen and collaborators. The turbulence decays due to shock dissipation within a few dynamical times. They typically take values of α_{TURB} (the ratio of turbulent kinetic energy to gravitational potential energy) to be unity. When account is taken of the thermal energy, the cloud is initially unbound. However, the turbulent energy is dissipated in shocks so that the core eventually becomes gravitationally bound. The shocks produce over-dense regions which are liable to fragment if their mass is greater than the local Jeans mass.

Goodwin et al. (2004a, 2004b) investigate the evolution of lower-mass prestellar cores ($M_{\text{CORE}} = 5.4 M_{\odot}$) which are again supported by thermal pressure and turbulence. Goodwin et al. (2004a, 2004b) use smaller levels of turbulence ($\alpha_{\text{TURB}} \leq 0.25$) similar to those observed in isolated prestellar cores (Jijina et al. 1999). They find that even these relatively low levels of turbulence can promote the fragmentation of star-forming cores. Each core produces on average about 4 – 5 objects (although sometimes as many as 10). These stars then accrete material competitively as they move through the gas in the core. Some of the fragments are ejected before they accrete significant amounts of gas; these ejected protostars are often of such low mass as to be classed as brown dwarfs. Goodwin et al. (2004b) finds that this type of core evolution can produce a rather wide distribution of binary separations (although not as wide as the observations).

8.2 Model

8.2.1 Assumptions and Aims

We assume that prestellar cores fragment due to turbulence in the same way as modelled by Goodwin et al. (2004a, 2004b). We aim to expand the parameter space explored by Goodwin et al. (2004a, 2004b), in particular by extending the range of core masses. We investigate cores with masses $2.17 M_{\odot}$ and $4.34 M_{\odot}$ and keep a fixed value $\alpha_{\text{TURB}} = 0.2$. We aim to use this type of simulation as a case study to investigate how different prescriptions for artificial viscosity affect real simulations of star formation, as opposed to simple tests.

8.2.2 Initial conditions

We base our initial conditions on those used by Goodwin et al. (2004a, 2004b). We retain the same density distribution (although scaled to accommodate a core of different mass), the same temperature (since dense molecular clouds are approximately isothermal with $T \approx 10$ K), the same thermal virial parameter, α_{THERM} , and the same turbulent virial parameter, α_{TURB} . The gas density profile of the core is given by

$$\rho(r) = \frac{\rho_{\text{FLAT}}}{(1 + (r/R_{\text{FLAT}})^2)^2}. \quad (8.1)$$

This is similar to the density profile of a Plummer sphere. This particular profile has a roughly uniform density central region (i.e. a flat density profile) of density ρ_{FLAT} and radius R_{FLAT} . This is sometimes known as the *kernel* (not to be confused with the kernel in SPH). For larger values of r (i.e. $r \gg R_{\text{FLAT}}$), the density profile tends to a power law of the form $\rho \propto r^{-4}$. This density profile is plotted in Figure 8.1.

We retain the same thermal virial parameter, α_{THERM} as used in as the simulations of Goodwin et al. (2004a, 2004b). If we keep the temperature constant, the thermal energy in the cloud is simply proportional to the mass of the cloud, i.e. $U_{\text{THERM}} \propto M_{\text{CORE}}$; the gravitational potential energy of the cloud is related to the mass and radius by $|\Omega| \propto M_{\text{CORE}}^2/R_{\text{CORE}}$. Therefore the thermal virial parameter is related to the mass and radius of the cloud by $\alpha_{\text{THERM}} = U_{\text{THERM}}/|\Omega| \propto R_{\text{CORE}}/M_{\text{CORE}}$. To keep α_{therm} constant the mass and radius of the cloud must be related as $M_{\text{CORE}} \propto R_{\text{CORE}}$. To be consistent with the models of Goodwin et al. (2004a), the central density must scale with the radius of the central region as

$$\rho_{\text{FLAT}} = 3 \times 10^{-18} \text{ g cm}^{-3} \left(\frac{R_{\text{FLAT}}}{5000 \text{ AU}} \right)^{-2}. \quad (8.2)$$

8.2.3 Modelling turbulence in molecular clouds

Turbulence is modelled using a Gaussian random velocity field (e.g. Burkert & Bodenheimer 2000). The scale at which turbulence acts is represented by the wavenumber k ($= 2\pi/\lambda$), rather than wavelength λ . Turbulence transfers energy from larger scales to smaller scales; therefore turbulence acts on many scales. The initial turbulent power spectrum specifies how much energy is in the various scales of the cloud initially. The power spectrum, $P(k)$, is usually expressed as a power law of the form

$$P(k) \propto \begin{cases} 0, & k < k_{\text{MIN}}, \\ k^{-\alpha}, & k \geq k_{\text{MIN}}. \end{cases} \quad (8.3)$$

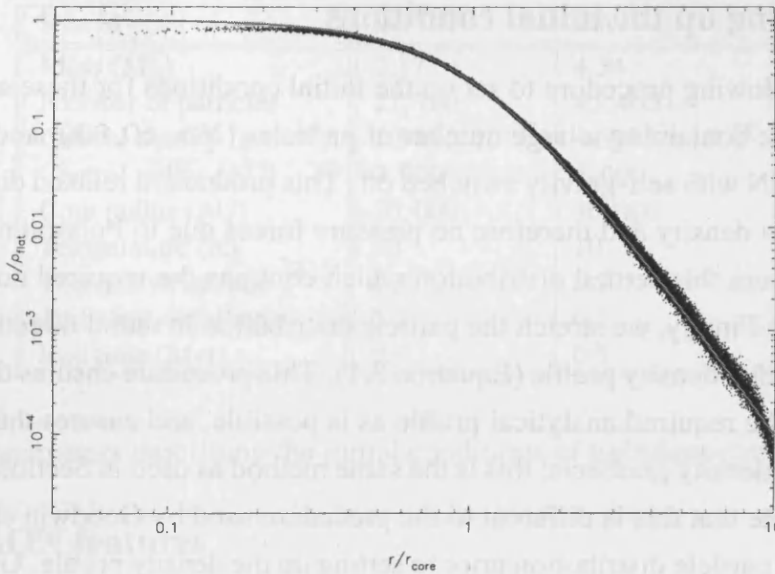


Figure 8.1: The initial density profile of the prestellar cores used in simulations. The solid line shows the analytical density profile (i.e. Equation 8.1) and the points represent the SPH initial density profile.

The minimum wavenumber therefore defines the largest scale which contains turbulent energy (typically the size of the cloud). A turbulent power spectrum with $\alpha = 4$ can reproduce Larson's scaling relation i.e. the size-linewidth relation (e.g. Burkert & Bodenheimer 2000). This form of the turbulent power spectrum is almost universally used in numerical simulations of star formation involving turbulence. This is the same prescription for turbulence as used by Bate et al. (2003a, 2003b) and by Goodwin et al. (2004a, 2004b).

We map the expected velocity field onto a 3-D grid. The velocity of each particle is obtained by linearly interpolating the velocity between grid points. We then scale the velocities of the turbulence so as to obtain the required value of α_{TURB} . We note that scaling the turbulence this way produces a velocity dispersion that does not exactly follow Larson's scaling relations. We refer to the results of Jijina et al. (1999) (See Goodwin et al. 2004a; their Figure 2) which shows there is little correlation between mass and turbulent energy for isolated prestellar cores.

8.2.4 Numerics

The evolution of the cloud is modelled using the Smoothed Particle Hydrodynamics code DRAGON. We used a version of DRAGON which is written using OpenMP, allowing multi-processor parallel jobs to be submitted, and resulting in a significant speed-up in the simulation run-time. We used the new Beowulf cluster in Cardiff to perform our simulations. The main features of SPH, in particular with reference to DRAGON, are described in Chapter 6.

8.2.5 Setting up the initial conditions

We use the following procedure to set up the initial conditions for these simulations. First, we generate a cube containing a large number of particles ($N > 60,000$) and allow them to settle using DRAGON with self-gravity switched off. This produces a relaxed distribution of particles having uniform density and therefore no pressure forces due to Poisson noise. Second, we cut out a sphere from this settled distribution which contains the required number of particles for the simulation. Finally, we stretch the particle distribution in radial directions such as to obtain the required radial density profile (Equation 8.1). This procedure ensures that the density profile is as close to the required analytical profile as is possible, and ensures that any pressure forces are due to real density gradients; this is the same method as used in Section 7.5 to set the density profile. We note that this is different to the procedure used by Goodwin et al. (2004a) who did not relax their particle distribution prior to setting up the density profile. Goodwin et al. (2004a, 2004b) therefore had both turbulence and Poisson noise in their initial conditions. We only have turbulence, so our results are ‘cleaner’.

8.2.6 Resolution

These simulations only model gravitational and hydrodynamical forces; therefore gravitational fragmentation due to the Jeans instability is likely to occur. We must resolve the Jeans length and Jeans mass at all times to ensure that fragmentation is not suppressed by poor resolution (See Section 7.5). The Jeans mass is

$$M_J \approx \rho \lambda_J^3 = \frac{6a_0^3}{G^{3/2} \rho^{1/2}}. \quad (8.4)$$

For isothermal collapse, the Jeans mass decreases as $M_J \propto \rho^{-1/2}$. Once the density of the fragment increases beyond the critical density, ρ_{AD} , the gas becomes opaque. As the fragment collapses further, it responds adiabatically so the temperature increases, i.e. $a \propto \rho^{1/3}$. The Jeans mass is thus related to the density as $M_J \propto \rho^{1/2}$, i.e. the Jeans mass now increases with increasing density. Therefore there exists a minimum Jeans mass at the critical density, $M_{MIN} \approx 0.01M_\odot$. To ensure that the Jeans mass is resolved at all times in the simulation, we must select an appropriate number of particles so that M_{MIN} is always resolved. Using the Bate & Burkert (1997) Jeans condition for SPH with 50 neighbours, the minimum Jeans mass must be equal to the mass of $2N_{NEIB}$ particles, i.e. $2N_{NEIB}m = M_{MIN} = 0.01M_\odot$, so $m = 10^{-4}M_\odot$. Goodwin et al. (2004a, 2004b) use $m = 2 \times 10^{-4}M_\odot$ which is not as well resolved as our simulations.

Run id	U0	UA
Mass (M_{\odot})	2.17	4.34
Number of particles	21,700	43,400
Central density ($g\ cm^{-3}$)	1.875×10^{-17}	4.6875×10^{-18}
Central radius (AU)	2,000	4,000
Core radius (AU)	20,000	40,000
Temperature (K)	10	10
Thermal virial ratio	0.3	0.3
Turbulent virial ratio	0.2	0.2
Run time (Myr)	0.5	0.5

Table 8.1: Parameters describing the initial conditions of turbulent-core simulations.

8.2.7 DRAGON features

Sink particles (Section 6.10.4; Bate et al. 1995) are employed in DRAGON to increase the speed of the simulations. We use a sink density $\rho_{\text{SINK}} = 2 \times 10^3 \rho_{\text{AD}} = 2 \times 10^{-10} g\ cm^{-3}$. Goodwin et al. (2004a, 2004b) use a sink density $\rho_{\text{SINK}} = 10^{-11} g\ cm^{-3}$. The higher sink density is to ensure further dynamical fragmentation is not ignored by implementing the sinks too early in the simulation.

We use three prescriptions for artificial viscosity to test how well they perform and how they affect the results in a typical simulation involving star formation. We test our simulations using (i) standard viscosity (Section 6.7), (ii) the Balsara switch (Section 6.7.1), and (iii) time-dependent viscosity (Section 6.7.2) with parameters $\alpha_{\text{MAX}} = 2$ and $\alpha_* = 0.1$.

Each simulation had a 4 character identification. Simulations using parameters for the $2.17 M_{\odot}$ cores (Table 8.2.8, column 2) had an id of the form U0XX, where XX is a 2-digit number, and simulations using parameters for the $4.34 M_{\odot}$ cores (Table 8.2.8, column 3) had an id of the form UAXX.

8.2.8 Input parameters

Goodwin et al. (2004a, 2004b) model cores with fixed mass, $M = 5.4 M_{\odot}$ and vary the turbulent virial ratio, α_{TURB} , with values 0.01, 0.025, 0.05, 0.1 and 0.25.

We model cores with different masses, $M = 2.17 M_{\odot}$, $4.34 M_{\odot}$ and keep the turbulent virial ratio fixed, $\alpha_{\text{TURB}} = 0.2$. This allows us to investigate the dependence of stellar and binary properties on core mass. The exact parameters for each set of simulations are shown in Table 8.2.8.

The simulations are run for 0.5 Myr, after which time we expect most of the gas to be either accreted or dispersed (i.e. becoming unbound from the central potential well). Goodwin et al.

(2004a, 2004b) follow their cores for 0.3 Myr.

8.3 Results

The results for the parameter set $M = 2.17 M_{\odot}$, $\alpha_{\text{turb}} = 0.2$ (set U0) and parameter set $M = 4.34 M_{\odot}$, $\alpha_{\text{TURB}} = 0.2$ (set UA) are shown in Tables 8.2 and 8.3 respectively. Table 8.4 summarises the statistical properties of the systems produced for each parameter set. Here we limit our description of the results to simulations using standard viscosity.

8.3.1 Number of objects formed

$\overline{N_{\text{obj}}}$ is the mean number of objects formed per core, $\Delta\overline{N_{\text{obj}}}$ is the uncertainty in $\overline{N_{\text{obj}}}$, and σ_N is the standard deviation of N_{obj} about the mean $\overline{N_{\text{obj}}}$. The number of protostars formed is dependent on the mass of the parent core. The average number of objects produced from the ensemble of $2.17 M_{\odot}$ cores is $\overline{N_{\text{obj}}} \pm \Delta\overline{N_{\text{obj}}} = 2.0 \pm 0.2$. For $4.34 M_{\odot}$ cores, $\overline{N_{\text{obj}}} \pm \Delta\overline{N_{\text{obj}}} = 2.6 \pm 0.3$. This increase with respect to mass is expected since higher mass cores will contain a greater number of minimum Jeans-masses. There is more chance for a fragment to become gravitationally unstable to collapse before the core reaches the adiabatic phase and further fragmentation is prevented. The standard deviation of N_{obj} is $\sigma_N = 0.47$ for $2.17 M_{\odot}$ cores and $\sigma_N = 0.81$ for $4.34 M_{\odot}$ cores. Higher mass cores thus produce a greater statistical spread of object numbers. Goodwin et al. (2004b) found that for $5.4 M_{\odot}$ cores with $\alpha_{\text{TURB}} = 0.25$ (the closest to our value of $\alpha_{\text{TURB}} = 0.2$), the average number of objects produced was $\overline{N_{\text{obj}}} \pm \Delta\overline{N_{\text{obj}}} = 6.0 \pm 0.5$. This follows with the trend that increasing M_{CORE} increases $\overline{N_{\text{obj}}}$, although this is a relatively large difference compared to the jump from $2.17 M_{\odot}$ to $4.34 M_{\odot}$. This large increase suggests that the differences between the initial conditions and parameters of these simulations (i.e. higher resolution, relaxed particle distribution, higher sink density) may affect the results systematically. An alternative explanation is that the number of objects formed is simply due to the difference in α_{TURB} , although this would require a steep dependence between N_{obj} and α_{TURB} . I plan on performing further simulations of $5.4 M_{\odot}$ solar mass cores to confirm if this is the case. Goodwin et al. (2004b) also obtain a larger standard deviation, $\sigma_N = 2.2$.

8.3.2 Mass distribution

Figure 8.2 shows the mass distribution resulting from the ensemble of $2.17 M_{\odot}$ and $4.34 M_{\odot}$ turbulent cores. The stellar mass distribution resulting from the lower-mass cores ($2.17 M_{\odot}$, Figure 8.2a) is a very narrow peak with the majority of stars in a single bin ($-0.25 \leq \log_{10} M \leq 0.0$). This is because most cores fragment into two relatively close protostars; they both accrete

Run id	Viscosity	N_{obj}	System	M/M_{\odot}	a/AU	e	q	T/yrs
U001	ST	2	Binary	0.90, 0.87	64.6	0.97	0.97	389
	BS	1	Single	1.79				
	TD	2	Binary	0.88, 0.84	22.9	0.83	0.95	83.9
U002	ST	1	Single	1.86				
	BS	2	Binary	0.84, 0.82	36.2	0.91	0.97	169
	TD	2	Binary	0.91, 0.84	55.8	0.94	0.92	316
U003	ST	2	Binary	0.90, 0.89	43.7	0.92	0.99	216
	BS	2	Binary	1.43, 0.044	781	0.86	0.031	17,983
	TD	2	Binary	0.91, 0.86	46.6	0.93	0.95	239
U004	ST	2	Binary	0.88, 0.85	10.0	0.37	0.97	24
	BS	2	Binary	0.90, 0.81	55	0.95	0.90	306
	TD	2	Binary	0.99, 0.78	38	0.90	0.78	173
U005	ST	2	Binary	0.919, 0.844	59.4	0.957	0.918	344
	BS	1	Single	0.18				
	TD	2	Binary	1.21, 0.59	83.0	0.98	0.48	564
U006	ST	2	Binary	1.17, 0.60	49.8	0.934	0.513	263
	BS	2	Binary	0.92, 0.82	73	0.97	0.89	468
	TD	2	Binary	0.90, 0.89	40.5	0.91	0.99	192
U007	ST	2	Binary	0.86, 0.85	66.8	0.98	0.98	417
	BS	1	Single	1.81				
	TD	2	Binary	0.90, 0.85	53	0.95	0.94	287
U008	ST	2	Binary	0.93, 0.84	33.3	0.88	0.90	144
	BS	2	Binary	0.88, 0.86	60.7	0.96	0.98	359
	TD	2	Binary	0.91, 0.86	22.3	0.79	0.95	79
U009	ST	2	Binary	0.92, 0.76	67.6	0.97	0.83	429
	BS	2	Single	1.24				
			Single	0.080				
TD	2	Binary	0.97, 0.80	56.4	0.98	0.82	319	
U010	ST	3	Binary	0.526, 0.523	9.75	0.76	0.99	29.7
			Single	0.49				
	BS	2	Binary	0.90, 0.87	28.2	0.83	0.96	113
	TD	2	Binary	0.88, 0.87	22.8	0.81	0.99	82.5

Table 8.2: Systems formed in simulations of turbulent cores with mass $M_{\text{CORE}} = 2.17 M_{\odot}$ and with turbulent virial ratio $\alpha_{\text{TURB}} = 0.2$. Each set of initial conditions is simulated using the three different viscosities, Standard Viscosity (ST), the Balsara switch (BS), and time-dependent viscosity (TD).

Run id	Viscosity	N_{obj}	System	M/M_{\odot}	a/AU	e	q	T/yrs
UA01	ST	2	Binary	1.78, 1.70	129	0.989	0.956	789
	BS	2	Binary	1.77, 1.70	113	0.976	0.960	643
	TD	3	Binary Single	1.06, 1.03 0.43	71.5	0.955	0.972	419
UA02	ST	4	Binary Single Single	1.59, 1.53 0.0361 0.0430	650.0	0.98	0.96	297
	BS	2	Binary	1.75, 1.73	27.1	0.797	0.989	75.6
	TD	2	Binary	1.84, 1.56	58.4	0.98	0.849	242
UA03	ST	3	Binary Single	1.42, 1.35 0.263	26.8	0.62	0.95	83.5
	BS	3	Binary Single	1.03, 0.76 0.56	137	0.993	0.738	1198
	TD	3	Binary Single	1.62, 1.50 0.090	72.6	0.94	0.93	350
UA04	ST	3	Binary Single	0.85, 0.75 0.51	23.0	0.85	0.88	87.4
	BS TD	2	Binary	1.75, 1.73	95.2	0.966	0.989	498
UA05	ST	2	Binary	1.81, 1.57	138	0.99	0.87	877
	BS	2	Binary	1.75, 1.74	71.7	0.93	0.99	325
	TD	4	Triple Single	0.91, 0.89 B, 0.030 0.753	47.8 1, 672	0.95 0.72	0.98 0.017	24.6 50, 453
UA06	ST	1	Single	3.591				
	BS	1	Single	3.021				
	TD	1	Single	3.605				
UA07	ST	3	Binary Single	0.71, 0.71 0.44	65.7	0.92	0.99	447
	BS TD	2	Binary	2.39, 1.098	141	0.99	0.46	898
UA08	ST	3	Binary Single	1.67, 1.64 0.046	37.8	0.83	0.98	128
	BS TD							
UA09	ST	2	Binary	1.90, 1.57	159	0.99	0.83	1,073
	BS	2	Binary	1.74, 1.74	122	0.99	0.999	722
	TD	2	Binary	1.84, 1.66	143	0.99	0.90	919
UA10	ST	2	Binary	1.82, 1.66	170	0.99	0.91	1,186
	BS	2	Binary	1.98, 1.49	146	0.99	0.75	947
	TD	3	Binary	1.70, 1.65	55.4	0.92	0.97	225

Table 8.3: Systems formed in simulations of turbulent cores with mass $M_{\text{CORE}} = 4.38 M_{\odot}$ and with turbulent virial ratio $\alpha_{\text{TURB}} = 0.2$. Each set of initial conditions is simulated using the three different viscosities, Standard Viscosity (ST), the Balsara switch (BS), and time-dependent viscosity (TD).

Run id	$M_{\text{CORE}}/M_{\odot}$	Viscosity	N_{sims}	$\overline{N_{\text{obj}}} \pm \Delta N_{\text{obj}}$	σ_N	$\overline{\log_{10} a} \pm \Delta \log_{10} a$	$\sigma_{\log a}$	\bar{e}	\bar{q}
U0	2.17	ST	10	2.00 ± 0.16	0.47	1.57 ± 0.11	0.38	0.86	0.90
		BS	10	1.7 ± 0.15	0.46	1.68 ± 0.07	0.16	0.91	0.79
		TD	10	2.00 ± 0.00	0.00	1.60 ± 0.06	0.17	0.90	0.88
UA	4.34	ST	10	2.50 ± 0.25	0.81	1.96 ± 0.15	0.46	0.91	0.93
		BS	8	2.00 ± 0.18	0.50	1.96 ± 0.09	0.22	0.95	0.92
		TD	8	2.50 ± 0.31	0.87	1.90 ± 0.05	0.14	0.93	0.87

Table 8.4: Summary of main results of turbulent core simulations. The columns from left to right: Run id - the parameter set id; M_{core} - the initial core mass; Viscosity - the viscosity used (ST - Standard, BS - Balsara switch, TD - time-dependent viscosity); N_{sims} - the total number of simulations in the ensemble; $\overline{N_{\text{obj}}} \pm \Delta N_{\text{obj}}$ - the mean number of objects (plus uncertainty); σ_N - the standard deviation of the object number; $\overline{\log_{10} a} \pm \Delta \log_{10} a$ - the mean of the logarithm of the separation (plus uncertainty); $\sigma_{\log a}$ - the standard deviation of $\log_{10} a$; \bar{e} - the mean eccentricity; \bar{q} - the mean mass-ratio.

material at approximately the same rate (since they share the same potential well) and therefore grow to the same mass.

The stellar mass distribution resulting from the higher-mass cores ($4.34 M_{\odot}$, Figure 8.2b) is noticeably wider than for lower-mass cores. Higher-mass cores fragment into a larger number of objects. For $N_{\text{obj}} > 2$, the dynamical evolution of the fragments is non-linear so the accretion rate is more stochastic. This allows for the creation of different mass objects as opposed to equal-mass objects. The standard deviation of N_{obj} is also larger so there will be a greater spread of masses due to the greater spread of object numbers.

Goodwin et al. (2004b) obtain a mass distribution for $5.4 M_{\odot}$ cores (their Figure 3, bottom panel) which is comparable to our mass-distribution for $4.34 M_{\odot}$ cores for $M > 0.1 M_{\odot}$. Both graphs show a peak at around $1 M_{\odot}$ and have a similar width. The main difference is that Goodwin et al. (2004b) also produces a tail of low-mass objects. This tail consists almost entirely of unbound, ejected protostars. Since Goodwin et al. (2004b) produce more objects per core, there is a greater chance of some objects being dynamically ejected from the core; this will likely occur before an object has the chance to accrete a significant amount of material. The mass-distribution, and in particular the number of low-mass stars formed, is highly dependent on the number of objects formed. Further simulations of $5.4 M_{\odot}$ cores will clarify this.

8.3.3 Binary separation distribution

Figure 8.3 shows the binary separation distribution resulting from the evolution of $2.17 M_{\odot}$ and $4.34 M_{\odot}$ turbulent cores. The low-number of simulations and binaries produced requires large bin sizes. Also, we have not divided the sample into different mass-ranges.

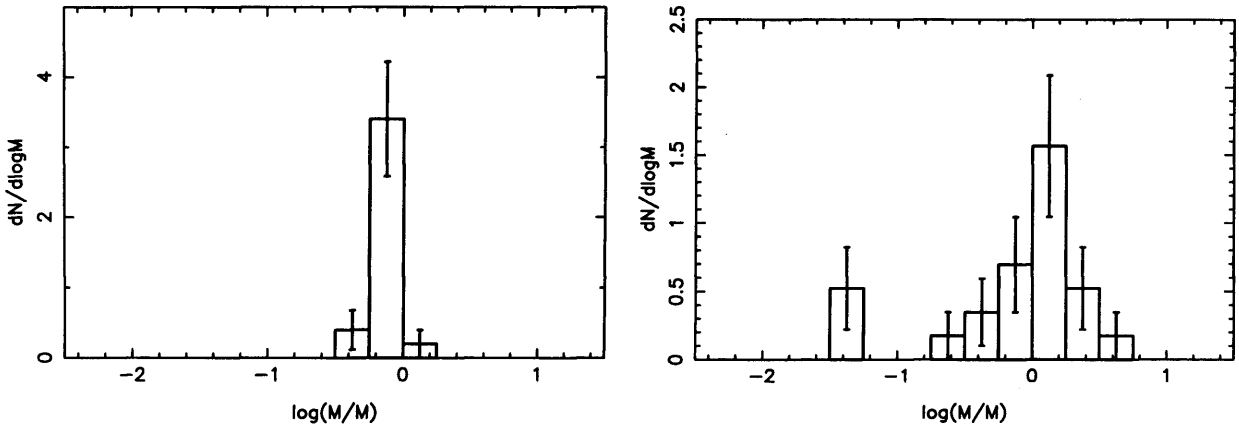


Figure 8.2: The mass distribution, $dN/d \log_{10} M$, resulting from turbulent cores with masses (a) $2.17 M_{\odot}$, and (b) $4.34 M_{\odot}$. All cores have an initial turbulent virial ratio $\alpha_{\text{TURB}} = 0.2$.

The binary separation distribution resulting from $2.17 M_{\odot}$ cores (Figure 8.3a) is very narrow ($\sigma_{\log a} = 0.38$), with the majority of binaries in the bin spanning separations $10 \text{ AU} \leq a \leq 100 \text{ AU}$. This is considerably narrower than the observed separation distribution (e.g. Patience et al. 2002 - dashed line on Figure 8.3). This is due to the fact that a $2.17 M_{\odot}$ core with $\alpha_{\text{TURB}} = 0.2$ will have some residual angular momentum (Burkert & Bodenheimer 2000). The range of possible angular momentum is quite small. If these cores fragment into two objects, the separation of the binary (which will be determined somewhat by the angular momentum) will also fall in a narrow range.

The binary separation distribution for the higher-mass cores ($4.34 M_{\odot}$, Figure 8.3b) covers a larger range of values ($\sigma_{\log a} = 0.46$) than the distribution for the lower-mass cores. Binaries now occupy the bins in the separation range $10 \text{ AU} \leq a \leq 1000 \text{ AU}$. This increase is mainly due to the greater number of objects formed in these cores, plus the greater spread in object numbers. Cores with two objects will form a binary where the separation is determined by the specific angular momentum of the accreted material. When three or more objects are formed, some angular momentum will necessarily be removed when stars are ejected. This hardens the remaining binary (i.e. reduces the separation). A spread of object numbers therefore produces a greater spread in binary separations (This is the same effect that happens in the pure N-body simulations in Chapter 4, see Figure 4.3). We note that in this case the average value of $\log a$ is greater for the $4.34 M_{\odot}$ cores than for the $2.17 M_{\odot}$ cores (Table 8.4). This is because the radius of the core has increased by a factor of two and so the average binary separation is increased by a similar amount.

The binary separation distribution found by Goodwin et al. (2004b) covers approximately two and a half orders of magnitude in separation, from approximately 5 AU (the sink radius) up to approximately 10^3 AU (the size of the central region of the core). The greater spread in binary

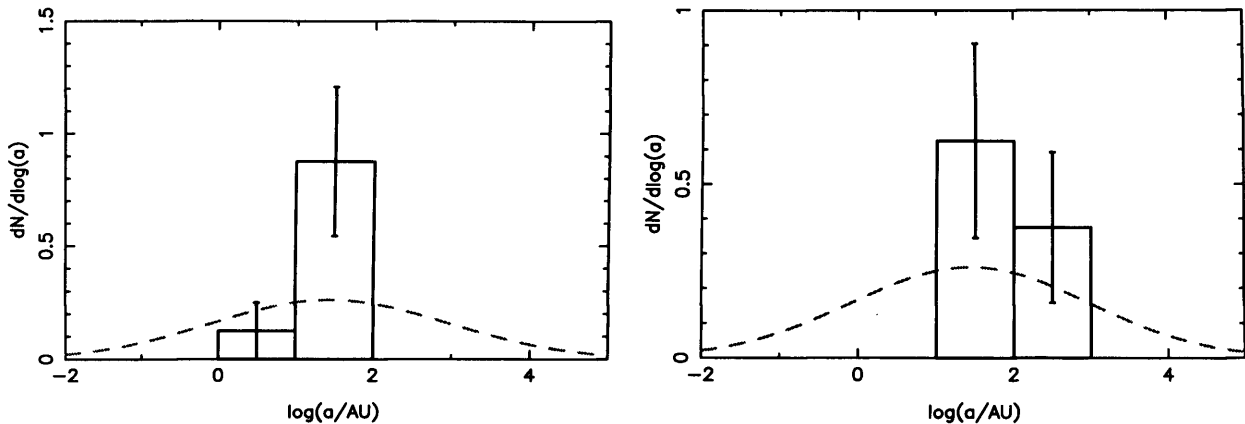


Figure 8.3: The distribution of binary separations, $dN/d \log_{10} a$, resulting from turbulent cores with masses (a) $2.17 M_{\odot}$, and (b) $4.34 M_{\odot}$. All cores have an initial turbulent virial ratio $\alpha_{\text{TURB}} = 0.2$. The dashed line shows the separation distribution of PMS binaries (Patience et al. 2002). The curve and the histogram are normalised to contain unit area rather than to the multiplicity.

separations is due to those reasons discussed in the previous paragraph (i.e. high- N_{obj} results in hardening of binaries and spread of separations). The larger number of objects produced in $5.4 M_{\odot}$ cores leads to a larger spread in resultant separations.

8.3.4 Eccentricity distribution

The eccentricity of the binaries produced is shown in Tables 8.2 and 8.3 (Column 7). The majority of binaries produced for both the $2.17 M_{\odot}$ and $4.34 M_{\odot}$ have eccentricities greater than 0.8 and have an average value of 0.86 and 0.91 respectively. There are very few low eccentricity binaries produced in these simulations, contrary to the observations (See Section 2.4.5).

8.3.5 Mass-ratio distribution

The mass-ratio of the binaries produced is shown in Tables 8.2 and 8.3 (Column 8). The majority of binaries produced for both the $2.17 M_{\odot}$ and $4.34 M_{\odot}$ have roughly equal mass-components (i.e. $q \approx 1$). As with the eccentricity distribution, this is contrary to the observations (See Section 2.4.4). The proto-stellar seeds first form in a region very close to the centre of the core and thus in the middle of the potential well of the core. As the gas falls into the centre of the core, the two fragments accrete roughly equal amounts of matter, and therefore form approximately equal mass components.

8.4 Discussion

8.4.1 Multiplicity

The number of stars produced per core, \mathcal{N}_{obj} , and its standard deviation, $\sigma_{\mathcal{N}}$, can influence most of the final stellar and binary properties (as shown in Chapter 4 for the decay of small-N clusters). We should expect the overall distribution of binary properties to be dependent on the distribution of \mathcal{N}_{obj} and $\sigma_{\mathcal{N}}$ with core mass.

Our simulations show that the average number of objects appears to increase with increasing core mass. This is expected since lower-mass cores contain fewer minimum Jeans masses, (M_{MIN}), and thus have a lower chance of fragmenting into multiple objects.

Goodwin et al. (2004a, 2004b) found that increasing the levels of turbulence increased the average number of objects produced per core. He found that a minimum threshold of $\alpha_{\text{TURB}} = 0.05$ was required to induce fragmentation. Due to the smaller values of \mathcal{N}_{obj} , we may expect the threshold value of α_{TURB} for fragmentation to be higher for lower-mass cores.

The simulations of small-N clusters performed in Chapter 4 assumed a constant number of fragments. The work in this Chapter, plus that Goodwin et al. (2004a, 2004b) shows that this assumption may be an over-simplification, although simulations of different mass rotating cores should be performed to gain more insight.

8.4.2 Binary separation distribution

The binary separation distribution cannot be reproduced using a single core mass and a single value of α_{TURB} . Our simulations show that separations of binaries covers around two orders of magnitude; The simulations of Goodwin et al. (2004a, 2004b) for $5.4 M_{\odot}$ cores produce binaries that cover about three orders of magnitude in separation. We require a distribution of α_{TURB} values in order to be able to reproduce the observed binary separation distribution (this is analogous to the assumptions in Chapter 4 about having a distribution of β values). We must first perform simulations of turbulent cores with different values of α_{TURB} for different mass cores.

8.4.3 Eccentricity and mass-ratio distributions

The eccentricity and mass-ratio distributions from our simulations do not match the observations very well. Almost all the binaries produced have equal mass components and highly eccentric orbits. Goodwin et al. (2004a, 2004b) noted that simulations with lower levels of turbulence tended to result in a flatter distribution of mass-ratios. This suggests again the need to perform simulations with different values of α_{TURB} .

8.4.4 Viscosity

Due to the non-linear nature of the equations of self-gravitating hydrodynamics, any small change in the initial conditions of each individual simulation or any change in the algorithm used can alter the final outcome of the simulation. We expect that changing the viscosity prescription could change the stellar and binary properties at the end of the simulation. It is thus prudent to compare the statistical properties of each ensemble of runs rather than compare the results of individual runs with different viscosities.

There are no significant differences between the simulations with the standard artificial viscosity and those involving the Balsara switch. However, for both parameter sets, invoking the Balsara switch does produce on average fewer objects than both the standard artificial viscosity and the time-dependent artificial viscosity cases, although the difference is only about 2σ in both cases. The time-dependent artificial viscosity case produces roughly the same average number of fragments per core as the standard artificial viscosity simulations.

There are some differences in the separation distribution between simulations with different viscosities. The average value of the logarithm of the separation, $\log_{10} a$, is approximately the same between the different viscosity prescription. However, in both the $2.17 M_{\odot}$ and $4.34 M_{\odot}$ cores, the standard deviation of $\log_{10} a$, $\sigma_{\log a}$, is dependent on the viscosity used. The value of $\sigma_{\log a}$ when using standard viscosity is approximately double that obtained when using either the Balsara switch or time-dependent viscosity.

8.4.5 Future work

We plan to perform further simulations of turbulent cores in order to expand the parameter space explored so far by this work and by Goodwin et al. (2004a, 2004b). Initially, we plan to perform further simulations of $2.17 M_{\odot}$, $4.34 M_{\odot}$ prestellar cores with different values of the turbulent virial ratio, $\alpha_{\text{TURB}} = 0.1$ and 0.05 . It is also desirable to improve the statistics of the parameter sets we have explored in this work by performing more realisations.

8.5 Summary

We extend the work of Goodwin et al. (2004a, 2004b) by performing simulations of turbulent prestellar cores with masses $2.17 M_{\odot}$ and $4.34 M_{\odot}$, and with turbulent virial ratio $\alpha_{\text{TURB}} = 0.2$. We perform ten realisations of each parameter set and compare the statistics to previous work, and to the observations. The main results are summarised below.

1. $2.17 M_{\odot}$ prestellar cores with $\alpha_{\text{TURB}} = 0.2$ fragment on average into two objects, which almost always results in a bound binary system. Higher-mass cores ($4.34 M_{\odot}$) fragment

into two or three objects, usually resulting in a bound binary system with an ejected single. This single star is typically the lowest mass object produced (i.e. dynamical biasing; McDonald & Clarke 1993)

2. The mass distribution of stars resulting from $2.17 M_{\odot}$ cores is extremely narrow. When the core fragments into two objects, these objects accrete at a roughly equal rate producing two equal-mass stars, typically of mass $\sim 1 M_{\odot}$. As a consequence, the mass-ratios of binaries produced is usually near unity. Higher-mass cores have a larger number of fragmentation paths and thus produces a larger spread in the masses of any objects produced.
3. The separations of the binaries produced occupy a narrow range of values between ~ 10 AU and $\sim 10^3$ AU. This is much narrower than the observed separation distribution (e.g. Duquennoy & Mayor 1991). This is due to using only a single value of α_{TURB} .
4. The eccentricity distribution and mass-ratio distribution are both highly skewed towards unity and thus do not reproduce the observed distributions very well. Goodwin et al. (2004b) found that higher values of α_{TURB} resulted in more equal-mass binaries. This suggests that reducing α_{TURB} may produce a mass-ratio distribution closer to the observations.
5. We plan to extend the explored parameter space further to include simulations of $2.17 M_{\odot}$, $4.34 M_{\odot}$ cores using different values of α_{TURB} .

Chapter 9

Summary

9.1 Observations of Binary stars

In Chapter 2, we performed a literature review of binary star observations and discussed the main findings. In brief, the main results were:

1. Binary stars are as common, if not more common, than single stars for solar-mass primary stars in the field. There is an apparent trend of increasing multiplicity with increasing primary mass. The multiplicity frequency for M-dwarf, K-dwarf and G-dwarf primaries in the solar vicinity is 0.42 ± 0.09 , 0.45 ± 0.07 and 0.57 ± 0.08 respectively.
2. The multiplicity of stars in low-mass star forming regions like Taurus appears to be very high ($\mathbf{mf} \geq 90\%$). In comparison, the multiplicity of stars in high-mass star forming regions like Orion appears to be of order that of the field, if not lower. This suggests that binary properties are dependent on the star formation environment in which they are born.
3. The field-binary separation distributions for M-dwarf, K-dwarf and G-dwarf primaries are approximately lognormal over a large range of spatial scales (from 10^{-2} AU up to 10^5 AU) peaking at $a \approx 20$ AU. The binary separation distribution for pre-Main Sequence stars in low-mass star forming regions like Taurus has a similar form peaking in the range $a \approx 50 - 100$ AU.
4. The principal mechanism of binary star formation is believed to be fragmentation of prestellar cores within molecular clouds. The most favourable of the various models is turbulent fragmentation.

9.2 Binary star formation from Ring Fragmentation

In Chapter 4, we performed numerical N-body simulations of small-N clusters in the context of binary star formation. We assumed that a prestellar core fragments into a ring of \mathcal{N} protostars. This newly-formed small-N cluster then decays due to gravitational interactions forming an ensemble of multiple systems and single stars. We assumed a distribution of core rotations constrained by observations, and produced statistical distributions of the binary parameters which we then compared to the observations. The main results were:

1. N-body simulations show that rings dissolve typically after a few tens of dynamical crossing times. The decaying cluster produces binary stars, multiple stars and ejected singles. (Table 4.1).
2. We obtain a multiplicity distribution using our model which is consistent with that of pre-Main Sequence primaries in low-density regions like Taurus.
3. We can reproduce the separation distribution of PMS stars, such as in Taurus, by assuming that the distribution of core rotation rates, parameterized by β (the ratio of rotational to gravitational potential energy), is lognormal. We must extend the distribution of β to lower values than the observed distribution to match the separation distribution correctly. We assume lower- β cores are not detected due to selection effects.
4. The discrepancy between the PMS and field binary populations is assumed to be due to interactions between binaries in a larger cluster, which is not modelled here.

This model is the first that can successfully explain the origin of the binary star statistics in isolated star forming regions, such as Taurus, and using observational constraints, and with a minimum of free parameters. This work has been published in *A&A* (Hubber & Whitworth 2005).

9.3 Binary star formation in a cluster environment

In Chapter 5, we extend the model of Chapter 4 by including the effects of the cluster environment. Following observations, we model many small-N clusters in a larger cluster environment and observe the effect on the binary statistics. In contrast to previous work in this field (e.g. Kroupa 1995a), we use fractal clusters. The main results are:

1. Interactions between binaries and stars in clusters can destroy binaries and therefore reduce the multiplicity in the cluster. The efficiency of binary disruption increases with increasing stellar density.

2. Wide, soft (i.e. low-binding energy) binaries are disrupted more often than tight, hard binaries. The separation distribution of binaries is affected by shifting the peak value to lower separations. However, no significant hardening of binaries occurs, i.e. the binary separations are not reduced considerably by dynamical interactions.
3. Clusters with lower-fractal dimension (and hence more substructure) disrupt low mass-ratio binaries more frequently than uniform clusters.

This model demonstrates that the amount of sub-structure in a cluster can affect the final binary properties. Since observations suggest young clusters are fractal, this work may represent a more realistic treatment of the initial conditions of young clusters than spherically symmetric equilibrium clusters, such as those used by Kroupa (1995a, b).

9.4 Tests of Smoothed Particle Hydrodynamics

In Chapter 7, we performed tests of the Smoothed Particle Hydrodynamics (Chapter 6) code DRAGON. In particular, we investigated the effectiveness of the artificial viscosity prescription used, and also on the ability of SPH to resolve gravitational fragmentation correctly (The Jeans Test). The main results were:

1. Despite its inherent limitations, SPH can capture shocks well using standard artificial viscosity. However, tests using shear flows show that the effects of unwanted artificial shear viscosity are significant. This affects the transport of angular momentum in discs.
2. The Balsara switch, which is designed to only switch on viscosity in genuine shocks, can also capture shocks well. The effects of shear viscosity are reduced, although still present.
3. Time-dependent viscosity captures shocks well, but only using viscosity parameters higher than those suggested by Morris & Monaghan (1997). The effects of shear viscosity are reduced but not eliminated, similar to when using the Balsara switch.
4. The Jeans test shows that well-resolved SPH simulations model gravitational fragmentation very well. Under-resolved SPH prohibits real fragmentation rather than promoting artificial fragmentation.

The Jeans test has contributed to the debate over whether SPH can accurately model gravitational fragmentation, and hence whether SPH simulations give tenable results. This work places confidence in SPH that simulations (previous and current) give accurate results. This work has been published by A&A (Hubber, Goodwin & Whitworth 2006).

9.5 Simulations of turbulent prestellar cores

In Chapter 8, we perform simulations of turbulent prestellar cores extending the work of Goodwin et al. (2004a, 2004b). We explore the fragmentation of $2.17 M_{\odot}$ and $4.34 M_{\odot}$ cores with relatively low levels of turbulence. We also perform simulations using the Balsara switch and time-dependent viscosity. The main results are:

1. Lower-mass ($2.17 M_{\odot}$) cores fragment on average producing a bound binary system. Higher-mass ($4.34 M_{\odot}$) cores often fragment into 3 components resulting in a binary system with an ejected single. As with the pure N-body simulations, the ejected single is typically the lowest-mass object of the system.
2. The mass distribution of stars produced by $2.17 M_{\odot}$ cores is extremely narrow. Most objects have masses $\sim 1 M_{\odot}$. The higher mass cores have a wider spread of masses due to the spread in objects produced.
3. The separation distribution is very narrow in comparison to the observations. A spread of core masses and turbulence used could widen this distribution.

9.6 Future work

9.6.1 N-body codes

I plan to explore using alternative N-body codes in the future. In particular I plan to use the freely available STARLAB suite. STARLAB contains an N-body integrator called KIRA. KIRA uses the Hermite integration scheme (Section 3.3.2), similar to the NBODY series, but does not include any of the regularisation algorithms which greatly simplifies the coding. Alternative treatments of close-encounters are employed to ensure accurate computation of the orbits and small integration errors. However the smaller amount of code present makes the process of adding and modifying subroutines less laborious compared to working with the NBODY codes. If STARLAB is not appropriate for my work or does not include the desired features, in particular the ability to perform multiple simulations to obtain statistical distributions, I will consider writing my own code based on the Hermite integration scheme and other features described in Chapter 3.

9.6.2 N-body simulations

I plan to continue the simulations of fractal clusters and expand the parameter space already explored in Chapter 5. This would include simulating clusters with different fractal dimensions

and different numbers of stars. I would like to increase the number of simulations performed for each parameter set to improve the results and obtain better statistics of the resulting properties.

9.6.3 SPH codes

I will continue to help developing the Cardiff star formation group SPH code, DRAGON. There are a number of features which I would like to implement to improve the code. These include the Godunov-SPH algorithm (e.g. Cha & Whitworth 2003a) which eliminates the need for artificial viscosity and thus removes any associated problems. I plan to include a more realistic equation of state for the low-density ISM, as opposed to the simple isothermal equation of state commonly used for molecular clouds.

I plan to investigate how well SPH captures the turbulent velocity field and more importantly how well SPH models important hydrodynamical instabilities such as the Rayleigh-Taylor and Kelvin-Helmholtz instabilities. These are, amongst others, likely to be important in determining the cascade of turbulent energy to lower scales and the formation of clumps and cores.

I plan to implement an improved treatment of sink particles in DRAGON. Sinks should represent the formation of a gravitationally bound hydrostatic core which is certain to form a star. However, sink particles currently do not feel or exert pressure forces and only feel gravitational forces. This can result in an artificially high accretion rate which will affect the simulation results. Boyd (PhD thesis 2003) developed a more sophisticated sink which does interact hydrostatically with neighbouring particles, and also includes treatments of discs and outflows. This may provide the basis for future treatment of sinks.

9.6.4 SPH simulations

I will continue to perform simulations of turbulent prestellar cores expanding the work performed in Chapter 8. I intend to perform more simulations of the parameter space already explored to obtain similar statistics to that of Goodwin et al. (2004a, 2004b), i.e. 20 simulations per parameter set. I also intend to expand the parameter space performing simulations with different values of α_{TURB} , and different mass cores, and attempt to extract useful theorems, for example the dependence of mean stellar mass on core mass.

As discussed in Chapter 2, the properties of binary stars are likely to be determined by the properties of their parent prestellar cores, and the properties of the prestellar cores are likely to be determined by the properties of their parent molecular cloud. I intend to investigate, using hydrodynamical simulations, the factors that influence the properties of prestellar cores (e.g. the mass spectrum, the angular-momentum distribution, the density distribution etc..) in molecular clouds and how the properties of these cores compare with observations.

Bibliography

- [1] Aarseth, S. J., 1963, MNRAS, 126, 223
- [2] Aarseth, S. J., 1999, PASP, 111, 1333
- [3] Aarseth, S. J., 2001a, in 'The Restless Universe', ed. B.A. Steves & A.J. Maciejewski, IoP, p. 93
- [4] Aarseth, S. J., 2001b, NewA, 6, 277
- [5] Aarseth, S. J. & Zare, K., 1974, Celestial Mechanics, 10, 185
- [6] Ahmad, A. & Cohen, L., 1973, J. Comp. Phys., 12, 389
- [7] André, P., Ward-Thompson, D. & Barsony, B., 1993, ApJ, 406, 122
- [8] André, P., Ward-Thompson, D. & Barsony, B., 2000, "Protostars and Planets IV", ed. Mannings, V., Boss, A. P. & Russell, S. S., The University of Arizona Press, p. 59
- [9] Bally, J., Reipurth, B. & David, C. J., 2006, "Protostars and Planets V", in press
- [10] Balsara, D. S., 1995, JCompPhys, 121, 357
- [11] Barnes, J., Hut, P., 1986, Nature, 324, 446
- [12] Barsony, M., Koresko, C. & Matthews, K., 2003, ApJ, 591, 1064
- [13] Bate, M. R., Bonnell, I. A. & Price, N. M., 1995, 277, 362
- [14] Bate, M. R., Burkert, A., 1997, MNRAS, 288, 1060
- [15] Bate, M. R., 2000, MNRAS, 314, 33
- [16] Bate, M. R., Bonnell, I. A. & Bromm, V., 2002a, 332, 65
- [17] Bate, M. R., Bonnell, I. A. & Bromm, V., 2002b, 336, 659

- [18] Bate, M. R., Bonnell, I. A. & Bromm, V., 2002c, 336, 705
- [19] Bate, M. R., Bonnell, I. A. & Bromm, V., 2003, MNRAS, 339, 577
- [20] Bhattal, A. S., Francis, N., Watkins, S. J. & Whitworth, A. P., 1998, MNRAS, 297, 435
- [21] Binney, J, Tremaine, S., 1987, 'Galactic Dynamics' (Princeton University Press; Princeton, NJ, USA)
- [22] Blitz, L. & Williams, J. P., 1999, in 'The Origin of Stars and Planetary Systems', ed. Lada, C. J. & Kylafis, N. D., Kluwer Academic Publishers, p. 3
- [23] Boffin, H. M. J., Watkins, S. J., Bhattal, A. S., Francis, N. & Whitworth, A. P., 1998, MNRAS, 300, 1189
- [24] Bonnell, I. A. & Bate, M. R., 1994, MNRAS, 271, 99
- [25] Bonnell, I. A., Vine, S. G., Bate, M. R., 2004, MNRAS, 349, 735
- [26] Bontemps, S., André, P., Terebey, S., Cabrit, S., 1996, A&A, 311, 858
- [27] Bouvier, J., Rigaut, F. & Nadeau, D., 1997, A&A, 323, 139
- [28] Bouvier, J., Duchêne, G., Mermilliod, J.-C. & Simon, T., 2001, A&A, 375, 989
- [29] Boss, A. P., Bodenheimer, P., 1979, ApJ, 234, 289
- [30] Boyd, D. F. A., 2003, 'Modelling Feedback in Turbulent Cloud Cores' PhD Thesis
- [31] Brandner, W. & Köhler, R., 1998, ApJ, 499, 79
- [32] Briceño, C., Luhman, K. L., Hartmann, L., Stauffer, J. R., Kirkpatrick, J. D., 2002, ApJ, 580, 31
- [33] Burkert, A. & Bodenheimer, P., 1993, MNRAS, 264, 798
- [34] Burkert, A. & Bodenheimer, P., 2000, ApJ, 543, 822
- [35] Cartwright, A. & Whitworth, A. P., 2004, MNRAS, 348, 589
- [36] Cha, S.-H. & Whitworth, A. P. 2003a, MNRAS, 340, 73
- [37] Cha, S.-H. & Whitworth, A. P. 2003b, MNRAS, 340, 91
- [38] Courant, R., Friedrichs, K. O. & Lewy, H. 1928, 1967, "On the partial difference equations of mathematical physics", IBM journal, 11, 215

- [39] Clark, P. C., Bonnell, I. A., 2004, MNRAS, 347, L36
- [40] Clarke, C. J. & Pringle, J. E., 1993, MNRAS, 261, 190
- [41] Delgado-Donate, E. J., Clarke, C. J. & Bate, M. R. 2003, MNRAS, 342, 926
- [42] Delgado-Donate, E., Clarke, C. J., Bate, M. R., 2004a, MNRAS, 347, 759
- [43] Delgado-Donate, E., Clarke, C. J., Bate, M. R., Hodgkin, S. T., 2004b, MNRAS, 351, 617
- [44] Duchêne, G., 1999, A&A, 341, 547
- [45] Duchêne, G., Bouvier, J., Bontemps, S, André & Motte, F., 2004, A&A, 427, 651
- [46] Duquennoy, A. & Mayor, M., 1991, A&A, 248, 485 (DM91)
- [47] Durisen, R. H., Gingold, R. A., Tohline, J. E. & Boss, A. P., 1986, ApJ, 305, 281
- [48] Eggenberger, A., Halbwachs, J.-L., Udry, S. & Mayor, M., 2004, RevMexAA (Serie de Conferencias), 21, 28
- [49] Elmegreen, B. G. 2000, ApJ, 530, 227
- [50] Fischer, D. A. & Marcy, M. 1992, ApJ, 396, 178 (FM92)
- [51] Ghez, A. M., McCarthy, D. W., Patience, J. L. & Beck, T. L., 1997, ApJ, 481, 378
- [52] Ghez, A. M., Neugebauer, G. & Matthews, K. 1993, AJ, 106, 2005
- [53] Gliese, W., 1969, Veröffentlichungen des Astronomischen Rechen-Instituts Heidelberg, No. 22
- [54] Gingold, R. A., Monaghan, J. J., 1977, MNRAS, 181, 375
- [55] Gingold, R. A., Monaghan, J. J., 1982, J. Comp. Phys., 46, 429
- [56] Goodman, A. A., Benson, P. J., Fuller, G. A. & Myers, P.C. 1993, ApJ, 406, 528 (G93)
- [57] Goodwin, S. P. & Whitworth, A. P., 2004, A&A, 413, 929
- [58] Goodwin, S. P., Whitworth, A. P., Ward-Thompson, D., 2004a, A&A, 414,633
- [59] Goodwin, S. P., Whitworth, A. P., Ward-Thompson, D., 2004b, A&A, 419, 543
- [60] Goodwin, S. P., Whitworth, A. P., Ward-Thompson, D., 2004c, A&A, 423, 169

- [61] Grenier, I. A., 2005, in 'The Young Local Universe - Star formation in our and nearby galaxies', ed. Chalabaev, A., Montmerle, T. & Trần Thang Vân, J., Thê Giói Publishers, p. 249
- [62] Griffin, R. F., Griffin, R. E. M., Gunn, J. E. & Zimmerman, B. A., 1988, AJ, 96, 172
- [63] Halbwachs, J. L., Mayor, M., Udry, S. & Arenou, F., 2003, A&A, 397, 159
- [64] Heggie, D. C. & Mathieu, R. D., 1986, LNP, 267, 233
- [65] Hennebelle, P., Whitworth, A. P., Gladwin, P. P. & André, Ph, 2003, MNRAS, 340, 870
- [66] Hennebelle, P., Whitworth, A. P., Cha, S.-H. & Goodwin, S. P., 2004, MNRAS, 348, 687
- [67] Hernquist, L., Bouchet, F. R. & Suto, Y., 1991, ApJS, 75, 231
- [68] Hubber, D. A., Goodwin, S. P. & Whitworth, A. P., 2006, A&A, 450, 881
- [69] Hubber, D. A. & Whitworth, A. P., 2005, A&A, 437, 113
- [70] Inutsuka, S., Miyama, S. M., 1992, ApJ, 388, 392
- [71] Jeans, J. H., 1929, Astronomy and Cosmogony (Cambridge University Press:Cambridge, UK)
- [72] Jijina, J., Myers, P. C. & Adams, F. C., 1999, ApJS, 125, 161
- [73] Johnstone, D., Wilson, C. D., Moriarty-Schieven, G., Joncas, G., Smith, G., Gregersen, E. & Fich, M., 2000, ApJ, 545, 327
- [74] Johnstone, D., Fich, M., Mitchell, G. F., & Moriarty-Schieven, G., 2001, ApJ, 559, 307
- [75] Kitsionas, S. & Whitworth, A. P., 2002, MNRAS, 330, 129
- [76] Klein, R. I., Fisher, R. & McKee, C. F., 2004, RevMexAA (Serie de Conferencias) 22, 3
- [77] Klessen, R. S., 1997, MNRAS, 292, 11
- [78] Klessen, R. S., Heitsch, F. & Mac Low M-M. 2000, ApJ, 535, 887
- [79] Köhler, R. & Leinert, C., 1998, A&A, 331, 977
- [80] Köhler, R., Kunkel, M., Leinert, C. & Zinnecker, H., 2000, A&A, 356, 541
- [81] Köhler, R., 2001, AJ, 122, 3325

- [82] Köhler, R., 2004, *RevMexAA (Serie de Conferencias)*, 21, 104
- [83] Kouwenhoven, M. B. N., Brown, A. G. A., Zinnecker, H., Kaper, L. & Portegies Zwart, S. F., 2005, *A&A*, 430, 137
- [84] Kroupa, P. 1995a, *MNRAS*, 277, 1491
- [85] Kroupa, P. 1995b, *MNRAS*, 277, 150
- [86] Kroupa, P., 2001, *MNRAS*, 322, 231
- [87] Kroupa, P., Aarseth S. & Hurley J. 2001, *MNRAS*, 321, 699
- [88] Kroupa, P. & Bouvier, J., 2003, *MNRAS*, 346, 343
- [89] Kroupa, P. & Bouvier, J., 2003, *MNRAS*, 346, 369
- [90] Kroupa, P., Bouvier, J., Duchêne, G. & Moraux, E., 2003, *MNRAS*, 346, 354
- [91] Kroupa, P. & Burkert, A 2001, *ApJ*, 555, 945
- [92] Lada, C. J. & Lada, E. A., 1991, *ASPC*, 13, 3
- [93] Lada, C. J., 1999, in 'The Origin of Stars and Planetary Systems', ed. Lada, C. J. & Kylafis, N. D., Kluwer Academic Publishers, p. 143
- [94] Lada, C. J. & Lada, E. A., 2003, *ARA&A*, 41, 57
- [95] Lada, C. J, Alves, J. F. & Lombardi, M., 2006, "Protostars and Planets V", in press
- [96] Larson, R. B., 1981, *MNRAS*, 194, 809
- [97] Larson, R. B., 2003, *Reports on Progress in Physics*, 66, 1651
- [98] Leinert, Ch., Zinnecker, H., Weitzel, N., Christou, J., Ridgway, S. T., Jameson, R. & Haas, M., 1993, *A&A*, 278, 129
- [99] Lucy, L. B., 1977, *AJ*, 82, 1013
- [100] Luhman, K. L., Briceño, C., Stauffer, J. R., et al., 2003, *ApJ*, 590, 348
- [101] Luhman, K. L. 2004, *ApJ*, 617, 1216
- [102] McCaughrean, M., Rayner, J. & Zinnecker, H., 1991, *MmSAI*, 62, 715
- [103] McDonald, J. M. & Clarke, C. J., 1993, *MNRAS*, 262, 800

- [104] Makino, J., 1991, *ApJ*, 369, 200
- [105] Makino, J. & Aarseth, S. J., 1992, *PASJ*, 44, 141
- [106] Martín, E. L., Brander, W., Bouvier, J., Luhman, K. L., Stauffer, J., Zapatero Osorio, M. R. & Barrado y Navascués, D., 2000, *ApJ*, 543, 299
- [107] Mathieu, R. D., 1994, *ARA&A*, 32, 465
- [108] Mayor, M., Duquennoy, A., Halbwachs, J.-L. & Mermilliod, J.-C., 1992, *Complementary Approaches to Double and Multiple Star Research*, ASP Conference Series, Vol. 32, IAU Colloquium 135, ed. H.A. McAlister & W.I. Hartkopf, p. 73
- [109] Maxted, P. F. L. & Jeffries, R. D., 2005, *MNRAS*, 362, 45
- [110] Mazeh, T., Goldberg, D., Duquennoy, A. & Mayor, M., 1992, *ApJ*, 401, 265
- [111] Mazzei, P. & Pigatto, L., 1989, *A&A*, 213, L1
- [112] Melo, C. H. F., 2003, *A&A*, 410, 269
- [113] Mermilliod, J.-C., Rosvick, J. M., Duquennoy, A. & Mayor, M., 1992, *A&A*, 265, 513
- [114] Mermilliod, J.-C. & Mayor, M., 1999, *A&A*, 352, 479
- [115] Mikkola, S. & Aarseth, S. J., 1993, *Celestial Mechanics and Dynamical Astronomy*, 57, 439
- [116] Monaghan, J. J., 1992, *ARA&A*, 30, 54
- [117] Monaghan, J. J., Lattanzio, J. C., 1985, *A&A*, 149, 135
- [118] Morris, J. P., Monaghan, J. J., 1997, *JCompPhys*, 136, 41
- [119] Motte, F. A., André, P. & Neri, R., 1998, *A&A*, 336, 150
- [120] Motte, F. A., André, P., Ward-Thompson, D. & Bontemps, S., 2001, *A&A*, 372, L41
- [121] Myers, P. C., 1983, *ApJ*, 1983, 270
- [122] Myhill, E. A. & Kaula, W. M., 1992, *ApJ*, 386, 578
- [123] Padgett, D. L., Strom, S. E. & Ghez, A., 1997, *ApJ*, 477, 710
- [124] Patience, J., Ghez, A. M., Reid, I. N., Weinberger, A. J. & Matthews, K., 1998, *AJ*, 115, 1972

- [125] Patience, J., Ghez, A. M., Reid, I. N. & Matthews, K. 2002, *AJ*, 123, 1570
- [126] Perryman, M. A. C., Brown, A. G. A., Lebreton, Y., Gomez, A., Turon, C., de Strobel, G. Cayrel, Mermilliod, J. C., Robichon, N., Kovalevsky, J. & Crifo, F., 1998, *A&A*, 331, 81
- [127] Petr, M. G., Coudé Du Foresto, V., Beckwith, S. V. W., Richichi, A. & McCaughrean, M. J., 1998, *ApJ*, 500, 825
- [128] Pfalzner, S. & Gibbon, P., 1996, 'Many-body tree methods in physics' (Cambridge University Press)
- [129] Pinfield, D. J., Dobbie, P. D., Jameson, R. F., Steele, I. A., Jones, H. R. A. & Katsiyannis, A. C., 2003, *MNRAS*, 342, 1241
- [130] Press, W. H., Teukolsky, S. A., Vetterling, W. T. & Flannery, B. P., 1992, 'Numerical recipes in FORTRAN. The art of scientific computing' (Cambridge University Press)
- [131] Price, D. J., 2004, 'Magnetic fields in Astrophysics', PhD Thesis
- [132] Prosser, C. F., Stauffer, J. R., Hartmann, L., Soderblom, D. R., Jones, B. F., Werner, M. W. & McCaughrean, M. J., 1994, *ApJ*, 421, 517
- [133] Ratzka, Th., Köhler, R. & Leinert, Ch., 2005, *A&A*, 437, 611
- [134] Rees, M. J., 1976, *MNRAS*, 176, 483
- [135] Rosswog, S., Davies, M. B., Thielemann, F.-K. & Piran, T., 2000, *A&A*, 360, 171
- [136] Reipurth, B. & Zinnecker, H. 1993, *A&A*, 278, 8
- [137] Salpeter, E. E, 1955, *ApJ*, 121, 161
- [138] Scally, A, Clarke, C. & McCaughrean, M. J., 1999, *MNRAS*, 306, 253
- [139] Shatsky, N. & Tokovinin, A., 2002, *A&A*, 382, 92
- [140] Shu, F. H., Adams, F. C. & Lizano, S., 1987, *ARA&A*, 25, 23
- [141] Simon, M., Chen, W. P., Howell, R. R., Benson, J. A. & Slowik, D. 1992, *ApJ*, 384, 212
- [142] Simon, M., Ghez, A. M., Leinert, Ch., Cassar, L., Chen, W. P., Howell, R. R., Jameson, R. F., Matthews, K., Neugebauer, G & Richichi, A., 1995, *ApJ*, 443, 625
- [143] Simon, M., Close, L. M. & Beck, T. L., 1999, *ApJ*, 117, 1375

- [144] Sod, G. A., 1978, *J. Comp. Phys.*, 27, 1
- [145] Stahler, S. W. & Palla, F., 2004, *The Formation of Stars* (Wiley-VCH Verlag GmbH & Co. KGaH, Weinheim)
- [146] Stefanik, R. P. & Latham, D. W., 1992, *Complementary Approaches to Double and Multiple Star Research*, ASP Conference Series, Vol. 32, IAU Colloquium 135, ed. H.A. McAlister & W.I. Hartkopf, p. 173
- [147] Sterzik, M. F. & Durisen, R. H. 1998, *A&A*, 339, 95
- [148] Sterzik, M. F. & Durisen, R. H. 2003, *A&A*, 400, 1031
- [149] Stiefel, E. L. & Scheifele, G., 1971, 'Linear and regular celestial mechanics' (Springer-Verlag)
- [150] Testi, L. & Sargent, A. L., 1998, *ApJ*, 508, L91
- [151] Thomas, P. A. & Couchman, H. M. P., 1992, *MNRAS*, 257, 11
- [152] Tohline, J. E. 2002, *ARA&A*, 40, 349
- [153] Torres, G., Neuhäuser, R. & Guenther, K. W., 2002, *AJ*, 123, 1701
- [154] Truelove, J. K., Klein, R. I., McKee, C. F., Holliman, J. H., II, Howell, L. K., Greenough, J. A., 1997, 489, L179
- [155] Truelove, J. K., Klein, R. I., McKee, C. F., Holliman, J. H., II, Howell, L. K., Greenough, J. A., Woods, D. T., 1998, *ApJ* 495, 821
- [156] Udry, S., Mayor, M., Delfosse, X., Forveille, T. & Perrier-Bellet, C., 2000, *Birth and Evolution of Binary Stars*, Poster Proceedings of IAU Symposium No. 200, ed. Bo Reipurth & Hans Zinnecker, p. 158.
- [157] Valtonen, M. & Mikkola, S. 1991, *ARA&A*, 29, 9
- [158] Van Albada, T. S. 1968, *BAN*, 19, 479
- [159] Watkins, S. J., Bhattal, A. S., Boffin, H. M. J., Francis, N. & Whitworth, A. P., 1998a, *MNRAS*, 300, 1205
- [160] Watkins, S. J., Bhattal, A. S., Boffin, H. M. J., Francis, N. & Whitworth, A. P., 1998b; *MNRAS*, 300, 1214

- [161] White, R. J. & Ghez, A. M., 2001, *ApJ*, 556, 265
- [162] Whitworth, A. P., Chapman, S. J., Bhattal, A. S., Disney, M. J., Pongracic, H., Turner, J. A., 1995, *MNRAS*, 277, 727
- [163] Whitworth, A. P. 1998, *MNRAS*, 296, 442
- [164] Whitworth, A. P. & Stamatellos, D., 2006, Accepted by *A&A*
- [165] Whitworth, A. P. & Ward-Thompson, D. 2001, *ApJ*, 547, 317
- [166] Woitas, J., Leinert, Ch. & Köhler, R. 2001, *A&A*, 376, 982
- [167] Wood, D., 1981, *MNRAS*, 194, 201

